

**CARBON NANOTUBE/Ce<sub>x</sub>Sr<sub>1-x</sub>Fe<sub>y</sub>Co<sub>1-y</sub>O<sub>3</sub> PEROVSKITE NANO-  
COMPOSITES: SYNTHESIS AND PHYSICAL-CHEMICAL  
CHARACTERIZATION FOR LOW TO INTERMEDIATE  
TEMPERATURE SOLID OXIDE FUEL CELLS**



Durban

School of Chemistry and Physics

By

**Mlungisi Ntuthuko Sithole**

BSc (UKZN), BSc (Hons) (UKZN)

**Master's Degree**

June 2015

As the candidate's supervisors we have approved this thesis/dissertation for submission

Signed: 

Name: Patrick G. Ndungu Date: 09<sup>th</sup> June 2015 Supervisor

Signed: 

Name: Bernard O Owaga Date: 09<sup>th</sup> June 2015 Co-Supervisor

## **Preface**

The experimental work described in this dissertation for Masters was carried out in the School of Chemistry and Physics, University of KwaZulu-Natal, Westville campus from June 2012 to June 2014, under the close supervision of Dr Patrick G. Ndungu and co-supervised by Dr B. Omondi Owaga (University of KwaZulu-Natal).

These studies represent original work by the author and have not otherwise been submitted in any form for degree or diploma to any tertiary institution. Where use has been made of the work of others it is duly acknowledged in the text.

This dissertation has been prepared according to the format outlined in the guidelines from the Faculty of Science and Agriculture of UKZN, (FHDR Approved 13 March 2007).

## Declaration 1–Plagiarism

I Mlungisi Ntuthuko Sithole declare that

1. The research reported in this thesis, except where otherwise indicated, is my original research.
2. This thesis has not been submitted for any degree or examination at any other university.
3. This thesis does not contain other persons' data, pictures, graphs or other information, unless specifically acknowledged as being sourced from other persons.
4. This thesis does not contain other persons' writing, unless specifically acknowledged as being sourced from the researchers. Where other written sources have been quoted, then:
  - a. Their words have been re-written but the general information attributed to them has been referenced.
  - b. Where their exact words have been used, then their writing has been placed in italics and inside quotation marks and referenced.
5. This thesis does not contain text, graphics or tables copied and pasted from the internet, unless specifically acknowledge, and the source being detailed in the thesis and in the references sections.

Signed...  .....

## Declaration 2–Scientific Communications

Details of contributions to publications that form part and include research presented in this thesis.

### Presentation

Parts of this work have been presented at an international conference.

### List of conferences

1. CATSA international conference Port Edward, South Africa between 14 to 17 November 2013.

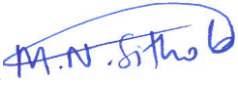
Title of paper presented: **Carbon Nanotube Perovskites Nano-Composites as cathode materials for Low–Intermediate Temperatures Solid Oxide Fuel Cells**

Authors: Mlungisi N. Sithole, Patrick G. Ndungu (Supervisor), Bernard Owaga (Co–supervisor)

### List of publications

#### Manuscripts in preparation

1. M. N. Sithole, P.G. Ndungu, B. Omondi, Synthesis and characterization of  $\text{Ce}_{0.6}\text{Sr}_{0.4}\text{Fe}_{0.8}\text{Co}_{0.2}\text{O}_3$  perovskite materials synthesized by sol–gel and CVD methods at low–intermediate temperatures for application as cathodes in the Solid Oxide Fuel Cells, 2015
2. M. N. Sithole, P.G. Ndungu, B. Omondi, Novel synthesis and characterization of MWCNT /  $\text{Ce}_{0.6}\text{Sr}_{0.4}\text{Fe}_{0.8}\text{Co}_{0.2}\text{O}_3$  perovskite materials synthesized by sol–gel and CVD methods at low–intermediate temperatures for application as cathodes in the Solid Oxide Fuel Cells, 2015

Signed ...  .....

## Abstract

Carbon nanotubes (CNTs) are among the most studied and extremely versatile and useful materials when it comes to nanoscience and nanotechnology. CNTs are considered chemically stable, have excellent electrical and thermal conducting characteristics, and have excellent mechanical properties. Their unique physical–chemical properties are the main reason they have found use in various applications that include sensors, batteries, supercapacitors, polymer composites, catalyst supports, display technology, absorbents, and construction materials. One of the biggest challenges with low to intermediate temperature solid oxide fuel cells (SOFC) is developing a material that exhibits superior electrochemical performance and excellent ionic and electronic conductivity at 300–600 °C, i.e. low to intermediate temperatures, for solid oxide fuel cell operation. To address this challenge, MWCNT/perovskite type ( $\text{Ce}_{0.6}\text{Sr}_{0.4}\text{Fe}_{0.8}\text{Co}_{0.2}\text{O}_3$ ) nanocomposites have been synthesized by Chemical Vapour Deposition (CVD) and sol–gel techniques. The materials were characterized by Fourier Transform Infrared Spectroscopy (FTIR), Raman Spectroscopy, Thermogravimetric Analysis (TGA), X–Ray Diffraction (XRD) and temperature programmed X–Ray Diffraction (XRD), Scanning Electron Microscopy Energy Dispersive X–Ray Spectroscopy (SEM/EDS), Transmission Electron Microscopy (TEM) and High Resolution Transmission Electron Microscopy (HRTEM). It was found that the CNT's allowed for the formation of perovskite phases at temperatures as low as 600 °C. The nanocomposites have some thermal stability at 560 °C and above this temperature MWCNTs will rapidly burn. CVD and sol–gel synthesis methods resulted in some coverage of the MWCNTs with the perovskite materials. Tests at 300, 400 and 500 °C showed moderate power outputs of 44, 74 and 117  $\text{mW}\cdot\text{cm}^{-2}$ , respectively. These were better than the control system without nanotubes.

## Acknowledgements

My sincere gratitude goes to my academic supervisors Dr Patrick Ndungu and Dr Bernard Owaga. Their patient support, encouragement and thirst for making change gave me strength throughout this research work. Their faith in me has given me great determination and a persevering attitude to this point.

I thank my family for their consistent support, and my fiancée Sbongile Nkala for supporting me by all means in the residence. This work would not have been possible without her assistance since I had no time of going over all necessary house services. She had no time too because she was also studying Social Work degree but she sacrificed for me. I really appreciated that.

Special thanks go to the members of the Microscopy Unit, for their valuable microscopy lesson, and assisting in setting up the instrument. Sincere appreciations to the Physical Chemistry laboratory colleagues for making my stay in the laboratory seem normal during awkward days and hours.

I am also grateful to the Academic staff, technical staff of School of Chemistry and Physics, in particular.

This work would not have been possible without the financial contributions of the National Research Foundation of South Africa through a Scarce skills scholarship and the Eskom TESP program.

## Table of contents

Preface .....	ii
Declaration 1–Plagiarism.....	iii
Declaration 2–Scientific Communications .....	iv
Abstract .....	v
Acknowledgements.....	vi
Table of contents.....	vii
List of figures.....	xi
Abbreviations.....	xvii
Chapter One .....	1
Introduction.....	1
1.1 Research Motivation.....	3
1.2 Problem Identification.....	4
1.3 Hypothesis.....	4
1.4 Aims and Objectives.....	5
Chapter Two.....	6
Literature Review.....	6
2.1 Fuel Cells.....	6
2.2 Solid Oxide Fuel Cells (SOFC).....	8
2.2.1 SOFC components and materials.....	9
2.2.1.1 Electrolyte.....	9
2.2.1.2 Anode.....	10
2.2.1.3 Cathode.....	11
2.2.2 Synthesis of SOFC materials.....	11
2.2.2.1 Synthesis of Cathode Materials Using Carbon Nanotubes.....	12
2.2.3 Current Challenges with SOFCs.....	12
2.2.3.1 Development of low to intermediate temperature SOFC.....	13
2.2.3.2 Composite Approach.....	13
2.3 Nanoscience, nanotechnology and nanomaterials.....	14
2.3.1 Properties of Nanomaterials: Size Effects.....	15
2.3.2 Synthesis of Nanomaterials: Bottom–up approach.....	16

2.3.2.1	Chemical Vapour Deposition (CVD).....	17
2.3.2.2	Chemical Vapour Deposition and Solid Oxide Fuel Cell Development.....	18
2.3.2.3	Sol–Gel method.....	19
2.3.2.4	Sol–Gel processes for Solid Oxide Fuel Cells .....	21
2.4	Carbon Nanotubes: Basic Structures and Properties .....	22
2.4.1	Synthesis of carbon nanotubes .....	22
2.4.2	The structure of carbon nanotubes .....	23
2.4.3	Uses of carbon nanotubes in SOFC .....	24
2.5	Perovskites: Basic Structure and Properties .....	26
2.5.1	The structure of perovskite .....	26
2.5.2	Uses of perovskites .....	28
2.6	Characterisation of nanomaterials .....	28
2.6.1	Fourier Transform Infrared Spectroscopy (FTIR) .....	28
2.6.2	Raman Spectroscopy.....	30
2.6.3	Thermogravimetric Analysis (TGA).....	31
2.6.4	Powder X–Ray Diffraction (PXRD).....	33
2.6.5	Electron Microscopy .....	34
2.6.5.1	Scanning Electron Microscopy (SEM) .....	34
2.6.5.2	Transmission Electron Microscopy (TEM) .....	35
2.6.5.3	High Resolution Transmission Electron Microscopy (HRTEM).....	37
2.7	Testing the electrochemical performance of nanomaterials .....	37
2.7.1	Mathematical model of SOFCs.....	37
2.7.2	Current density and overpotential .....	38
2.8	Summary.....	40
Chapter Three.....		42
Experimental Techniques.....		42
3.1	Materials .....	42
3.2	Synthesis.....	43
3.2.1	Surfactant Preparation.....	43
3.2.2	Synthesis of $Ce_xSr_{1-x}Fe_yCo_{1-y}O_3$ Perovskites .....	43
3.2.3	Synthesis of Carbon Nanotube– $Ce_xSr_{1-x}Fe_yCo_{1-y}O_3$ composite materials .....	45
3.3	Characterisation of the synthesized MWCNT/CSFC composites .....	47
3.3.1	Fourier–Transform Infrared Spectroscopy (FTIR) .....	47

3.3.2	Raman Spectroscopy.....	48
3.3.3	Thermogravimetric Analysis (TGA).....	49
3.3.4	X-Ray Diffraction (XRD) Analysis.....	49
3.3.5	Electron Microscopy.....	51
3.3.5.1	Scanning Electron Microscopy (SEM).....	51
3.3.5.2	Transmission Electron Microscopy (TEM).....	52
3.3.5.3	High Resolution Transmission Electron Microscopy (HRTEM).....	53
3.4	Button Cell Fabrication and Electrochemical Measurements.....	54
3.4.1	Cell Assembly.....	54
3.4.2	Electrochemical measurements.....	55
3.4.2.1	Polarization curves.....	55
3.4.3	Fuel Cell Parameter Calculations.....	57
3.5	Summary.....	59
Chapter Four.....		60
Characterization of MWCNT/Ce <sub>x</sub> Sr <sub>1-x</sub> Fe <sub>y</sub> Co <sub>1-y</sub> O <sub>3</sub> Nanocomposite Materials for Low to Intermediate Temperatures Solid Oxide Fuel Cells (LIT-SOFC).....		60
4.1	Fourier Transform Infrared Spectroscopy (FTIR) Analysis.....	60
4.1.1	Effect of MWCNT:CSFC ratio on FTIR spectra.....	65
4.2	Raman Spectroscopy.....	67
4.3	X-Ray Diffraction Studies.....	70
4.3.1	<i>In-situ</i> XRD experiment.....	71
4.3.2	Influence on different MWCNT/CSFC mass ratios.....	79
4.3.3	Influence of Varying x and y on CSFC with a 1:1 MWCNT/CSFC mass ratio.....	82
4.4	Thermogravimetric Analysis (TGA).....	89
4.4.1	Comparison of CVD versus sol-gel Synthesized Composites.....	89
4.4.2	Influence of different MWCNTs to CSFC mass ratios.....	91
4.4.3	Influence of Varying x and y on CSFC using a 1:0.5 MWCNT/CSFC mass ratio.....	95
4.5	Electron microscopy analysis of MWCNTs and CSFCs composites.....	97
4.5.1	SEM/EDS.....	97
4.5.2	TEM/HRTEM/STEM.....	100
4.6	Conclusions.....	102
Chapter Five.....		60
Electrochemical Performance of MWCNT/Ce <sub>x</sub> Sr <sub>1-x</sub> Fe <sub>y</sub> Co <sub>1-y</sub> O <sub>3</sub> Composites Applied as Cathodes for Low to Intermediate Temperatures Solid Oxide Fuel Cells (LIT-SOFC).....		104

5.1	Electrochemical Properties of MWCNT/CSFC Nanocomposites Synthesized by CVD method .....	105
5.1.1	Influence of ratios of MWCNT: CSFC on Polarization Curves .....	105
5.1.2	Influence of Varying x and y ratio on Electrochemical Properties with a 1:3 MWCNT/CSFC mass ratio.....	107
5.1.2.1	Half–Cell Testing on 1 MWCNT/3 CSFC with $x = y = 0.2$ , $x = 0.6$ , $y = 0.8$ and $x = y = 0.8$ in cerium and in iron .....	107
5.1.2.2	Symmetrical Cell Testing on 1 MWCNT/3 CSFC with $x = y = 0.2$ , $x = 0.6$ , $y = 0.8$ and $x = y = 0.8$ in cerium and in iron .....	110
5.1.2.3	Asymmetrical Cell Testing on 1 MWCNT/3 CSFC with $x = y = 0.2$ , $x = 0.6$ , $y = 0.8$ and $x = y = 0.8$ in cerium and in iron.....	113
5.2	Electrochemical Properties of MWCNT/CSFC Perovskite Nanocomposites Synthesized by Sol–Gel method .....	116
5.2.1	Influence of different ratios of MWCNT/CSFC Perovskite on Polarization Curves.....	116
5.2.2	Influence of Varying x and y ratio with a 1:3 MWCNT/CSFC mass ratio.....	118
5.2.2.1	Half–Cell Testing on 1 MWCNT/3 CSFC with $x = y = 0.2$ , $x = 0.6$ , $y = 0.8$ and $x = y = 0.8$ in cerium and in iron .....	119
5.1.2.2	Symmetrical Cell Testing on 1 MWCNT/3 CSFC with $x = y = 0.2$ , $x = 0.6$ , $y = 0.8$ and $x = y = 0.8$ in cerium and in iron .....	121
5.2.2.3	Asymmetrical Cell Testing on 1 MWCNT/3 CSFC with $x = y = 0.2$ , $x = 0.6$ , $y = 0.8$ and $x = y = 0.8$ in cerium and in iron.....	123
5.3	Stability over long period .....	127
5.4	Conclusions .....	129
	Chapter Six.....	131
	General Conclusions .....	131
6.1	Recommendations and Future Work.....	132
	References.....	134

## List of figures

Figure 2.1: Schematic drawing of a fuel cell comprised of an electrolyte, an anode and a cathode .....	8
Figure 2.2: The basic steps in the CVD process: (i) formation of volatile compounds, (ii) transportation and (iii) deposition of coatings .....	17
Figure 2.3: Mechanism of the sol–gel process: (i) mixing of liquid and alcohols, (ii) addition of acid and water, (iii) formation of the sol and (iv) formation of the gel .....	20
Figure 2.4: The structure of carbon nanotubes: (a) graphite, (b) (n, m) nanotube and (c) graphene layer, rolled to form SWCNT or MWCNT .....	24
Figure 2.5: The perovskite structure (ABO <sub>3</sub> ) type: (a) 12–fold coordination of the larger A–cation (blue), (b) 6–fold coordination of the B–cation (red), (c) The BO <sub>6</sub> octahedra link all vertices forming the cubic framework.....	27
Figure 2.6: Schematic diagram of an FTIR instrument.....	29
Figure 2.7: Schematic diagram of a Raman spectrometer .....	31
Figure 2.8: Schematic of a TGA instrument .....	32
Figure 2.9: Schematic diagram of a powder X–ray diffractometer.....	33
Figure 2.10: Schematic diagram of Scanning Electron Microscope.....	35
Figure 2.11: Schematic diagram of the Transmission Electron Microscope .....	36
Figure 2.12: Polarization plot showing the relationship between cell voltage and current density .....	38
Figure 3.1: The reactor used for calcining MWCNT/perovskite composites in the Labofurnace .....	44
Figure 3.2: Experimental apparatus used for calcination of Ce <sub>x</sub> Sr <sub>1-x</sub> Fe <sub>y</sub> Co <sub>1-y</sub> O <sub>3</sub> .....	45
Figure 3.3: (a) MWCNTs under sonication, (b) metal acacs, and the numbers referred to perovskites without MWCNTs (c) Surfactant Pluronic F–127 in ethanol water solvent system .....	46
Figure 3.4: Instrument used for FTIR Spectroscopy.....	48
Figure 3.5: Instrument used for Raman Spectroscopy .....	48
Figure 3.6: Thermogravimetric Analysis instrument used.....	49
Figure 3.7: Bruker D8 ADVANCE diffractometer used for the <i>in-situ</i> XRD.....	50
Figure 3.8: Instrument used for Scanning Electron Microscopy (LEO 1450) .....	52
Figure 3.9: Instrument used for Transmission Electron Microscopy (JEOL JEM–1010) .....	53
Figure 3.10: Instrument used for High Resolution Transmission Electron Microscopy ( JEOL JEM–2100) .....	54
Figure 3.11: Schematic diagram of the SOFC set–up showing all cell components: (1) and (2) electrodes, (3) to (6) bottom view of the open flanges test set–up .....	56

Figure 3.12: SOFC apparatus for measuring electrical performance. (1) Top view of the open flanges test fixture, (2) complete set-up .....	57
Figure 3.13: Schematic diagram of the experimental work .....	59
Figure 4.1: Representative Fourier transform infrared spectra of 1 MWCNT/3 Ce <sub>0.6</sub> Sr <sub>0.4</sub> Fe <sub>0.8</sub> Co <sub>0.2</sub> O <sub>3</sub> nanocomposite: Synthesized by (a) CVD and (b) sol-gel method after heat treatment at 400 °C.....	63
Figure 4.2: Representative Fourier transform infrared spectra of MWCNT/Ce <sub>0.6</sub> Sr <sub>0.4</sub> Fe <sub>0.8</sub> Co <sub>0.2</sub> O <sub>3</sub> nanocomposite with varying compositions, (i) (1:0.5), (ii) (1:1) and (iii) (1:3), synthesized by (a) CVD and (b) sol-gel method and heat treated at 400 °C .....	66
Figure 4.3: Raman spectra of MWCNT/CSFC (x = 0.6, y = 0.8) nanocomposite: Synthesized by (a) CVD and (b) sol-gel methods, after heat treatment at 400 °C .....	68
Figure 4.4: <i>In-situ</i> powder XRD diffractions synthesized by CVD method: (a) Ce <sub>0.6</sub> Sr <sub>0.4</sub> Fe <sub>0.8</sub> Co <sub>0.2</sub> O <sub>3</sub> under air and (b) MWCNT/Ce <sub>0.6</sub> Sr <sub>0.4</sub> Fe <sub>0.8</sub> Co <sub>0.2</sub> O <sub>3</sub> composite under N <sub>2</sub> gas. The samples were heat treated at different temperatures from 100–650 °C in 50 °C increments. Perovskite phases formed are indexed with (*).....	73
Figure 4.5: <i>In-situ</i> powder XRD diffractions synthesized by sol-gel method: (a) Ce <sub>0.6</sub> Sr <sub>0.4</sub> Fe <sub>0.8</sub> Co <sub>0.2</sub> O <sub>3</sub> under air and (b) MWCNT/Ce <sub>0.6</sub> Sr <sub>0.4</sub> Fe <sub>0.8</sub> Co <sub>0.2</sub> O <sub>3</sub> composite under N <sub>2</sub> gas. The samples were heat treated at different temperatures from 100–650 °C in 50 °C increments. Perovskite phases formed are indexed with (*).....	75
Figure 4.6: Room temperature XRD pattern of MWCNT/Ce <sub>0.6</sub> Sr <sub>0.4</sub> Fe <sub>0.8</sub> Co <sub>0.2</sub> O <sub>3</sub> nanocomposites: (i) (1:0.5), (ii) (1:1) and (iii) (1:3) synthesized by (a) CVD and (b) sol-gel method after heat treatment at 400 °C.....	81
Figure 4.7: Room temperature XRD diffractogram of 1 MWCNT/1 Ce <sub>x</sub> Sr <sub>1-x</sub> Fe <sub>y</sub> Co <sub>1-y</sub> O <sub>3</sub> (0.2 ≤ (x, y) ≤ 0.8) nanocomposite synthesized by CVD method after heat treatment at 400 °C .....	83
Figure 4.8: Room temperature XRD pattern of the 1 MWCNT/1 Ce <sub>x</sub> Sr <sub>1-x</sub> Fe <sub>y</sub> Co <sub>1-y</sub> O <sub>3</sub> (0.2 ≤ (x, y) ≤ 0.8) nanocomposites synthesized by sol-gel method after heat treatment at 400 °C .....	85
Figure 4.9: TGA curves of MWCNT/Ce <sub>0.6</sub> Sr <sub>0.4</sub> Fe <sub>0.8</sub> Co <sub>0.2</sub> O <sub>3</sub> synthesized by (a) CVD and (b) sol-gel method. Purge gas: air at 50 mL/min. Temperature program: ambient–1000 °C, and with a heating rate of 10 °C /min .....	91
Figure 4.10: TGA curves of MWCNT/Ce <sub>0.6</sub> Sr <sub>0.4</sub> Fe <sub>0.8</sub> Co <sub>0.2</sub> O <sub>3</sub> with different mass ratios, synthesized by (a) CVD and (b) sol-gel method. Purge gas: air at 50 mL/min. Temperature program: ambient–1000 °C, and with a heating rate of 10 °C /min .....	93

Figure 4.11: TGA curves of MWCNT/Ce<sub>x</sub>Sr<sub>1-x</sub>Fe<sub>y</sub>Co<sub>1-y</sub>O<sub>3</sub> (0.2 ≤ (x, y) ≤ 0.8) synthesized by CVD method. Purge gas: air at 50 mL/min. Temperature program: ambient–1000 °C, and with a heating rate of 10 °C /min..... 95

Figure 4.12: SEM images of 1MWCNT/1 Ce<sub>0.6</sub>Sr<sub>0.4</sub>Fe<sub>0.8</sub>Co<sub>0.2</sub>O<sub>3</sub> composites materials heat treated at 400 °C: (a) synthesized by CVD, (b) synthesized by sol–gel methods, (c) EDS elemental maps for Co, Sr, Ce, C, O and Fe and (d) EDS layered image of the composite materials synthesized by CVD method and heat treated at 400 °C..... 98

Figure 4.13: EDS spectrum of the mapped 1 MWCNT/1CSFC (x = 0.6, y = 0.8) composite synthesized by CVD method and heat treated at 400 °C ..... 99

Figure 4.14: HRTEM images of MWCNT/Ce<sub>0.6</sub>Sr<sub>0.4</sub>Fe<sub>0.8</sub>Co<sub>0.2</sub>O<sub>3</sub> (1:1) nanocomposite after heat treatment at 400 °C. CVD method: (a) low, (b) high magnification and (c) dark field imaging; sol–gel method samples (d) low, (e) high magnification and (f) dark field imaging of the samples 101

Figure 5.1: *I–V* and *I–P* curves of MWCNT/Ce<sub>0.6</sub>Sr<sub>0.4</sub>Fe<sub>0.8</sub>Co<sub>0.2</sub>O<sub>3</sub> composites with different ratios synthesized by CVD method. The cathodes were tested under symmetrical cells for 2 hours at 500 °C under air (100 mL.min<sup>-1</sup>) as an oxidant and humidified H<sub>2</sub> as a fuel (200 mL.min<sup>-1</sup>)..... 106

Figure 5.2: *I–V* and *I–P* curves of 1MWCNT/3Ce<sub>x</sub>Sr<sub>1-x</sub>Fe<sub>y</sub>Co<sub>1-y</sub>O<sub>3</sub> cathodes synthesized by CVD method. (a) x = y = 0.2, (b) x = 0.6, y = 0.8 and (c) x = y = 0.8. The cathodes were tested under single cells for 2 hours at each temperature under air (100 mL.min<sup>-1</sup>) as an oxidant and humidified H<sub>2</sub> as a fuel (200 mL.min<sup>-1</sup>) ..... 109

Figure 5.3: *I–V* and *I–P* curves of 1MWCNT/3Ce<sub>x</sub>Sr<sub>1-x</sub>Fe<sub>y</sub>Co<sub>1-y</sub>O<sub>3</sub> cathodes synthesized by CVD method. (a) x = y = 0.2, (b) x = 0.6, y = 0.8 and (c) x = y = 0.8. The cathodes were tested under symmetrical cells for 2 hours at each temperature under air (100 mL.min<sup>-1</sup>) as an oxidant and humidified H<sub>2</sub> as a fuel (200 mL.min<sup>-1</sup>)..... 112

Figure 5.4: *I–V* and *I–P* curves of 1MWCNT/3Ce<sub>x</sub>Sr<sub>1-x</sub>Fe<sub>y</sub>Co<sub>1-y</sub>O<sub>3</sub> cathodes synthesized by CVD method. (a) x = y = 0.2, (b) x = 0.6, y = 0.8 and (c) x = y = 0.8. The cathodes were tested under asymmetrical cells with NiO–YSZ as the anode for 2 hours at each temperature under air (100 mL.min<sup>-1</sup>) as an oxidant and humidified H<sub>2</sub> as a fuel (200 mL.min<sup>-1</sup>) ..... 114

Figure 5.5: *I–V* and *I–P* curves of MWCNT/Ce<sub>0.6</sub>Sr<sub>0.4</sub>Fe<sub>0.8</sub>Co<sub>0.2</sub>O<sub>3</sub> composite cathodes with different ratios synthesized by sol–gel method. The cathodes were tested under symmetrical cells for 2 hours at each temperature under air (100 mL.min<sup>-1</sup>) as an oxidant and humidified H<sub>2</sub> as a fuel (200 mL.min<sup>-1</sup>)..... 118

Figure 5.6:  $I-V$  and  $I-P$  curves of  $1\text{MWCNT}/3\text{Ce}_x\text{Sr}_{1-x}\text{Fe}_y\text{Co}_{1-y}\text{O}_3$  synthesized by sol-gel method. (a)  $x = y = 0.2$ , (b)  $x = 0.6, y = 0.8$  and (c)  $x = y = 0.8$ . The cathodes were tested under single cells for 2 hours at each temperature under air ( $100 \text{ mL}\cdot\text{min}^{-1}$ ) as an oxidant and humidified  $\text{H}_2$  as a fuel ( $200 \text{ mL}\cdot\text{min}^{-1}$ ) ..... 120

Figure 5.7:  $I-V$  and  $I-P$  curves of  $1\text{MWCNT}/3\text{Ce}_x\text{Sr}_{1-x}\text{Fe}_y\text{Co}_{1-y}\text{O}_3$  composite cathodes synthesized by sol-gel method. (a)  $x = y = 0.2$ , (b)  $x = 0.6, y = 0.8$  and (c)  $x = y = 0.8$ . The cathodes were tested under symmetrical cells for 2 hours at each temperature under air ( $100 \text{ mL}\cdot\text{min}^{-1}$ ) as an oxidant and humidified  $\text{H}_2$  as a fuel ( $200 \text{ mL}\cdot\text{min}^{-1}$ )..... 122

Figure 5.8:  $I-V$  and  $I-P$  curves of  $1\text{MWCNT}/3\text{Ce}_x\text{Sr}_{1-x}\text{Fe}_y\text{Co}_{1-y}\text{O}_3$  composite cathodes synthesized by sol-gel method. (a)  $x = y = 0.2$ , (b)  $x = 0.6, y = 0.8$  and (c)  $x = y = 0.8$ . The cathodes were tested under asymmetrical cells with NiO-YSZ as the anode for 2 hours at each temperature under air ( $100 \text{ mL}\cdot\text{min}^{-1}$ ) as an oxidant and humidified  $\text{H}_2$  as a fuel ( $200 \text{ mL}\cdot\text{min}^{-1}$ ) ..... 125

Figure 5.9: Long term stability measurement for a test cell,  $1\text{MWCNT}/3\text{Ce}_{0.6}\text{Sr}_{0.4}\text{Fe}_{0.8}\text{Co}_{0.2}\text{O}_3$  |YSZ| $1\text{MWCNT}/3\text{Ce}_{0.6}\text{Sr}_{0.4}\text{Fe}_{0.8}\text{Co}_{0.2}\text{O}_3$  synthesized by sol-gel method and tested under symmetrical cells at a constant cell voltage of 0.7 V at  $500 \text{ }^\circ\text{C}$  for 15 hours..... 128

Figure 5. 10: (a) and (b) SEM images of the cathode composite after a test for over 15 hours, (c) and (d) TEM images of low performance ( $1\text{MWCNT}/3\text{Ce}_{0.6}\text{Sr}_{0.4}\text{Fe}_{0.8}\text{Co}_{0.2}\text{O}_3$ ) and high performance ( $1\text{MWCNT}/3\text{Ce}_{0.6}\text{Sr}_{0.4}\text{Fe}_{0.8}\text{Co}_{0.2}\text{O}_3$ ), respectively ..... 129

## List of Tables

Table 3.1: Required masses of metal acacs for the preparation of $Ce_xSr_{1-x}Fe_yCo_{1-y}O_3$ perovskites by CVD technique.....	43
Table 3.2: Required masses of metal acacs and volumes of Pluronic F-127 for the synthesis of.....	44
Table 3.3: Required amounts for the synthesis of MWCNT/CSFC composites with different mass ratio .....	46
Table 3.4: Composites synthesized by either CVD or sol-gel methods .....	47
Table 4.1: Characteristic wavenumbers of functional groups in MWCNT/CSFC ( $x = 0.6, y = 0.8$ ) composites in FTIR .....	64
Table 4.2: Raman D and G bands intensity ratios of the MWCNT/CSFC composites before and after heat treatments at 400 °C for both CVD and sol-gel composites .....	70
Table 4.3: Diffraction angles ( $2\theta$ ), d values and Miller indices (h k l) for the CSFC and 1MWCNT/1 CSFC ( $x = 0.6, y = 0.8$ ) nanocomposite materials from <i>in-situ</i> experiments between 100 and 650 °C .....	76
Table 4.4: XRD reference data for the metal oxides used in the phase identifications .....	78
Table 4.5: Calculated crystallite sizes of perovskite nanoparticles from the <i>in-situ</i> XRD experiment.....	79
Table 4.6: Room temperature diffraction angles ( $2\theta$ ) and Miller indices of the (1MWCNT/0.5 $Ce_{0.6}Sr_{0.4}Fe_{0.8}Co_{0.2}O_3$ ) composite heat treated at 400 °C .....	82
Table 4.7: Room temperature diffraction angles and their Miller indices for the MWCNT and $Ce_xSr_{1-x}Fe_yCo_{1-y}O_3$ composite synthesized by CVD .....	84
Table 4.8: Room temperature diffraction angles and their Miller indices for the 1 MWCNT and 1 $Ce_xSr_{1-x}Fe_yCo_{1-y}O_3$ composites synthesized by sol-gel.....	87
Table 4.9: Calculated crystallite size for the MWCNT/ $Ce_xSr_{1-x}Fe_yCo_{1-y}O_3$ nanocomposites.....	88
Table 4.10: TGA results of the MWCNT/ $Ce_{0.6}Sr_{0.4}Fe_{0.8}Co_{0.2}O_3$ composites with different mass ratios synthesized by sol-gel and CVD methods and heat treated at 400 °C .....	94
Table 4.11: TGA results for the MWCNT/ $Ce_xSr_{1-x}Fe_yCo_{1-y}O_3$ ( $0.2 \leq (x, y) \leq 0.8$ ) nanocomposites synthesized by CVD and heat treated at 400 °C .....	96
Table 4.12: TGA results for MWCNT/ $Ce_xSr_{1-x}Fe_yCo_{1-y}O_3$ ( $0.2 \leq (x, y) \leq 0.8$ ) nanocomposites with different mass ratios synthesized by sol-gel method and heat treated at 400 °C .....	97
Table 4.13: EDS elemental analysis of the 1 MWCNT/1 $Ce_{0.6}Sr_{0.4}Fe_{0.8}Co_{0.2}O_3$ nanocomposites synthesized by CVD method.....	99

Table 5.1: Electrochemical performances of MWCNT/Ce <sub>x</sub> Sr <sub>1-x</sub> Fe <sub>y</sub> Co <sub>1-y</sub> O <sub>3</sub> cathode materials synthesized by CVD .....	115
Table 5.2: Electrochemical performance of MWCNT/Ce <sub>x</sub> Sr <sub>1-x</sub> Fe <sub>y</sub> Co <sub>1-y</sub> O <sub>3</sub> cathode materials synthesized by sol-gel technique .....	126

## Abbreviations

---

AFC	Alkaline Fuel Cell
AACVD	Aerosol Assisted Chemical Vapour Deposition
ASR	Area Specific Resistance
CVD	Chemical Vapour Deposition
CGO	Gadolinia doped ceria
CHP	Combined heat and power
CSFC	CeSrFeCoO <sub>3</sub>
DMFC	Direct Methanol Fuel Cell
DWCNTs	Double Wall Carbon Nanotubes
EDS	Energy Dispersive X-Ray Spectroscopy
EIS	Electrochemical Impedance Spectroscopy
FACVD	Flame-Assisted Chemical Vapour Deposition
FEGSEM	Field-Emission Gun Scanning Electron Microscopy
FTIR	Fourier Transform Infrared Spectroscopy
GBCO	GaBaCoO
HAADF	High Angle Annular Dark Field
HRTEM	High Resolution Transmission Electron Microscopy
LIT-SOFC	Low to Intermediate Temperature Solid Oxide Fuel Cell
LCC	La <sub>0.6</sub> Ca <sub>0.4</sub> CoO <sub>3</sub>
LSC	LaSrCrO <sub>3</sub>
LSFC	LaSrFeCoO <sub>3</sub>
LSGM	LaSrGdMgO <sub>3</sub>
MCFC	Molten Carbon Fuel Cell
MOCVD	Metal-Organic Chemical Vapour Deposition
MIEC	Mixed Ionic-Electronic Conductors

MWCNT	Multi Wall Carbon Nanotube
OCV	Open Circuit Voltage
PAFC	Phosphoric Acid Fuel Cell
PVD	Physical Vapour Deposition
PSFC	$\text{PrSrFeCoO}_3$
PEMFC	Proton Exchange Membrane Fuel Cell
RBM	Radial Breathing Mode
R & D	Research and Development
SEM	Scanning Electron Microscopy
SDC	Samarium Doped Ceria
SOFC	Solid Oxide Fuel Cell
STEM	Scanning Transmission Electron Microscopy
SWCNT	Single Wall Carbon Nanotube
TEC	Thermal Expansion Coefficient
TEM	Transmission Electron Microscopy
TGA	Thermal Gravimetric Analysis
TPB	Triple Phase Boundary
XRD	X-Ray Diffraction
YSZ	Yttria-stabilized zirconia

---

# Chapter One

## Introduction

Solid oxide fuel cells (SOFCs) are known as electrochemical energy conversion devices that produce electricity through chemical reactions between an oxidant and a fuel gas. The important components for the chemical reactions in SOFC systems are an anode, a cathode and an electrolyte. An external oxidant, normally oxygen from the air, is supplied at the cathode. Molecular oxygen is then reduced at the porous air electrode (cathode) to give oxygen anions [1, 2]. The produced ions migrate through the solid electrolyte (in this case yttria-stabilized zirconia (YSZ)) to the fuel electrode, and chemically react with the fuel, H<sub>2</sub> or a hydrocarbon (e.g. CH<sub>4</sub>), to give H<sub>2</sub>O or CO<sub>2</sub> plus heat and electricity. The advantages of SOFC over other types of fuel cells are higher energy efficiency and excellent fuel flexibility [3-5]. The applications of SOFCs can be found in mobile and also in stationary energy systems. Some of the examples of stationary SOFCs are heat and power systems for a house, factory or off grid power for a small settlement [6-12]. In terms of transportation systems and portable equipment, some SOFC systems have been developed and demonstrated as auxiliary power units for commercial trucks, and as portable generators for home-based and commercial environments [6, 7, 10-13].

It is known that SOFC processes are mainly possible at higher temperatures (800–1000 °C). These higher temperatures are problematic because they result in various forms of degradation, provide immense technological challenges and economic obstacles [14]. In order to commercialize SOFC technology, operating temperatures need to be further reduced so that more conventional materials can be used. In addition, this will allow more widespread applications in various mobile and portable systems. Unfortunately, SOFC performance decreases as the operating temperature is reduced especially due to increased ohmic resistance at the cathode. Therefore, low temperature (300–600 °C) solid oxide fuel cells (LT-SOFCs) with improved electrochemical performance have been the subject of extensive investigation for several decades and still continue to be an active area of research [15].

Extensive research on the development of LT-SOFCs has been done by re-designing the cell, reducing the electrolyte thickness, or by developing new materials with higher ionic conductivities, high electrolytic activity, low chemical reactivity and superior physical characteristics [14]. Despite the fact that IT-SOFC materials operating at temperatures between 600 - 800 °C have been reported in the literature there is still room for improvement to develop new systems that can operate below these temperatures [5, 16, 17]. This can be achieved by introducing materials with high mixed ionic-electronic conductivities (MIECs). Additionally, a buffer layer of CGO can be used to avoid reactions between YSZ and GBCO and achieve high performance [18, 19].

Perovskites ( $ABO_3$ ) with lanthanides or group two rare earth metals in the A-site and a mixture of transition metal occupying the B-site have shown excellent ionic-electronic conductivities. Previous research on perovskites as candidate materials for IT-SOFCs operating at temperatures ranging from 600–800 °C have found that the performance of the SOFC is not only dependent on the operating temperature of the system, but also depends on the particle size and morphology [17].

Past research efforts have been focused on improving the electrochemical performance of LT-SOFC materials by reducing the particle size of the material through the modification of sol-gel methods. Stability under atmospheres containing CO and chemical compatibility of  $GdBaCo_2O_{5+x}$  with different oxide ion conductors as cathode materials for SOFC have been studied by Tarancon et al. [18, 19]. The introduction of multiwall carbon nanotubes (MWCNTs) as templates in the development of perovskite materials with reduced particle size has been found to be a promising strategy for developing LT-SOFCs with small particle size. It was found that CNTs improve the performance of LT-SOFCs, and when used as composite materials with perovskite-type oxides resulted in enhanced electrical characteristics of LT-SOFCs [16, 17, 20].

The parameters of synthesis play a significant role in determining the microstructure of SOFC materials. Currently, sol-gel methods are being used to synthesize MWCNT/perovskite type oxides as cathode materials that operate at 700–800 °C for SOFCs. Little is known about the performance of these materials in SOFCs operating at temperatures of 300–500 °C. The present work is focused on the synthesis and characterization of the electrochemical performance of

cathode composites for LT-SOFCs. The use of MWCNTs as templates is proposed, as a possible way to achieving reduced particle size for the LT-SOFCs.

The purpose of the present work is to investigate the electrochemical performance of new SOFC composite cathode materials developed for low operating temperatures (300–500 °C), using MWCNTs as templates. Two synthesis methods will be compared; these are a modified sol–gel methodology, and a dry mix Chemical Vapour Deposition (CVD) method. One of the main problems with SOFCs is the high polarization at the cathode during the reduction of oxygen [21]. Improvement can be achieved by reducing the particle size to the nanoscale, hence, increasing the active area of the material [17]. The use of nanostructured materials seems as the most promising strategy at these temperatures with the high surface area compensating for the increase in resistance at lower temperatures [17, 22]. Perovskites such as  $\text{Pr}_{0.6}\text{Sr}_{0.4}\text{Fe}_{0.8}\text{Ce}_{0.2}\text{O}_3$  (PSFC) have shown promising performance for SOFCs operating at temperatures around 700 °C. Further reduction of temperatures seems possible. Therefore, this study is focused on the synthesis and electrochemical characterization of  $\text{MWCNT}/\text{Ce}_x\text{Sr}_{1-x}\text{Fe}_y\text{Co}_{1-y}\text{O}_3$  (MWCNT/CSFC) composites with  $0.2 \leq (x, y) \leq 0.8$  for SOFCs operating at temperatures of 300–500 °C. New methods need to be developed in order to prevent degradation issues caused by thermal cycling or diffusion at the interfaces as well as the reducibility of some materials at high temperatures. Furthermore, the high costs of the current SOFC fabrication processes can be reduced by replacing expensive praseodymium (Pr) by the more abundant and commercially available cerium (Ce) in the A–site of the  $\text{ABO}_3$  structure [14, 19].

## 1.1 Research Motivation

The chemical and physical properties of  $\text{MWCNT}/\text{Ce}_x\text{Sr}_{1-x}\text{Fe}_y\text{Co}_{1-y}\text{O}_3$  nanocomposite cathodes are influenced by the perovskite composition and microstructure in the nanocomposite. Synthesis method and heat treatment are factors which determine the physical–chemical properties and hence the electrical properties of these materials. Mixed ionic–electronic conducting perovskites (MIEC) have been widely used as cathodes in SOFCs at high temperatures (700–1000 °C). These high operating temperatures are problematic though and result in high costs and other issues like material incompatibility and degradation.

Here, the use of MWCNTs as template in the synthesis of CSFC perovskite nanocomposites materials is proposed. Nanocomposites will be tested as cathode materials in SOFCs at reduced operating temperatures (300–600 °C). A novel, sol–gel method is compared with the dry–mix CVD method. It is therefore important to investigate the variation of the structural and hence the electrochemical properties of the MWCNT/CSFC cathode composites. Chemical and physical characteristics of MWCNT/Ce<sub>x</sub>Sr<sub>1-x</sub>Fe<sub>y</sub>Co<sub>1-y</sub>O<sub>3</sub> nanocomposite materials where  $0.2 \leq (x, y) \leq 0.8$  in steps of 0.2 will be studied using Fourier Transform Infrared Spectroscopy (FTIR), Raman Spectroscopy, Thermogravimetric Analysis (TGA), X–Ray Diffraction (XRD) and temperature programmed X–Ray Diffraction (XRD), Scanning Electron Microscopy Energy Dispersive X–Ray Spectroscopy (SEM/EDS), Transmission Electron Microscopy (TEM) and High Resolution Transmission Electron Microscopy (HRTEM). Current, power densities (polarization curves) and area specific resistances (ASR) will be measured as indicators of electrochemical performance.

## **1.2 Problem Identification**

One of the biggest challenges with LT–SOFCs is developing materials that exhibit superior electrochemical performance and excellent ionic and electronic conductivity at 300–600 °C i.e. at low temperatures. To address this challenge, the use of MWCNT/perovskite nanocomposites has been proposed [17]. Here MWCNT/Ce<sub>x</sub>Sr<sub>1-x</sub>Fe<sub>y</sub>Co<sub>1-y</sub>O<sub>3</sub> nanocomposites for LT–SOFCs have been synthesized using CVD and a novel sol–gel technique. The reduction of the SOFC high operating temperatures affects the materials performance negatively. It has been shown that SOFC performances are based on materials microstructure. So, a good method of fabricating cathode nanoparticles at low to intermediate temperatures is needed in order to control the particle size growth and achieve good electrochemical performances of the cell.

## **1.3 Hypothesis**

It is proposed that the use of MWCNTs as template in the synthesis of cathode nanocomposite materials is a suitable technique for controlling the perovskite particle size and providing a suitable material for use at low operating temperatures for SOFCs. The reduced particle size is significant in the improvement of the MWCNT/perovskite nanocomposites electrochemical characteristics at low to intermediate operating temperatures. The substitution of Pr by Ce in the

MIEC perovskite ( $\text{Pr}_x\text{Sr}_{1-x}\text{Fe}_y\text{Co}_{1-y}\text{O}_3$ ) structure on the A-site, can further improve the electrochemical performance at 300–600 °C. The comparison of dry mix CVD and wet sol–gel methods at the above mentioned temperatures will reveal the contribution of chemical composition versus particle size in the improvement of MWCNT/perovskite nanocomposites for SOFC.

#### **1.4 Aims and Objectives**

The aim of this project is the design and fabrication of perovskite nanomaterials for the cathodes of low temperature SOFCs using carbon nanotubes as templates. The perovskites will be synthesized in the presence of MWCNTs to form nanocomposites with reduced particle sizes compared to conventional synthesis techniques. The morphology and microstructure of MWCNT/ $\text{Ce}_x\text{Sr}_{1-x}\text{Fe}_y\text{Co}_{1-y}\text{O}_3$  nanocomposites will be characterized before testing them as cathodes in a suitable SOFC button cell configuration operating at low temperatures. The correlation between structural and chemical properties will be established. The aim will be achieved via the following objectives:

- (i) Synthesize nano perovskites using wet (sol–gel) and dry (CVD) chemistry.
- (ii) Calcine the nanocomposite materials to form perovskites within the carbon nanotubes.
- (iii) Test the electrochemical performance of these nanocomposite materials as cathodes in low temperature regimes (300–500 °C) for SOFC applications.
- (iv) Compare microstructure and electrochemical properties for nanocomposites obtained by sol–gel or by CVD techniques.

## **Chapter Two**

### **Literature Review**

This Chapter gives background information on the properties of materials at the nanoscale level. It will give some explanation on why materials behave differently when they are at the nanoscale level. A brief discussion on the structure, synthesis techniques, chemical properties and their potential applications is presented. An overview of nanocomposites is given with specific reference to the use of MWCNTs as templates for the fabrication of MWCNT/perovskite oxide cathodes for low temperature SOFC. The key effort in this Chapter is to develop background knowledge that will be used in understanding and analysing the chemical and physical properties of nanocomposite materials under investigation in Chapters 4 and 5.

#### **2.1 Fuel Cells**

Fuel cells are electrochemical devices that convert the chemical energy of a reaction directly into electrochemical energy [6-10]. In every fuel cell there are two electrodes; an anode and a cathode. The electricity is produced by the reaction taking place at the electrodes [8, 9]. Every fuel cell also has an electrolyte which carries the electrically charged particles from one electrode to the other, and a catalyst for increasing the rate of reactions at the electrodes [10]. One big advantage of using fuel cells is that they do not greatly affect the environment negatively; they produce low levels of CO<sub>2</sub>, sulphur and nitrogen oxides (compared to fossil fuels), hence, they are taken as one of the promising power generation devices [6-8, 10].

Different types of fuels can be used in fuel cells; however, it is the type of electrolyte used that determines the type of fuel cell. Five major types are known, and these are alkaline fuel cell (AFC), polymer electrolyte membrane fuel cell (PEMFC), phosphoric acid fuel cell (PAFC), molten carbonate fuel cell (MCFC) and solid oxide fuel cell (SOFC) [8, 9]. AFCs use KOH as the electrolyte (OH<sup>-</sup> are the mobile ions) and operate at 100–250 °C. Their first successful use was in space vehicles e.g. in the Apollo and Shuttle programs by NASA [7, 9]. PEMFCs have a sulfonated polymer membrane as the electrolyte (H<sup>+</sup> are the mobile ions) and

operate at 60–120 °C and were initially used by NASA in the Gemini space program [7, 9]. Currently PEMFCs are favoured in cars, scooters, and many other types of vehicles and have been used in combined heat and power (CHP) systems [9]. PEMFCs use hydrogen and oxygen to operate; however there exist other types of fuel cells that use methanol (direct methanol fuel cell–DMFC), ethanol, formic acid, or ethylene glycol but operate in a similar way to PEMFCs [9]. PAFCs operate at approximately 200 °C with concentrated phosphoric acid as the electrolytes and  $H^+$  as the mobile ions. PAFCs were the first commercially successful fuel cells developed and are usually applied as CHP systems [7-9]. In the MCFC, the electrolyte is a liquid carbonate salt of sodium, potassium or lithium, and  $CO_3^{2-}$  acts as the source of mobile ions. MCFCs operate at ~ 650 °C, are used in medium–large scale CHP systems, with capacities ranging from kilowatts to megawatts, and are the most common type of fuel cell based CHP installed globally [9, 23].

Solid oxide fuel cells (SOFCs), commercial systems, operate at 800–1000 °C and use  $O^{2-}$  as the mobile ions and a solid ceramic as the electrolyte. The applications of SOFCs are in all sizes of CHP systems, with kilowatt to megawatt units on the market [7-9]. SOFCs do not suffer from the disadvantages of liquid electrolytes like all other types of fuel cells, and can use hydrocarbons as a fuel. With SOFCs, solid electrolytes are used to allow oxide ions to move from one electrode to the other. A common solid electrolyte is yttria–stabilized zirconia (YSZ). Oxide ions typically migrate slowly in solid  $Y_2O_3$  and in  $ZrO_2$ , but in YSZ, the ion conductivity increases [24, 25]. The basic fuel in all fuel cells is normally hydrogen, but oxygen is also essential, the aim being to generate electrical current that can be used to do work outside the cell [6]. The production of electrical current is dependent on the chemical reaction taking place in the fuel cell [7]. Figure 2.1 presents a schematic diagram that summarizes the operation of a fuel cell.

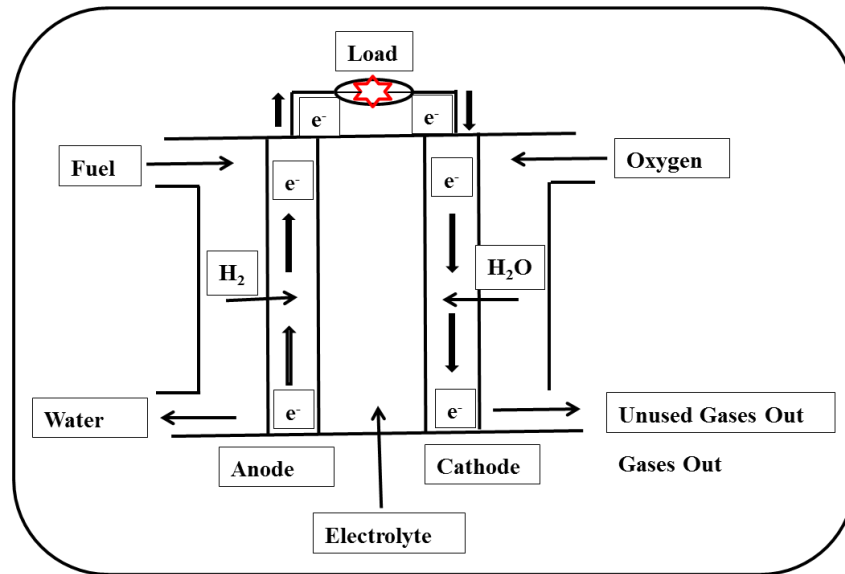


**Figure 2.1:** Schematic drawing of a fuel cell comprised of an electrolyte, an anode and a cathode [8]

Generally, an external oxidant, normally oxygen from the air, is supplied at the cathode. Molecular oxygen is then reduced at the porous air electrode (cathode) to give oxygen anions [1, 2]. The produced ions migrate through the solid electrolyte to the fuel electrode, and chemically react with the fuel,  $H_2$  to give  $H_2O$ , plus heat and electricity as shown in the equation below [8-10].



The fuel cell requires an external source of fuel to operate [4, 7-10]. The production of electricity or usable energy by fuel cells is limited by the amount of fuel put in. Fuel cells are a desirable alternative to battery technology, since they can produce usable current continuously for as long as fuel and oxidant are supplied—this makes the fuel cell a thermodynamically open system.

## 2.2 Solid Oxide Fuel Cells (SOFC)

Solid oxide fuel cells contain a solid ceramic electrolyte which in most cases is a metal oxide between an anode and a cathode [7-9, 24, 26-28]. In the operation of the SOFC, an external oxidant, normally oxygen from the air, is supplied at the cathode. Molecular oxygen is then reduced at the porous air electrode (cathode) to give oxygen anions ( $O^{2-}$ ) [1, 2]. The produced ions migrate through the solid electrolyte to the fuel electrode. The fuel is oxidized

at the anode, and if H<sub>2</sub> or a hydrocarbon (or CO) is used, H<sub>2</sub>O and CO<sub>2</sub> are produced. Additional, products are heat and electricity as in the equation shown below [7-9, 24, 26-28].



High temperature SOFCs achieve a high efficiency of conversion to power reactions, up to ~ 60 % overall efficiency (versus less than 30 % with combustion engines) [7-9], and have the added advantage that the high operating temperatures can be used for internal reforming or direct use of hydrocarbons [8, 9, 29]. The SOFC is widely known as fuel-flexible as it can use a number of fuels without any external reforming [2, 29]. Examples of fuels that can be used in SOFCs include methane, diesel, bio-fuels, jet fuel and others [2, 29]. Other than the proton exchange membrane fuel cell, which operates at low temperatures but is dependent on noble metal catalysts, high temperature SOFCs do not depend on noble metal catalysts. Therefore, CO can be used as a fuel rather than act as a poison. Hence, SOFC are considered as a promising emerging technology for stationary power generation systems [4, 8, 12].

## **2.2.1 SOFC components and materials**

### **2.2.1.1 Electrolyte**

The most essential part of a SOFC is the electrolyte, which is a gas-tight ceramic membrane [12, 25]. The electrolyte must have high ionic conductivity, low electronic conductivity and good thermal and chemical stability in relation to the surrounding reactants and the contacting electrode materials [4, 30]. Additionally, the thermal expansion coefficient (TEC) of the electrodes and contacting components must be similar. The electrolyte must be completely dense in order to optimize conductivity and reduce reactant cross-over [4, 31]. Finally the electrolyte in the SOFC system must be cost effective and not lead to environmental problems [4]. Materials that are currently used as electrolytes for SOFC are zirconia-based solids, and for LT-SOFCs ceria-based oxides with (Li/Na) carbonates and perovskite materials [32-34].

Perovskites are a class of materials that can be used as oxygen-ion conductors, e.g. in SOFCs [4, 32-34]. In the crystal structure of the perovskite, there are two cationic sites which can be occupied by lower valence cations, resulting in a wide range of possible oxygen-ion conducting materials [35, 36]. Lanthanum with strontium doping on the A-site of the perovskite and magnesium on the B-site are employed as electrolytes at temperatures as low

as 600 °C and have good ionic conductivity at a composition of  $\text{La}_{0.9}\text{Sr}_{0.1}\text{Gd}_{0.8}\text{Mg}_{0.2}\text{O}_{2.85}$  (LSGM) [4]. The problem with LSGM lies in the preparation of single phase electrolytes and the challenge of matching the thermal expansion coefficients [4]. Perovskites meeting all the requirements for the electrolytes still need to be developed.

### 2.2.1.2 Anode

The anode plays an important role in the electro-oxidation of fuel by catalysing the reaction as well as facilitating fuel access and product elimination. For optimal operation, anodes should have: (i) high stability under reducing conditions at elevated temperatures, (ii) electronic and ionic conductivity, therefore no loss of materials, (iii) comparable TEC to the electrolyte, (iv) good catalytic activity to oxidize the fuel ( $\text{H}_2$ ) and (v) relatively low resistance at high temperatures [26, 32, 37]. In terms of yttria-stabilized zirconia (YSZ), it is important that the YSZ in the electrolyte is well connected to the anode, and this is usually accomplished by using YSZ in the anode. This provides a conduction path for  $\text{O}^{2-}$  ions into the anode and increases the triple phase boundary (TPB) in the electrodes which helps optimise the overall reaction within the electrode system [4, 26, 32, 37, 38].

The limitations of the anode materials with lower temperature fuel cells (PEMFCs, AFCs and OAFCs) are that the catalysts are based on platinum group metals. With SOFCs, non-precious metal catalysts can be used, and the most common metal used is nickel. Nickel-based anodes can withstand the reducing conditions, high operating temperatures, possess high electron conductivity and the Ni can form excellent interconnecting networks within the electrode [26, 32, 37]. The most widely used anode materials are made up of nickel and solid electrolytes, such as Ni/YSZ cement or Ni/samarium doped ceria (SDC). These materials are targeted at maintaining porosity by avoiding sintering of the Ni particles and matching the TEC of anode and electrolyte [4, 26, 29, 37]. Nickel gives a good electronic conducting phase and helps transport electrons from the reaction site. YSZ or SDC support for Ni particles inhibits sintering and improves the TEC. However, because hydrocarbon fuels tend to deposit carbon on nickel-based anodes, quick carbon accumulation over the anode is often observed and leads to rapid degradation of the fuel cell's performance, and as a result copper is often used to replace the nickel [2, 26, 29, 32, 37-40]. Here, in this thesis, NiO-YSZ is used as an anode electrode for the asymmetrical cells in Chapter 5.

### **2.2.1.3 Cathode**

The reduction of molecular oxygen happens at the cathode in SOFCs. The cathode must be able to transport charged species directly to the electrolyte and to distribute the electrical current associated with the oxygen reduction reaction. SOFC cathode materials therefore need to have the following properties: (i) be stable in oxidizing condition, (ii) have sufficient electronic and ionic conductivities, (iii) have a porous structure, and (iv) be stable at high temperature with (v) a thermal expansion coefficient (TEC) closely matching that of the electrolyte materials [2, 4, 28, 32, 41, 42].

Currently, there are many oxides that have been studied as cathode materials for SOFC, and these are usually perovskite-type materials. There are a wide range of perovskite-structured materials that have been used as cathode materials in SOFC with interchanged A-site and B-site compositions. These include simple perovskites, layered perovskites and double perovskites [19, 32, 41]. For an oxide material to be used as a cathode in SOFCs it must have intrinsic p-type conductivity like the lanthanum strontium manganite (LSM) perovskites sometimes used with YSZ based electrolytes. Furthermore, perovskites must possess both ionic and electronic conduction [32, 38, 41, 42]. Highly mixed ionic-electronic conductivity is necessary to obtain high performance cathodes. In addition there have been several studies conducted on mixed oxygen ion and electron/hole conducting electrodes (MICEs) [43-45].

### **2.2.2 Synthesis of SOFC materials**

Electrolytes for SOFCs are normally processed by tape casting [33], citrate method [21] or uniaxial die-pressing [46]. These processing methods offer reduced reactive grain structures, controlled microstructural nanocrystalline grains and lower the diffusion distance of oxygen ions and the electrolytes resistance. In this work, a commercial YSZ electrolyte is used because of its high ionic conductivity.

The fabrication processes of cermet anode materials for SOFCs include a wide range of techniques such as solid-state reaction, sol-gel, glycine-nitrate, oxalate co-precipitation and carbon co-precipitation [47]. Additionally, anode and electrolyte powders can be mixed together by pressing and sintering the anode and electrolyte powders at high temperatures to

achieve dense Ni/YSZ anodes [26]. In this work Ni/YSZ is used which is made by mixing commercial nickel and YSZ powders.

Pure perovskite powders are the most commonly used cathode materials. They can be prepared by e.g. sol–gel process, solid–state reaction, nitrate and citrate routes or Penchini method [20, 45]. The performance is determined by the synthetic route and more specifically the particle size. The problem with perovskite materials is the control of particle size during the fabrication processes and during operation at the desired high temperatures [19, 28, 41, 42].

### **2.2.2.1 Synthesis of Cathode Materials Using Carbon Nanotubes**

Previously, a template–assisted route has been developed for achieving controlled perovskites particle sizes. Santillan et al. [16] synthesized  $\text{La}_{0.6}\text{Sr}_{0.4}\text{Fe}_{0.8}\text{Co}_{0.2}\text{O}_3$  (LSFC) perovskites in the presence of carbon nanotubes using an electrophoretic co–deposition method. Pinedo et al. [17, 48] used carbon nanotubes as composite material with perovskite–type oxides  $\text{Pr}_{0.6}\text{Sr}_{0.4}\text{Fe}_{0.8}\text{Co}_{0.2}\text{O}_3$  (PSFC) and  $\text{Pr}_{0.6}\text{Sr}_{0.4}\text{Fe}_{0.8}\text{Co}_{0.2}\text{O}_3/\text{Ce}_{0.8}\text{Sm}_{0.2}\text{O}_2$  (PSFC/SDC) giving rise to improved electrochemical behaviour at intermediate temperatures. Most of the previous reports use a sol–gel method and ionic surfactants. New cathode materials using non–ionic surfactants for SOFC devices operating at low to intermediate temperatures have not been reported.

### **2.2.3 Current Challenges with SOFCs**

High temperature SOFCs were first developed at Siemens Westinghouse and Rolls–Royce operating at temperatures of 850 °C and above [49]. The high operating temperatures (800–1000 °C) that these fuel cells required were problematic because of the thermal expansion mismatch, and high operating temperatures which lead to degradation of the cell [14, 32, 50]. Consequently, low (300–500 °C) to intermediate (600–800 °C) temperature SOFCs with good performances have been the focus of recent research efforts globally [15, 32, 42, 50]. This has been achieved by decreasing the thickness of the electrolyte, anode, cathode or all three. In addition, the application of materials with higher ionic conductivities has had some success in decreasing operating temperatures [14, 15, 32, 34, 42, 50]. However, one problem associated with the reduction of temperature is an increase in the cell polarisation which then results in the lowering of the SOFC cell performance. Controlling the particle size of the materials is another issue to be considered in developing low to intermediate temperature

SOFCs [32, 50]. Here, MWCNTs are used in trying to reduce the particle size of the perovskite cathodes.

### **2.2.3.1 Development of low to intermediate temperature SOFC**

The current challenge in LT-SOFC is to reduce the internal resistance. SOFC internal resistance can be due to various reasons such as the resistance of the electrolyte or the low oxygen ion conductivity of electrolyte materials [21]. Furthermore, electrode kinetics and polarisation resistance of the cathode are affected by the decrease in temperature [21].

The operating temperatures for SOFC could be further decreased if suitable materials were available. Using materials with high ionic conductivities, SOFC operating temperatures can be reduced while still attaining high cell performances. In the case of electrolyte materials, the thickness needs to be reduced in order to reduce the area specific resistance of the fuel cell and to improve the ionic conductivity of the electrolyte and hence the performance of the electrodes [21]. Issues such as property-microstructure relationships need to be considered in developing LT-SOFCs [21, 51, 52]. In this work, mixed ionic-electronic conducting (MIECs) perovskites with controlled particle size are developed in an effort to achieve improved electrochemical performance at reduced operating temperatures.

### **2.2.3.2 Composite Approach**

Composite electrolytes and electrodes are a combination of two or more solid phases that have been mixed physically. These materials possess unique ionic conductivities. The conductivity of the fabricated material can be enhanced depending on the combination of the materials.

Herein, the composite approach is applied to MWCNT/Ce<sub>x</sub>Sr<sub>1-x</sub>Fe<sub>y</sub>Co<sub>1-y</sub>O<sub>3</sub> nanocomposites as cathodes for LT-SOFC. In this case, MWCNTs are used for two reasons: (i) to enhance electrical performance by enhancing electronic conductivity of the composite materials [53], and (ii) to control the particle size growth of the perovskite nanoparticles for use in LT-SOFCs [17]. This approach relies heavily on nanoscience, nanotechnology and nanomaterials.

### 2.3 Nanoscience, nanotechnology and nanomaterials

Nanoscience focuses on the synthesis, characterisation and exploration of the physical and chemical properties of nanomaterials, while nanotechnology deals with the development of functional systems that exploit the properties of nanostructured materials [54]. Materials in nanoscience are classified as aggregates of atoms or molecules that characteristically have at least one dimension in the nanometer ( $1 \text{ nm} = 10^{-9} \text{ m}$ ) range, i.e.  $1 < 100 \text{ nm}$ . In this size range materials exhibit unique properties that differ from those in the bulk due to quantum confinement and surface effects [54, 55]. This has led to intense research worldwide that attempts to understand the unique chemical and physical properties exhibited by these nanomaterials [54]. Amid increasing global interest, strong national and international research and development (R&D) plans based on nanoscience have been developed in many countries. Materials at nanoscale level can be either synthesized by using bottom-up or top-down approaches [56]. Materials properties such as melting point, electrical or magnetic properties and chemical reactivity depend on the particle size [55]. Hence, fabrication methods for nanomaterials that allow the control of particle size are very important.

Nanotechnology has had a significant impact on R&D in energy related materials, e.g. materials for SOFCs [34]. Bottom-up approaches have been used to fabricate electrolyte, cathode and anode with controlled thickness or particle size [56]. One of the problems in SOFCs is the high operating temperature of  $800\text{--}1000 \text{ }^\circ\text{C}$ . By applying nanocomposite synthesis methods, the reduction of SOFC operating temperatures down to  $300 \text{ }^\circ\text{C}$  seems possible. The current focus is on reducing the particle size of these components to nanoscale level. The approaches from nanotechnology are presenting an interesting pathway in fabricating advanced fuel cell materials and technologies for LIT-SOFC with superior performance.

Nanomaterials possess extremely reduced sizes with at least one of the dimension less than  $100 \text{ nm}$ . The nanoscale can be in one (nanowires), two (surface films or free standing structures) or three dimensions particles [57, 58]. Nanoparticles can have many different shapes. They can e.g. be spherical, rod- or tube-shaped [58]. Examples of these range from zero-dimensional nanoparticles and one-dimensional nanowires to two-dimensional graphene sheets. Individual particles can agglomerate and form nanocomposites or they can fuse together and build more complex structures. Fabrication procedures of these different forms of nanomaterials play a significant role in achieving desired properties. Moreover,

quantum confinement of electrons leads to the development of nanomaterials with novel electrical, optical and magnetic properties [57, 58]. Carbon nanotubes have found wide use in nanotechnology because of their easy bulk fabrication and interesting mechanical, chemical and electronic properties [57].

The potential applications that use nanotechnology include nanoscale electronics and optics, nano-biological systems, nano-medicine, various areas in materials science, analytical applications, and fine chemical synthesis. Furthermore, it has become the backbone for the development of new materials based on the unique chemical and physical characteristics observed at the nanoscale level [59].

Nanotechnology may contribute to obtaining better sustainable energy systems and the more efficient use of finite energy sources. Renewable energy technologies are considered as substitutes for the current technologies in order to reduce costs [60] and be more environmentally friendly than conventional energy generations [60, 61]. Based on the need for affordable energy technologies, it is important to consider some potential solutions leading to a cleaner energy technology [62]. Some of the examples of these solutions are energy conservation through advanced energy efficiency, a reduction in the fossil fuel use and an increase in the use of renewable energy sources and technologies [62].

As a result of greenhouse gases emitted by conventional fossil fuel systems used for generation of energy in South Africa, the country is exposed to greenhouse effects and CO<sub>2</sub> emissions. This forces South Africa to develop new energy strategies that are not dependent on the use of coal to generate electricity. Some of the examples of the applications of nanomaterials to renewable energy technological systems are hydrogen fuel cells, solar cells and biotechnology. The SOFC is considered as a good alternative for the problematic use of fossil fuels because it uses hydrogen instead of a fuel to produce clean energy [63].

### **2.3.1 Properties of Nanomaterials: Size Effects**

Size effects are an important aspect of nanomaterials [64]. The effects on the fundamental properties of nanomaterials can be generally divided into two types. The first one is based on the change in distribution of electrons, i.e. change in density of states (e.g., magic numbers of atoms in metal clusters, quantum mechanical effects at small sizes). The second one is based on the increase in the relative surface area associated with nanostructures [65].

The electron distribution in materials especially in the case of shorter and stronger bonds between under-coordinated atoms plays an important role when a substance exists at the nanoscale [66]. Bulk materials do not have lone pairs of electrons around their bond but when those bonds are broken for self-assembly, lone pairs of electrons appear [3]. These lone electron pairs and the lone pair-induced dipoles result in the formation of functional groups [3].

Another factor to consider, is that the decrease in particle size results in an increase in the fraction of atoms present at the surface versus those that are surrounded by other atoms on all sides [67]. Such atoms are much more energetic. This is one reason why nanomaterials show distinct properties especially those related to reactivity compared to the bulk [67].

In the quantum size effect, electronic properties of solids change with a reduction in particle size as a result of confinement in the movement of electrons [68]. This phenomenon can be explained by the fact that the molecular orbital changes to delocalised band states [69]. In the case of semiconductors, an increase in the band gap is observed when the particle size is reduced to nanometer range [51]. Hence, physical and chemical characteristics of materials at the nanoscale change when the particle size is reduced and this gives nanomaterials their unique properties.

### **2.3.2 Synthesis of Nanomaterials: Bottom-up approach**

The processes involved in the synthesis or assembly of nanoscale materials and devices involve either bottom-up or top-down approaches [56]. In the bottom-up approach chemical and physical forces are employed to assemble basic units such as atoms, ions or molecules into more complex structures [56, 70]. In the top-down approach bulk materials are reduced in size to the nanometer scale using suitable tools [56]. Examples of the top-down approach are ball-milling, photolithography, dip-pen lithography, nano-moulding or nano-fluidics to mention a few [56, 70].

Bottom-up, nanomaterials can be synthesized using various methods such as membrane-based synthesis [71], template-based synthesis [72], sol-gel [73] and Chemical Vapour Deposition (CVD) methods [70]. Most of the methods for the fabrication of nanomaterials aim to achieve reduced particle size and uniform size distribution. Here, Chemical Vapour Deposition (CVD) and the sol-gel method, both examples of bottom-up approaches, are used

to synthesize MWCNT/perovskite nanocomposites. A brief review is provided in the following sections.

### 2.3.2.1 Chemical Vapour Deposition (CVD)

Chemical Vapour Deposition (CVD) was developed early in the 1880's for the production of incandescent lamps [74]. It was discovered that an improvement in the strength of the lamp filaments could be achieved by applying a coating of carbon or metal [74]. Since then, continuous development has improved the process and a number of reactions such as the carbonyl cycle, iodide decomposition and the magnesium–reduction reaction were developed for use in CVD [74, 75]. Figure 2.2 shows a schematic diagram of the basic CVD process [76, 77]. The general mechanism of the process involves three steps; (i) the generation of the volatile carrier compound, (ii) the delivery of volatile materials to the deposition chamber and (iii) the chemical reaction resulting in the formation of the desired product [77].

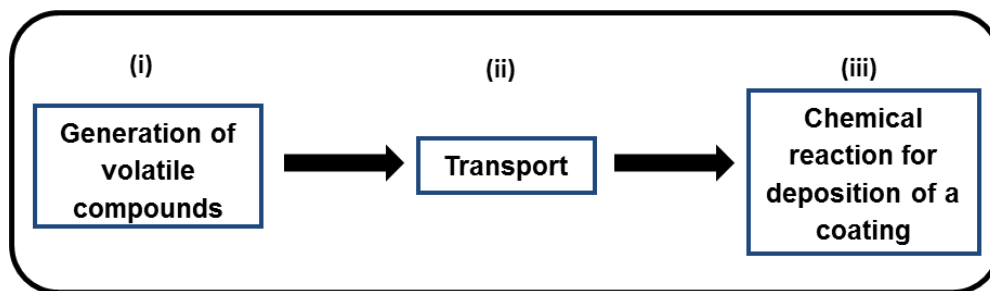


**Figure 2.2:** The basic steps in the CVD process: (i) formation of volatile compounds, (ii) transportation and (iii) deposition of coatings [53]

CVD is a chemical process that deposits a thin solid film or individual nanoparticles onto a substrate at high temperatures. In this process, reactant gases (precursors include gases, liquids or solids) are allowed to react with a heated substrate to form a solid surface film [75, 78]. This can be done under vacuum or at pressures close to or above atmospheric pressure [78].

In the development of CVD methods, it is important to use precursors that enable the deposition of films or nanoparticles with the desired stoichiometry. Precursors need to be stable at high enough temperatures for the process to achieve sufficient vapour pressures, and hence achieve good to high rates of deposition [79]. Precursors based on fluorinated and

non-fluorinated beta-diketone transition metal complexes such as copper and cobalt have been widely used in the CVD process since volatile and stable metal-containing species are formed [79, 80]. Here, desired elements are transported as volatile molecules (precursors), and the film is developed via chemical reactions of precursors, precursor fragments and with the substrate [81].

CVD is very widely used in industries and scientific research fields such as hard coatings and functional coatings on glass, semiconductors, dense structural parts, optical fibres and microelectronics [81]. Furthermore, CVD has been applied in industrial catalysis and synthesis of composites [53, 82]. The advantages of CVD are the fact that reactions are easy to monitor, and the production of high purity materials is possible [76, 82, 83]. The processing and the control of the CVD method depend on various factors such as surface reaction, volatility of compounds and reactivity of gases.

Dry deposition techniques taking place via surface modification of solid powders require the application of a reactive gas phase [76, 83]. In the CVD process, volatile chemical compounds are important in transporting non-volatile materials [76, 77, 83]. This leads to deposition due to chemical reactions such as reduction or thermal decomposition. The CVD method can be used for the synthesis of nanocomposite materials [84] and here, it is used for the fabrication of nanocomposite materials which are applied in SOFCs for reduced temperatures.

### **2.3.2.2 Chemical Vapour Deposition and Solid Oxide Fuel Cell Development**

CVD has been used to develop SOFC materials anodes, cathodes and electrolytes with high film qualities in an effort of reducing interfacial resistances which are a result of lower operating temperatures in LT and IT-SOFC [85]. This method has been used to modify film qualities for SOFC materials because it allows easy processing of vapour. The deposition rates are not high; hence, dense films can be prepared with amorphous or crystalline structures. It is also possible to fabricate films from dense to porous and nano-scale to micro-scale dimensions. Besides their low costs and simple apparatus, CVD also has the advantage of allowing for easy control of desired stoichiometry by dissolving metal precursors into organic solvents [85]. Due to the challenges of high operating temperatures of conventional SOFCs (as discussed in section 2.2.3), CVD has found applications in the

development of suitable thin film techniques for SOFC fabrication. Novel CVD techniques have been developed in the application of metal beta-diketone complexes as precursors to form thin films which are relevant to SOFC fabrication. The advantages of these novel CVD processes are seen in the IT-SOFC and micro-SOFC where the production of dense and porous films, manipulation of parameters and easy access to multi-layer films has been achieved [86]. Since SOFC processes require cathode-or anode-supported thin film electrolyte cells, metal-organic Chemical Vapour Deposition (MOCVD) techniques have been used to obtain highly crystalline, pure and dense oxide materials on porous substrates [87-90]. Torres et al. [89] have synthesized IrO<sub>2</sub>-YSZ composite films with high conductivities using MOCVD. A La<sub>0.8</sub>Sr<sub>0.2</sub>MnO<sub>3</sub> cathode fabricated by MOCVD was developed by Toro et al. [91] and applied in the IT-SOFC process. Activation losses occurring in the fuel cell which then decrease the performances can be prevented by applying materials prepared by Aerosol-Assisted Chemical Vapour Deposition (AA-CVD). The work done by Schulpp et al. [92] has shown high power densities of 850 mW.cm<sup>-2</sup> when fabricating gadolinia doped ceria (Ce<sub>0.8</sub>Ga<sub>0.2</sub>O<sub>2-δ</sub>) thin film for IT-SOFC using AA-CVD. CVD principles have also been used in the fabrication of unsupported anode or cathode electrodes, for example Sansernnivet et al. [93] synthesized La<sub>0.8</sub>Sr<sub>0.2</sub>CrO<sub>3</sub>-based perovskites (LSC) using Flame-Assisted Chemical Vapour Deposition (FA-CVD) [93].

Drawbacks of the CVD method are the requirement of dedicated equipment, its cost and the high temperatures required for deposition. New methods are needed in order to overcome these drawbacks. Sol-gel is the method of choice in trying to reduce costs and operating temperatures with the advantages of controlling microstructure and morphology of the targeted materials at low temperatures.

### **2.3.2.3 Sol-Gel method**

The sol-gel method was developed from different studies such as Bergman's [94, 95] studies on water around 1800, Ebelman's [96] on atmospheric oxygen and carbon dioxide in 1847 and Graham's [97] research on silica gels during the 1800s [98]. It was then widely used in the science of colloids during the 1800s. Since processing of ceramics and glasses requires high operating temperatures for the complete conversion of inorganic powders to dense materials through melting or sintering, the high temperature is the limiting parameter for the control of microstructure in these conventional ceramic processing methods [98, 99]. In

addition to the high operating temperatures, there are also limits to controlling the final materials properties, shape and surface features [99]. Based on this, sol–gel technologies operating at lower temperatures were introduced in hope of being able to fabricate novel shapes, unique and desirable surface properties, films, fibres and composites with improved performances [100]. It has been noticed that the low temperature sol–gel processes does require only few processing steps in order to develop nanosized particles. Currently the sol–gel process is used to achieve materials with controlled microstructures at nanometer level with physical and chemical properties different from the bulk [98]. This has led scientists to focus on the sol–gel process in attempting to design advanced nanomaterials with many advantageous applications in industries.

The sol–gel method is a wet chemical process, and this synthetic route involves the dispersion of colloidal particles in a liquid and the interconnection of pores to form a rigid network (gels) [99]. A gel is a network of pores of submicrometer dimensions and molecular chains with polymeric properties [99, 101]. Sol–gel is the evolution of a molecular network through the formation of a colloidal suspension (sol) and gelation of the sol to form a network in a continuous liquid phase (gel) [99]. When the solution is allowed to dry, it evaporates and leaves behind a gel with strong network of atoms clustered together by polymeric solutions. The sol–gel process allows the control of particle size during the formation of nanoparticles.

The general process of the sol–gel method involves homogenising and drying of the starting materials and solutions to form a gel. Liquid precursors are mixed with alcohols in order to obtain permanent connections with the orientation of bonds more significantly the metal–oxygen–carbons bonds which then lead to the formation of a gel. In the sol–gel mechanism shown in Figure 2.3, liquid precursors and alcohols are mixed with water under stirring followed by the addition of acid and water to give a solution mixture. Homogeneity is achieved with continuous stirring of the mixture.

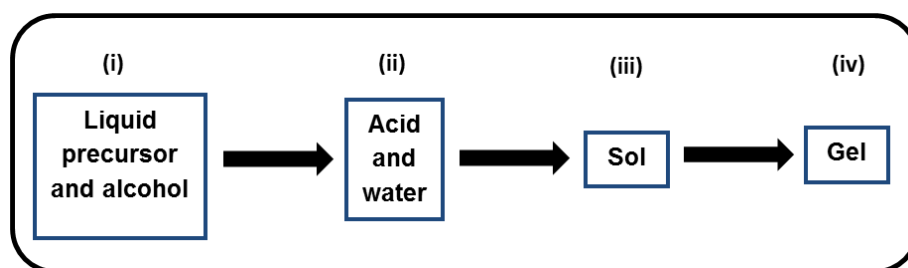


**Figure 2.3:** Mechanism of the sol–gel process: (i) mixing of liquid and alcohols, (ii) addition of acid and water, (iii) formation of the sol and (iv) formation of the gel [98, 99]

The sol-gel method has e.g. found use in the preparation of oxides and mixed oxides as catalytic materials. Debecker et al. [102] have developed a sol-gel route to fabricate advanced silica materials which are then used in many industrial applications such as inks and coatings, catalysts for fine and specialty chemicals, ceramics and nanocomposites [101]. This has been achieved by controlling the reaction rates of different molecular precursors, such as silicon and metal alkoxides, in hydrolysis and polycondensation reactions taking place in the sol-gel process [102]. In addition, the application of the sol-gel method is significant for materials for energy devices such as materials for SOFCs [17].

#### **2.3.2.4 Sol-Gel processes for Solid Oxide Fuel Cells**

Solid oxide fuel cell (SOFC) materials synthesized from sol-gel chemistry are important in trying to control the film thickness in the electrodes [103]. This technique allows deposition on the support using the dip-coating technique. Dip-coating and sol-gel can take place in series as in the case of the NiO-YSZ electrolyte synthesized by Kim et al. [104]. This can be achieved by monitoring the sol viscosity and adjusting the 'dipping rate', and hence manipulate the film thickness. Since SOFC performance is dependent on gas diffusion rates, a crack free film has to be prepared for SOFCs. Other researchers have developed SOFC electrode materials using sol-gel composites because of its affordability and possibilities of microstructure modifications [17, 22, 45, 103, 105-107]. To overcome SOFC difficulties reviewed in more details in section 2.3.3, a colloidal method is needed in order to prevent gas leakage during cell operation which then leads to reduced SOFC performance [104]. This can be achieved by depositing thin films of solid electrolyte with high ionic conductivity onto the porous anode support. Even though other chemical techniques can be used in the fabrication of dense SOFC electrodes, sol-gel is the method of choice because it produces highly homogeneous and fine grained films [104]. Kim et al. [104] and Gaudon et al. [108] have fabricated anode-supported electrolyte thin films and  $\text{La}_{1-x}\text{Sr}_x\text{MnO}_{3+\delta}$  ( $0 \leq x \leq 0.6$ ) perovskite type oxide for improving the SOFC performances at intermediate temperatures. Good electrical performances were obtained with peak power densities as high as  $550 \text{ mW.cm}^{-2}$  at  $850 \text{ }^\circ\text{C}$  [104]. Further advancement for fabrication of IT-SOFC materials have resulted from the preparation of high-performing perovskites, specifically  $\text{La}_3\text{NiO}_2$ , using a

non-ionic surfactant with the sol-gel method [3]. This material shows high peak power densities of  $848 \text{ mW.cm}^{-2}$  and very low interfacial resistance when applied as cathodes in the IT-SOFC at  $750 \text{ }^\circ\text{C}$  [3].

## **2.4 Carbon Nanotubes: Basic Structures and Properties**

Carbon nanotubes are defined as nanostructured materials with cylindrical shapes that consist of single- or multi-layers of rolled up graphitic planes [109]. The first discovery of carbon nanotubes was reported in 1991 by Iijima [110]. Single-walled carbon nanotubes (SWCNT) are made up of a single layer of graphene rolled into a cylindrical tube while multi walled carbon nanotubes are formed from several concentric layers of SWCNTs [111, 112]. Since the discovery of CNTs, synthesis, characterization, modification of properties and application of CNTs have received much attention [111, 112]. Carbon nanotubes exhibit interesting electronic, mechanical and structural properties [113]. These arise from their high surface area, high tensile strength and low density, with good mechanical, electrical, vibrational and thermal properties [109]. In nanotechnology applications, CNTs have been considered as an attractive metallic or semiconducting material. Some of the CNTs applications are found in the chemical industry, where they are used as gas adsorbents, templates, catalyst supports, composite reinforcements, chemical sensors and nanopipes [114]. One of the drawbacks of using CNTs is their low solubility in organic solvents which leads to limitations in their use. It is possible to disperse CNTs using some solvents by means of sonication [113]. In addition, one can functionalise, purify and oxidize CNT surfaces using oxidising agents such as concentrated nitric acid, sulphuric acid, aqua regia, hydrogen peroxide and others. Surface groups on the tubes serve as initiators for further chemistry on the tubes. Defects on the CNT surfaces might be increased while trying to functionalise, purify or oxidise [115-117].

### **2.4.1 Synthesis of carbon nanotubes**

The synthesis of carbon nanotubes in sizeable quantities follows a bottom-up approach [118]. Specific examples of producing carbon nanotubes include arc discharge [119, 120], laser ablation [121, 122] and chemical vapour deposition [123, 124]. Carbon nanotubes synthesized from these methods have both metallic and semiconducting properties [53, 119, 121]. Arc discharge involves the use of a direct-current arc voltage across two graphite

electrodes immersed in an inert gas such as He. In the presence of pure graphite rods, fullerenes are deposited in the chamber, and MWCNTs are deposited on the cathode. SWCNTs are generated when a graphite anode containing a metal catalyst (Fe or Co) is used with a pure graphite cathode [119, 120]. In the laser ablation method, a high power laser is used to vaporize carbon from a graphite target at high temperature. MWCNTs and SWCNTs can be obtained from this method. For SWCNTs production, metal particles as catalysts are added to the graphite targets similar to the arc discharge [121, 122]. Among several techniques of CNTs synthesis available today, Chemical Vapour Deposition (CVD) is most popular and widely used because of its low set-up cost, high production yield, and ease of scale-up. Compared to arc-discharge and laser-ablation techniques, CVD is a simple and economic technique for synthesizing CNTs at low temperature and ambient pressure. In this process, thermal decomposition of a hydrocarbon vapour is achieved in the presence of a metal catalyst. Generally, low-temperature CVD (600–900 °C) yields MWCNTs, whereas high-temperature CVD (900–1200 °C) favours SWCNT growth [81, 123-125].

#### 2.4.2 The structure of carbon nanotubes

In order to understand the structure of nanotubes it is important to start off with graphite, allotrope of carbon made entirely of carbon atoms just as diamond and fullerene. Graphite is the most stable form of crystalline carbon with carbon-carbon  $sp^2$  hybridisation under standard conditions. It has a layered planar structure with hexagonal rings (Figure 2.4 a). Graphene is the allotrope form of carbon in a two-dimensional sheet consisting of a single atomic layer of crystalline graphite (Figure 2.4 b) [57, 126]. The SWCNTs can be pictured as a rolled-up graphene structure which can be represented mathematically by a one-dimension vector  $\mathbf{V}$  in Equation 2.1 [126, 127]:

$$\mathbf{V} = n \mathbf{a}_1 + m \mathbf{a}_2 \quad (2.1)$$

where  $\mathbf{a}_1$  and  $\mathbf{a}_2$  represents unit vectors, and  $n$  and  $m$  are integers. This type of nanotube is called an  $(n, m)$  nanotube. Depending on the way the graphene sheet is rolled up, the structure can be described as a zig-zag  $(n, m = 0)$  tube or an armchair  $(n = m)$  tube [57, 127]. When the graphene sheet rolls up in the opposite direction of the symmetry, a chiral nanotube is formed [127]. Figure 2.4 shows the structure of graphite (a), a single layer of graphene (b), and the corresponding SWCNT and MWCNT (c).

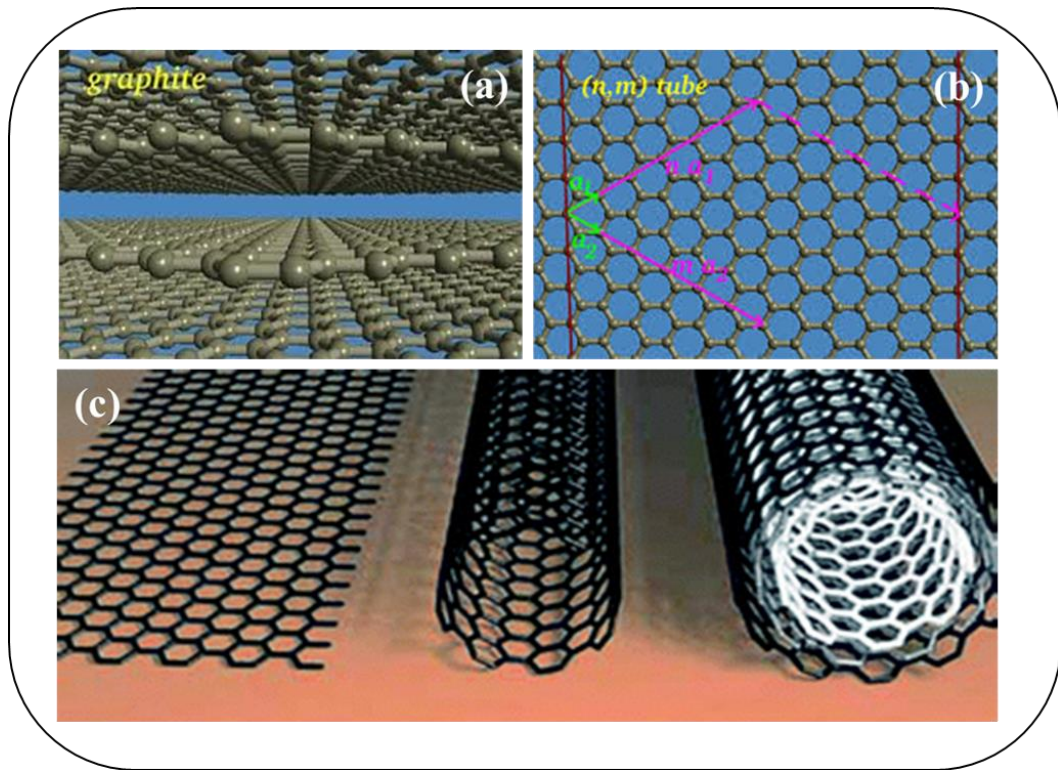


**Figure 2.4:** The structure of carbon nanotubes: (a) graphite, (b)  $(n, m)$  nanotube and (c) graphene layer, rolled to form SWCNT or MWCNT [127]

The outer diameter of MWCNTs ranges between 2 and 25 nm with interlayer distances of approximately 0.34 nm corresponding to the interlayer spacing in graphite [57, 126]. The nanotube is uniquely specified by the pair of integer numbers  $(n, m)$  or by its radius and chiral angle, theta ( $\theta$ ). Tubes have angles of  $0^\circ < \theta < 30^\circ$  and special tube types are the achiral tubes (tubes with mirror symmetry) [57, 126, 127]. All other tubes are referred to as chiral, tubes without mirror symmetry [57, 127]. The properties of CNTs are determined by the chiral angles in combination with their diameter. It has been found that CNTs can possess semiconducting or metallic behaviours [53].

### 2.4.3 Uses of carbon nanotubes in SOFC

Based on the properties displayed by carbon nanotubes, these nanomaterials have been proposed for use in many applications including conductive and high-strength composites, energy storage and conversion devices [128], membranes [129], nanosensors [57, 86, 130], field emission displays and radiation sources, hydrogen storage media, and nanometer-sized semiconductor devices, probes and interconnects [57, 126] as well as electronic devices,

electro-catalytic systems and composite materials as cathode templates especially for the SOFCs process [53, 101, 114, 131]. In the field of SOFCs, carbon nanotubes are used because of their conductivity. They can also contribute to the control of metal oxides particle size if used as templates with reports showing decreases in particle size from the order of micrometers to nano-scale [17]. The particle size can be modified by altering the CNT inner diameter. Smaller channel diameters produce smaller oxide particles while bigger channel diameters give large oxide particle sizes when these are formed inside the CNTs [101]. Oxide particles can also be formed outside the CNT surfaces as in the case of coatings with nanoparticles.

The interest in using CNTs as catalytic support materials arises due to their large surface area, high aspect ratio and their ability to disperse catalytically active metal particles [101]. Pan et al [132] have shown that the well-defined nanosized channels of CNTs give an interesting confinement environment for catalysis. Sub-nanometer-sized particles can be achieved within SWCNTs and DWCNTs. The electronic behaviour of the catalyst on the tube walls enhances the catalytic activity [132]. In electro-catalysis carbon nanotubes have been considered as advantageous supports for the catalyst, in that they increase the performance of the fuel cell at low costs [133, 134].

Recently, CNTs have been used in SOFCs as templates for the fabrication of cathode composites with perovskite-type oxides [17]. Carbon nanotubes are considered as potential materials to enhance the performance of these SOFC systems [135]. Furthermore, CNT/oxide composites with good electronic and ionic conductivities are employed as electrodes in some types of batteries and fuel cells [17].

In the SOFC technology, carbon nanotubes present an important advantage compared to polymeric templates as MWCNTs are thermally stable up to temperatures of around 650 °C. Here, the application of MWCNTs as a means of controlling the particle size of perovskites and improving the electrochemical performance of the electrode (cathode) is explored. These MWCNTs/metal oxide composites will be tested in SOFCs operating at low temperatures (300–500 °C).

## 2.5 Perovskites: Basic Structure and Properties

Perovskite is a ternary oxide structure type with the general formula ( $ABO_3$ ) named after L.A. Perovski who identified the mineral  $CaTiO_3$  [32, 35, 36, 41, 136]. A range of perovskites has been developed with A being either an alkaline earth or a rare earth metal and B a transition metal with partially filled d-orbitals [137]. Perovskites can adopt a wide range of chemical compositions. It is possible to occupy the A-sites with over 30% of the elements in the periodic table, and over half of the elements in the periodic table can be used in the B cation position, with almost 100% substitution [35, 137]. Advanced perovskites, e.g. for SOFC applications, have good ionic–electronic properties and are referred to as mixed ionic–conducting (MEIC) perovskites with cations of large ionic radii. An example of these MEIC perovskites is the one developed by Pinedo et al. [17],  $Pr_{0.6}Sr_{0.4}Fe_{0.8}Co_{0.2}O_3$  (PSFC), for solid oxide fuel cells. In this work, the A site  $Pr^{3+}$  cation is replaced by other lanthanides metals such as  $Ce^{3+}$ . The advantages of using  $Ce^{3+}$  over  $Pr^{3+}$  are its abundance and affordability. Furthermore the  $Ce^{3+}$  cation is larger than  $Pr^{3+}$ , hence the A-sites will be occupied by larger cations which may results in a perovskite with less distortions and higher conductivities compared to other perovskites with partially filled A-site [5, 35, 36, 41, 137].

### 2.5.1 The structure of perovskite

The oxygen sub-lattice of perovskite can be considered as cubic close-packed. The A-ion is most likely a pre- or post-transition element of lower charge (+1, +2 or +3) [137]. A occupies a site with 12-fold oxygen coordination. The B-site is filled by a transition-metal ion of higher charge (+3, +4 or +5) which is octahedrally coordinated by six oxygen atoms [4, 35, 41]. The A-site ions are larger than the B-site ions. The A-and-B cations occupy sites with cubic symmetry,  $O_h$  point group, whereas the O-anions occupy sites with  $D_{4h}$  symmetry (Figure 2.5) [35, 36, 41, 137].

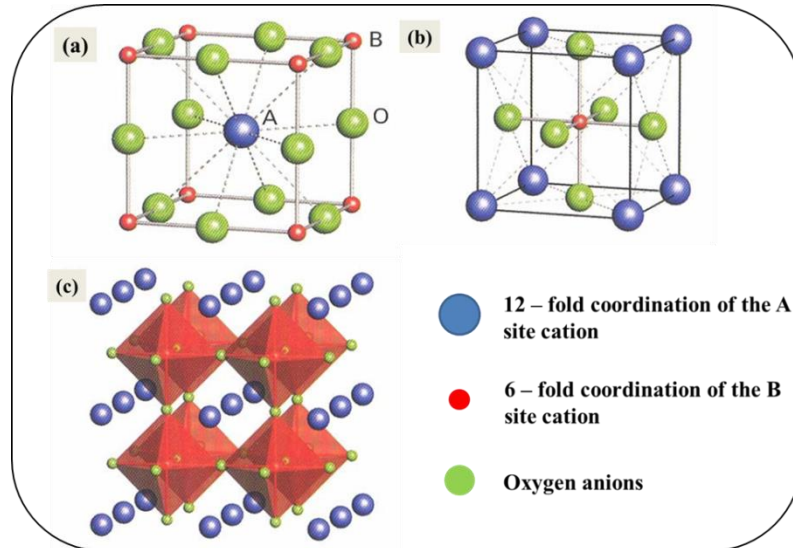


**Figure 2.5:** The perovskite structure (ABO<sub>3</sub>) type: (a) 12-fold coordination of the larger A-cation (blue), (b) 6-fold coordination of the B-cation (red), (c) The BO<sub>6</sub> octahedra link all vertices forming the cubic framework [36, 41, 137]

The ABO<sub>3</sub>-type perovskite structure consists of building units of BO<sub>6</sub>-octahedra that are corner connected with charge-balancing A-site cations occupying interstitial positions. In the high MEIC perovskites, a number of cations can occupy the A- and B positions. An example is the PSFC perovskite, where A = (Pr + Sr) and B = (Fe + Co). There are distortions in the perovskite structure as a result of displacement and first-order Jahn-Teller anti-symmetric breathing distortions of the BO<sub>6</sub>-octahedra [137, 138].

The relationship between ionic radii  $r_A$ ,  $r_B$  and  $r_O$  is geometrically expressed in a characteristic tolerance factor ( $t$ ) as shown in equation 2.2 [35, 36, 41, 137], which is a measure of site occupation by A and B cations:

$$t = \frac{\sqrt{2} \times (r_A + r_O)}{2 \times (r_B + r_O)} \quad (2.2)$$

In most cases, the ionic radii of A, B and O do not satisfy the condition that  $t = 1$ , hence, the perfect cubic structure of the perovskite shows structural distortions. The distortions that can usually be expected are due to the rotation of the BO<sub>6</sub> octahedra about high symmetry axes. In addition, the perovskite can also deviate from the ideal cubic structure by distortion of the rigid BO<sub>6</sub> octahedra by changes in B-O bond lengths. These alterations in the B-O bond lengths are possible and expected in systems with d<sup>4</sup> or d<sup>7</sup> electronic configurations on the B

atoms, leading to Jahn–Teller type anti–symmetric breathing of the  $\text{BO}_6$  octahedra. A change from the cubic symmetry to a structure of lower symmetry is common with a combination of rigid rotations and bond length distortions [5, 35, 36, 41, 137, 138].

### **2.5.2 Uses of perovskites**

Perovskite–type oxides possess high electronic conductivity, substantial electrocatalytic activity towards oxygen reduction at high temperatures and moderate thermal expansion coefficient compatible with commonly used solid electrolytes, such as yttria–stabilized zirconia (YSZ) [32, 35, 41, 138]. Perovskite materials are good candidates for the cathode in the field of SOFCs. Popular compositions for the cathode have included strontium–doped lanthanum cobaltite, strontium–doped lanthanum manganite and compositions from the quaternary system  $\text{Ln}_x\text{Sr}_{1-x}\text{Co}_y\text{Fe}_{1-y}\text{O}_3$  (Ln = Lanthanides, Ce or Pr). Lanthanides have a positive effect on the electrochemical activity for oxygen reduction reactions due to their redox couples like  $\text{Pr}^{3+} \leftrightarrow \text{Pr}^{4+}$  or  $\text{Ce}^{3+} \leftrightarrow \text{Ce}^{4+}$ . The perovskite systems containing lanthanides (Ce or Pr) allow high reaction rates due to the catalytic redox couple of Ce, ( $\text{Ce}^{4+}/\text{Ce}^{3+}$  and Pr, ( $\text{Pr}^{4+}/\text{Pr}^{3+}$ ). Consequently, the oxygen reduction steps are enhanced. Since there are oxygen vacancies, the oxidation state of the B–site cations varies ( $\text{Co}^{2+} \rightarrow \text{Co}^{3+} \rightarrow \text{Co}^{4+}$ ,  $\text{Fe}^{2+} \rightarrow \text{Fe}^{3+} \rightarrow \text{Fe}^{4+}$ ). These materials are applied as cathodes because they have high oxygen reaction rates due to the redox couple at intermediate temperatures and therefore improved performance [5, 32, 34, 35, 41].

## **2.6 Characterisation of nanomaterials**

### **2.6.1 Fourier Transform Infrared Spectroscopy (FTIR)**

Infrared Spectroscopy is used to detect functional groups present in a compound and it focuses on the infrared region of the electromagnetic spectrum, where the wavelength is longer than that of visible light [139]. This technique is based on vibrations in a molecule that show as absorption in a spectrum. The components of FTIR are; light source, interferometer, sample compartment, detector, amplifier, analogue-to-digital convertor and a computer. The source generates radiation which travels through the sample and reaches the detector [140]. The signal is digitalized by an amplifier and analog–to–digital convertor. By Fourier transform the signals can be read on a computer as a spectrum (Fig 2).

Samples selectively absorb radiation of specific wavelengths when exposed to infrared radiation, causing a change in their dipole moments. Vibrational excitations from ground states to higher excited states occur due to absorption of radiation [140]. The frequency of the absorption peak and the number of absorption peaks is dependent on the vibrational energy gap [140] the number of vibrational freedom of the molecule [140, 141] while the intensity of absorption peaks is related to the change of dipole moment and the possibility of the transition of energy levels [140].

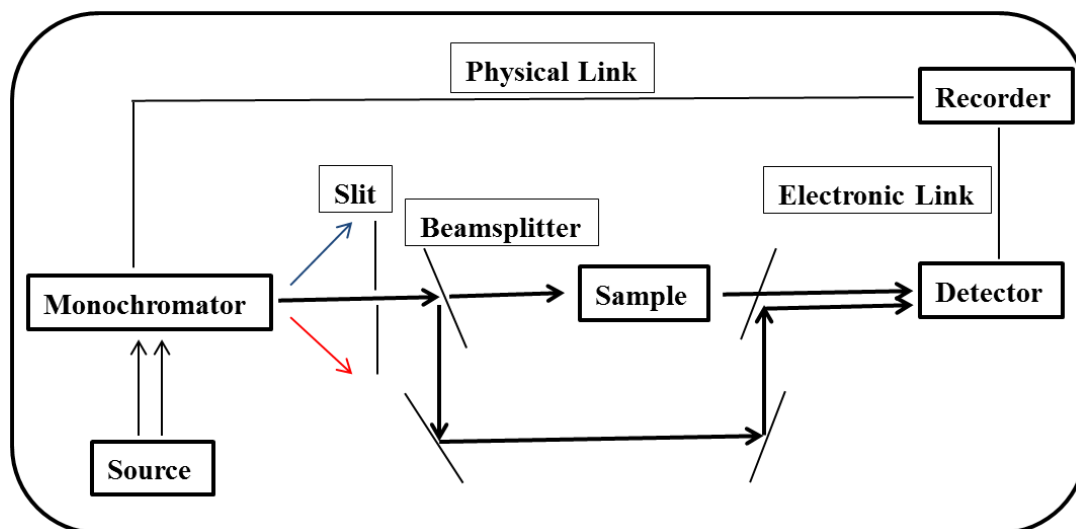


Figure 2.6: Schematic diagram of an FTIR instrument [140, 141]

In the case of pure CNTs, the functional groups could be considered as defects [139]. One can also apply FTIR in the analysis of impurities stemming from fabrication or coating of materials on the CNTs walls. This involves the determination of the infrared active modes which relies on the symmetry of the CNT which can either be chiral, zig-zag or armchair [115, 127]. In order for a vibrational mode in a molecule to be IR active, it must have a change in the dipole moment [115].

The important active modes for CNTs in IR spectroscopy are the  $A_{2u}$  and  $E_{1u}$  rotational modes which resonate at  $\sim 868$  and  $1575 \text{ cm}^{-1}$ , respectively [142-144]. The presence of functional groups on the walls of the tubes changes the wettability of the nanotubes in different surfactants and might change their toxicity [115, 127]. In the structure of CNTs, the rolled up graphene sheets consist of C-C and C=C bonds resonating at  $\sim 1440$  and  $\sim 1500 \text{ cm}^{-1}$ , respectively. In the structure of functionalised CNTs, there will be peaks corresponding to the bending modes of C-O at  $\sim 1450 \text{ cm}^{-1}$ , carbonyl groups (C=O) around 1600 and 1725

$\text{cm}^{-1}$  and hydroxide groups (OH) from water or ethanol at  $3450 \text{ cm}^{-1}$ . In addition to that, there will be several peaks resonating around  $3000 \text{ cm}^{-1}$  corresponding to  $\text{CH}_x$  groups [115, 127]. In a MWCNT/perovskite composite, the fingerprint of metal–oxide bonds in the perovskite structures will be visible at lower energies in the IR spectrum, at  $\sim 500\text{--}800 \text{ cm}^{-1}$ .

### 2.6.2 Raman Spectroscopy

Raman spectroscopy is a vibrational spectroscopy technique used to collect unique chemical fingerprint of a molecule from vibrational, rotational and other low–frequency modes of scattering [145]. There are three primary components to any Raman spectrometer: an excitation source, a sampling apparatus, and a detector. In Raman spectroscopy the sample is irradiated with monochromatic light and the photons are either inelastically or elastically scattered [140]. The inelastically scattered light, known as Raman scatter, has lost (Stokes) or gained (Anti–Stokes) energy during this interaction and the emitted photon contains information about the molecular structure of the sample [140, 146, 147]. The elastically scattered light has the same energy as the incident laser light and is called Rayleigh scatter [140, 148]. Each molecule has a different set of vibrational energy levels, and the photons emitted have unique wavelength shifts. Modern Raman instruments are designed to filter out the Rayleigh light as only one in every million photons will be Raman scattered [140, 148]. These modes are based on the Raman scattering of light in the visible, near infrared or near ultraviolet range. The information on the vibrational modes is obtained from the shift of energy that results from the interaction of the electromagnetic radiation used and the molecular vibrations [148]. The vibrational information is specific to the chemical bonds and symmetry of molecules, and therefore, provides a fingerprint by which a molecule can be identified. For a vibrational mode of a molecule to be Raman active it must possess a change in the overall polarisability [148]. A schematic diagram of a Raman spectrometer is presented in Figure 2.7.

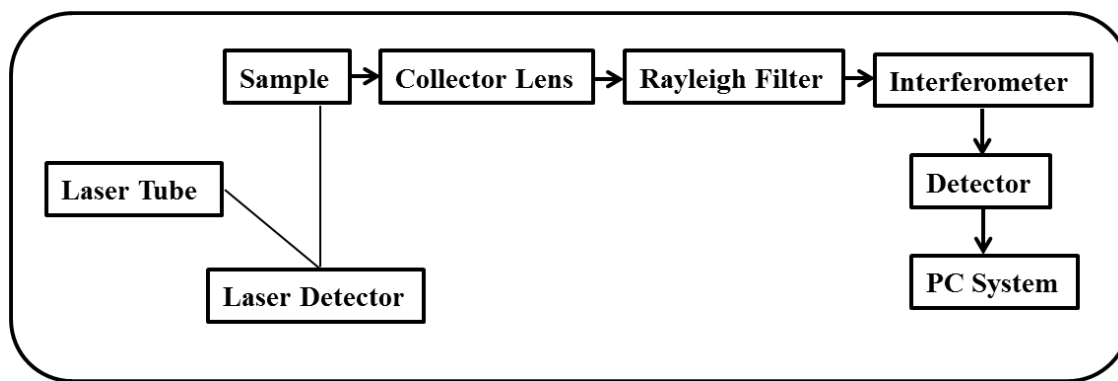


**Figure 2.7:** Schematic diagram of a Raman spectrometer [148]

Allotropic forms of carbon such as fullerenes, CNTs, amorphous carbon and crystalline carbon are known to be Raman active. Hence, Raman spectroscopy is applied in the characterisation of carbon nanotubes. The different forms of carbon can be determined by the position, width and relative intensity of bands [149]. The characteristic features are: (i) the low frequency peaks between  $100\text{--}400\text{ cm}^{-1}$ , usually seen with SWCNTs and not MWCNTS, are assigned to the radial breathing mode from  $A_{1g}$  vibrational modes and sensitive to tube diameter; (ii) the D band at  $\sim 1340\text{ cm}^{-1}$  comes from a double resonance vibration associated with amorphous carbons or defects on nanotube walls; (iii) the G band at  $\sim 1550\text{ cm}^{-1}$  which corresponds to tangential in-plane stretching vibrations of carbon-carbon bonds along a graphene sheet, which is a characteristic feature of CNTs or any carbon allotrope containing graphene sheets [115, 127, 149, 150]. Depending on the laser frequency and intensity used, other bands can be observed at  $\sim 1620\text{ cm}^{-1}$  for the D' band (shoulder peak of the G-band), and at  $\sim 2700\text{ cm}^{-1}$  for the 2D mode [115, 127, 149].

### 2.6.3 Thermogravimetric Analysis (TGA)

Thermogravimetric Analysis is a method of thermal analysis in which changes in chemical (such as combustion) and physical (such as melting) transitions of materials are analysed as a function of increasing temperature with constant heating rate, or as a function of time with constant temperature and/or constant mass loss. The analysis is carried out under controlled atmosphere as the mass of a material changes upon heating [151]. The results from TGA analysis provide information about physical-chemical phenomena, such as vaporisation, sublimation, adsorption, desorption and decomposition. Moreover, information on the

stability of composite materials in a particular temperature range can be obtained. Applications of this technique are the analysis of compounds, explosives, ceramics, polymers, carbon allotropes (especially carbon nanotubes) and other materials [151, 152]. When used to analyse the thermal stability of a material, there will be no observed mass change if a species is thermally stable in a desired temperature range. The maximum temperature at which a material is usable can also be determined. Beyond this temperature the material will begin to degrade [151]. The schematic diagram of a TGA is shown in Figure 2.8.

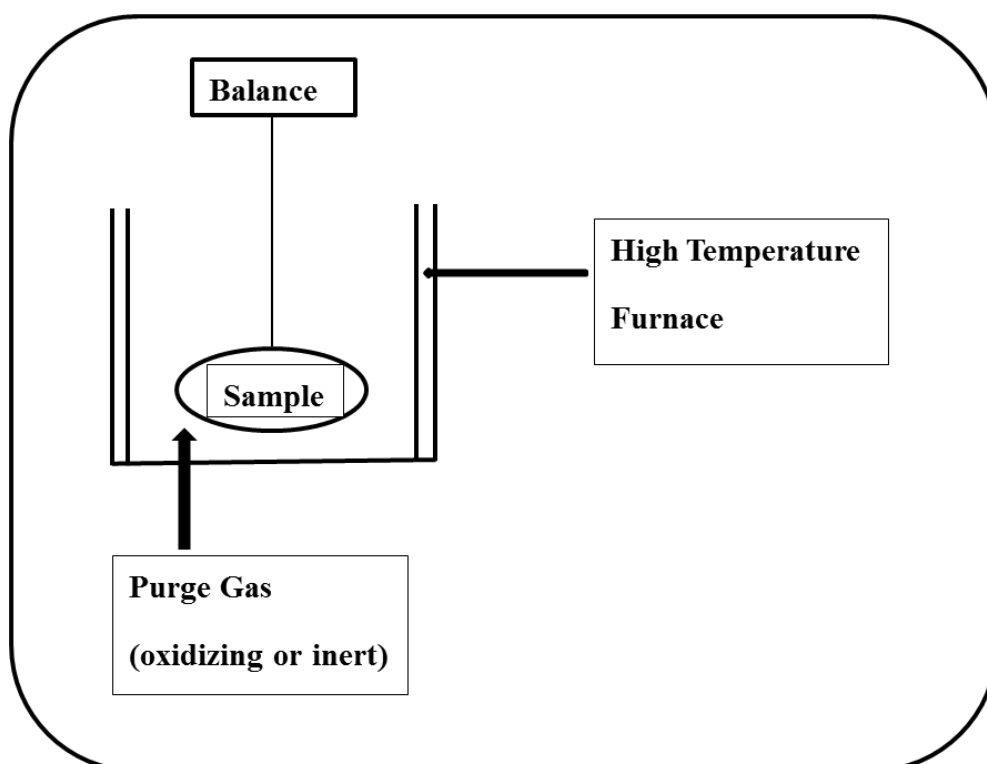


**Figure 2.8:** Schematic of a TGA instrument [152-154]

The basic principle of TGA involves the change in mass of a sample as it is heated, e.g. in an oxidative atmosphere (air or oxygen and inert gas mixtures) [154-156]. A sample can lose mass as it is heated up because of processes such as decomposition, reduction or evaporation [154]. On the other hand, a sample can also gain mass because of oxidation or absorption. The TGA tracks the change in mass of the sample using a micro-analytical balance inside the instrument [154]. Results can be plotted as weight percent versus time or temperature.

Thermogravimetric Analysis is a quick tool to identify purity and, to some extent, compositional carbon in MWCNT samples [115, 116, 157]. Furthermore, TGA gives important information on the relative amounts of amorphous carbon, catalytic metals and structured carbon (MWCNTs) within the sample [115, 116, 157, 158]. The complete decomposition of carbon in MWCNTs samples provides information about the oxidation temperature of carbon nanotubes and the residual mass [115-117, 157]. Knowing the decomposition temperature can be helpful in order to understand physical–chemical properties of MWCNTs in composite materials [158]. Furthermore the effect of functionalization or addition of external groups on MWCNTs can be revealed by TGA [115-117]. This allows e.g. to determine whether the adhesion of a coating on the MWCNT walls is good and if composites can be formed [158]. TGA does not require special sample preparation; hence, possibly fewer structural defects on MWCNTs surfaces are created before analysis.

#### 2.6.4 Powder X–Ray Diffraction (PXRD)

Powder X–ray diffraction is an analytical technique primarily used for phase identification of a crystalline material by comparing the “fingerprint” of a diffraction pattern from a sample with reference data. This technique can further provide unit cell dimensions and lattice spacings [159, 160]. During the analysis, the diffraction angles and intensities of X–ray beams from a small area of the sample are recorded [159, 160]. A schematic diagram of an X–ray diffractometer is shown in Figure 2.9.

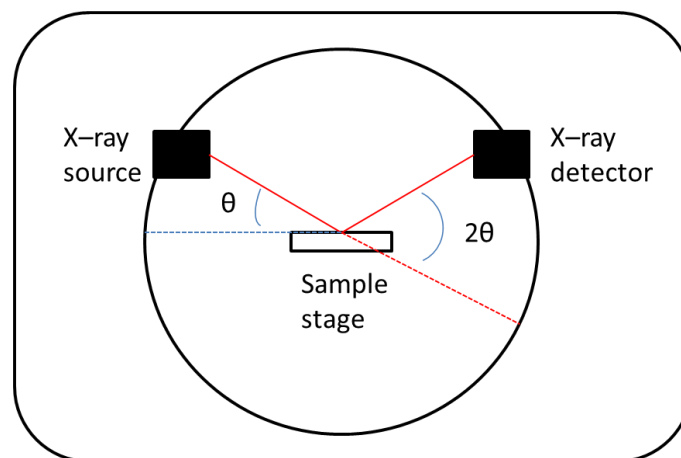


**Figure 2.9:** Schematic diagram of a powder X–ray diffractometer [159, 160]

In this technique, primary X-rays from the X-ray source are focused on a powder sample. Due to the wave like nature of the X-rays, the diffracted beams undergo either constructive or destructive interference and are diffracted to a certain angle [159, 160]. The position of a peak in the diffraction pattern depends on the lattice spacing of the diffracting lattice planes. The relationship is given by the Bragg condition [159, 160]:

$$n\lambda = 2d \sin \theta$$

In the characterisation of MWCNT composites by powder XRD the number of layers and tube diameters can be revealed. Thus, the main features in CNT X-ray diffraction patterns tend to be related to that of graphite. Measurements of the interlayer spacing can be done from the peak position and lattice parameters can also be calculated [127, 161]. The crystal systems in which perovskite phases crystallise such as cubic, rhombic and orthorhombic, can be identified using powder XRD analysis and suitable reference patterns [35, 36].

## **2.6.5 Electron Microscopy**

### **2.6.5.1 Scanning Electron Microscopy (SEM)**

Scanning Electron Microscopy (SEM) is a method that is used to investigate surface morphology and microstructure of materials [162-164]. Furthermore, the local composition of a material can be analysed using Energy Dispersive X-ray Spectroscopy (EDS). When SEM imaging is combined with EDS, the information can be used for elemental mapping [163].

In the MWCNT/perovskite composite materials, SEM is used to obtain information about perovskite particle distribution on the surface of MWCNTs, particle size and also the local elemental composition, surface morphology, elemental distribution and microstructure of the MWCNT/CSFC composites.

In this technique (Figure 2.10), an electron beam from an electron gun is focused onto the sample surface using electro-magnetic lenses [162-164]. The beam is then scanned over a selected area of the sample. In the sample, electrons get decelerated and scattered, back scattered electrons are fed to the detector and then to a cathode ray tube through an amplifier, where the images are formed, which gives the information on the surface of the sample [162-

164]. There are two imaging modes: secondary electrons (SE) give information mainly on morphology, backscattered electrons (BSE) give information on composition.

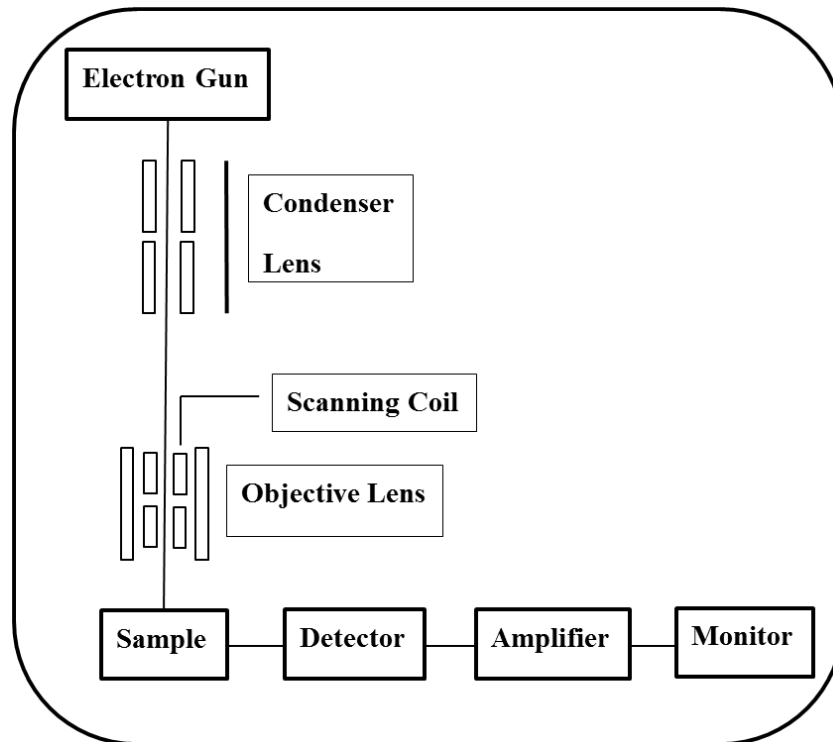


**Figure 2.10:** Schematic diagram of Scanning Electron Microscope [162]

The condenser lens controls the amount of current that passes down the rest of the column by focusing the electron beam to variable degrees.

### 2.6.5.2 Transmission Electron Microscopy (TEM)

Transmission Electron Microscopy is a tool used to obtain quantitative information on particle and/or grain size, morphology, size distribution and defects (in the case of CNTs) [161, 162]. Materials having electron densities exceeding that of amorphous carbon can be imaged straight forwardly. Some of the examples of these materials are polymer nanoparticles, carbon nanotubes, metals (e.g. silver, gold, copper, aluminium, etc.), oxides (e.g. silica, aluminium oxide, titanium oxide, etc.) and quantum dots [162, 165]. In the MWCNT/perovskite composite materials, carbon nanotube diameters can be obtained and it is possible to observe whether perovskites particles are seated on the outside or inside of the

CNTs [162]. Schematic diagram of a transmission electron microscope is shown in Figure 2.11.

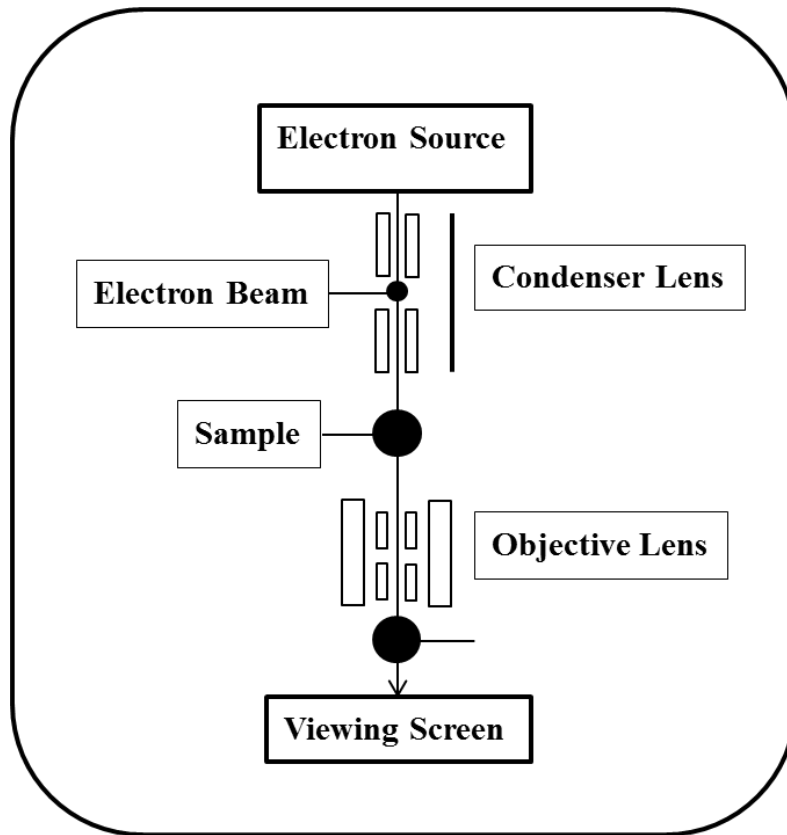


**Figure 2.11:** Schematic diagram of the Transmission Electron Microscope [163, 165-167]

The electron beam from the electron source (electron gun) is focused into a small, thin coherent beam by the condenser lens [163, 165, 166]. The focused beam is then restricted by the condenser aperture, excluding high angle electrons. The beam then hits the sample where it is scattered. The scattering angle depends on sample thickness and atomic number of the sample. An objective aperture is used to exclude high-angle scattered electrons in the transmitted beam from contributing to the image. Areas of the sample with high average atomic number or thicker areas appear darker than areas with lower average atomic number or thinner areas (mass–thickness–contrast). In crystalline materials diffraction of the incident beam of lattice plane is the dominant contrast mechanism. When the Bragg condition is fulfilled and the incident beam is diffracted enough to a higher angle, the corresponding grain or crystallite will appear dark [163, 166, 167]. The transmitted beam is recorded on film or using a charge couple device (CCD) camera [163, 165-167].

### **2.6.5.3 High Resolution Transmission Electron Microscopy (HRTEM)**

High resolution transmission electron microscopy (HRTEM) is an instrument for high-resolution studies of materials at the atomic scale [168]. This tool can be used to determine the way in which tubular structures are arranged, e.g. concentric or nested tubes, rolled sheets, stacked cup arrays, herringbone-types, etc. [169]. In addition, by the use of HRTEM it is possible to measure the inner and outer diameters of concentric tubes. The morphology and microstructure can be further studied from TEM/HRTEM in addition to SEM analysis. The lattice spacing in MWCNTs can be determined by HRTEM analysis. In addition to that, determination of the perovskite crystal structures and lattice spacings is possible.

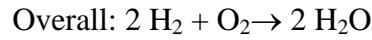
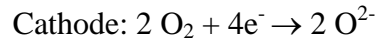
The operating principle of the high resolution electron microscopy involves the use of phase contrast and simulation is needed to interpret HRTEM images. While conventional TEM uses mass thickness and diffraction contrast [168].

## **2.7 Testing the electrochemical performance of nanomaterials**

Although the synthesis of nanocomposite materials for SOFCs is possible and easy to achieve, testing under application conditions is very important. The testing of the physical characteristics of synthesized materials is usually done on the zirconia-based solids, ceria-based oxides electrolyte with (Li/Na) carbonates and perovskite materials in the SOFCs. The parameters of interest are potential (V), current (mA), current density ( $\text{mA}\cdot\text{cm}^{-2}$ ) and power density ( $\text{mW}\cdot\text{cm}^{-2}$ ). The analysis is performed in the presence of an oxidant and a fuel gas at intermediate temperatures (300–600 °C). An estimate of power output of the cell is possible and provides information about the performance of the cell. Moreover, the stability of the cell over time can be determined.

### **2.7.1 Mathematical model of SOFCs**

The SOFC working mechanism is based on a co-ionic conducting electrolyte. Hydrogen is the fuel input and air is the oxidant. Assuming electrochemical reactions are occurring at the electrode-electrolyte interface only [170, 171], it is known that both  $\text{O}^{2-}$  (YSZ electrolytes) and  $\text{H}^+$  (proton conducting perovskites) can migrate via the electrolyte. Half-reactions taking place in the electrodes are as follows:



### 2.7.2 Current density and overpotential

The relationship between current density  $i$  (fuel cell current per unit area of the electrode, in units of  $\text{mA}\cdot\text{cm}^{-2}$ ) and cell voltage  $V$  (V) is shown in Figure 2.12.

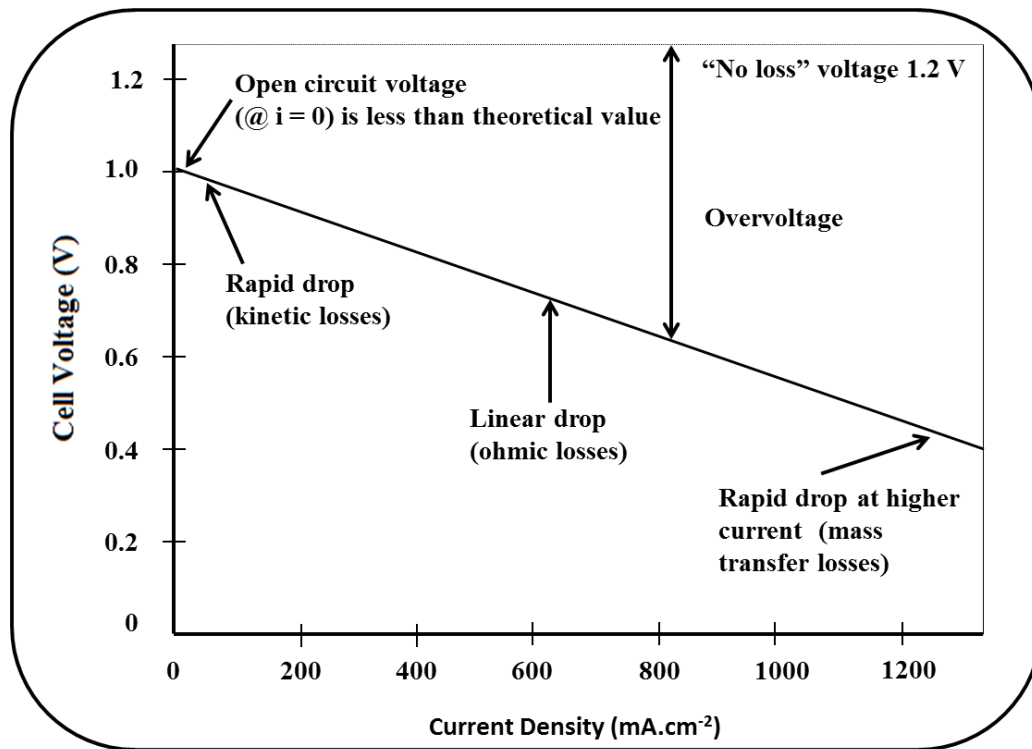


**Figure 2.12:** Polarization plot showing the relationship between cell voltage and current density [170]

The theoretical maximum voltage of this fuel cell is 1.2 V. This is called the open circuit voltage (OCV). The hydrogen reaction rate is directly proportional to the current, since for each hydrogen molecule that reacts, two electrons are formed. Any drop from this maximum value is termed overvoltage. It is desired to minimize the overvoltage so that the fuel cell can operate as efficiently as possible. There is a critical current density called the exchange current density with symbol  $i_o$ . For current densities  $i < i_o$ , the cell voltage is equal to the theoretical value. For current densities  $i > i_o$ , there is a rapid fall in cell voltage, due to a slow

reaction rate constant (kinetics). It is desirable to have as high a value of  $i_o$  as possible, and as rapid kinetics as possible. The effect of a linear fall in voltage as the current density increases is due to the fact that there is a resistance to current flow within the fuel cell. As the current increases, the voltage drop will increase. In physics and electrical engineering, this effect is referred to as Ohm's law. It is desired to have as small a resistance as possible. At very high current densities, the hydrogen reaction rate is high. However, the hydrogen cannot diffuse to the electrode fast enough to react. Thus, mass transfer is limiting and the voltage rapidly drops to zero. In fuel cells, the overvoltage  $\Delta V$  due to kinetics is a function of the current density (which is directly proportional to the reaction rate) and is often described by the Tafel equation given by Equation 2.3 [172]:

$$\Delta V = A \ln\left(\frac{i}{i_o}\right) = A \ln(i) - A \ln(i_o) \quad (2.3)$$

where  $A$  is called the Tafel constant (units of V) and  $i_o$  is called the exchange current density (units of mA.cm<sup>-2</sup>).

The Tafel equation will be used to model and predict overvoltage in SOFC systems (which operate at temperatures of about 300–500 °C). The Tafel equation is mostly used to estimate the cathode exchange current density  $i_o$  using a straight line relationship from the recorded data and transformed equation. To compute this exchange current density, the equation of the general straight line is used (Equation 2.4):

$$y = mx + c \quad (2.4)$$

where  $m$  = slope of the line,  $c$  = y-intercept. The exchange current density is equivalent to the constant term of the Tafel equation and can be equated to the general straight line constant, hence obtaining  $i_o$  [172]. The regression model of the polarization curve used for the parameter estimation of the experimental data is described in Equations 2.5, 2.6, 2.7 and 2.9 [170, 173, 174]:

$$V = E(T, p) - \eta_{activation} - \eta_{ohmic} - \eta_{concentration} \quad (2.5)$$

$$\eta_{activation} = \frac{RT}{1.4 \times F} \log\left(\frac{i}{i_{o,cat}}\right) \quad (2.6)$$

$$\eta_{ohmic} = R_{ohmic} \times i_c \quad (2.7)$$

where  $i_c$  is the current density and  $R_{ohm}$  is the internal resistance of the cell, which can be estimated from the effective distance between the cells components coupled with conductivity data (Equation 2.8).

$$R_{ohmic} = \frac{\delta_{anode}}{\sigma_{anode}} + \frac{\delta_{cathode}}{\sigma_{cathode}} + \frac{\delta_{electrolyte}}{\sigma_{electrolyte}} \quad (2.8)$$

parameters  $\delta_{anode}$ ,  $\delta_{cathode}$  and  $\delta_{electrolyte}$  are the thickness of the anode, the cathode and the electrolyte, respectively, and  $\sigma_{anode}$ ,  $\sigma_{cathode}$  and  $\sigma_{electrolyte}$  are the conductivities of the anode, the cathode and the electrolyte, respectively [173].

$$\eta_{concentration} = -\frac{RT}{2 \times F} \log \left(1 - \frac{i}{i_{as}}\right) \quad (2.9)$$

$i_{as}$  is the anode limiting current density [174]. The actual voltage calculation is shown in Equation 2.10.

$$V = OCV - R_{ohmic} \times i_c - \frac{RT}{1.4 \times F} \log \left(\frac{i}{i_{o,cat}}\right) + \frac{RT}{2 \times F} \log \left(1 - \frac{i}{i_{as}}\right) \quad (2.10)$$

The estimated parameters are the total ohmic cell resistance  $R_{ohmic, tot}$ , the cathode exchange current density  $i_{o, cat}$  and the anode limiting current density  $i_{as}$  [173, 174].

## 2.8 Summary

The application of nanoscience and nanotechnology plays a significant role in the synthesis of new materials with improved physical and chemical properties. The enhanced performance shown by materials at the nanoscale is based on their high surface area and quantum confinement. CNTs have gained wide applications in material science because of their properties based on surface and electronic effects at nanoscale level. They have been proposed as materials for SOFCs because of their high conductivities and the ability to act as

template in the synthesis of LT–SOFC materials. Cathode composites of MWCNTs and high mixed ionic conducting perovskites oxides are known as promising materials for SOFCs. Nanocomposites materials can be characterized by a number of complementary techniques FTIR, Raman spectroscopy, TGA, XRD, SEM, TEM and HRTEM. Moreover, electrochemical performance of nanomaterials in SOFCs can be determined in terms of polarization curves.

## Chapter Three

### Experimental Techniques

The following Chapter describes synthesis and physico-chemical characterization techniques used in this work. Methods used to synthesize nanomaterials are Chemical Vapour Deposition (CVD) and sol-gel. Metal acetylacetonate (acacs) complexes were coated onto MWCNT surfaces in an effort to develop perovskite structures within MWCNTs used as templates for particle size control. The composite approach was used in order to enhance chemical and physical properties of the nanocomposite materials. The performance of the nanocomposites was tested in the low temperature region (300–500 °C) for solid oxide fuel cell operations. The MWCNT/perovskite cathode materials were studied in single, symmetrical and asymmetrical cells with the use of YSZ electrolyte and NiO-YSZ as the standard anode under asymmetrical cells. Polarization curve characterization techniques for the cells were developed.

#### 3.1 Materials

Pluronic F-127, cerium (III) acetylacetonate hydrate (99.9%), strontium acetylacetonate hydrate (98.5%), iron (III) acetylacetonate (97%), and cobalt (III) acetylacetonate hydrate (99.9%) were purchased from Sigma Aldrich (South Africa, Durban) and were used without further purification. Multiwall carbon nanotubes were purchased from Cheaptubes™ (Brattleboro) and were used as received (with purity of > 95 wt. %, diameter range of 8–15 nm, average length of (10–20 μm as per the manufacturers). Deionized water was employed during the whole synthesis (sol-gel method). Crude ethanol was used for the preparation of polymeric solutions (sol-gel). An YSZ electrolyte (YSZ-SUB2.0D, purchased from fuelcellmaterials.com) was used as received with a thickness of 300 μm. Powders of YSZ and NiCO<sub>3</sub> were purchased from Sigma Aldrich and were used as received. For painting the materials electrodes on the YSZ electrolyte, Polvin walls and ceilings paint (Shalom Laboratory Suppliers) was used with a set of tensile paint brushes and stencils.

## 3.2 Synthesis

### 3.2.1 Surfactant Preparation

Using two measuring cylinders, 155 mL of ethanol were added to the first measuring cylinder (200 mL) and 45 mL of deionized water to the second measuring cylinder (50 mL). The content of the two measuring cylinders were added simultaneously to a 200 mL Erlenmeyer flask and mixed thoroughly by shaking and inverting the flask several times. The solution was then transferred to four 50 mL volumetric flasks (four aliquots). Pluronic F-127 (6.00 g) was added as the surfactant to the four different 50 mL solvent system solutions. The solutions were then sonicated for 5 minutes and left covered with foil in the fume hood for 3 days (this resulted in a viscous solution) at room temperature.

### 3.2.2 Synthesis of $\text{Ce}_x\text{Sr}_{1-x}\text{Fe}_y\text{Co}_{1-y}\text{O}_3$ Perovskites

In the CVD method for the preparation of perovskites the values of  $x$  and  $y$  were chosen as  $x = y$ . The method involves mixing four commercial metal acacs in stoichiometric amounts, by first weighing them in different weighing boats and transferring them into a mortar, grinding with a pestle for homogenisation of the mixture for about 2 minutes. The exact masses and ratios of the samples are given in Table 3.1.

**Table 3.1:** Required masses of metal acacs for the preparation of  $\text{Ce}_x\text{Sr}_{1-x}\text{Fe}_y\text{Co}_{1-y}\text{O}_3$  perovskites by CVD technique

Composition	Ce(acac) <sub>3</sub> /g	Sr(acac) <sub>2</sub> /g	Fe(acac) <sub>3</sub> /g	Co(acac) <sub>3</sub> /g
$x = y = 0.2$	0.0874	0.2286	0.0508	0.02057
$x = y = 0.4$	0.1749	0.1715	0.1016	0.1542
$x = y = 0.6$	0.2624	0.1143	0.1524	0.1028
$x = y = 0.8$	0.3499	0.0571	0.2032	0.0514

For the sol-gel method, the metal acacs were weighed stoichiometrically as described above. The metal acacs were then transferred into a 100 mL beaker and dissolved in 10 mL of the Pluronic F-127 pre-made solution. This mixture was stirred for 15 hours before placing the

beakers in a convection oven (ODWFH18 and GWD520) at 100 °C for 2 hours until the samples were dry. The exact masses and ratios of the samples are given in Table 3.2.

**Table 3.2:** Required masses of metal acacs and volumes of Pluronic F-127 for the synthesis of  $Ce_xSr_{1-x}Fe_yCo_{1-y}O_3$  perovskites by sol-gel technique

Composition	Ce(acac) <sub>3</sub> /g	Sr(acac) <sub>2</sub> /g	Fe(acac) <sub>3</sub> /g	Co(acac) <sub>3</sub> /g	Pluronic F-127 / mL
x = y = 0.2	0.0873	0.2285	0.0506	0.02054	10
x = y = 0.4	0.1748	0.1720	0.1009	0.1528	10
x = y = 0.6	0.2772	0.1103	0.1549	0.1121	10
x = y = 0.8	0.3396	0.0580	0.2046	0.0563	10

$Ce_xSr_{1-x}Fe_yCo_{1-y}O_3$  samples made by the two different methods were then packed into a homemade stainless steel reactor assembled from standard Swagelok™ parts (Figure 3.1) for heat treatment.

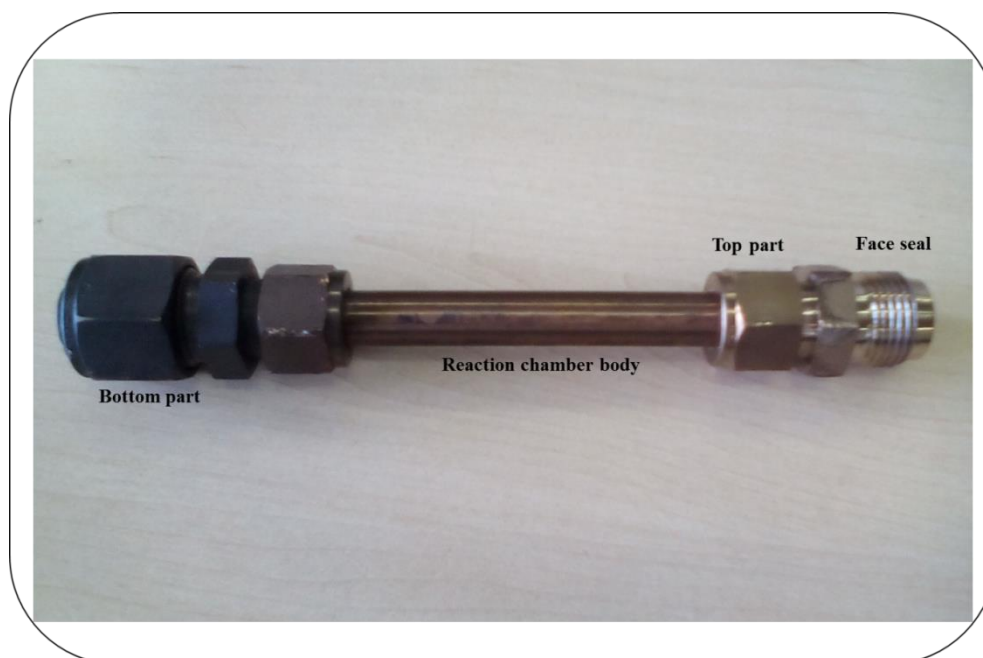


**Figure 3.1:** The reactor used for calcining MWCNT/perovskite composites in the Labofurnace

The sealed reactor was placed into a horizontal tube furnace, and the reactor was then connected to a vacuum pump, with appropriate valves along the vacuum line. The set-up used is shown in Figure 3.2. After evacuation to approximately  $10^{-3}$  mbar, valve 2 was closed and the furnace set to heat slowly to 400 °C with a ramp rate of 1 °C per minute for 8 hours. After allowing the furnace to cool down, the samples were taken for characterization.



**Figure 3.2:** Experimental apparatus used for calcination of  $Ce_xSr_{1-x}Fe_yCo_{1-y}O_3$

### 3.2.3 Synthesis of Carbon Nanotube– $Ce_xSr_{1-x}Fe_yCo_{1-y}O_3$ composite materials

(i) MWCNTs to CSFC ratios of 1:0.5, 1:1, 1:2 and 1:3 were prepared using the CVD method. MWCNTs were weighed in a beaker, added to the homogenized metal acacs, and further ground together for 2 minutes. Table 3.3 gives the exact quantities of the metal acacs and MWCNTs used.

**Table 3.3:** Required amounts for the synthesis of MWCNT/CSFC composites with different mass ratios

MWCNT/CSFC	MWCNT / g	$Ce_{0.6}Sr_{0.4}Fe_{0.8}Co_{0.2}O_3$ / g
(1:0.5)	0.5010	0.2511
(1:1)	0.5236	0.5289
(1:2)	0.5362	1.0548
(1:3)	0.5246	1.5241

(ii) In the sol–gel method, the general synthetic route involved first sonication of MWCNTs using Hielscher UP400S sonicator at 80% amplitude and 0.3 cycles per minute in water for 5 minutes to disperse MWCNTs. Stoichiometric amounts of metal acacs were then dissolved in 10 mL of Pluronic F–127 prepared as shown in section 3.2.1. This mixture was added to the dispersed MWCNTs and stirred for 15 hours. The stirred samples were transferred to a convection oven (ODWFH18 and GWD520) at 100 °C, and left for approximately 2 hours until the powders were dry. Figure 3.3 shows the MWCNTs under sonication, the metal acacs and the surfactant (Pluronic F–127 in ethanol water solvent system).

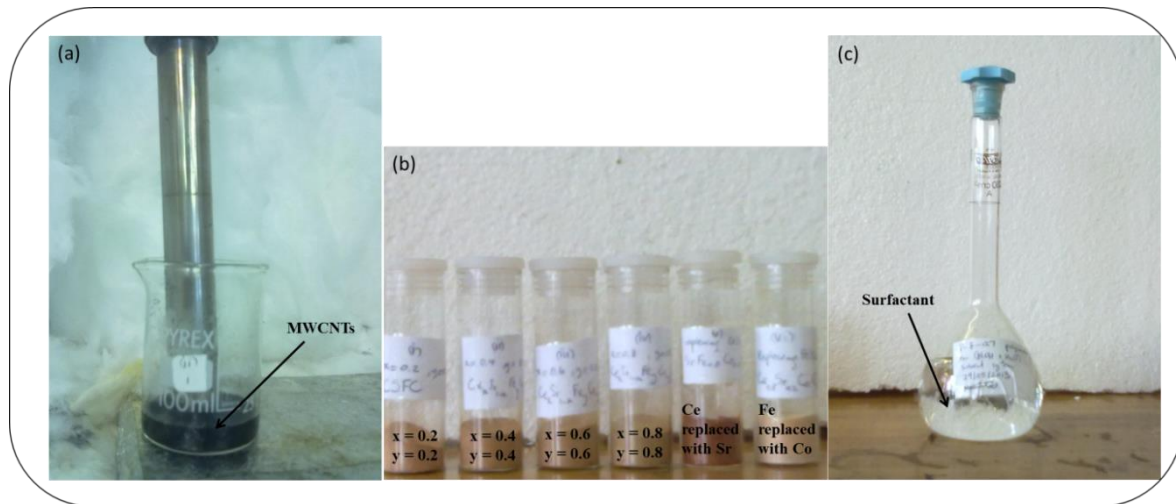


**Figure 3.3:** (a) MWCNTs under sonication, (b) metal acacs, and the numbers referred to perovskites without MWCNTs (c) Surfactant Pluronic F–127 in ethanol water solvent system

Synthesis of perovskites with  $x = 0.6$  and  $y = 0.8$  and with different MWCNTs amounts was done following the method of Pinedo et al. [17]. The ratios of MWCNT to CSFC were kept at 1:3 while varying  $x$  and  $y$  values in the perovskite structure (Table 3.4).

**Table 3.4:** Composites synthesized by either CVD or sol–gel methods

Sample number	Sample ID	Note
1.	1 MWCNT : 3 $\text{Ce}_{0.2}\text{Sr}_{0.8}\text{Fe}_{0.2}\text{Co}_{0.8}\text{O}_3$	New ratio in this work
2.	1 MWCNT : 3 $\text{Ce}_{0.4}\text{Sr}_{0.6}\text{Fe}_{0.4}\text{Co}_{0.6}\text{O}_3$	New ratio in this work
3.	1 MWCNT : 3 $\text{Ce}_{0.6}\text{Sr}_{0.4}\text{Fe}_{0.6}\text{Co}_{0.4}\text{O}_3$	New ratio in this work
4.	1 MWCNT : 3 $\text{Ce}_{0.6}\text{Sr}_{0.4}\text{Fe}_{0.8}\text{Co}_{0.2}\text{O}_3$	From reference [17]
5.	1 MWCNT : 3 $\text{Ce}_{0.8}\text{Sr}_{0.2}\text{Fe}_{0.8}\text{Co}_{0.2}\text{O}_3$	New ratio in this work

Heat treatments were performed as shown in Figure 3.2. After heat treatments, samples were allowed to cool down to room temperature before further characterisation and electrochemical testing.

### 3.3 Characterisation of the synthesized MWCNT/CSFC composites

#### 3.3.1 Fourier–Transform Infrared Spectroscopy (FTIR)

FTIR spectra of the samples were recorded using a PerkinElmer Spectrum 100 with Universal ATR sampling accessory between  $400\text{--}4000\text{ cm}^{-1}$  and a resolution of  $0.4\text{ cm}^{-1}$ . A small amount of the powder was placed on the ATR disc of the universal sampling accessory and pressed. The pressure exerted was monitored by a force gauge on the screen. When the pressure reached 20, the sample was scanned. Raw data were collected and infrared spectra drawn using Origin software. The FTIR instrument used is shown in Figure 3.4.



**Figure 3.4:** Instrument used for FTIR Spectroscopy

### 3.3.2 Raman Spectroscopy

Raman spectroscopy was performed on a DeltaNu advantage 532™ Raman Spectrometer equipped with a power of 100 mW Nd–YAG laser with an excitation wavelength of 532 nm (Figure 3.5). Spectra were recorded between 200 and 3500  $\text{cm}^{-1}$ . A small amount of the sample was loaded in a sample holder with a hole and the laser was shone on the surface of the powders in the dark. The instrument was set to a medium laser power with an integration time of 10 seconds. Twenty spectra were recorded for each sample and an average calculated and recorded. The raw data were saved and smoothed; the spectra plotted using Origin software.



**Figure 3.5:** Instrument used for Raman Spectroscopy

### 3.3.3 Thermogravimetric Analysis (TGA)

MWCNT/perovskite composites were thermally analysed using a SDT Q 600 (V 20.9 Instrument Build 20) TGA instrument. 10–20 mg of each sample were used for each run. The heating rate was kept to 10 °C/min with air as the purge gas at a flow rate of 50 mL/min. Heating was performed from ambient temperature to 1000 °C. The TGA instrument is shown in Figure 3.6.



**Figure 3.6:** Thermogravimetric Analysis instrument used

### 3.3.4 X-Ray Diffraction (XRD) Analysis

The X-ray powder diffraction (XRD) was carried out *in-situ* for the CSFC and the 1:1 MWCNT/CSFC composite on a Bruker Advance D8 diffractometer shown in Figure 3.7. The radiation used was Cu K $\alpha$  with a wavelength of 1.5401 Å, and the generator was operated at 40 kV. Data were collected in a  $2\theta$  range between 0° and 90° with a step size of 0.02° from 100–650 °C in 50 °C intervals. Data were collected in air for the perovskites and under N<sub>2</sub> for the composites.



**Figure 3.7:** Bruker D8 ADVANCE diffractometer used for the *in-situ* XRD

The remaining samples were analysed at iThemba LABS on a Phillips PW3710 operated at 40 kV and 35 mA, using Cu K $\alpha$  as the radiation source. The XRD patterns were recorded for  $2\theta$  values between  $0^\circ$  and  $90^\circ$  with a step size of  $2^\circ$  per minute. The particle sizes for all samples were estimated using the most intense peak (200) in the XRD patterns using the Debye Scherrer equation with a Gaussian curve fitted using Origin software (Equation 3.1).

$$D = \frac{0.9\lambda}{B \cos \theta} \quad (3.1)$$

where  $D$  = average particle size in Å,  $\lambda$  = the wavelength (1.5401 Å) of Cu  $K\alpha$  radiation,  $B$  the full width (in radian) of the XRD diffraction peak at half of its maximum intensity (FWHM),  $\theta$  the Bragg diffraction angle of the peak. The Miller indices were calculated as sine of the angle and the product was squared, the outcomes were multiplied by the integers 1, 2 and 3 then h k l values were obtained [175].

### **3.3.5 Electron Microscopy**

Electron microscopy was used to study the surface morphology, microstructure and particle distribution. Both the surface and the bulk of the materials were investigated.

#### **3.3.5.1 Scanning Electron Microscopy (SEM)**

A LEO 1450 Scanning Electron Microscope (SEM) (Figure 3.8) and a ZEISS Field–Emission Gun Scanning Electron Microscopy (FEG–SEM) Ultra Plus equipped with an Energy–Dispersive X–ray Spectrometer (EDS) were used to examine the morphology, size distribution and elemental composition of the samples. To obtain SEM images, powders were pressed onto carbon tape coated aluminium stubs and gold coated before being inserted into the instrument.



**Figure 3.8:** Instrument used for Scanning Electron Microscopy (LEO 1450)

### **3.3.5.2 Transmission Electron Microscopy (TEM)**

In order to get information about the bulk of the samples and to perform phase identification, a JEOL JEM-1010 Transmission Electron Microscopy (TEM) was used at an accelerating voltage of 200 kV. Samples for TEM were prepared by dispersing the powders in small vials in ethanol followed by sonication using an ultrasound bath. Lacey carbon grids were dipped into the solution. Ethanol was allowed to evaporate and carbon grids were inserted into the TEM sample holder and inserted into the instrument shown in Figure 3.9.



**Figure 3.9:** Instrument used for Transmission Electron Microscopy (JEOL JEM–1010)

### **3.3.5.3 High Resolution Transmission Electron Microscopy (HRTEM)**

The HRTEM instrument used to study the materials was a JEOL JEM–2100 Transmission Electron Microscope using an accelerating voltage of 200 kV. For HRTEM analysis, small amounts of the samples were dispersed in ethanol using an ultrasound bath. Carbon coated TEM grids were first dipped in ethanol and then immersed into the solution mixture. Ethanol was allowed to evaporate. Images were recorded on a 1K x 1K CCD camera. Particle sizes were measured using Image J software. The instrument is shown in Figure 3.10.



**Figure 3.10:** Instrument used for High Resolution Transmission Electron Microscopy (JEOL JEM-2100)

### **3.4 Button Cell Fabrication and Electrochemical Measurements**

In this section the fabrications of the cells using the YSZ electrolyte, NiO-YSZ anode and MWCNT/CSFC composite materials as cathode electrodes are outlined as well as the method for testing the electrochemical properties.

#### **3.4.1 Cell Assembly**

Button cells were assembled by painting a mixture of Polvin Walls and ceilings paint (Salon Laboratory suppliers) and anode or cathode material, onto 20 mm diameter Yttrium Stabilized Zirconia (YSZ) discs (Purchased from fuelcellmaterials.com). Paint was used since it has a suitable binder and also being insoluble material for pore formation [176]. The paint was used as received. Three drops (~ 0.0200 g) were mixed with 0.0100 g MWCNT/perovskite composite for the cathode and 0.0100 g of NiO and 0.0088 of YSZ

powder as the anode. MWCNT/CSFC composites were painted onto the YSZ discs using a fine paint brush and a stencil to ensure good coverage within a defined area. To prevent short circuiting in the cells, the paint slurry was applied to a defined area ( $\sim 1.76 \text{ cm}^2$ ) of the electrolyte. Samples were then sintered in air at low temperatures ( $300 \text{ }^\circ\text{C}$ ) for 5 hours.

Symmetrical cells with the configuration [composite material |YSZ| composite material] were prepared by painting cathode slurries on both sides of the YSZ electrolyte. The same procedure was employed for the preparation of the asymmetrical and single cells. In the single cells, cathode slurries were only painted on one side, leaving the other side blank. This configuration is [composite material |YSZ|].

For the fabrication of asymmetric cells, nickel carbonate was used as the precursor for the anode materials. To obtain NiO, two methods were compared: In the first method, nickel carbonate was mixed with the paint, then painted on one side of the YSZ electrolyte and sintered at  $800 \text{ }^\circ\text{C}$  for 5 hours. In the second method, nickel powders were first heat treated at  $800 \text{ }^\circ\text{C}$  for 5 hours, before being painted on the YSZ electrolyte. Finally, asymmetric cells were fabricated by taking NiO–YSZ |YSZ|, sintered at  $800 \text{ }^\circ\text{C}$ , and painting cathode powders (MWCNT/perovskites) on the blank side of the electrolyte. The button cells were then dried at  $300 \text{ }^\circ\text{C}$  for 5 hours.

Meshes of platinum and wires were used as current collectors and were adhered by paste on both sides of the electrolyte. YSZ was used as electrolyte because of its high ionic conductivity but with optimal performance at high temperatures. The cell was placed between the meshes on the anode and cathode sides electrodes with ceramic felts covering the cell button.

### **3.4.2 Electrochemical measurements**

#### **3.4.2.1 Polarization curves**

Button cells were mounted in an open flange test set-up from Fiaxell SOFC Technologies<sup>TM</sup>. The test-bed was placed in a Kitter Squadro muffle furnace and appropriate gas tight fittings were attached for the delivery of humidified air and hydrogen gas to the cell. The pressure exerted in the system was monitored by the use of callipers to find the uniform length of the spring after tightening the sandwiched cells. When the furnace had reached the desired temperature, the system was flushed with air as an oxidant to the cathode side at a flow rate

of 200–300 mL.min<sup>-1</sup>. After 5 minutes hydrogen gas was fed to the anode side as a fuel at a flow rate of 100 mL.min<sup>-1</sup>. The test cell was conditioned for 2 hours before beginning of the test. Current and voltage from the cell were measured with a NuVant™ Powerstat 05 Potentiostat and galvanostat power ware software. Polarization curves were recorded between 300–500 °C (at a potential of 1.2–0.1 V, in 0.1 V intervals) with a fuel consisting of hydrogen and 4–20% water on the anode side and air on the cathode side. Galvanostatic and Potentiostatic durability testing was carried out in order to assess long–term static stability of the cell at 500 °C for over 15 hours. Surface morphology and CNT modifications were studied by SEM and HRTEM after the test. Figure 3.11 shows a schematic diagram of the cell set–up inside the furnace for the SOFC process.

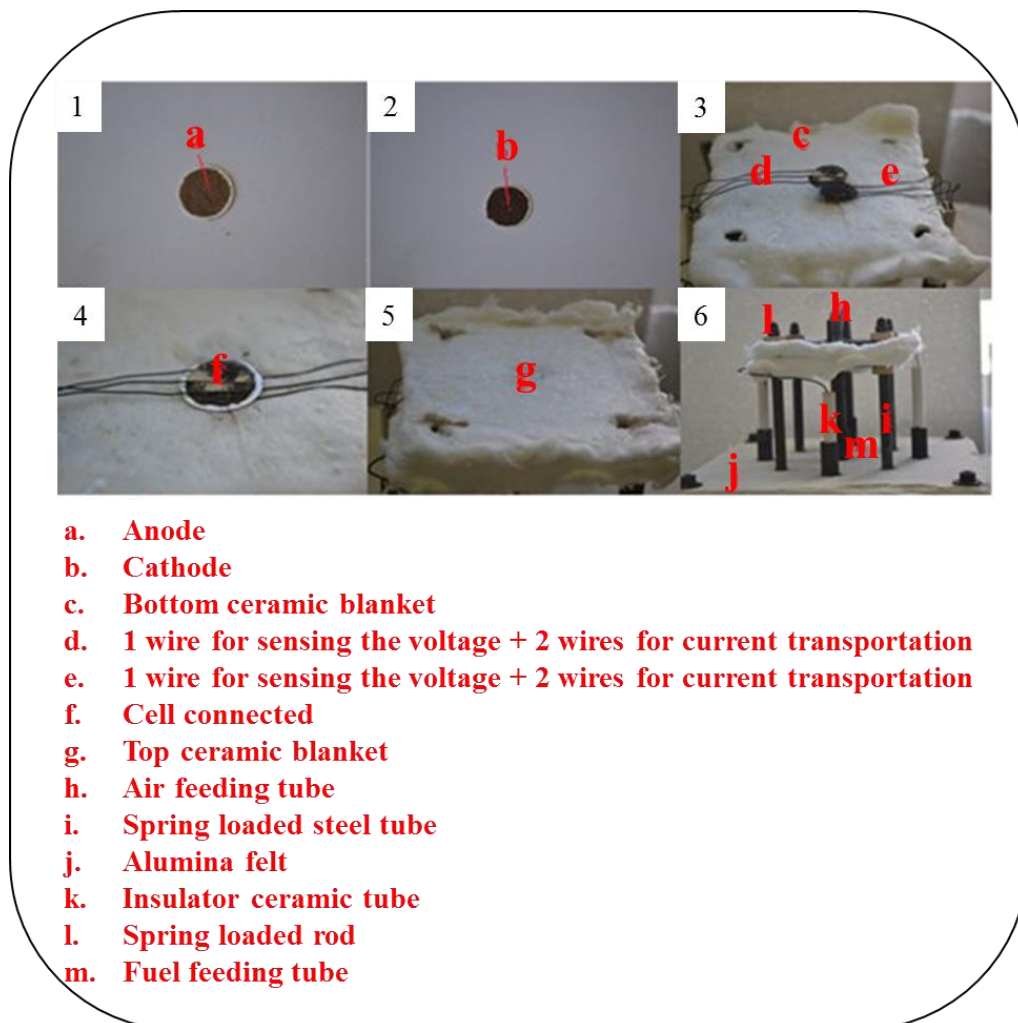


**Figure 3.11:** Schematic diagram of the SOFC set–up showing all cell components: (1) and (2) electrodes, (3) to (6) bottom view of the open flanges test set–up

The exterior view of the whole apparatus used is shown in Figure 3.12.

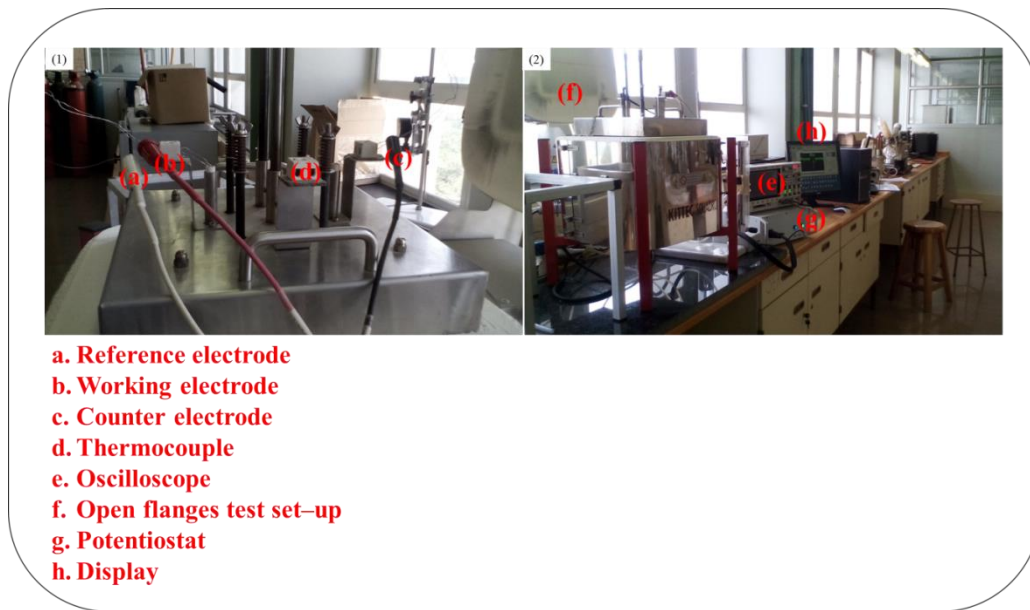


**Figure 3.12:** SOFC apparatus for measuring electrical performance. (1) Top view of the open flanges test fixture, (2) complete set-up

### 3.4.3 Fuel Cell Parameter Calculations

Raw data from the Potentiostat were obtained and polarization curves had to be plotted. The problem with the obtained raw data was that when current densities versus potential curves were plotted, curves with positive slopes were obtained instead of the expected curves with negative slopes. This means the voltage obtained from the Potentiostat was not the actual voltage. The data had to be manipulated in order to obtain a linear decrease in the voltage as the current density increases. The actual voltage was calculated from Equation 3.2 taking into account the ohmic, activation and concentration overpotentials [173]:

$$V = OCV - R_{ohmic} \times i_c - \frac{RT}{1.4 \times F} \log \left( \frac{i_c}{i_{o,cat}} \right) + \frac{RT}{2 \times F} \log \left( 1 - \frac{i_c}{i_{as}} \right) \quad (3.2)$$

where OCV (measured by a voltmeter during the course of the test) stands for open circuit voltage and  $R_{ohmic}$  is the ohmic resistance (the internal resistance of the cell) and was estimated using Equation 3.3 [173]:

$$R_{ohmic} = \frac{\delta_{anode}}{\sigma_{anode}} + \frac{\delta_{cathode}}{\sigma_{cathode}} + \frac{\delta_{electrolyte}}{\sigma_{electrolyte}} \quad (3.3)$$

$\delta_{anode}$ ,  $\delta_{cathode}$  and  $\delta_{electrolyte}$  are the thickness of the anode, cathode and the electrolyte, respectively, and  $\sigma_{anode}$ ,  $\sigma_{cathode}$  and  $\sigma_{electrolyte}$  are the conductivities of the anode, cathode and the electrolyte, respectively. The  $i_c$  is the current density obtained from the Potentiostat and  $i_{o, cat}$  is the cathode exchange current density which was calculated from the Tafel plot as described in Chapter 2 (section 2.8.2). The parameter R is the ideal gas constant, T the operating temperature (in K) and F the Faraday's constant. The  $i_{as}$  is the anodic limiting current density and is calculated by taking into account the diffusion coefficient associated with anode/cathode gas transport (diffusivity) as shown in Equation 3.4 [177]:

$$i_{as} = \frac{4 \times F \times P_{H_2}^0 D_{H_2-H_2O}^{eff}}{RTl_a} \quad (3.4)$$

$P_{H_2}^0$  is the partial pressure of hydrogen,  $D_{H_2-H_2O}^{eff}$  is the effective binary diffusivity and  $l_a$  is the thickness of the electrode (anode). The effective diffusion coefficient of a porous layer is calculated using Equation 3.5 [173, 177].

$$D_{H_2-H_2O} = \frac{10^{-3} \times T^{1.75} \sqrt{\frac{1}{M_{H_2}} + \frac{1}{M_{H_2O}}}}{p[(\sum v_{H_2})^{1/3} + (\sum v_{H_2O})^{1/3}]^2} \quad (3.5)$$

p is the total pressure,  $M_{H_2}/M_{H_2O}$  is the molecular weight of hydrogen/water and  $\sum v$  is the diffusion volume [173, 177]. The output voltage is expressed as the difference between the sum of the ohmic, activation and concentration overpotentials and the open-circuit voltage as shown in Equation 3.2 [173]. After calculating the actual voltage and plotting it against the current density, the slope of the line was negative as manipulated. Polarization curves were then plotted and maximum current and power densities determined for different test

temperatures. The performance was further studied by means of area specific resistances (ASRs) which were obtained from the slopes of the polarization curves.

### 3.5 Summary

The synthesis of cathode materials in this work involved two different techniques, CVD and sol-gel. In the CVD method, no solvent was employed; metal acacs were dry mixed, while in the sol-gel method solvent has been used. Starting materials (metal complexes, [Ce (acac)<sub>3</sub>], [Co (acac)<sub>3</sub>], [Fe (acac)<sub>3</sub>] and [Sr (acac)<sub>2</sub>]) were commercial available. Pluronic F-127 was used as a surfactant and it was prepared by dissolving Pluronic F-127 in ethanol and water solvent system solution. The properties of synthesized materials were determined by a range of characterisation techniques. Lastly, cell preparation was accomplished by brush painting cathodes and anodes slurries on an YSZ electrolyte and letting them dry. The parameters determined were current and power densities and ASRs. The summary of the whole process is shown in the schematic diagram depicted in Figure 3.13.

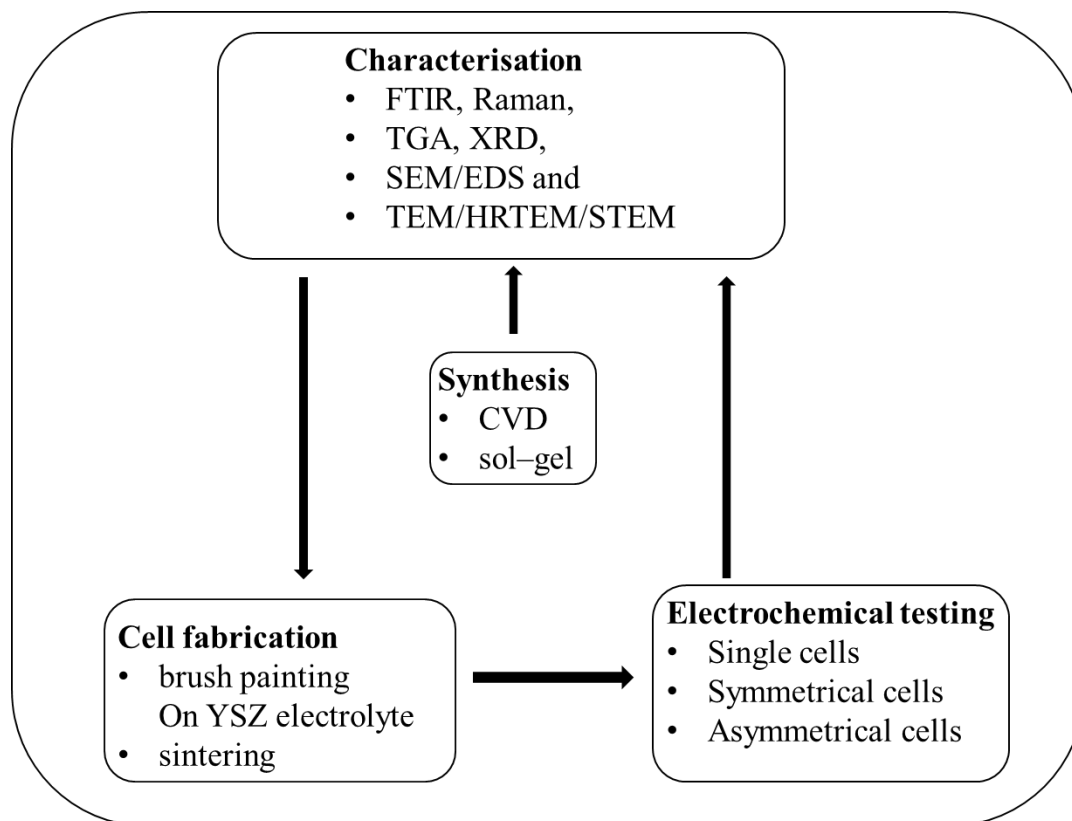


**Figure 3.13:** Schematic diagram of the experimental work

## Chapter Four

### Characterization of MWCNT/Ce<sub>x</sub>Sr<sub>1-x</sub>Fe<sub>y</sub>Co<sub>1-y</sub>O<sub>3</sub> Nanocomposite Materials for Low to Intermediate Temperatures Solid Oxide Fuel Cells (LIT-SOFC)

The chemical properties of carbon nanotubes/perovskite composites depend on composition, synthesis technique and heat treatment. In this Chapter the results of a variation of the chemical composition of the MWCNT/Ce<sub>x</sub>Sr<sub>1-x</sub>Fe<sub>y</sub>Co<sub>1-y</sub>O<sub>3</sub> (MWCNT/CSFC) nanocomposite (where  $0.2 \leq (x, y) \leq 0.8$  in 0.2 intervals), are presented.

The aim of the current work is to synthesize nanoparticles of Ce<sub>x</sub>Sr<sub>1-x</sub>Fe<sub>y</sub>Co<sub>1-y</sub>O<sub>3</sub> perovskite for SOFC cathodes using MWCNTs as templates. The hypothesis is that MWCNTs can be used to control the particle size and growth. Pinedo et al. [17, 22] have synthesized Pr<sub>0.6</sub>Sr<sub>0.4</sub>Fe<sub>0.8</sub>Co<sub>0.2</sub>O<sub>3</sub> perovskite using the sol-gel technique (citrate and glycol) at 700 °C. In this work, a non-ionic surfactant (Pluronic F-127) has been employed. Praseodymium (Pr) is substituted by the more abundantly and economically available cerium (Ce). The temperature of perovskite formation has been reduced to 300–600 °C. Here, it was investigated how MWCNT/CSFC properties changes as the MWCNT: CSFC ratio is varied. For comparison, the CVD method was also used to synthesize MWCNT/Ce<sub>x</sub>Sr<sub>1-x</sub>Fe<sub>y</sub>Co<sub>1-y</sub>O<sub>3</sub> (MWCNT/CSFC) nanocomposites for low to intermediate temperature (300–600 °C). The nanocomposite materials were characterized using a range of techniques such as Fourier Transform Infrared Spectroscopy (FTIR), Raman Spectroscopy, X-ray Diffraction (XRD), Thermogravimetric Analysis (TGA), Scanning Electron Microscopy with Energy Dispersive X-Ray Spectroscopy (SEM/EDS), Transmission Electron Microscopy (TEM) and High Resolution Transmission Electron Microscopy (HRTEM).

#### 4.1 Fourier Transform Infrared Spectroscopy (FTIR) Analysis

To identify functional groups, Infrared spectroscopy was used on both for starting materials with  $x = 0.6$  and  $y = 0.8$  and for composites. Figure 4.1 shows FTIR spectra for a ratio of 1:3 MWCNTs to CSFC. This material is representative, but showed more intense peaks than those of lower loadings of CSFC perovskites. The IR spectrum of a perovskite prepared by the CVD method and recorded before heat treatment shows vibrational modes with broad bands at 1371 and 3357 cm<sup>-1</sup>. In addition to that, there are two vibrational bands at around

700 and 800  $\text{cm}^{-1}$  and small peaks at 1642 and 2420  $\text{cm}^{-1}$  (Appendix A1). The peaks at 700 and 800  $\text{cm}^{-1}$  are attributed to symmetric stretching of metal–oxygen, O–(FeCo)–O and O–(CeSr)–O bonds. The sharp and broad peaks at 1371 and 3357 are assigned to the  $\text{FeCoO}_6$  octahedra and adsorbed water molecules, respectively.

After heat treatment at 400 °C, there is a shift to lower frequencies in the metal–oxygen peaks at 533 and 870  $\text{cm}^{-1}$ . The peak assigned to the  $\text{FeCoO}_6$  octahedra shifted slightly to a higher frequency of 1458  $\text{cm}^{-1}$ . The peak for adsorbed water molecules at 3357  $\text{cm}^{-1}$  is diminished after heat treatment at 400 °C. The remaining peak can be attributed to adsorbed moisture during the cooling process of the CSFC perovskite (Appendix A1). The most significant vibrational bands occur at 500 and 1400  $\text{cm}^{-1}$  due to the stretching of the metal–oxygen bonds in the perovskite structure. The peak assigned to the rigid octahedra does not change much during the heat treatment process [5, 18, 178].

In the IR spectrum of the CSFC synthesized from sol–gel before heat treatment, there are vibrations at 435, 668, 931, 1103, 1366, 1562, 2861 and 3388  $\text{cm}^{-1}$  (Appendix A1). The peaks at 668 and 931  $\text{cm}^{-1}$  are attributed to symmetric stretching of metal–oxygen O–(FeCo)–O and O–(CeSr)–O bonds. The sharp peak at 1103  $\text{cm}^{-1}$  is attributed to the C–O band, carbon from the acac and oxygen from water or alcohol. Other sharp peaks at 1366 and ~ 1500  $\text{cm}^{-1}$  are attributed to the  $\text{FeCoO}_6$  octahedra and C=C and C=O groups originating from the polymeric solution. The bands at 2861 and 3388  $\text{cm}^{-1}$  are assigned to the OH groups from alcohol and water, respectively. After heat treatment at 400 °C, the spectrum has vibrational bands at 429, 607, 822, 1090, 1323, 1501 and 2000  $\text{cm}^{-1}$ . Bands have shifted to lower frequencies and the peaks for OH groups disappear [5, 18, 178] (Appendix A1).

The FTIR spectra of MWCNT/CSFC synthesized by sol–gel and by CVD are shown in Figure 4.1 (a) and (b), respectively. For the MWCNTs, bands are attributed to the symmetric (2674  $\text{cm}^{-1}$ ) and asymmetric (2098  $\text{cm}^{-1}$ ) stretch of  $\nu\text{CH}$  groups,  $\nu\text{C–H}$   $\text{sp}^3$  hybridized (2423  $\text{cm}^{-1}$ ), carbonyl stretching mode  $\nu\text{C=O}$  (1764  $\text{cm}^{-1}$ ), graphene layers  $\nu\text{C=C}$   $\text{sp}^2$  hybridized (1540  $\text{cm}^{-1}$ ), vibrations of methylene ( $\text{CH}_2$ ) groups (1400  $\text{cm}^{-1}$ ), vibrational bands of  $\nu\text{C–O}$  bonds (1057  $\text{cm}^{-1}$ ) and a C–C stretching mode at 997  $\text{cm}^{-1}$  [59, 179]. The CSFC perovskite in the composites vibrates at around 800  $\text{cm}^{-1}$  with symmetric stretching of (FeCo)–O and (CeSr)–O and at around 500  $\text{cm}^{-1}$  showing the asymmetric stretching mode of O–(FeCo)–O, and O–(CeSr)–O in the spectrum [5, 18, 88]. The metal to oxygen (O–FeCo–O and O–CeSr–O) bonds at ~ 500  $\text{cm}^{-1}$ , the H–O bonds at ~ 1550  $\text{cm}^{-1}$  and the H bond at ~ 3330  $\text{cm}^{-1}$  might

come from intermolecular condensation of the perovskite [18, 87, 88, 180]. The IR spectra of MWCNT/CSFC composites show three broad IR adsorption peaks at positions similar to those of perovskites. There are strong interactions between the polar groups on the perovskites and MWCNTs. Additional functional groups in the sol-gel originate from MWCNTs (–OH, C–H, C=C, CH<sub>2</sub>, C–C), ethanol and water and residual acacs ligands (C–H, C=C, C=O, CH<sub>2</sub>, C–C, –OH) present in the perovskite structure.

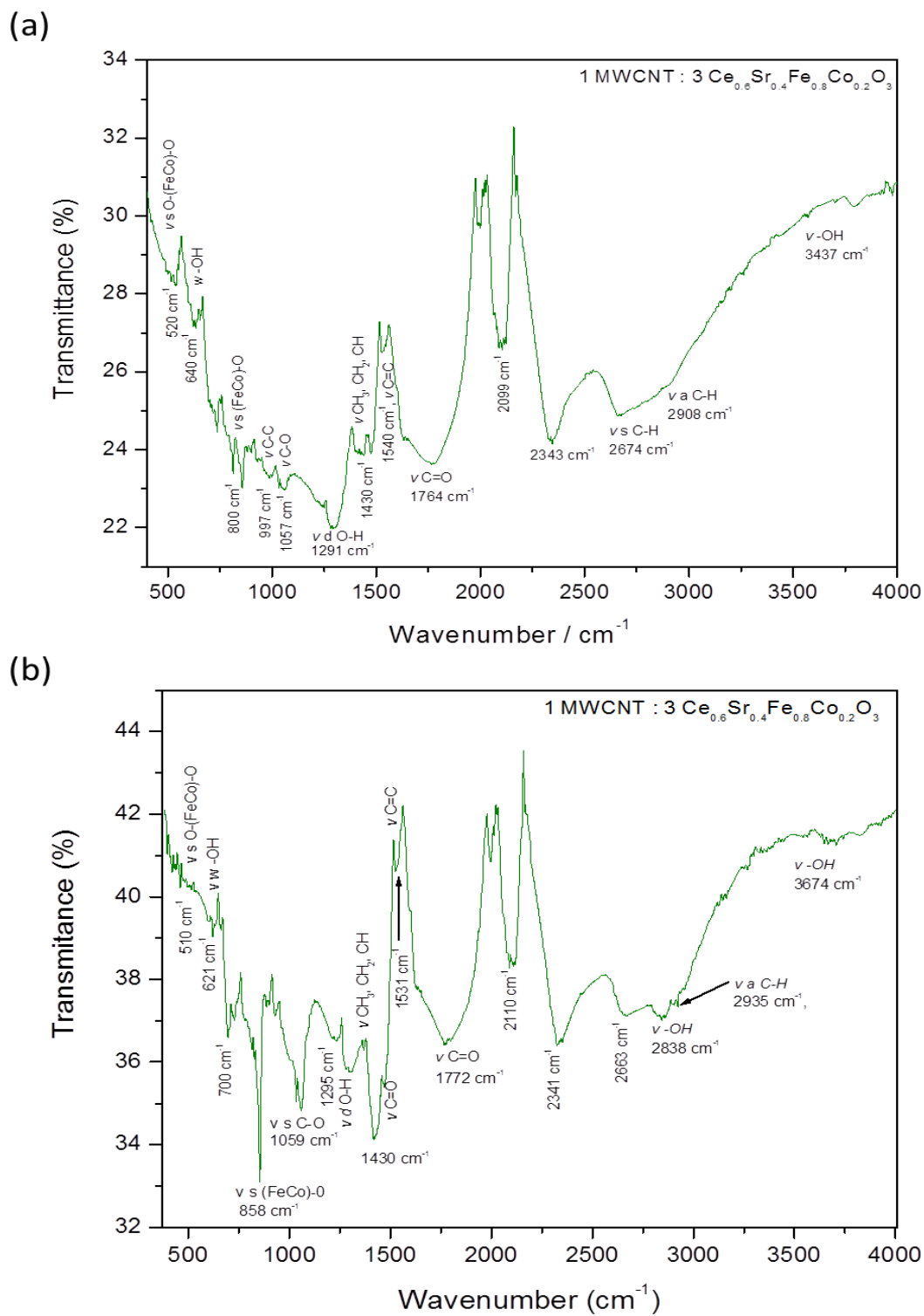


**Figure 4.1:** Representative Fourier transform infrared spectra of 1 MWCNT/3 Ce<sub>0.6</sub>Sr<sub>0.4</sub>Fe<sub>0.8</sub>Co<sub>0.2</sub>O<sub>3</sub> nanocomposite: Synthesized by (a) CVD and (b) sol-gel method after heat treatment at 400 °C

Table 4.1 summarizes the functional groups and corresponding wavenumbers of MWCNT/CSFC ( $x = 0.6$ ,  $y = 0.8$ ) composite materials synthesized by CVD and sol-gel methods. The wavenumbers of functional groups in MWCNT/CSFC composites synthesized from sol-gel method are slightly shifted to lower frequencies compared to those synthesized by CVD. The main differences in the spectra are the peaks at 1430, 1295 and 858  $\text{cm}^{-1}$  which are dominant in the composites synthesized by sol-gel method. These peaks are attributed to residual carbon after heat treatment at 400 °C for 8 hours. The acacs functional groups in the sol-gel method have reacted with the polymeric solution and some of the functional groups were burned off during heat treatment. Other peaks could be due to the MWCNT walls and the peak at around 800  $\text{cm}^{-1}$  is associated with the stretching of the perovskite in the composite [5, 18, 87, 88, 180].

**Table 4.1:** Characteristic wavenumbers of functional groups in MWCNT/CSFC ( $x = 0.6$ ,  $y = 0.8$ ) composites in FTIR

CVD		sol-gel	
Wavenumber/ $\text{cm}^{-1}$	Functional group	Wavenumber/ $\text{cm}^{-1}$	Functional group
518	O-(FeCo)-O	500	O-(FeCo)-O
520	O-(CeSr)-O	510	O-(CeSr)-O
640	wagging-OH	621	wagging-OH
800	(FeCo)-O	858	(FeCo)-O
820	(CeSr)-O	870	(CeSr)-O
997	C-C	997	C-C
1057	C-O	1059	C-O
1291	deformation O-H	1295	deformation O-H
1430	CH <sub>3</sub> , CH <sub>2</sub> , CH	1430	CH <sub>3</sub> , CH <sub>2</sub> , CH
1540	C=C	1531	C=C
1764	C=O	1772	C=O
2841	symmetric C-H	2838	symmetric C-H
2909	asymmetric C-H	2935	asymmetric C-H
3437	stretching O-H	3674	stretching O-H

#### 4.1.1 Effect of MWCNT:CSFC ratio on FTIR spectra

The FTIR spectra of composites showed some differences in the functional groups when depending on the MWCNT to CSFC ratios. In Figure 4.2 (a), the CVD synthesized composites exhibit the same peaks assigned to functional groups as discussed in section 4.1 for the 1:3 composites. An increase in the perovskite peak intensities at around 500 and 800  $\text{cm}^{-1}$  was observed when changing the ratio from 1:0.5 to 1:3. Since the perovskite nanoparticles are being formed within the MWCNTs, composites with low perovskite loadings 1:0.5 do not show all the functional groups. As the loading increases from 1:1 to 1:3 the perovskite functional groups start to appear in the spectrum. There was no significant difference in the nature of the functional groups with varying ratios. The only difference was in the intensities of the peaks indicating increased mass ratios of the perovskites. The same functional groups were observed and the major ones are indicated with dotted lines in Figure 4.2 (a). As the perovskite loading increases from 1:0.5 to 1:1, the functional groups of the MWCNTs dominate. This is an indication that the perovskite nanoparticles are formed on the outer walls of MWCNTs surface. But high perovskite loadings like in the ratio 1:3 have high peak intensities of the perovskite functional groups at around 800  $\text{cm}^{-1}$ . This is an indication of increased perovskite concentration in the composite.

The same trend is observed in the sol-gel synthesized composites (Figure 4.2 (b)), but here the number of functional groups on the surface of MWCNTs has increased. Some of the peaks develop and disappear as the perovskite loading is increased from 1:0.5 to 1:1. Perovskite functional groups at around 700–800  $\text{cm}^{-1}$  appear in the composites with low perovskite loadings, but as the ratio increases to 1:1, those groups start to disappear and they re-appear for the 1:3 composite. This is because at 1:1 sample ratio, the MWCNT suppresses the perovskite functional groups but as the loading increases to 1:3, perovskite peaks start to develop. The perovskite nanoparticles are formed within the MWCNTs as in the case of composites synthesized by CVD in Figure 4.2 (a). For the sol-gel method the number of functional groups has increased, probably due to the liquid solution used in the sol-gel method (Pluronic F-127 in ethanol and water and the groups resulting from the reactions of metal acacs and polymer). The most dominant peaks are marked with dotted lines in the spectrum. The major perovskite functional groups at around 1200  $\text{cm}^{-1}$  [88] are dominating in the composite with low CSFC ratio (i).

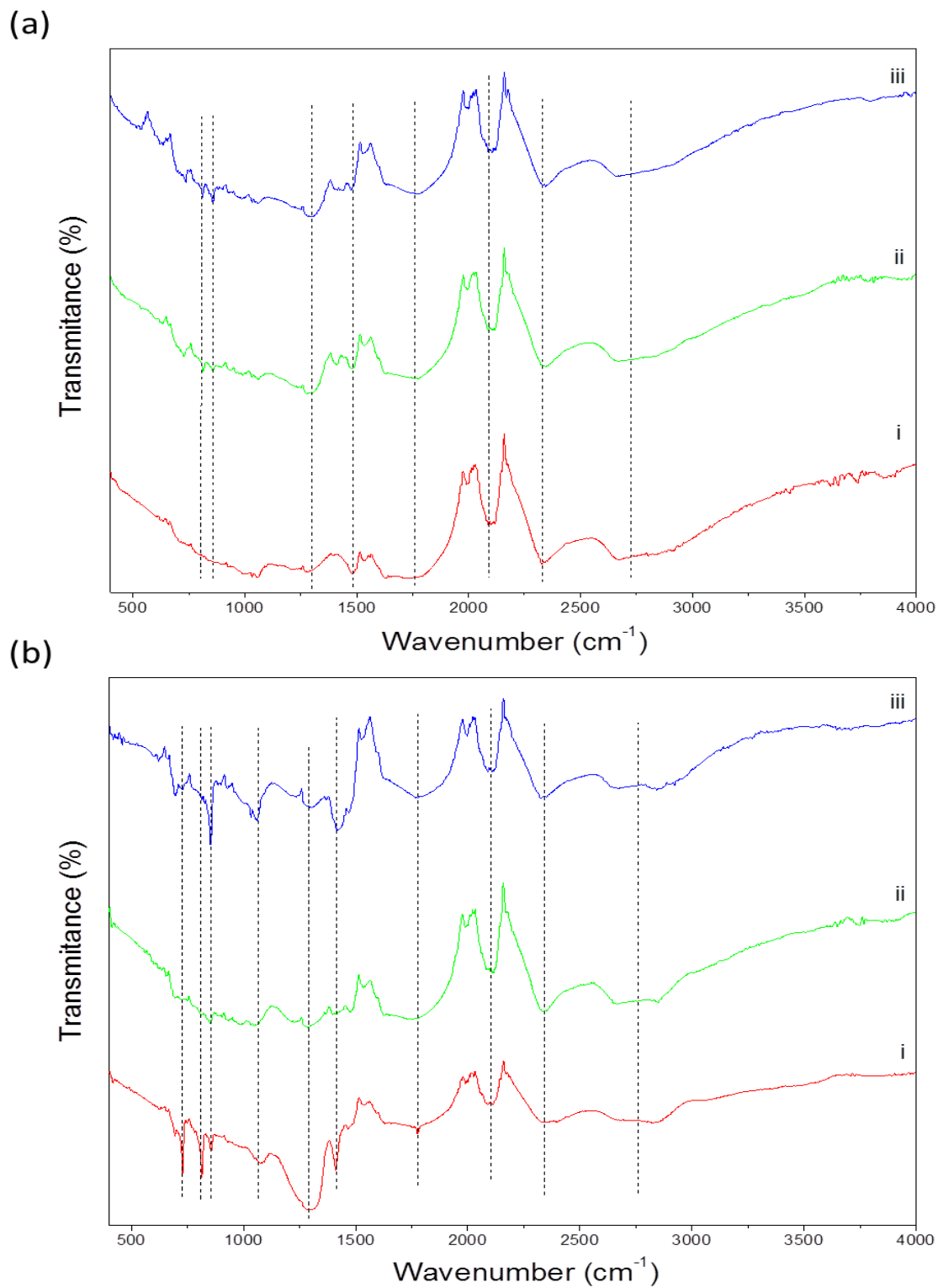


**Figure 4.2:** Representative Fourier transform infrared spectra of MWCNT/Ce<sub>0.6</sub>Sr<sub>0.4</sub>Fe<sub>0.8</sub>Co<sub>0.2</sub>O<sub>3</sub> nanocomposite with varying compositions, (i) (1:0.5), (ii) (1:1) and (iii) (1:3), synthesized by (a) CVD and (b) sol-gel method and heat treated at 400 °C

## 4.2 Raman Spectroscopy

Raman spectroscopy was used to study the vibrational modes of the MWCNT/CSFC composite materials. Figure 4.3 shows Raman spectra of composites synthesized by CVD and sol-gel methods. The 1:0.5 composite is used as representative example. The spectra have been adjusted with base line correction using a linear function and smoothing function, afterwards both the peak position and line width were determined by fitting to a Lorentzian curve. For the MWCNTs in the composite, there are two important bands, one is at  $\sim 1575 \text{ cm}^{-1}$  (G-band) and the other at  $1338 \text{ cm}^{-1}$  (D-band), which represents the  $sp^2$  and  $sp^3$  hybridized carbons, respectively. Here the D-band mode is found at  $1342 \text{ cm}^{-1}$  for the CVD sample and at  $1345 \text{ cm}^{-1}$  for the sol-gel sample. The D band is due to defects present on the MWCNTs surface and carbonaceous particles that might be present along with the tubes. FTIR results showed that there are groups attached to MWCNTs surfaces (C=O, metal-oxygen bonds and other oxygen containing groups) as discussed in section 4.1. Raman spectroscopy also confirmed the presence of defects on the MWCNTs which are due to the presence of these functional groups on the MWCNTs walls. Moreover, the G-band mode was found at  $1599 \text{ cm}^{-1}$  and  $1594 \text{ cm}^{-1}$  in the Raman spectra of the composites synthesized by CVD and sol-gel methods, respectively. The G-band mode was assigned to the tangential modes  $E_{2g}$  of the two dimensional graphite.

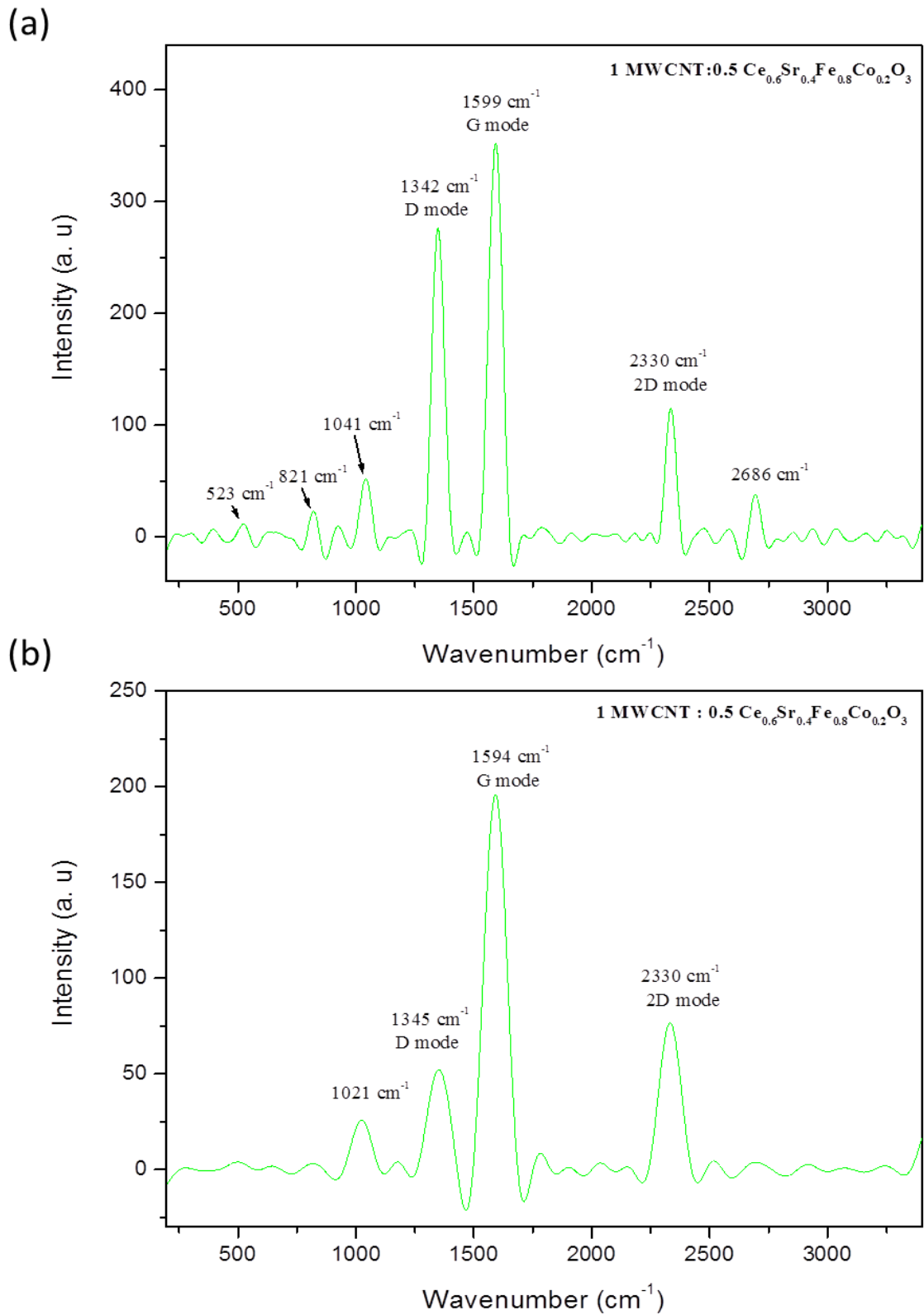


**Figure 4.3:** Raman spectra of MWCNT/CSFC (x = 0.6, y = 0.8) nanocomposite: Synthesized by (a) CVD and (b) sol-gel methods, after heat treatment at 400 °C

There are 15 Raman active modes in the spectrum of the  $ABO_3$  ( $Ce_xSr_{1-x}Fe_yCo_{1-y}O_3$ ) perovskite structure [18]. Here, three Raman active modes for the cubic structure are observed; these are  $A_{1g}$ ,  $E_{2g}$ , and  $T_{2g}$  modes at  $\sim 523$ ,  $821$  and  $1041\text{ cm}^{-1}$ , respectively, in the CVD sample. The peak at  $1041\text{ cm}^{-1}$  is due to asymmetric stretching of the FeCo–O–FeCo bond. No additional modes were observed at lower frequencies even after heating. Only weak bands were observed at higher frequencies, i.e. the band at  $\sim 1500\text{ cm}^{-1}$ . Vacancies within the perovskite structure arise because of the redox couple reactions taking place in the A and B-site metals [18, 87]. In the Raman spectrum of the composite synthesized by sol-gel method, low frequency bands normally at about  $523$  and  $821\text{ cm}^{-1}$  for perovskite, are absent. This might be attributed to the removal of acacs groups by heat treatment or the interactions of acacs ligands with liquid solution (unlike in the CVD) whereby the presence of acacs ligands aids in the formation of perovskite (to be discussed in section 4.3). In the Raman spectrum of the composite, an additional Raman active mode appears at  $\sim 2330\text{ cm}^{-1}$ . This can be attributed to the 2D mode of the MWCNTs and/or to the vibrations of  $H_3O^+$  in the crystal structure of the perovskite due to the substitution of cations by  $H_3O^+$  from the metal site [90]. These two bands for MWCNTs and perovskite crystal structure occur at the same wavenumber of the Raman spectrum.

The integrated band intensity ratio ( $I_D/I_G$ ) gives information on the distribution of defect sites on the MWCNTs. The ratio increases as more covalent bonds are formed due to the formation of  $sp^3$  hybridized carbon defect sites, and less graphitic carbon is present within the sample [115]. This  $I_D/I_G$  ratio is taken as the quality index of MWCNTs. Table 4.2 shows the intensity ratios of the D and G-band of the MWCNTs in the MWCNT/CSFC nanocomposite materials synthesized by CVD and sol-gel methods before and after heat treatment.

**Table 4.2:** Raman D and G bands intensity ratios of the MWCNT/CSFC composites before and after heat treatments at 400 °C for both CVD and sol–gel composites

Composites	CVD (D/G band peak areas)		sol–gel (D/G band peak areas)	
	Before heat treatment	After heat treatment	Before heat treatment	After heat treatment
(1:0.5)	0.13	0.01	0.19	0.19
(1:1)	2.48	2.50	0.41	0.28
(1:3)	0.68	0.17	0.06	0.04

From Table 4.2, it can be seen that the  $I_D/I_G$  ratio generally was low for the 1:0.5 ratio but increased for the 1:1 ratio and dropped again for the 1:3 ratio, for heat treated and untreated samples. For all samples, there was generally a decrease in this ratio between the unheated samples and the heat treated samples, except for the 1:1 ratio sample prepared by CVD method. This increase might have been caused by the disorder on the MWCNTs surfaces. The disorder decreases as the perovskite loading was raised to 1:3. The same trend occurs in the sol–gel method. This might be because perovskite metal precursors and acac ligands form more bonds with the MWCNTs surface groups (carbonyl, etc identified from FTIR), which then lead to fewer disorder sites on the MWCNTs walls, which could in turn decrease the D–band intensity. More clearly, the disorder on the 1:0.5 sample decreases after heat treatment for the samples synthesized by CVD method. For the 1:0.5 sol–gel composites there was no change in the disorder even after heat treatments at 400 °C. Lastly, sol–gel synthesized composites with 1:3 ratio showed less disorder on the MWCNTs walls before and after heat treatment. The composite materials with increased values of  $I_D/I_G$ , were more graphitic with vacancies or defects occupied as in 1:1 ratios of all samples.

### 4.3 X–Ray Diffraction Studies

The crystallographic structures of the as prepared and heat treated CSFC perovskites and MWCNT/CSFC composites at 400 °C were examined by X–ray diffraction. The measurements were performed on an XRD diffractometer with Cu  $K\alpha$  radiation of wavelength  $\lambda = 1.5406 \text{ \AA}$ . The analysis of the data shows the perovskite–type oxide structure and different phases of  $\text{CeO}_2$  (JCPDS: 000340394),  $\text{SrFe}_{12}\text{O}_{19}$  (JCPDS: 0000391083),  $\text{Fe}_3\text{O}_4$  (JCPDS: 000030863) and  $\text{SrCoO}_{2.29}$  (JCPDS: 000391083). These perovskite structures were

formed after the heat treatments at 400 °C for 8 hours. The major peaks correspond to the reflections from the (111), (200), (210), (211), (300), (221), (310), (311), (321), (410), (322), (420), (422), (511) and (521) planes. These planes were attributed to different phases of perovskite structures. The crystallite sizes of the nanocomposites materials were calculated from the peak broadening of the most intense peak, the (200) peak, using the Scherrer equation as described in Chapter 3 (section 3.3.4).

The temperature at which perovskite phases start to form was determined by *in-situ* XRD experiments. The changes in the relative amounts of perovskites and nanotubes were studied. In addition to that, the effects of different compositions of the perovskite structures were investigated.

#### 4.3.1 *In-situ* XRD experiment

The temperature at which the perovskite phases start to form was determined by powder *in-situ* powder XRD of the perovskites ( $\text{Ce}_{0.6}\text{Sr}_{0.4}\text{Fe}_{0.8}\text{Co}_{0.2}\text{O}_3$ ) and the MWCNT/ $\text{Ce}_{0.6}\text{Sr}_{0.4}\text{Fe}_{0.8}\text{Co}_{0.2}\text{O}_3$  composites synthesized by both CVD and sol-gel methods. The perovskite and carbon nanotubes composite materials were heat treated in the XRD chamber in the temperature range from 100–650 °C in 50 °C intervals. In the XRD patterns in Figure 4.4 (a) the phase formation starts at low temperatures; from 300 °C for perovskites synthesized by CVD method. This may indicate that the acetylacetonate exothermic decomposition in air aids in the formation of these complex materials. For the composite materials, synthesized in a 1:1 ratio by CVD method, (Figure 4.4 (b)), phase formation starts at temperature of ~ 300 °C as with the case of perovskites. These acac ligands would still be present in the composites formed by CVD method unlike in the case of a wet chemical method whereby these ligands react with any liquid present in the reaction. The diffractogram in Figure 4.4 (b), with MWCNTs also shows peaks at ~ 24.90 and 45.29° which were indexed to the reflections of hexagonal graphite in the MWCNT structure [84]. The XRD diffractogram in Figure 4.4 (a) show the peak for the CSFC perovskite at ~ 25.20° and this peak also appear in the diffractogram of the composites with MWCNTs (Figure 4.4 (b)) [181]. The peaks observed in the powder patterns were mainly for perovskites and metal acacs as marked with an asterisk in the diffractogram. The diffraction peaks at  $2\theta$  values of 24.90, 31.02, 32.80, 34, 90, 36,30, 41.00, 43.80, 47.20, 49.62, 56.09, 58.55, 68.94, 76.32, 78.71, 84.37 and 87.89° correspond to the (111), (200), (210), (211), (202), (300), (310),

(311), (321), (410), (420), (422), (333), (432) and (521) planes of the  $\text{Ce}_{0.6}\text{Sr}_{0.4}\text{Fe}_{0.8}\text{Co}_{0.2}\text{O}_3$  phase, indicating a perovskite structure adopted during calcination. In the XRD diffraction patterns of the composite with MWCNTs in Figure 4.4 (b), there was no significant difference except for two additional peaks for the MWCNTs. The additional diffraction peaks at  $2\theta$  values of  $\sim 24.90$  and  $45.29^\circ$  for the MWCNTs reflections overlap with those of perovskite at these  $2\theta$  angles.

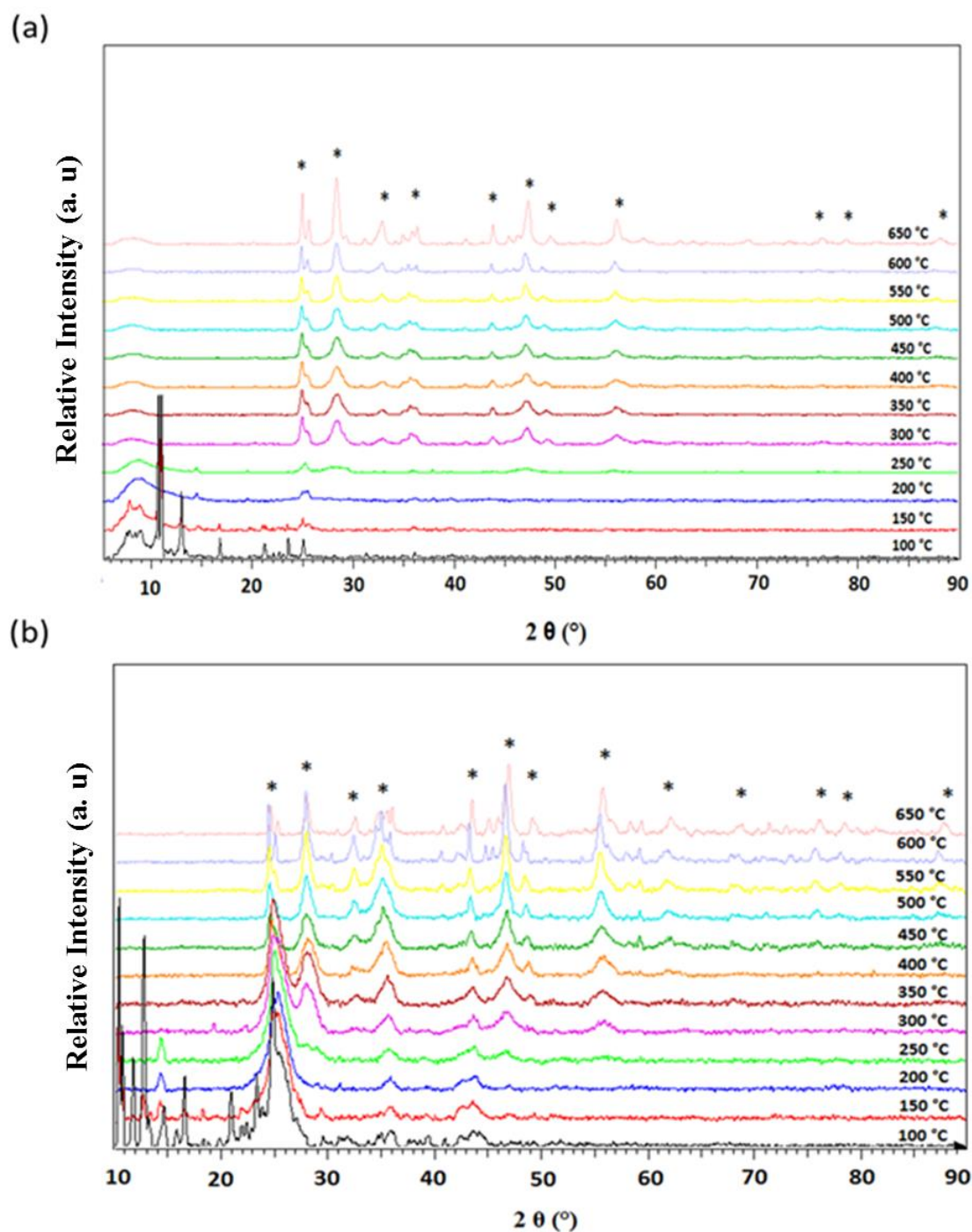


**Figure 4.4:** *In-situ* powder XRD diffractions synthesized by CVD method: (a)  $\text{Ce}_{0.6}\text{Sr}_{0.4}\text{Fe}_{0.8}\text{Co}_{0.2}\text{O}_3$  under air and (b)  $\text{MWCNT}/\text{Ce}_{0.6}\text{Sr}_{0.4}\text{Fe}_{0.8}\text{Co}_{0.2}\text{O}_3$  composite under  $\text{N}_2$  gas. The samples were heat treated at different temperatures from 100–650 °C in 50 °C increments. Perovskite phases formed are indexed with (\*)

Figure 4.5 shows the XRD diffraction patterns of the samples synthesized by sol-gel method and dried in the oven at 100 °C for 2 hours. The dried materials were heat treated in the instrument from 100–650 °C in 50 °C intervals using the same procedure as that for the CVD

method. The XRD patterns in Figure 4.5 (a) shows that perovskite phases did not form well. The phases formed were not only for the perovskite, but also for metal oxides as marked with an asterisk. The XRD diffraction peaks at  $2\theta$  values of 25.53, 26.46, 44.54, 45.29, 55.68 and  $81.85^\circ$  correspond to the (111), (200), (310), (311), (321), (432) and (521) planes of the perovskite and the other metal oxides. The metal oxides are present since in the sol–gel method there is no decomposition of acetylacetonate as in the case of the CVD method. The acacs reacts with the polymeric surfactant solution and the ligands fall off to produce acetylacetone [182]. The composites are also synthesized at the low temperature due to the reactor limits ( $550^\circ\text{C}$ ) and also to keep the MWCNTs intact. The composite materials, synthesized in the 1:1 ratio by sol–gel method Figure 4.5 (b) seem to only start developing perovskite phases at about  $300^\circ\text{C}$  as in the case of the perovskite alone. The diffractogram in Figure 4.5 (b) shows peaks at  $\sim 24.90$  and  $45.29^\circ$  which were indexed to the reflections of hexagonal graphite in the MWCNT structure [84]. The XRD diffractogram in Figure 4.5 (a) shows a peak for the CSFC perovskite at  $\sim 25.20^\circ$  which also appears in the diffractogram of the composites with MWCNTs (Figure 4.5 (b)) [181]. The phases formed are for perovskites and metal acacs and are marked with an asterisk in the diffractogram.

The absence of acacs resulted in the incomplete formation of perovskites in these materials. Sol–gel use a liquid to form networking array of atoms, so these acacs ligands react with any liquid present in the reaction and eventually form acetylacetone [182]. As seen from the FTIR results in section 4.1, the presence of polymeric solution in the reaction for the sol–gel process resulted in the formation of additional functional groups and new bonds, which can be attributed to the acetylacetone formation.

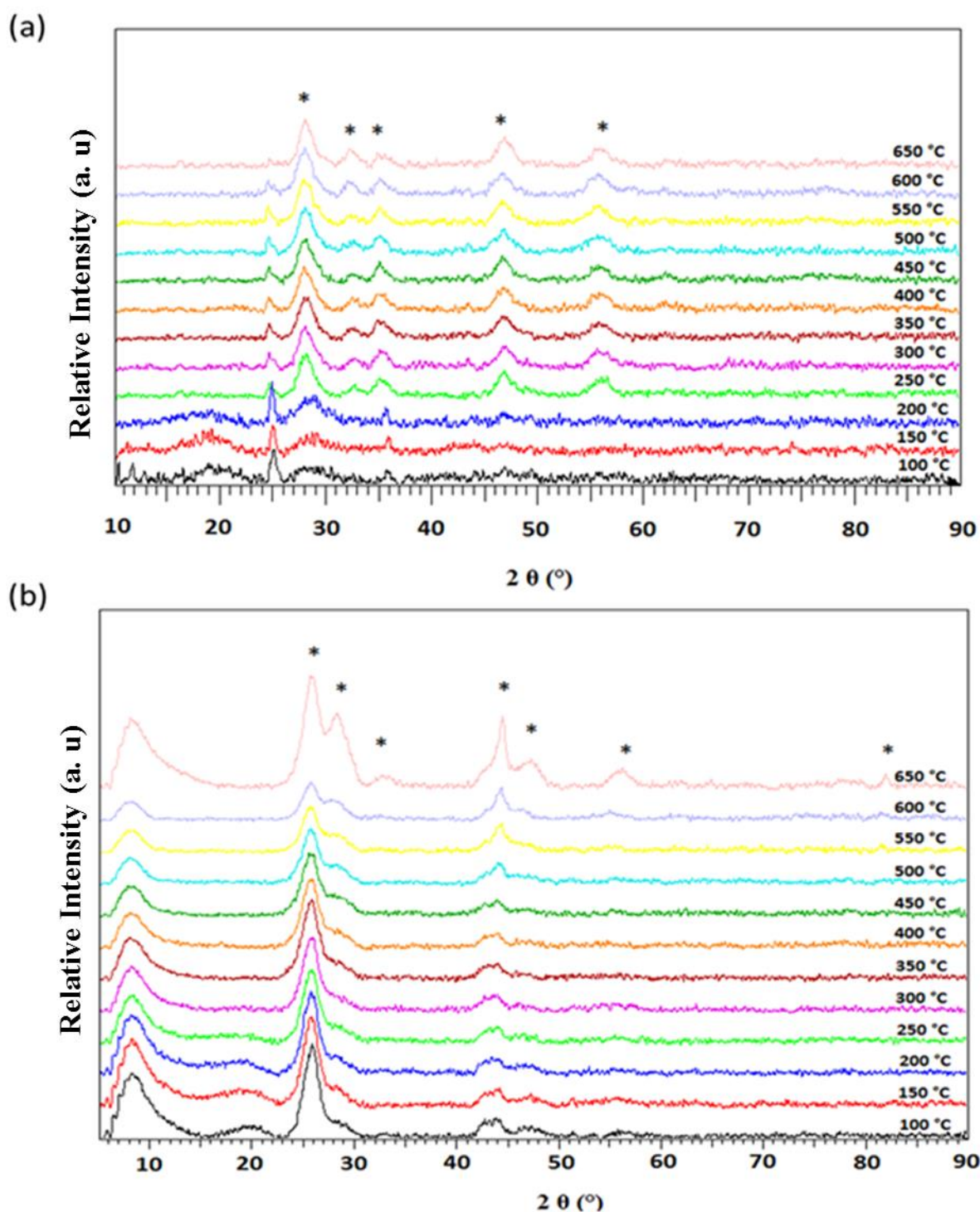


**Figure 4.5:** *In-situ* powder XRD diffractions synthesized by sol-gel method: (a)  $\text{Ce}_{0.6}\text{Sr}_{0.4}\text{Fe}_{0.8}\text{Co}_{0.2}\text{O}_3$  under air and (b)  $\text{MWCNT}/\text{Ce}_{0.6}\text{Sr}_{0.4}\text{Fe}_{0.8}\text{Co}_{0.2}\text{O}_3$  composite under  $\text{N}_2$  gas. The samples were heat treated at different temperatures from 100–650 °C in 50 °C increments. Perovskite phases formed are indexed with (\*)

Table 4.3 shows the actual values of the angle  $2\theta$ , diffraction spacings (d) and Miller indices of the peaks obtained from the in house XRD instrument for the perovskite synthesized by CVD and MWCNT/CSFC composite synthesized by sol–gel methods.

**Table 4.3:** Diffraction angles ( $2\theta$ ), d values and Miller indices (h k l) for the CSFC and 1MWCNT/1 CSFC ( $x = 0.6$ ,  $y = 0.8$ ) nanocomposite materials from *in-situ* experiments between 100 and 650 °C

$2\theta$ (°)		d value (Å)		Miller Indices (h k l)	
CSFC	MWCNT:CSFC	CSFC	MWCNT:CSFC	CSFC	MWCNT:CSFC
7.33	8.45	12.04	10.45	-	-
24.9	25.53	3.57	3.48	(111)	(111)
28.32	26.46	3.14	3.36	(200)	(200)
31.02	30.54	2.88	2.92	(210)	(210)
32.8	-	2.72	-	(210)	-
34.9	-	2.56	-	(211)	-
36.3	-	2.46	-	(211)	-
41.0	-	2.19	-	(202)	-
43.8	-	2.06	-	(300)	-
47.2	44.54	1.92	2.03	(310)	(310)
49.62	45.29	1.83	2.00	(311)	(311)
56.09	55.68	1.63	1.64	(321)	(321)
58.55	59.41	1.57	1.55	(410)	(410)
68.94	61.18	1.36	1.51	(420)	(420)
76.32	66.97	1.24	1.39	(422)	(422)
78.71	75.32	1.21	1.26	(333)	(333)
84.37	81.85	1.14	1.17	(432)	(432)
87.89	85.49	1.10	1.13	(521)	(521)

The perovskite phases from the study were compared with XRD data from JCPDS files of  $\text{CeO}_2$ ,  $\text{Fe}_2\text{O}_3$ ,  $\text{Fe}_3\text{O}_4$  and  $\text{SrCoO}_{2.29}$  obtained from iThemba Labs. The  $2\theta$  values of the prepared materials matched those from data base and the perovskite and metal oxides phases

present. The unknown wide peak at  $2\theta = 7.33^\circ$  was attributed to the effects of working at low angles in the XRD instrument.

From these XRD diffraction data base for metal oxides used in the phase identification, it was possible to index  $\text{Ce}_x\text{Sr}_{1-x}\text{Fe}_y\text{Co}_{1-y}\text{O}_3$  perovskite planes. The materials formed revealed all the phases present in these data base set. The major XRD diffraction angles for the perovskites present were at the  $2\theta$  values of 28.55, 31.04, 33.08, 34.18, 35.61, 36.04, 40.85, 44.92, 47.47, 49.48, 56.08, 57.67, 69.08, 76.70, 78.76, 83.93 and  $88.41^\circ$ . These XRD diffraction patterns corresponds to the (111), (008), (200), (114), (110), (202), (205), (207), (310), (311), (222), (218), (400), (422), (333), (432) and (521) planes for the  $\text{Ce}_x\text{Sr}_{1-x}\text{Fe}_y\text{Co}_{1-y}\text{O}_3$  perovskite. Table 4.4 shows the XRD reference data base for the metal oxides used in the phase identifications to try and show the individual metal oxides were not present.

**Table 4.4:** XRD reference data for the metal oxides used in the phase identifications

Cerium Oxide (CeO <sub>2</sub> )		Strontium Iron Oxide SrFe <sub>12</sub> O <sub>19</sub>		Strontium Cobalt Oxide SrCoO <sub>2.29</sub>		Iron (III) Oxide Fe <sub>2</sub> O <sub>3</sub>	
2θ (°)	(h k l)	2θ(°)	(h k l)	2θ (°)	(h k l)	2θ (°)	(h k l)
-	-	23.15	(006)	22.71	(100)	24.13	(012)
28.55	(111)	29.06	(106)	-	-	-	-
-	-	31.04	(008)	-	-	-	-
33.08	(200)	32.35	(107)	32.28	(110)	-	-
-	-	34.18	(114)	-	-	33.15	(104)
-	-	36.04	(202)	-	-	35.61	(110)
-	-	40.37	(205)	39.91	(111)	40.85	(113)
-	-	44.92	(207)	-	-	43.51	(202)
47.47	(220)	46.85	(100)	46.35	-	-	-
-	-	50.24	(110)	52.26	(210)	49.48	(024)
56.08	(222)	56.41	(304)	-	-	56.15	(211)
-	-	57.50	(218)	57.67	(211)	57.42	(122)
69.08	(400)	69.01	(211)	67.69	(220)	66.02	(208)
76.70	(331)	76.69	(106)	77.03	(310)	75.43	(220)
79.07	(420)	79.11	(406)	-	-	78.76	(223)
-	-	83.93	(432)	81.58	(311)	82.94	(034)
88.41	(422)	-	-	86.04	(222)	88.54	(226)

The grain sizes, crystallite sizes of perovskite nanoparticles formed within MWCNTs were calculated using the Debye–Scherrer formula as mentioned in Chapter 3 (section 3.3.4). The crystallite size was calculated using the (200) peak occurring at  $2\theta = 28.32^\circ$  in the diffractogram of CSFC perovskite and MWCNT/CSFC composite synthesized by CVD. The peak at  $2\theta = 44.45^\circ$  was used for the same sample but synthesized by sol–gel since the peak at  $2\theta = 28.32^\circ$  only develops at high temperatures. The crystallite sizes increased with an increase in temperature. It must be stressed that the presence of MWCNTs as templates have facilitated the reduction of crystallite sizes as can be seen from Table 4.5 for the perovskite synthesized by CVD and MWCNT/CSFC composite synthesized by sol–gel from the *in-situ* XRD experiment.

**Table 4.5:** Calculated crystallite sizes of perovskite nanoparticles from the *in-situ* XRD experiment

Temperature / °C	Particle Size / Å	
	CSFC	MWCNT/CSFC
300	80.96	5.98
350	74.33	4.65
400	83.77	5.15
450	76.46	6.55
500	105.15	8.51
550	105.15	7.29
600	143.26	59.07
650	191.76	33.73

From the *in-situ* XRD results it was concluded that the formation of perovskite nanoparticles occurred at temperatures of 300–650 °C. Since the study focuses on low to intermediate temperatures, the remaining samples were prepared at 400 °C. The samples were first prepared and heat treated at 400 °C for 8 hours then X-rayed at room temperature. The *in-situ* XRD experiment was used to determine the temperature at which perovskite phases start to form.

#### 4.3.2 Influence on different MWCNT/CSFC mass ratios

The powder X-ray diffraction patterns for the composites prepared by CVD and by sol-gel methods at the ratios of 1:0.5, 1:1 and 1:3 are given in Figure 4.6 (a) and 4.6 (b) respectively. For the CVD method all the ratios were calcined to 400 °C over 8 hours. All the high intensity peaks for the perovskites some of which disappear as the loading increases from (i), to (ii) to (iii) as shown in Figure 4.6 (a). The major peaks that disappear are (200), (210), (310), (420), (511) and (521) seen in the 1:0.5 composite. There seems also to be a change in peak intensity as the loading of CSFC increases. In contrast, for the higher loadings of CSFC in the sol-gel method (Figure 4.6 (b)) perovskite peaks are still present. It also seems like the presence of MWCNTs do not aid the formation of perovskite probably due to the low operating temperatures. The (200), (210), (310), (420), (422), (511) and (521) reflections diminish as the perovskite loadings were raised from 1:0.5 to 1:3 MWCNT to CSFC ratios.

In fact the intention here was to keep the MWCNTs intact throughout the process suggesting that MWCNTs catalyze the formation of the perovskite phases at low temperatures. Furthermore, as the CSFC ratio increases the formation of full perovskites and other new phases start to develop. The important reflections of the MWCNTs are marked with the dotted line at  $2\theta = 25.50^\circ$ . The phases formed from both methods were not different from each other, but the influence of different MWCNT/CSFC mass ratio was not the same.

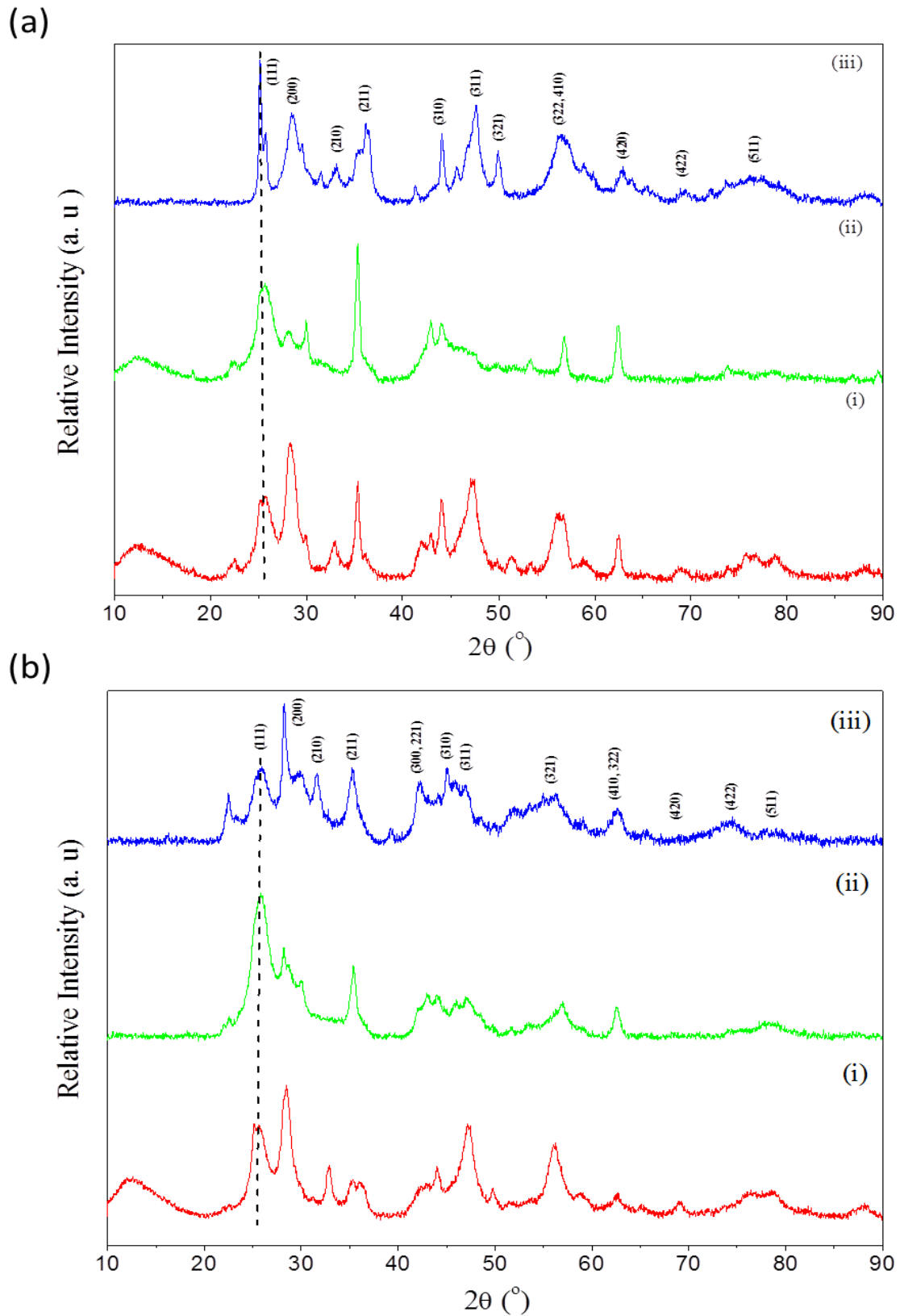


**Figure 4.6:** Room temperature XRD pattern of MWCNT/Ce<sub>0.6</sub>Sr<sub>0.4</sub>Fe<sub>0.8</sub>Co<sub>0.2</sub>O<sub>3</sub> nanocomposites: (i) (1:0.5), (ii) (1:1) and (iii) (1:3) synthesized by (a) CVD and (b) sol-gel method after heat treatment at 400 °C

Table 4.6 shows the  $2\theta$  values and Miller indices for MWCNT/Ce<sub>0.6</sub>Sr<sub>0.4</sub>Fe<sub>0.8</sub>Co<sub>0.2</sub>O<sub>3</sub> composites. Only the peaks at  $2\theta = 42.21$  and  $49.91^\circ$  are absent for the samples synthesized by CVD method. In all different ratios of nanotubes to perovskites there was a consistent phase formation, irrespective of the synthetic method.

**Table 4.6:** Room temperature diffraction angles ( $2\theta$ ) and Miller indices of the (1MWCNT/0.5 Ce<sub>0.6</sub>Sr<sub>0.4</sub>Fe<sub>0.8</sub>Co<sub>0.2</sub>O<sub>3</sub>) composite heat treated at 400 °C

Chemical Vapour Deposition		sol-gel	
$2\theta / ^\circ$	(h k l)	$2\theta / ^\circ$	(h k l)
25.70	(111)	25.57	(111)
28.19	(200)	28.32	(200)
32.45	(210)	32.58	(210)
35.20	(211)	35.33	(211)
-	-	42.21	(300, 221)
47.16	(310)	47.44	(310)
-	-	49.91	(311)
56.79	(321)	56.24	(321)
62.56	(322, 410)	62.43	(410, 322)
69.03	(420)	69.18	(420)
76.60	(422)	76.45	(422)
78.53	(511)	78.79	(511)
88.42	(521)	88.42	(521)

### 4.3.3 Influence of Varying x and y on CSFC with a 1:1 MWCNT/CSFC mass ratio

In this section the values of x and y are kept the same in each perovskite structure, Ce<sub>x</sub>Sr<sub>1-x</sub>Fe<sub>y</sub>Co<sub>1-y</sub>O<sub>3</sub>, but varied from 0.2 to 0.8 for the different perovskites (Figure 4.7). For the composites synthesized by CVD method, as the values of x and y are varied perovskite phases are formed. The difference is observed by the change in the peak intensity of the (111), (200) and (211) planes as x and y increases from 0.2 to 0.8. The measurement conditions used such as step size; sample size and preparation were kept standard for each

increase. Perovskite phases are formed in all compositions from  $x = y = 0.2$  to  $x = y = 0.8$ . The only difference was in the peak intensities. This can be attributed to the site occupation in the  $ABO_3$  structure of the perovskite as the cation compositions were altered. There is unfilled A and B site which lead to perovskite with distortions. The plane (200) is fully formed at high values of  $x$  and  $y$  and this has been matched with the plane seen in the perovskite with  $x = 0.6$  and  $y = 0.8$  when comparing different MWCNT to CSFC ratios. There was a significant difference in the composites with varying  $x$  and  $y$  values. A number of phases have changing peak intensities. The MWCNT reflection peaks are marked with a dotted line in the diffractogram at around  $25.50^\circ$ .

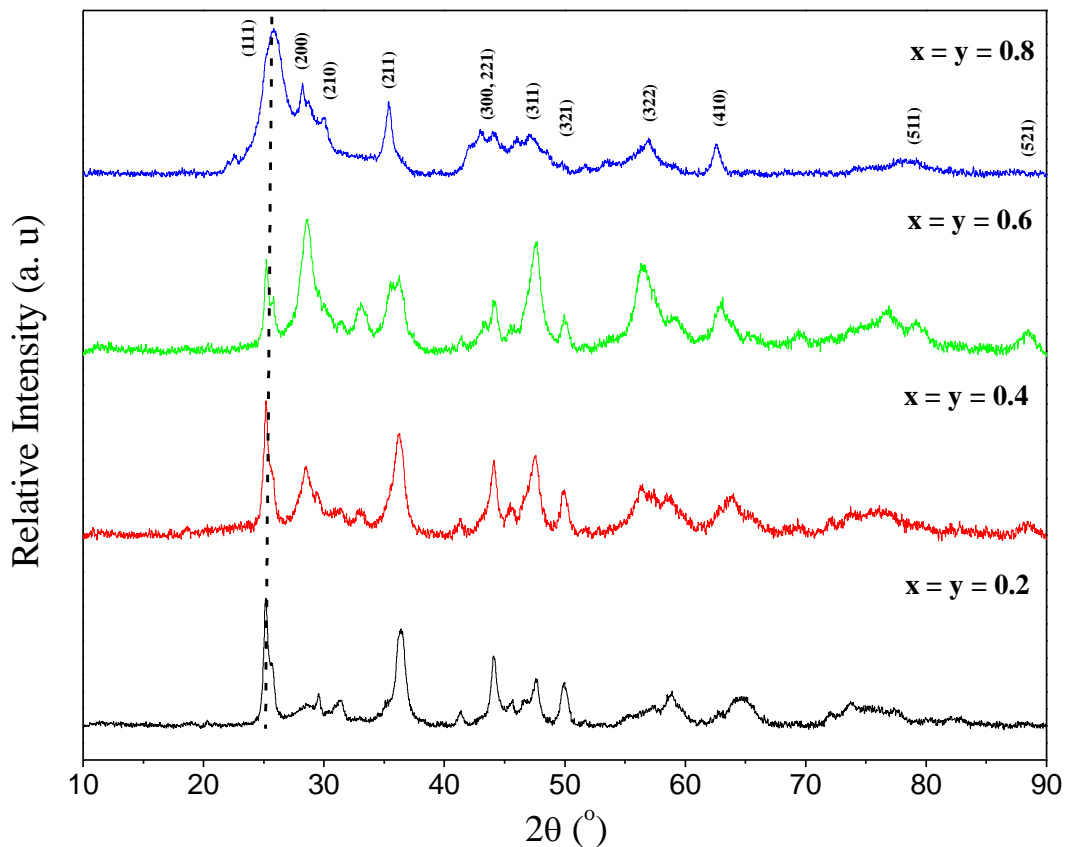


**Figure 4.7:** Room temperature XRD diffractogram of 1 MWCNT/1  $Ce_xSr_{1-x}Fe_yCo_{1-y}O_3$  ( $0.2 \leq (x, y) \leq 0.8$ ) nanocomposite synthesized by CVD method after heat treatment at  $400^\circ\text{C}$

The actual  $2\theta$  values and their corresponding Miller indices are listed in Table 4.7 for different compositions ( $x$  and  $y$ ) of perovskites. The diffraction peak at  $2\theta = 28.32^\circ$  has very

low intensity in the composites with  $x = y = 0.2$  but as the values were raised to 0.6 and 0.8 this phase start to develop with high intensity. Other missing peaks are marked with dash lines in the table. This shows that, high amounts of Ce and Fe cations are needed in order to form complete perovskite structure of this type and they play a major role in the oxygen reduction reaction for electrochemical performance in Chapter 5.

**Table 4.7:** Room temperature diffraction angles and their Miller indices for the MWCNT and  $Ce_xSr_{1-x}Fe_yCo_{1-y}O_3$  composite synthesized by CVD

$x = y = 0.2$		$x = y = 0.4$		$x = y = 0.6$		$x = y = 0.8$	
$2\Theta / ^\circ$	h k l						
25.27	(111)	25.27	(111)	25.27	(111)	25.27	(111)
28.32	(200)	28.34	(200)	28.62	(200)	28.49	(200)
29.64	(200)	29.60	(200)	29.46	(200)	-	-
31.42	(210)	31.42	(201)	31.27	(201)	-	-
-	-	32.95	(210)	33.10	(210)	33.10	(201)
36.17	(211)	36.30	(211)	36.17	(211)	35.46	(210)
41.48	(220)	41.35	(220)	41.35	(220)	43.4	(303)
44.13	(300)	44.00	(300)	44.13	(300)	44.13	(303)
45.54	(300)	45.54	(300)	45.54	(300)	-	-
47.50	(310)	47.50	(310)	47.63	(310)	47.77	(310)
49.86	(311)	49.86	(311)	49.86	(311)	49.86	(310)
-	-	56.30	(321)	56.43	(321)	56.30	(321)
58.95	(321)	58.40	(321)	58.81	(321)	-	-
64.83	(330)	63.84	(330)	63.00	(330)	62.87	(322)
-	-	-	-	69.44	(422)	69.44	(420)
75.86	(333)	76.01	(422)	76.85	(422)	76.85	(321)
-	-	-	-	79.37	(431)	79.50	(431)
-	-	88.32	(521)	88.59	(521)	88.59	(521)

The room temperature XRD of the composites synthesized by sol-gel method and heat treated at 400 °C for 8 hours is shown in Figure 4.8. The perovskite planes did not form well;

there is a combination of perovskites and metal oxide and secondary phases. The reason why perovskite peaks were not formed alone might be due to the low synthesis temperature as explained before. The low calcination temperature was applied in order to prevent the decomposition of MWCNTs and the limiting temperature of a reactor was 550 °C.

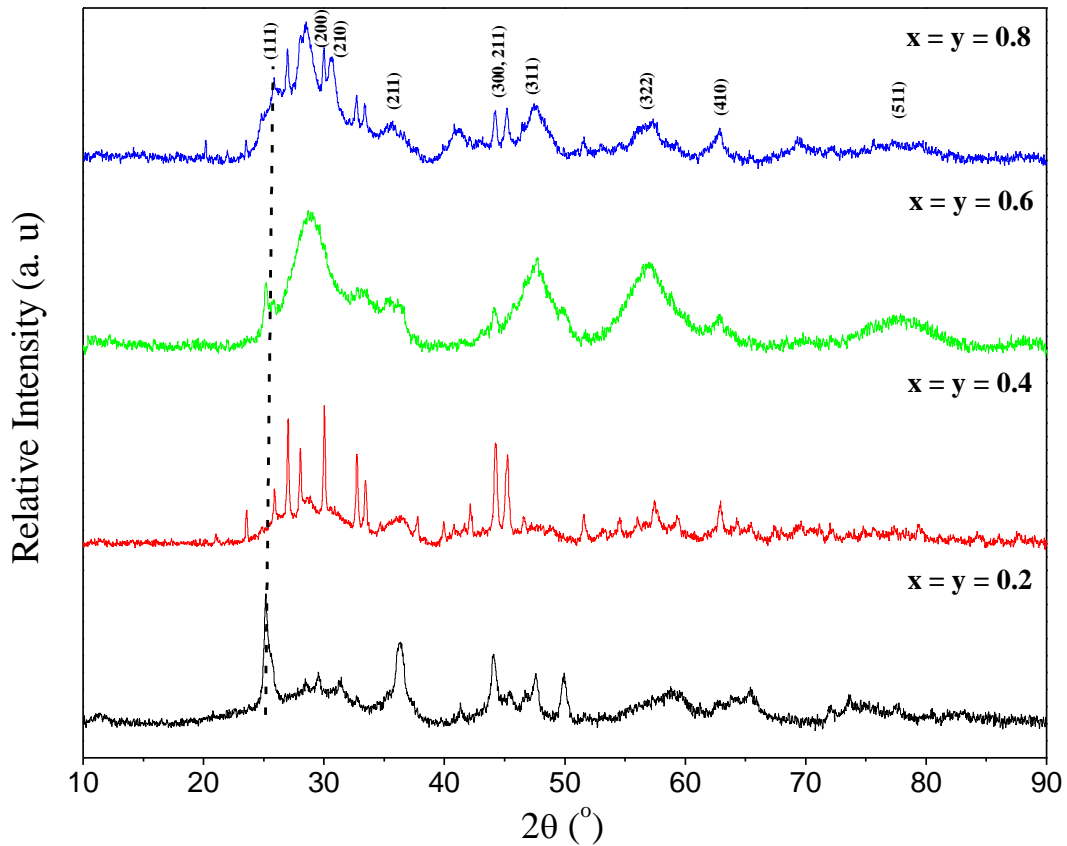


**Figure 4.8:** Room temperature XRD pattern of the 1 MWCNT/1  $\text{Ce}_x\text{Sr}_{1-x}\text{Fe}_y\text{Co}_{1-y}\text{O}_3$  ( $0.2 \leq (x, y) \leq 0.8$ ) nanocomposites synthesized by sol–gel method after heat treatment at 400 °C

Table 4.8 shows the actual  $2\theta$  values of nanocomposite materials synthesized by sol–gel method and their corresponding h k l values. The phases formed were not uniform for different compositions of  $x$  and  $y$  values with a number of missing peaks in the diffractogram. For the composites with  $x = y = 0.2$ , most of the diffraction peaks have shifted to different  $2\theta$  values in the diffractogram of the composites. In the case of the composites with  $x = y = 0.4$  there are a number of developing peaks, here perovskites together with metal oxides phases were formed and these metal oxides were not fully converted to perovskites because of low

operating temperatures. When compared to the XRD diffraction patterns of the perovskites synthesized from the *in-situ* XRD, there is a number of diffraction peaks that were not observed.

**Table 4.8:** Room temperature diffraction angles and their Miller indices for the 1 MWCNT and 1 Ce<sub>x</sub>Sr<sub>1-x</sub>Fe<sub>y</sub>Co<sub>1-y</sub>O<sub>3</sub> composites synthesized by sol-gel

<b>x = y = 0.2</b>		<b>x = y = 0.4</b>		<b>x = y = 0.6</b>		<b>x = y = 0.8</b>	
2 $\Theta$ / °	h k l	2 $\Theta$ / °	h k l	2 $\Theta$ / °	h k l	2 $\Theta$ / °	h k l
-		23.44	(111)	-	-	23.44	(111)
25.12	(111)	25.12	(111)	25.27	(111)	25.12	(111)
-	-	25.96	(200)	25.96	(111)	25.82	(200)
-	-	26.95	(200)	-	-	26.95	(200)
28.62	(200)	28.05	(200)	28.91	(200)	28.49	(200)
29.60	(200)	30.01	(210)	-	-	30.59	(201)
31.42	(201)	32.81	(211)	-	-	32.68	(211)
32.68	(210)	33.52	(211)	33.10	(210)	33.37	(211)
36.30	(211)	36.30	(211)	36.17	(211)	35.61	(211)
-	-	37.71	(220)	-	-	-	-
41.35	(220)	40.09	(221)	-	-	41.06	(300)
-	-	42.03	(300)	-	-	-	-
44.13	(300)	44.13	(310)	44.13	(300)	44.13	(310)
45.25	(300)	45.25	(311)	-	-	45.25	(311)
46.66	(301)	46.66	(311)	-	-	-	-
47.50	(310)	-	-	47.63	(310)	47.35	(311)
49.86	(311)	-	-	-	-	-	-
-	-	51.69	(321)	-	-	51.54	(321)
-	-	54.62	(321)	-	-	-	-
-	-	56.17	(400)	56.85	(321)	-	-
-	-	57.56	(410)	-	-	57.00	(322)
58.95	(321)	59.37	(411)	-	-	-	-
62.59	(322)	63.00	(322)	62.87	(322)	63.00	(420)
65.52	(330)	-	-	-	-	-	-
-	-	-	-	-	-	69.58	(430)
71.96	(322)	-	-	-	-	-	-
73.63	(332)	-	-	-	-	-	-
77.54	(430)	-	-	77.82	(430)	-	-
-	-	-	-	-	-	79.21	(521)
-	-	-	-	88.87	(521)	-	-

The crystallite sizes of the nanoparticles have been calculated for different x and y values in order to see which composition of MWCNTs and CSFCs have reduced particle size. It was

believed that the composites with small particle size would have high electrical performance as discussed in Chapter 5. Tabulated results (Table 4.9) show the change in the crystallite growth as the x and y values in the perovskite structure changes. The presence of MWCNTs as templates seems not contribute to reducing the crystallite sizes of the perovskites. However from the *in-situ* XRD analysis, MWCNTs seems to play a significant role in reducing crystallite sizes of nanoparticles. In some cases, perovskites formed in the absence of MWCNTs have small crystallite sizes as in the case of CSFC perovskite with x = y = 0.8 while in other cases, the presence of MWCNTs reduced the crystallite sizes for example MWCNT/CSFC composite with x = y = 0.2 synthesized by sol-gel method (Table 4.9). Generally, the CVD synthesized nanomaterials had reduced crystallite sizes.

**Table 4.9:** Calculated crystallite size for the MWCNT/Ce<sub>x</sub>Sr<sub>1-x</sub>Fe<sub>y</sub>Co<sub>1-y</sub>O<sub>3</sub> nanocomposites

Electrode Material	Particle size / Å			
	x	y	CVD	sol-gel
CSFC	0.2	0.2	138.5	177.1
CSFC	0.4	0.4	188.2	119.0
CSFC	0.6	0.6	292.7	125.1
CSFC	0.6	0.8	72.36	95.36
CSFC	0.8	0.8	43.51	32.49
1CNT:1CSFC	0.2	0.2	92.83	25.37
1CNT:1CSFC	0.4	0.4	61.58	497.7
1CNT:1CSFC	0.6	0.6	104.3	30.82
1CNT:1CSFC	0.8	0.8	43.51	67.36
1CNT:0.5CSFC	0.6	0.8	68.82	91.75
1CNT:1CSFC	0.6	0.8	83.27	243.25
1CNT:2CSFC	0.6	0.8	96.16	221.00
1CNT:3CSFC	0.6	0.8	54.28	176.82

#### **4.4 Thermogravimetric Analysis (TGA)**

Thermogravimetric analysis has been used to study the thermal stability of the MWCNT/CSFC composite materials. From the weight loss curves the initiation temperature, the oxidation temperature and the residual mass has been determined using the TA universal analysis software. The initiation temperature is defined as the temperature at which material starts to decompose. The oxidation temperature is the point of maximum rate of weight loss and is identified as the peak in the derivative of the weight loss as a function of temperature [115]. Furthermore, the heat flow curve gives information on the heat lost or gained as exothermic (pointing upwards) or endothermic (pointing downwards) peaks. The oxidation temperature can be taken as the thermal stability of the material. The residual mass is the mass remaining after heating. In the case of MWCNTs, the residual mass is attributed to the metal catalyst present in the MWCNTs synthesis.

Here, the above discussed parameters are measured in different composites, with changing MWCNT to CSFC ratio and perovskite compositions. In this case the purity of MWCNTs is expected to alter because of defects as the perovskite loading is raised from 1:0.5 to 1:3. For confirming different phases from room temperature XRD, TGA analysis for different MWCNT/CSFC ratios has been conducted.

##### **4.4.1 Comparison of CVD versus sol–gel Synthesized Composites**

Results of the thermogravimetric analysis of the MWCNT/CSFC 1:0.5 composites synthesized from both CVD and sol–gel methods are plotted in Figure 4.9. The initiation temperature of these composites is at around 300 °C and the oxidation temperature is at 560 °C, and occurs at the same point as the maximum rate of change of weight percent in the derivative weight curve. Heat flow curves show that these materials maximum exothermic peak is at the same point as the maximum rate of change of weight percent. Heat flow curves have peaks pointing upwards, then this process is exothermic in nature and these materials give off heat at the maximum rate of weight loss. Since the oxidation temperature is taken as an indicator of thermal stability [115], then the MWCNT/CSFC nanocomposite is thermally stable up to 560 °C and above this temperature MWCNTs will rapidly burn. It is important not to exceed the temperature at which MWCNTs thermally decompose in order to keep them for characterizations and applications (electrochemical testing in Chapter 5). At temperatures above 580 °C only the residual mass is left up to the end of the heating process at 1000 °C.

There was no significant difference between the two syntheses methods. The composites have fewer defects exposed on the MWCNTs surface as results of coating with perovskites nanoparticles. This corresponds to the results from Raman spectroscopy which pointed out that the low loading perovskites composites have low values of  $I_D/I_G$  ratios which was due to less disorder from the covered defects. The small peaks on the derivative weight curves were assigned to the loss of weakly adsorbed water molecules at  $\sim 330$  °C for the composite synthesized by CVD. In the sol-gel synthesized composite the small peak at  $\sim 180$  °C was associated with the loss of weakly adsorbed water molecules in combination with other organic groups present from acacs and polymeric solution. Here, this peak is at very low temperature, this confirms the formation of other functional groups in the FTIR results for the sol-gel synthesized composites. From TGA curves (Figure 4.9 (a) and (b)), there is a small peak observed in the derivative weight curve at 800 °C and it was assigned to the loss of unknown moieties (possibly OH groups, or trapped carbon) from the perovskites materials.

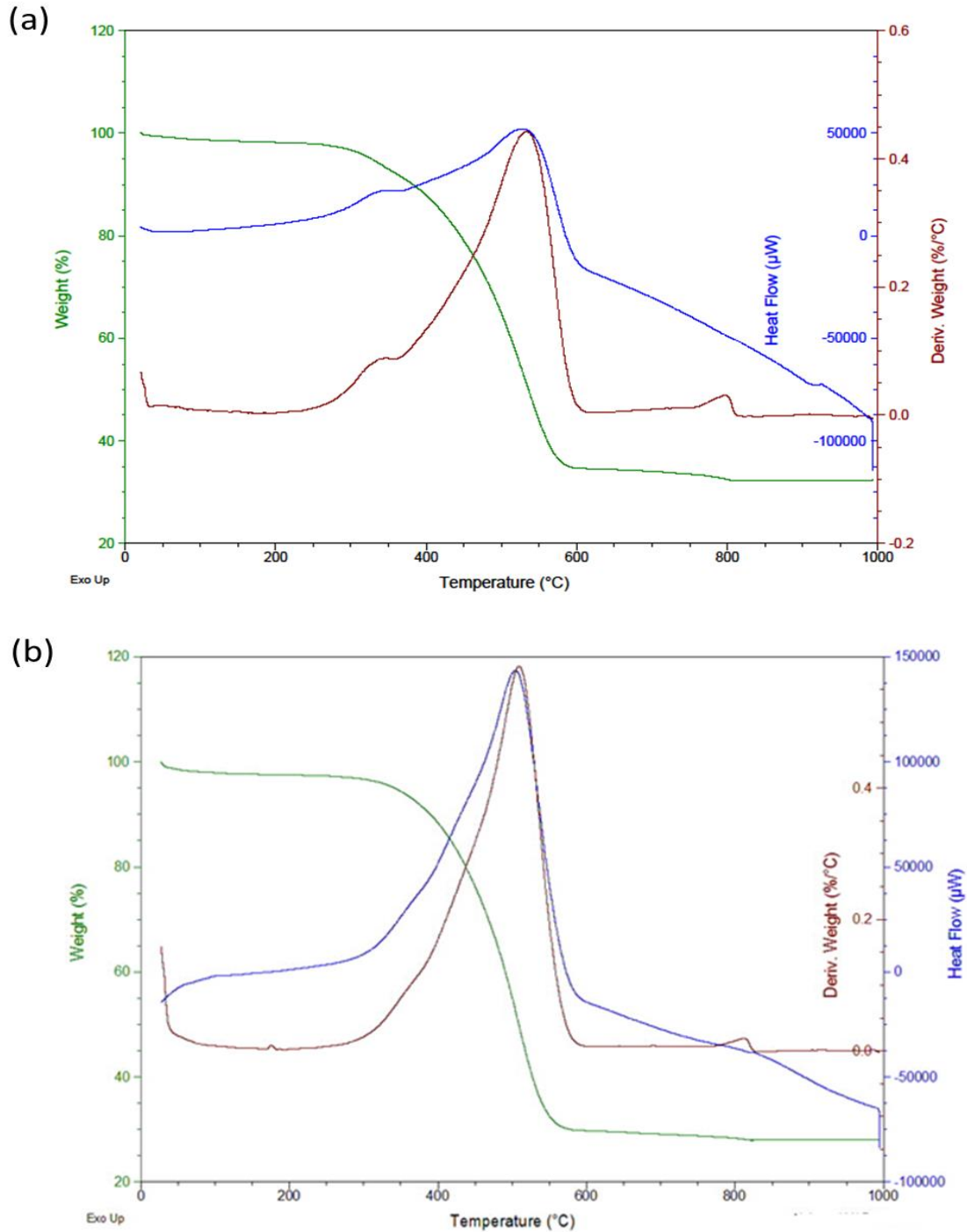


**Figure 4.9:** TGA curves of MWCNT/Ce<sub>0.6</sub>Sr<sub>0.4</sub>Fe<sub>0.8</sub>Co<sub>0.2</sub>O<sub>3</sub> synthesized by (a) CVD and (b) sol–gel method. Purge gas: air at 50 mL/min. Temperature program: ambient–1000°C, and with a heating rate of 10 °C /min

#### 4.4.2 Influence of different MWCNTs to CSFC mass ratios

As the ratios of CSFC perovskites to MWCNTs were raised to 1:1, 1:2 and 1:3, the thermal stability of MWCNT/CSFC altered. In the TGA curves of the samples synthesized by CVD

method (Figure 4.10 (a)), there was no trend observed on the decomposition temperatures based on different ratios of CSFC. The composite with 1:3 ratio decomposes first followed by the composites with the 1:0.5 and 1:2 ratio. The composite with the 1:1 ratio has the maximum weight loss at higher temperatures  $\sim 800$  °C. In the sol–gel synthesized composites (Figure 4.10 (b)), the composites with increased perovskite concentration were found to be less stable and decompose at an earlier temperature as compared to that with low  $\text{Ce}_{0.6}\text{Sr}_{0.4}\text{Fe}_{0.8}\text{Co}_{0.2}\text{O}_3$  loadings 1:0.5. Heat treatment reduces the disorder on the MWCNTs walls, high loading of CSFC on the surface of nanotubes reveal the decrease in defects after heat treatment at 400 °C for 8 hours. The increase in the  $\text{Ce}_{0.6}\text{Sr}_{0.4}\text{Fe}_{0.8}\text{Co}_{0.2}\text{O}_3$  perovskite concentration led to more defects. In the 1:0.5 composites, the CSFC perovskites have covered the defects sites, thus there is an increase in stability when compared to other samples. Furthermore, the increase in the perovskites loading resulted in more than one decomposition temperatures indicating weak complexation of the perovskites to the MWCNT surfaces. The polymeric solution used in the sol–gel method was easily burned off at the heat treatment temperature (400 °C) [84]. TGA shows that MWCNTs completely decompose at 560 °C and as a result these composites should be used at low temperatures in order to keep MWCNT present in the whole process.

The difference in the TGA curves of the composites synthesized by CVD and sol–gel methods is that, in the CVD method, materials start to loss weakly bounds groups such as adsorbed water molecules at lower temperatures. The composite with high loadings of perovskites losses water first because there is a high concentration of perovskites, hence, more adsorbed water molecules. For the low perovskite loadings, the material only decompose at high temperature, there is no significant removal of adsorbed water molecules because the perovskite loading is low. This agrees with the Raman results that, materials with high perovskite loadings on the MWCNTs walls have more defects. In the sol–gel synthesized materials, same trend was observed. But here, there is no removal of the adsorbed water molecules, because there were removed during the drying of these samples at 100 °C in the oven.

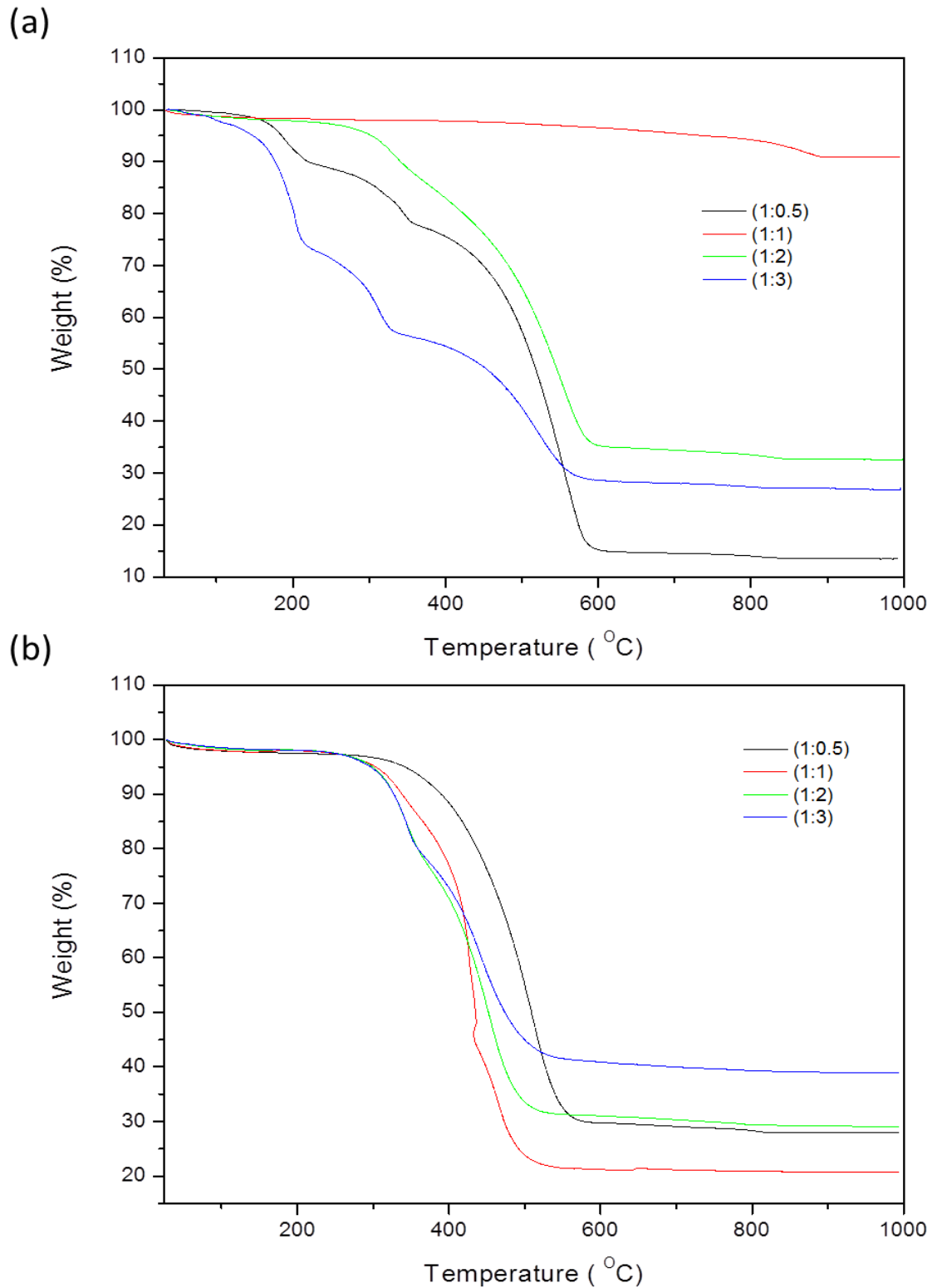


**Figure 4.10:** TGA curves of MWCNT/Ce<sub>0.6</sub>Sr<sub>0.4</sub>Fe<sub>0.8</sub>Co<sub>0.2</sub>O<sub>3</sub> with different mass ratios, synthesized by (a) CVD and (b) sol-gel method. Purge gas: air at 50 mL/min. Temperature program: ambient–1000°C, and with a heating rate of 10 °C /min

The exact % weight losses, and oxidation temperatures of all composites synthesized from the CVD and sol–gel methods are shown in Table 4.10. The data represents replicates that could be done factoring in instrument availability. Here, the values of the composites with varying MWCNTs to CSFC mass ratios are shown. In the sol–gel synthesized composites, the maximum weight loss of 79.28% occurred with the composites with 1:1 MWCNTs to CSFC ratio at 506.3 °C. While in the composites synthesized by CVD method, the observed maximum weight loss of 68.55% was in the 1:0.5 MWCNTs to CSFC ratio at 555.2 °C. The minimum weight loss in the composites synthesized by sol–gel occurred with the sample with high loading of the perovskite, 1:3 ratio; which is expected since these samples have the most perovskite material. While in the CVD synthesized composite the minimum weight loss occurs with the composite with the 1: 1 ratio, which is most likely an outlier.

**Table 4.10:** TGA results of the MWCNT/Ce<sub>0.6</sub>Sr<sub>0.4</sub>Fe<sub>0.8</sub>Co<sub>0.2</sub>O<sub>3</sub> composites with different mass ratios synthesized by sol–gel and CVD methods and heat treated at 400 °C

<b>Sol–Gel</b>			
<b>Sample</b>	<b>Theoretical % Weight Loss</b>	<b>Actual % Weight Loss</b>	<b>Oxidation Temperature (°C)</b>
1MWCNT:0.5CSFC	66	71.98	564.10
1MWCNT:1CSFC	50	79.28	506.3
1MWCNT:2CSFC	33	26.11	288.2
1MWCNT:2CSFC	33	44.77	511.5
1MWCNT:3CSFC	25	23.46	278.3
1MWCNT:3CSFC	25	37.65	523.9
<b>CVD</b>			
<b>Sample</b>		<b>% Loss (%)</b>	<b>Oxidation Temperature (°C)</b>
1MWCNT:0.5CSFC	66	68.55	555.2
1MWCNT:1CSFC	50	7.949	869.1
1MWCNT:2CSFC	33	13.15	326.1
1MWCNT:2CSFC	33	49.77	550.0
1MWCNT:3CSFC	25	27.80	201.6
1MWCNT:3CSFC	25	16.33	310.2
1MWCNT:3CSFC	25	27.44	550.4

#### 4.4.3 Influence of Varying x and y on CSFC using a 1:0.5 MWCNT/CSFC mass ratio

Figure 4.11 shows the TGA curves of the MWCNT/Ce<sub>x</sub>Sr<sub>1-x</sub>Fe<sub>y</sub>Co<sub>1-y</sub>O<sub>3</sub> composites where x and y ranges from 0.2 to 0.8 in 0.2 intervals. The composite with 1:0.5 ratio have been chosen because it has one oxidation temperature other composites decompose at different temperatures. The perovskite with the composition x = 0.6 and y = 0.8 does not cover all defects site on the MWCNTs surface, since the composites start to decompose at temperatures of around 560 °C (as shown in Figure 4.9). The other perovskites with unique values of x and y covers the defects on the MWCNT walls; this can be seen from the thermal stability of the composites. These composite materials are more stable towards thermal oxidative destruction. The composites containing perovskites with x = y = 0.8, show two exothermic peaks the first one at ~ 560 °C followed by the second peak at ~ 800 °C. This means that not all MWCNTs defects sites has been covered by CSFC perovskites, the decomposition at 560 °C corresponds to the defected MWCNTs and the decomposition at 800 °C is due to the MWCNTs without defects. Additionally, the rest of the perovskites structures with x = y = 0.2, 0.4, 0.6 covers these defects sites and provide MWCNTs composites with more stability towards oxidative destruction. In these composites, the major decomposition temperature is occurring at temperature more than 800 °C.

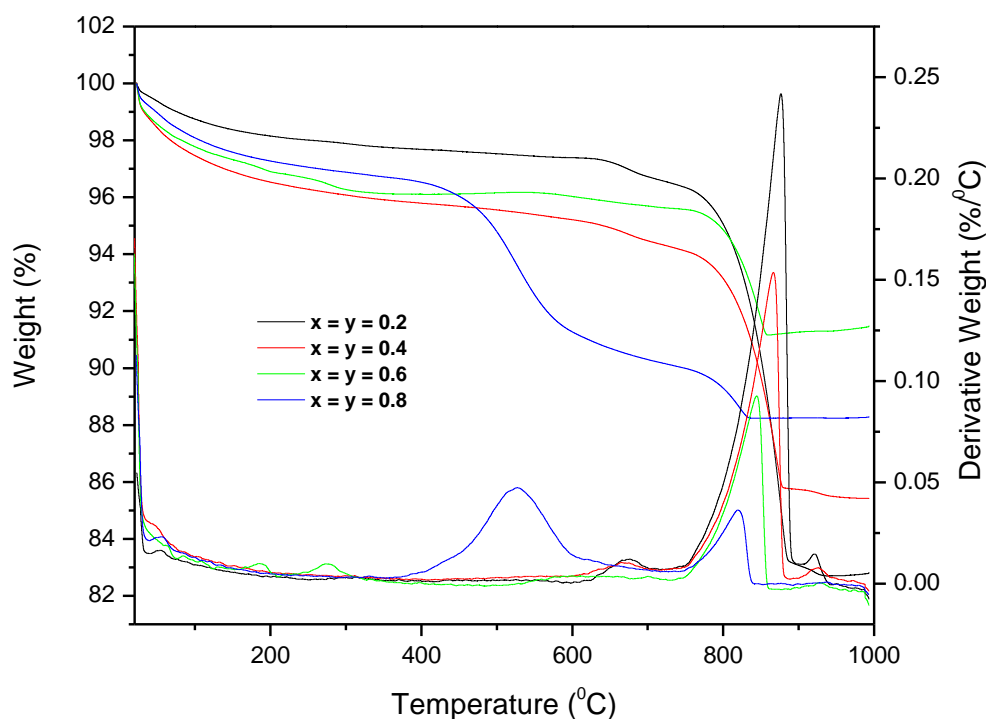


**Figure 4.11:** TGA curves of MWCNT/Ce<sub>x</sub>Sr<sub>1-x</sub>Fe<sub>y</sub>Co<sub>1-y</sub>O<sub>3</sub> (0.2 ≤ (x, y) ≤ 0.8) synthesized by CVD method. Purge gas: air at 50 mL/min. Temperature program: ambient–1000 °C, and with a heating rate of 10 °C /min

The exact weight losses, oxidation temperatures and residual masses of all composites synthesized by CVD method are shown in Table 4.11. Here, the values of the composites with perovskites of varying x and y values in the structure are shown. The maximum weight loss of 65.31% is occurring in the composite with x = 0.6 and y = 0.8 at 522.7 °C. When the values of x and y were increased in the same order (x = y), the loss is low about 16.28%. There was a huge loss in the composites as the perovskite compositions were increased.

**Table 4.11:** TGA results for the MWCNT/Ce<sub>x</sub>Sr<sub>1-x</sub>Fe<sub>y</sub>Co<sub>1-y</sub>O<sub>3</sub> (0.2 ≤ (x, y) ≤ 0.8) nanocomposites synthesized by CVD and heat treated at 400 °C

Sample	x	y	Loss (%)	Oxidation Temperature (°C)	Size (mg)	Residual Mass (mg)
1MWCNT:0.5CSFC	0.2	0.2	16.28	856.2	3.722	3.306
1MWCNT:0.5CSFC	0.4	0.4	7.802	861.4	4.485	3.841
1MWCNT:0.5CSFC	0.6	0.6	8.603	838.3	4.317	3.934
1MWCNT:0.5CSFC	0.6	0.8	65.31	522.7	3.423	1.912
1MWCNT:0.5CSFC	0.8	0.8	9.045	512.1	5.524	5.001
1MWCNT:0.5CSFC	0.8	0.8	8.719	813.9	5.001	4.873

The same analysis as in Table 4.11 was done for the sol–gel composites in order to present the actual values of the important parameters from the TGA curves. Table 4.12 shows the results of all x and y values from 0.2 to 0.8 as well as different MWCNTs to CSFC mass ratios, 1:0.5, 1:1, 1:2 and 1:3. The composite with x = 0.6 and y = 0.8 have major weight loss while those with x = y = 0.2, 0.4, 0.6 and 0.8 possess low loss. The major weight loss in the composite with x = 0.6 and y = 0.8 is about 79.28% at oxidation temperature of 506.3 °C. There was no observable trend in the composites with different MWCNTs to CSFC ratios.

**Table 4. 12:** TGA results for MWCNT/Ce<sub>x</sub>Sr<sub>1-x</sub>Fe<sub>y</sub>Co<sub>1-y</sub>O<sub>3</sub> (0.2 ≤ (x, y) ≤ 0.8) nanocomposites with different mass ratios synthesized by sol–gel method and heat treated at 400 °C

Sample	x	y	% Loss (%)	Oxidation Temperature (°C)	Size (mg)	Residual Mass (mg)
1MWCNT:0.5CSFC	0.2	0.2	15.61	700.5	8.911	7.765
1MWCNT:0.5CSFC	0.2	0.2	1.64	906.2	7.765	7.372
1MWCNT:0.5CSFC	0.4	0.4	6.10	933.9	9.087	8.525
1MWCNT:0.5CSFC	0.6	0.8	71.98	564.1	7.540	2.110
1MWCNT:1CSFC	0.6	0.8	79.28	506.3	10.97	2.271
1MWCNT:2CSFC	0.6	0.8	26.11	288.2	5.078	3.733
1MWCNT:2CSFC	0.6	0.8	44.77	511.5	3.731	1.475
1MWCNT:3CSFC	0.6	0.8	23.46	278.3	11.55	8.840
1MWCNT:3CSFC	0.6	0.8	37.65	523.9	8.845	4.491
1MWCNT:0.5CSFC	0.8	0.8	3.524	54.28	6.834	6.106

## 4.5 Electron microscopy analysis of MWCNTs and CSFCs composites

### 4.5.1 SEM/EDS

The morphology of the MWCNT/CSFC nano composite materials was borne out from the SEM micrographs. The SEM images of the synthesized powders showed carbon nanotubes with nanosized perovskite particles in combination with agglomerates. Figure 4.12 (a) and (b) represent the SEM images of the composites materials synthesized by CVD and sol–gel methods respectively. It is seen in the SEM images that the synthesized powders consisted of an irregular aggregate of CSFC perovskites and MWCNTs. Perovskite particles are distributed over the MWCNTs surfaces (Figure 4.12 (d)) and are also covered by carbon nanotubes. In addition to that, the particles agglomerate into big structures as can be seen in the SEM micrograph of the composite in Figure 4.12 (a) and (b).

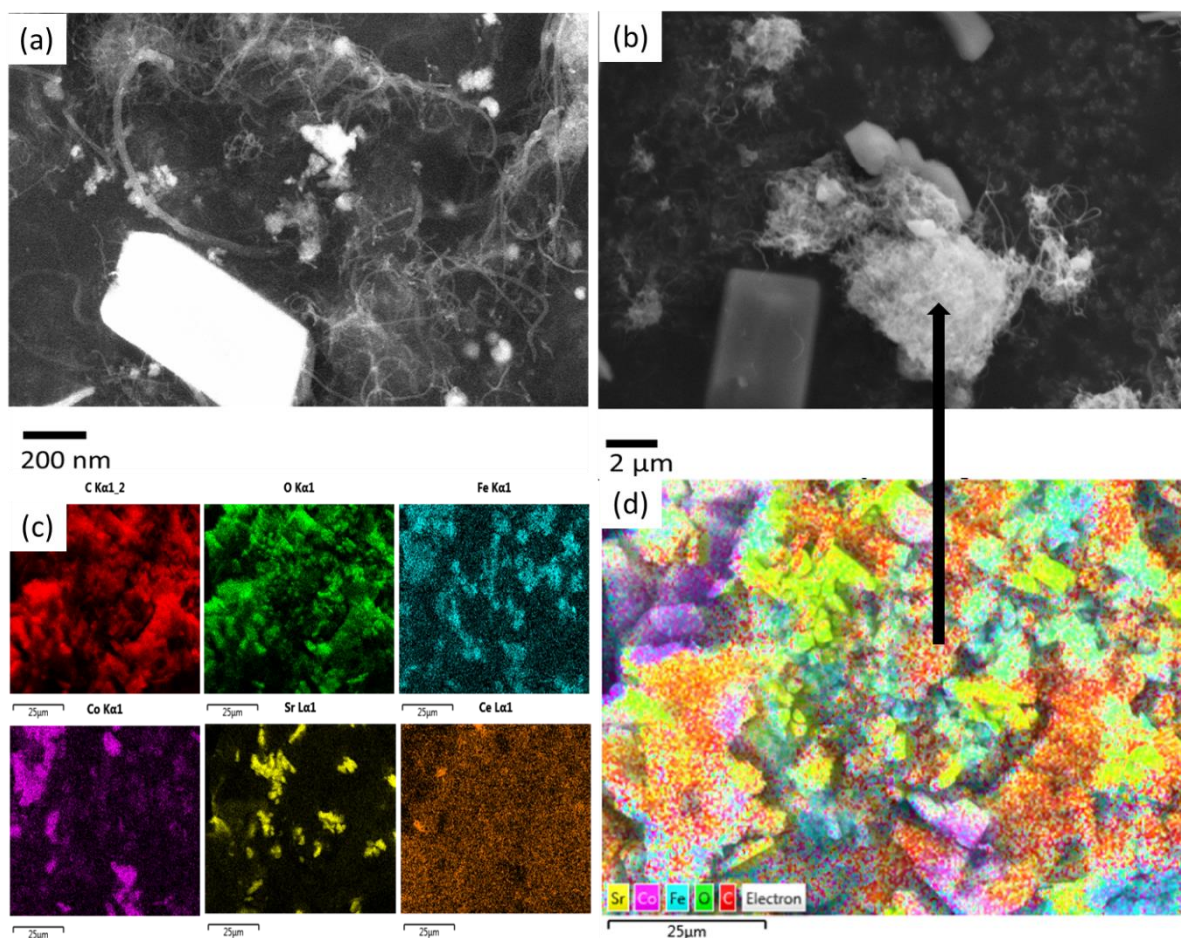


**Figure 4.12:** SEM images of 1MWCNT/1  $\text{Ce}_{0.6}\text{Sr}_{0.4}\text{Fe}_{0.8}\text{Co}_{0.2}\text{O}_3$  composites materials heat treated at 400 °C: (a) synthesized by CVD, (b) synthesized by sol–gel methods, (c) EDS elemental maps for Co, Sr, Ce, C, O and Fe and (d) EDS layered image of the composite materials synthesized by CVD method and heat treated at 400 °C

Furthermore, elemental distribution was confirmed by EDS analysis on the marked area in the SEM image of the composite (Figure 4.12 (b)). Elements are well distributed over the MWCNT surfaces this can be seen from the EDS layer of the composites in Figure 4.12 (d). Elemental distribution spectrum of the powders show the presence of Ce, Sr, Fe, Co, C and O peaks Figure 4.13. The carbon content had not been change even after heat treatment at 400 °C, the composite is carbon rich. This shows that MWCNTs has not been burned out at this temperature (400 °C).

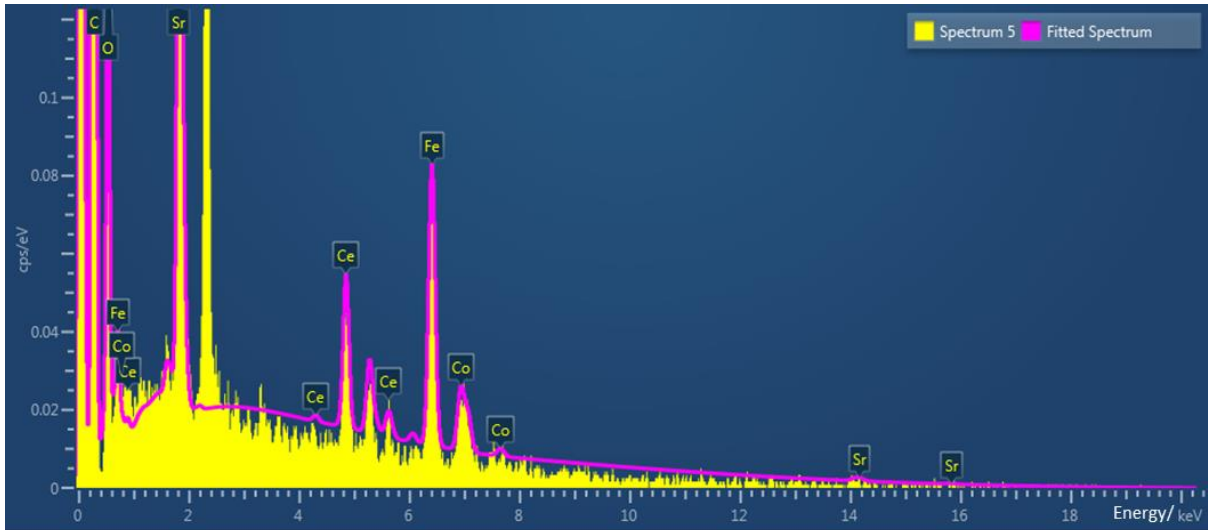


**Figure 4.13:** EDS spectrum of the mapped 1 MWCNT/1CSFC ( $x = 0.6, y = 0.8$ ) composite synthesized by CVD method and heat treated at 400 °C

The EDS spectrum in Figure 4.13 and Table 4.13 reveal that only 1.27 wt. % of Ni was present and this is a metal impurity most likely from the catalyst used in the synthesis of MWCNTs. For the EDS analysis, a built in standard is used and the detector is pre-calibrated and the software has a library of standards to reference to. The EDS mapping shows the distribution of elements over the surface of the carbon nanotubes.

**Table 4.13:** EDS elemental analysis of the 1 MWCNT/1Ce<sub>0.6</sub>Sr<sub>0.4</sub>Fe<sub>0.8</sub>Co<sub>0.2</sub>O<sub>3</sub> nanocomposites synthesized by CVD method

Element	Weight %
Oxygen (O)	45.28
Iron (Fe)	9.29
Cobalt (Co)	9.17
Nickel (Ni)	1.27
Strontium (Sr)	18.73
Cerium (Ce)	16.28
Total	100

#### 4.5.2 TEM/HRTEM/STEM

Figure 4.14 represents high resolution TEM micrographs of MWCNTs and CSFC composites synthesized by CVD and sol-gel and heat treated at 400 °C for 8 hours. High Resolution Transmission Electron Microscopy (HRTEM) images of CSFC show the presence of different lattice planes within the perovskite structure (Appendix A6). This confirms the formation of the perovskite structures in the composites. In the HRTEM micrograph of MWCNTs and CSFC composite, perovskite particles cover the surface of MWCNTs (Figure 4.14 (a), (d)). The lattice fringes of the perovskites are seen on top of the MWCNTs surface and the atoms are 0.34 nm apart; hence MWCNTs are coated with CSFC perovskite nanoparticles (Figure 4.14 (b), (e)). The insert in Figure 4.14 (b) shows the lattice fringes of the perovskite and the distance between them. Dark field imaging and Scanning Transmission Electron Microscopy (STEM) confirmed the coating of CSFC onto MWCNT walls (Figure 4.14 (c), (f)).

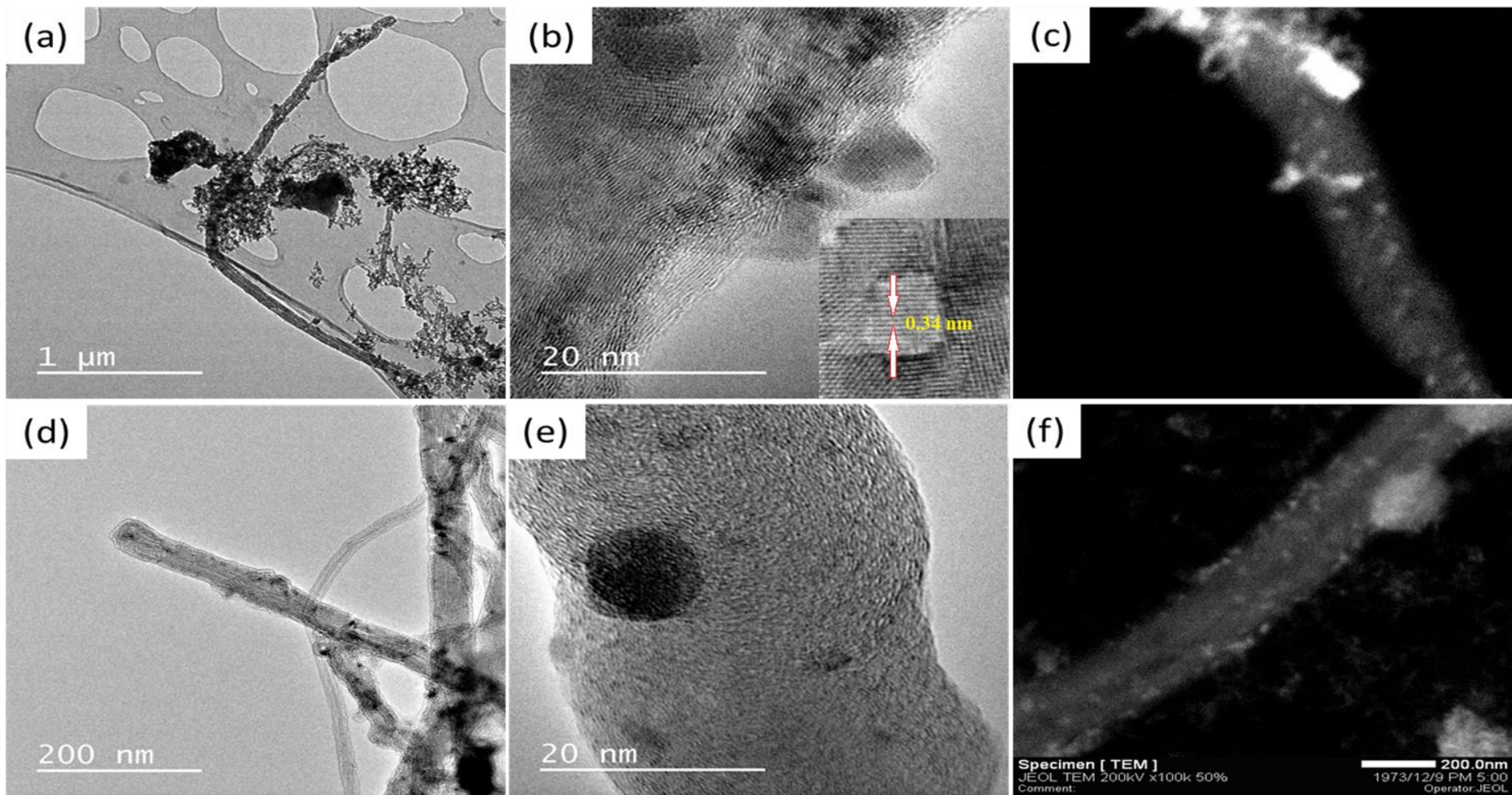


**Figure 4.14:** HRTEM images of MWCNT/Ce<sub>0.6</sub>Sr<sub>0.4</sub>Fe<sub>0.8</sub>Co<sub>0.2</sub>O<sub>3</sub> (1:1) nanocomposite after heat treatment at 400 °C. CVD method: (a) low, (b) high magnification and (c) dark field imaging: sol-gel method samples (d) low, (e) high magnification and (f) dark field imaging of the samples

In the HRTEM micrographs, the perovskite ( $\text{Ce}_{0.6}\text{Sr}_{0.4}\text{Fe}_{0.8}\text{Co}_{0.2}\text{O}_3$ ) is seen coated onto the MWCNTs outer walls. This gives the composite enhanced conductivities, because the conductivities of the MIECs have been combined with that of the MWCNTs. This could give the composite high electrochemical performance when these nanocomposites are tested as cathodes in SOFC at low temperatures (Chapter 5).

The outer diameter of MWCNTs was calculated to be  $\sim 18.19$  nm and an inner diameter of 8.882 nm using Image J software on the image by taking the average from different locations. Moreover, MWCNTs thickness was determined to be 6.114 nm using Image J software. The perovskite particles were well dispersed and deposited on the surface of MWCNTs.

#### 4.6 Conclusions

The MWCNT/ $\text{Ce}_{0.6}\text{Sr}_{0.4}\text{Fe}_{0.8}\text{Co}_{0.2}\text{O}_3$  nanocomposite powders were successfully fabricated by the sol-gel and CVD methods. FTIR results show the presence of expected functional groups in the MWCNT,  $\text{Ce}_{0.6}\text{Sr}_{0.4}\text{Fe}_{0.8}\text{Co}_{0.2}\text{O}_3$  and additionally chelating agent. In the sol-gel method, liquids (polymeric solution) used have added functional groups on the MWCNTs walls. The FTIR results of the composites synthesized by sol-gel method showed many vibrational bands because of the additional functional groups from the polymeric solution (Pluronic F-127 in ethanol and water solvent system). Heat treatment temperature removed the organic groups originated from the polymeric solution. In the case of the composites synthesized by CVD method, there were no additional functional groups different from those of MWCNTs and CSFC, except the functional group of adsorbed water molecules resulting from waters of hydration in the metal complexes. Perovskites are formed on the MWCNT walls and as the loading increases, perovskite peaks were seen form both CVD and sol-gel methods. In addition to that, Raman spectroscopy indicated the presence of defects in the composites which decrease by heat treatments and high perovskite loadings.

There were three Raman active modes for the perovskites,  $A_{1g}$  ( $523\text{ cm}^{-1}$ ),  $B_{2g}$  ( $821\text{ cm}^{-1}$ ) and  $T_{2g}$  ( $1041\text{ cm}^{-1}$ ) as well as the mode corresponded to the crystalline perovskite at high wavenumbers ( $2330\text{ cm}^{-1}$ ). In addition to that, the disorder on the MWCNTs walls decreased as the perovskite loadings were raised after heat treatments at  $400\text{ }^\circ\text{C}$ . This suggests that, most of the defect sites on the MWCNTs have been occupied.

XRD analysis showed that perovskite phases start to develop at low temperatures as low as  $300\text{ }^\circ\text{C}$  from the *in-situ* XRD experiment. The *in-situ* XRD experiment showed it may be

possible to get a reduction in crystallite sizes while the room temperature XRD of the final calcined samples showed reduced crystallite sizes in some cases, most of the time this was with the CVD method. Sol-gel method did not form complete perovskites phases under the *in-situ* conditions. However the room temperature XRD, showed that both CVD and sol-gel resulted in the formation of perovskites phases, due to the long treatment time of 8 hours at 400 °C. As the perovskite loadings on the MWCNTs were changed, perovskites phases were not fully formed with the sol-gel method. This was because of the low operating temperature for the sol-gel method and the absence of metal acacs that aided in the formation of perovskites as in the case of CVD. Additionally, the presence of MWCNTs in the CVD method catalyzed the formation of the perovskite phases.

TGA results showed that, the composites with  $\text{Ce}_{0.6}\text{Sr}_{0.4}\text{Fe}_{0.8}\text{Co}_{0.2}\text{O}_3$  perovskites are stable up to temperatures of  $\sim 560$  °C. On the other hand, composites with  $\text{Ce}_x\text{Sr}_{1-x}\text{Fe}_y\text{Co}_{1-y}\text{O}_3$  perovskites with  $0.2 \leq (x, y) \leq 0.8$  are more thermally stable and decompose at  $\sim 800$  °C. High loadings of perovskite in the composites resulted in more defects and the materials start to lose weight at earlier temperatures from both CVD and sol-gel methods.

Perovskite nanosized particles cover the surface of MWCNTs with the outer and inner diameters of 18.19 and 6.114 nm respectively. The perovskite particles were formed and at the same time, the particles agglomerated to form big structures. This can be also confirmed by the big crystallite sized that has been determined by XRD analyses most of the time in the sol-gel method. To sum up, the observed properties of MWCNT/ $\text{Ce}_x\text{Sr}_{1-x}\text{Fe}_y\text{Co}_{1-y}\text{O}_3$  implies that, these nanocomposites powders can be used as cathode materials in the SOFCs at low to intermediate temperatures as can be seen in Chapter 5.

## Chapter Five

### **Electrochemical Performance of MWCNT/Ce<sub>x</sub>Sr<sub>1-x</sub>Fe<sub>y</sub>Co<sub>1-y</sub>O<sub>3</sub> Composites Applied as Cathodes for Low to Intermediate Temperatures Solid Oxide Fuel Cells (LT-SOFC)**

This chapter focuses on the electrochemical performance of the MWCNT/Ce<sub>x</sub>Sr<sub>1-x</sub>Fe<sub>y</sub>Co<sub>1-y</sub>O<sub>3</sub> ( $0.2 \leq (x, y) \leq 0.8$ ) nanocomposite cathode materials synthesized by modified sol-gel technique with a non-ionic surfactant Pluronic F-127. For comparisons, materials synthesized by CVD method are also tested. Materials are applied as cathodes following their characterizations. Here the study is focused on the electrochemical performance of the cathode materials under different mass ratios, perovskite compositions and cell geometries.

The performance is studied by looking at the current and power densities as outputs produced by the cells with the potential as the input into the cells at low temperatures (300–500 °C). The reduction of molecular oxygen in the cathode was monitored by determining the area specific resistance values (ASR) from tangents slopes of polarization curves. ASR values are normally crystallite size dependent and is directly proportionate, a property that is vital for a materials used as cathode for LT-SOFC [183-185]. The values calculated for the composites were low and these compared well with the best literature values [5, 183, 186]. Three types of cells are tested for the above quantities. The cells comprised of; (i) yttria-stabilized zirconia [YSZ] electrolyte; single cells comprising of [composite |YSZ|] to study cathode performance and symmetrical cells comprising of [composite |YSZ| composite] to study anode and cathode. (ii) asymmetrical cells comprising of [NiO-YSZ |YSZ| composite] in which the composite is the cathode and nickel oxide (NiO) is the anode. This was obtained by heat treating a mixture of NiCO<sub>3</sub>, Zirconium acac and yttrium acac (in a 50%: 50 % compositions) in air. NiO-YSZ cement meet the requirement for electronic conductivity and an YSZ phase for ionic conduction has excellent electrical conductivity, good mechanical strength and high electrochemical activity in H<sub>2</sub> [38, 187]. The results obtained from CVD and sol-gel methods were discussed in the same manner since the mechanism behind for the cell performance was the same.

## **5.1 Electrochemical Properties of MWCNT/CSFC Nanocomposites Synthesized by CVD method**

A number of studies have been carried out in order to monitor the performance of MWCNT/CSFC composite. The study has been focused on the effect of ratios of MWCNT:CSFC by altering the loading of CSFCs and also by changing the CSFC structure in altering compositions of cerium and iron. Polarization properties were tested in air as oxidant and humidified hydrogen ( $H_2 + 10\% H_2O$ ) as fuel at temperature intervals of 300–500 °C. The thickness of the electrolyte was 0.03 mm, the cathode material was 0.02 mm and the anode was 0.045 mm. The aim is to verify that the materials can be active at reduced operating temperatures and decreased interfacial polarization resistances.

### **5.1.1 Influence of ratios of MWCNT: CSFC on Polarization Curves**

The ratios of MWCNTs and CSFCs with  $x = 0.6$  and  $y = 0.8$  in the composites tested are 1:1, 1:2 and 1:3. Figure 5.1 is a plot of polarization curves of the cells with 1:1, 1:2 and 1:3 MWCNT: CSFC, ratios operated at 500 °C. The cells used are symmetrical, [composite |YSZ| composite], meaning the composite is used both as anode and cathode. It was observed that there was a general linear fall in the voltage (overvoltage) for all three ratios. The cell with 1:2 composite had the higher voltage at lower current densities but all three were fairly the same at higher current densities. Normally the aim is to minimize overvoltage in order to minimize the use of  $H_2$  as a fuel [5, 188-190]. This overvoltage is caused by resistance flow from the cathode as the current density increases [5, 188-190]. The power density on the other hand equally increases for three composite ratios as current density increases.

The open circuit voltage (OCV) of the cell decreased and was stable at 0.7 V. This value is lower than the Nernst thermodynamic value and is caused by a reduction in hydrogen pressure at the anode/electrolyte interface caused by the gas crossover that flows through the electrolyte due to cold power compacting temperature [105, 191-194]. These could leave residual pores and leakages through the connected pore in the cathode electrolyte layer, composite |YSZ|. However, another factor could be the low temperature used affects the YSZ electrolyte.

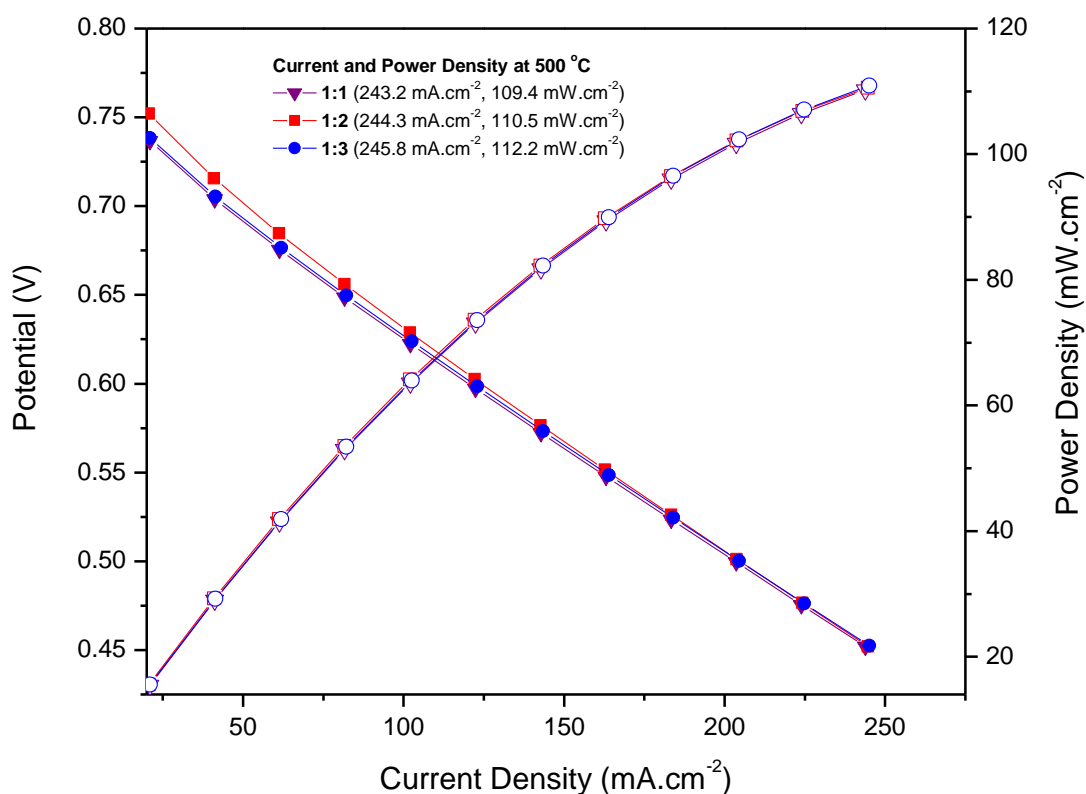


**Figure 5.1:**  $I$ - $V$  and  $I$ - $P$  curves of MWCNT/Ce<sub>0.6</sub>Sr<sub>0.4</sub>Fe<sub>0.8</sub>Co<sub>0.2</sub>O<sub>3</sub> composites with different ratios synthesized by CVD method. The cathodes were tested under symmetrical cells for 2 hours at 500 °C under air (100 mL.min<sup>-1</sup>) as an oxidant and humidified H<sub>2</sub> as a fuel (200 mL.min<sup>-1</sup>)

The current density for the 1:1 mass ratio is 243.2 mA.cm<sup>-2</sup> while the peak power density was 109.4 mW.cm<sup>-2</sup>. For the 1:2 and 1:3 composites, the current densities are 243.3 mA.cm<sup>-2</sup>, 245.8 mA.cm<sup>-2</sup> with the corresponding peak power densities being 110.5 mW.cm<sup>-2</sup> and 112.2 mW.cm<sup>-2</sup>, respectively. The performance exhibited by the three composites is not significantly different. Polarization results are much lower than that reported by other researchers for the perovskites of this type [3, 5, 17, 184, 195]. This decrease is attributed to the microstructure of the cathode composites. The minimum slope in the polarization curves ( $I$ - $V$ ) give lowest area specific resistance (ASR) in the linear regime. Here, the minimum slopes (ASR) values are lower for all composites ratios; 0.2341 Ω.cm<sup>2</sup> for 1:1, 0.2334 Ω.cm<sup>2</sup> for 1:2 and 0.2318 Ω.cm<sup>2</sup> for 1:3 ratios at 500 °C. It is clear from this that even though the crystallite sizes were smaller for the 1:3 (54.28 Å) composite; the ASR value was comparable to those of 1:1 and 1:2 ratios. These ASR values are much lower than that reported for other

perovskites such as BSFC; this indicates that CSFC has a catalytic activity for oxygen reduction reaction [5, 183, 186]. However there was a general slight decrease associated with the ratios, thus there is a possibility of using these as LT-SOFCs [183-185]. Based on these results, the 1:3 composites were used to further test electrochemical performance. This is also because the composite had strong perovskite phases from the powder XRD.

### **5.1.2 Influence of Varying x and y ratio on Electrochemical Properties with a 1:3 MWCNT/CSFC mass ratio**

The nanocomposites cathode materials were tested under different cell configurations (half-cells, symmetrical cells and asymmetrical cells) in order to investigate the effect of the cell geometry. Under each cell configuration, the compositions of x and y in the perovskite structure were varied in the manner  $x = y = 0.2$ ,  $x = 0.6$  and  $y = 0.8$ , and  $x = y = 0.8$ . The investigation was on the electrochemical performance of different perovskite compositions over MWCNTs at different temperatures 300, 400 and 500 °C. Furthermore, the effect of changing the composition of cerium and iron in the perovskite structure was studied. This is because the mixed ionic–electronic conductors (MIECs) have a positive effect in the electrochemical activity for oxygen reduction reaction due to their redox couples like  $\text{Ce}^{3+} \leftrightarrow \text{Ce}^{4+}$ . Since there are more oxygen vacancies in the perovskite structure, then, the oxidation state of the B–site cations varies in the manner  $\text{Co}^{2+} \rightarrow \text{Co}^{3+} \rightarrow \text{Co}^{4+}$ ,  $\text{Fe}^{2+} \rightarrow \text{Fe}^{3+} \rightarrow \text{Fe}^{4+}$  which then enhances the oxygen reduction steps [5].

#### **5.1.2.1 Half–Cell Testing on 1 MWCNT/3 CSFC with $x = y = 0.2$ , $x = 0.6$ , $y = 0.8$ and $x = y = 0.8$ in cerium and in iron**

Figure 5.2 shows polarization curves of the cathodes tested under a single cell with different compositions of cerium and iron in the composite [MWCNT/CSFC |YSZ|] at 300, 400 and 500 °C. The electrochemical performances of the MWCNT/CSFC composites were investigated by using as the cathode with no anode. The obtained polarization curves exhibited a linear fall in voltage as the current density increased. This overvoltage limits the fuel to operate efficiently due to the resistance flow. This indicates an increase in the overvoltage caused by the increase in the current density. This increase in overvoltage is associated to the fact that there is a resistance to current flow within the fuel cell (in the

cathode). The increase in current density and the drop in voltage is referred to as Ohm's Law [188-190]. At very high current densities, the hydrogen reaction rate is high, however, the hydrogen cannot diffuse to the electrolyte fast enough to react. The OCV was changing with operating temperature and stabilizes at 0.7 V. The cell with  $x = y = 0.2$  in Figure 5.2 (a) gave maximum current densities of 229.0, 226.3 and 225.0 mA.cm<sup>-2</sup> with corresponding peak power densities of 40.42, 73.20 and 106.8 mW.cm<sup>-2</sup> at 300, 400 and 500 °C, respectively. When the loadings of cerium and iron were increased to  $x = 0.6$  in cerium and  $y = 0.8$  in iron, the cell performances were not significantly different from those of the cathodes with low cerium and iron ( $x = y = 0.2$ ). The 1 MWCNT/3 Ce<sub>0.6</sub>Sr<sub>0.4</sub>Fe<sub>0.8</sub>Co<sub>0.2</sub>O<sub>3</sub> composites tested as single cells had maximum current densities of 225.7, 226.1 and 224.5 mA.cm<sup>-2</sup> with the corresponding peak power densities of 43.01, 73.54 and 108.9 mW.cm<sup>-2</sup> at 300, 400 and 500 °C, respectively (Figure 5.2 (b)). The electrochemical performance of the cell with perovskite of high compositions of cerium ( $x = 0.8$ ) and iron ( $y = 0.8$ ) show slight improvement, in terms of current density when compared to the cell with  $x = 0.6$  and  $y = 0.8$ . This cathode display maximum current densities of 230.4, 239.1 and 239.5 mA.cm<sup>-2</sup> at 300, 400 and 500 °C. The corresponding peak power densities are 40.62, 68.38 and 104.1 mW.cm<sup>-2</sup> at same temperatures (Figure 5.2(c)). At 300 °C the current density for the cathode increased from 225.7 by about 5 mA.cm<sup>-2</sup> from that of the composite with  $x = 0.6$  and  $y = 0.8$ . But as the operating temperatures are raised to 400 and 500 °C, the increase in the current densities is more pronounced.

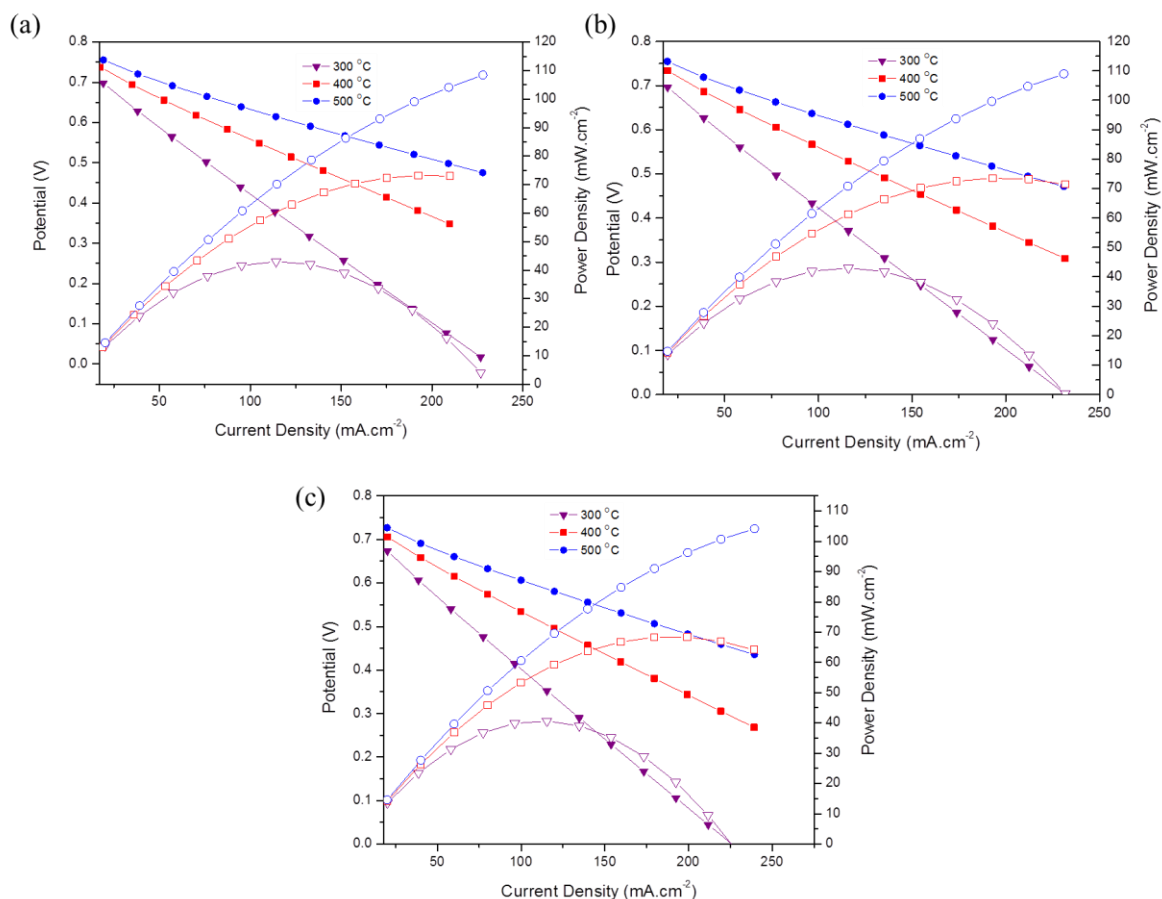


**Figure 5.2:**  $I$ - $V$  and  $I$ - $P$  curves of 1MW/CNT/3Ce<sub>x</sub>Sr<sub>1-x</sub>Fe<sub>y</sub>Co<sub>1-y</sub>O<sub>3</sub> cathodes synthesized by CVD method. (a)  $x = y = 0.2$ , (b)  $x = 0.6$ ,  $y = 0.8$  and (c)  $x = y = 0.8$ . The cathodes were tested under single cells for 2 hours at each temperature under air (100 mL.min<sup>-1</sup>) as an oxidant and humidified H<sub>2</sub> as a fuel (200 mL.min<sup>-1</sup>)

From all polarization curves it is clear that there is a drop in the power density at 300 °C and this is attributed to the conductivity of the YSZ electrolyte which performs well at higher temperatures. As the measuring temperature increase from 400–500 °C the ionic conductivity of the electrolyte increases, this influence the reduction of adsorbed molecular oxygen to O<sup>2-</sup> ions and improves the diffusion of these ions to the electrode/electrolyte interface. The increase in temperature increases the diffusion of the ions in the electrodes, the discharge of the ions to form hydrogen atoms and oxygen atoms on the surface of the electrode and the formation of water molecules [5]. An increase in the overall rate of the diffusion process reduces polarisation resistance; hence, the losses are smaller at 400 and 500 °C. The minimum ASR values are lower for all temperatures, 0.2286 Ω.cm<sup>2</sup> at 300 °C, 0.2256 Ω.cm<sup>2</sup> at 400 °C and 0.2243 Ω.cm<sup>2</sup> at 500 °C in the cathode with  $x = y = 0.2$ . The

slope of the curves (ASR) decreases in high current density because of the decreasing internal resistance. For the composite with  $x = 0.6$  and  $y = 0.8$  in Figure 5.2 (b), the ASR of these curves are lower for all temperatures: CNT/ $\text{Pr}_{0.6}\text{Sr}_{0.8}\text{Fe}_{0.2}\text{Co}_{0.8}\text{O}_3 = 0.14$  and  $0.23 \text{ } \Omega\cdot\text{cm}^2$  (at 700 and 600 °C, respectively) [17]; MWCNT/ $\text{Ce}_{0.6}\text{Sr}_{0.8}\text{Fe}_{0.2}\text{Co}_{0.8}\text{O}_3 = 0.2064$ ,  $0.2066$  and  $0.2051 \text{ } \Omega\cdot\text{cm}^2$  at 300, 400 and 500 °C, respectively. When the cerium and iron compositions were raised to  $x = y = 0.8$ , the ASR values were  $0.2298 \text{ } \Omega\cdot\text{cm}^2$  at 300 °C,  $0.2296 \text{ } \Omega\cdot\text{cm}^2$  at 400 °C and  $0.2268 \text{ } \Omega\cdot\text{cm}^2$  at 500 °C. The slopes of the curves (ASR) decreases in high current densities because of the decreasing internal resistances in the cell [183, 184]. The obtained results are much lower than those reported on the cells with similar perovskite [17]. A possible explanation for this decrease in the performance of the composite cathode can be attributed to several factors such as the electrolyte used, the change in the perovskite microstructure, the presence of MWCNTs as template [17, 40, 196] and the incomplete redox reaction in the half-cell. The change in the temperature is significant in the performance of this cathode material when tested under single cell conditions and is mainly due to the electrolyte used since ionic conductivity of YSZ is not optimized at low temperatures [197-199].

#### **5.1.2.2 Symmetrical Cell Testing on 1 MWCNT/3 CSFC with $x = y = 0.2$ , $x = 0.6$ , $y = 0.8$ and $x = y = 0.8$ in cerium and in iron**

The performance of the composite materials 1 MWCNT/3  $\text{Ce}_{0.2}\text{Sr}_{0.8}\text{Fe}_{0.2}\text{Co}_{0.8}\text{O}_3$  used in symmetrical cells with configuration [composite|YSZ|composite] generally showed very low performance. The maximum current densities were 132.9, 133.4 and 133.8  $\text{mA}\cdot\text{cm}^{-2}$  with peak power densities of 43.24, 65.66 and 79.12  $\text{mW}\cdot\text{cm}^{-2}$  at 300, 400 and 500 °C as shown in Figure 5.3 (a). The reduction in the current and power densities produced by the cathode can be attributed to the lack of pores formation and the composition of the perovskite nanoparticles. The same cathode material used in a single cell (section 5.1.2.1), gave current and power densities that were significantly higher. This might suggest that, 1 MWCNT/3  $\text{Ce}_{0.2}\text{Sr}_{0.8}\text{Fe}_{0.2}\text{Co}_{0.8}\text{O}_3$  cathodes is not suitable for use as the anode and the cathode. This reduced performance is attributed to the lack of fine particles and pore formation in this cathode material. This is also associated to the synthetic method of the nanoparticles (CVD) which does not incorporate the use of any solvent [200, 201]. The electrochemical performance of the cell with increased perovskite compositions in cerium ( $x = 0.6$ ) and iron

( $y = 0.8$ ) show current densities of 244.6, 242.8 and 242.3 mA.cm<sup>-2</sup> with corresponding power densities of 43.68, 73.85 and 110.2 mW.cm<sup>-2</sup> at 300, 400 and 500 °C, respectively. Here the performance is higher than those reported in the case of perovskite with reduced cerium and iron compositions (Figure 5.3 (b)). Figure 5.3 (c) shows polarization curves of the cathode composite with maximum compositions of cerium and iron ( $x = y = 0.8$ ) in the composite. Obtained results show maximum current densities of 238.6, 237.2 and 237.4 mA.cm<sup>-2</sup> with corresponding peak power densities of 42.43, 72.81 and 109.1 mW.cm<sup>-2</sup> at 300, 400 and 500 °C, respectively. Here the performance has decreased slightly and this decrease is attributed to the synthetic approach of the perovskite nanocomposites. The electrochemical performance of this cathode is not significantly different when tested under symmetrical cells as compared to the single cell testing discussed before. The performance of the composite is seen to be dependent on the operating temperature. The change in the temperature is significant in the performance of this cathode material. There is no drop in voltage for the cathode with low cerium and iron compositions (Figure 5.3 (a)) at 300 °C as compared to polarization curves in Figures 5.3 (b) and (c). The OCV changes with operating temperature and became stable at 0.7 V in all cathode composites.

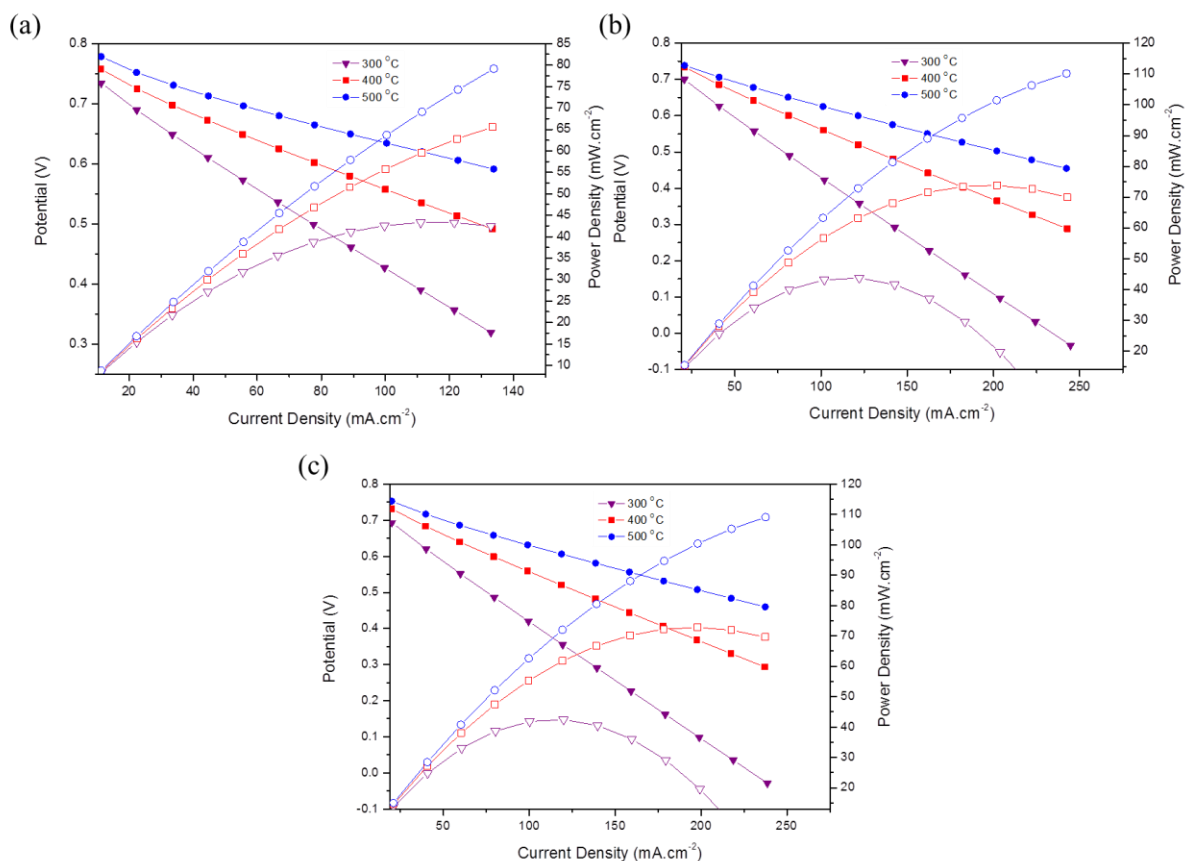


**Figure 5.3:**  $I$ - $V$  and  $I$ - $P$  curves of 1MWCNT/3Ce<sub>x</sub>Sr<sub>1-x</sub>Fe<sub>y</sub>Co<sub>1-y</sub>O<sub>3</sub> cathodes synthesized by CVD method. (a)  $x = y = 0.2$ , (b)  $x = 0.6$ ,  $y = 0.8$  and (c)  $x = y = 0.8$ . The cathodes were tested under symmetrical cells for 2 hours at each temperature under air (100 mL.min<sup>-1</sup>) as an oxidant and humidified H<sub>2</sub> as a fuel (200 mL.min<sup>-1</sup>)

From all polarization curves in Figure 5.3, a linear fall in overvoltage is observed. The explanation for this is the same as stated before. Cathode materials with  $x = 0.6$  and  $y = 0.8$  and  $x = y = 0.8$  can work simultaneously as the anode and the cathode electrodes in the symmetrical cells due to the enhanced electrochemical properties in both reducing and oxidising conditions. In order to improve the electrochemical performance of these cells, a standard anode such as NiO-YSZ has to be used.

### 5.1.2.3 Asymmetrical Cell Testing on 1 MWCNT/3 CSFC with $x = y = 0.2$ , $x = 0.6$ , $y = 0.8$ and $x = y = 0.8$ in cerium and in iron

The electrochemical performance of the cathode materials was tested for the asymmetrical cells employing nickel oxide and YSZ as the anode with the cell configuration [NiO–YSZ|YSZ| composite]. In the polarization curves shown in Figure 5.4, there is a linear fall in the voltage as the current density increased and this is due to the resistance flow in the cathode which shows an increase in the current density. It can be seen from the polarization curves that, cell performance increases as the temperature increases 400 to 500 °C. At 300 °C there is a huge drop in the voltage (ohmic loss) because of low ionic conductivity of YSZ electrolyte at low temperatures. The OCV increases with the increase in the operating temperature and stabilizes at 0.7 V for all the cells in Figure 5.4. The cathode with  $x = y = 0.2$  gave maximum current and power densities of 248.0, 246.3 and 244.1 mA.cm<sup>-2</sup> and 43.32, 72.94 and 111.3 mW.cm<sup>-2</sup> at 300, 400 and 500 °C, respectively (Figure 5.4 (a)). There is a slight improvement in the performance of this cathode when tested under asymmetrical cell configurations. For the first time the cathode synthesized by CVD method show high current and power densities. The improved performance might be due to the complete redox reaction occurring in the anode, cathode and electrolyte electrodes. The anode plays an important role in the electro-oxidation of fuel by catalysing the reaction as well as facilitating fuel access and product elimination. Nickel oxide (NiO) anode has high stability under reducing conditions, sufficient electronic and ionic conductivity for conducting electrons and porous structure to allow the fuel to flow towards the electrolyte [4, 38, 202, 203]. As the perovskite compositions were increased to  $x = 0.6$  and  $y = 0.8$  in Figure 5.4 (b), the current and power densities became 246.7, 247.0 and 246.2 mA.cm<sup>-2</sup> and 44.27, 74.03 and 117.1 mW.cm<sup>-2</sup> at 300, 400 and 500 °C, respectively. The improvement in the current and power densities is attributed to the increase in the composition of cerium and iron in the perovskite structure which then enhances the redox couple. Moreover, the presence of nickel as the anode catalyzes the electro-oxidation reaction of fuel and facilitates fuel access. The perovskite cathode composite with  $x = 0.8$  in cerium and  $y = 0.8$  in iron has slightly reduced current and power densities as compared to the composite with  $x = 0.6$  and  $y = 0.8$ , but the values are still high. The maximum values were 243.3, 241.8 and 240.8 mA.cm<sup>-2</sup> for the current densities, and 44.41, 75.20 and 110.6 mW.cm<sup>-2</sup> for the power outputs at 300, 400 and 500 °C, respectively (Figure 5.4 (c)).

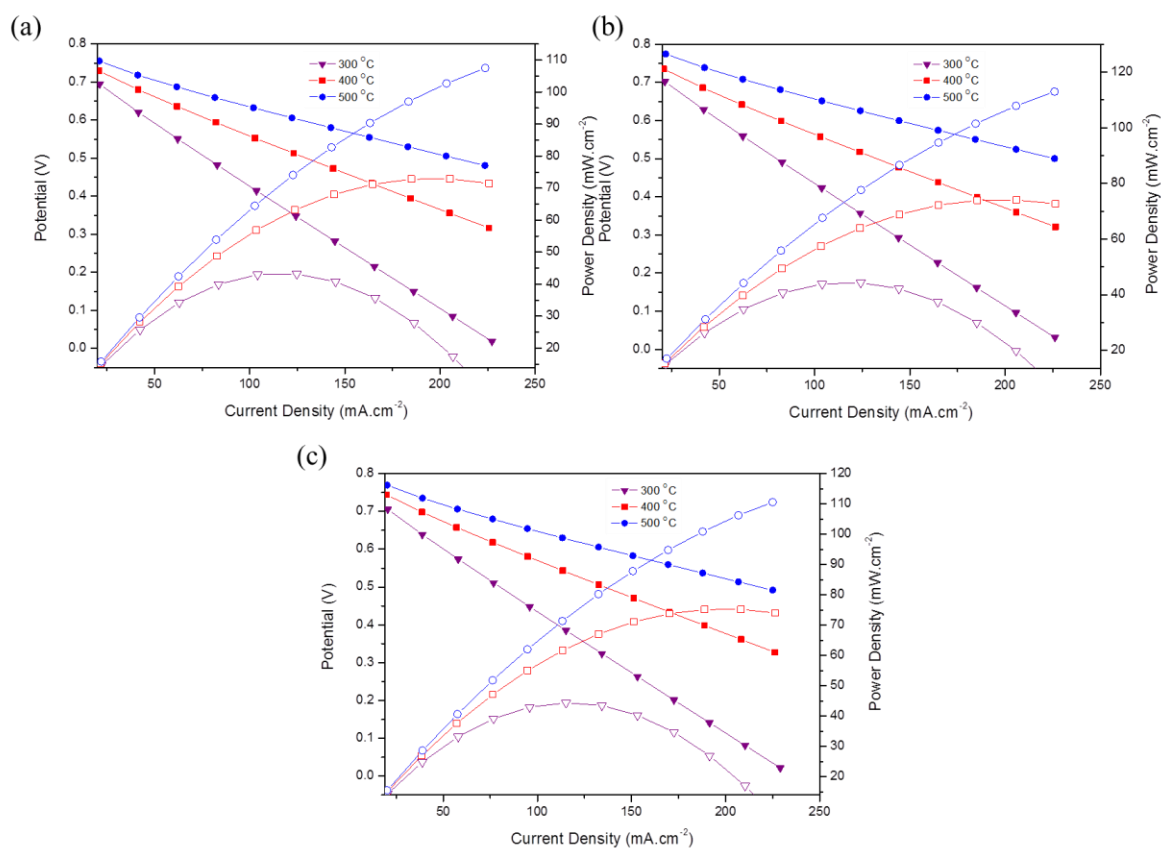


**Figure 5.4:**  $I$ - $V$  and  $I$ - $P$  curves of 1MWCNT/3Ce<sub>x</sub>Sr<sub>1-x</sub>Fe<sub>y</sub>Co<sub>1-y</sub>O<sub>3</sub> cathodes synthesized by CVD method. (a)  $x = y = 0.2$ , (b)  $x = 0.6$ ,  $y = 0.8$  and (c)  $x = y = 0.8$ . The cathodes were tested under asymmetrical cells with NiO–YSZ as the anode for 2 hours at each temperature under air (100 mL.min<sup>-1</sup>) as an oxidant and humidified H<sub>2</sub> as a fuel (200 mL.min<sup>-1</sup>)

The minimum ASR values decreases with an increase in temperature: 0.2473, 0.2456 and 0.2433  $\Omega$ .cm<sup>2</sup> at 300, 400 and 500 °C for the composite with  $x = y = 0.2$ . In the cathode with  $x = 0.6$  and  $y = 0.8$ , the obtained ASR values were low at all operating temperatures, 0.2460, 0.2462 and 0.2454  $\Omega$ .cm<sup>2</sup> at 300, 400 and 500 °C, respectively. Lastly, the ASR values decreases when the temperature increases, 0.2283  $\Omega$ .cm<sup>2</sup> at 300 °C, 0.2255  $\Omega$ .cm<sup>2</sup> at 400 °C and 0.2242  $\Omega$ .cm<sup>2</sup> at 500 °C in the perovskite with high compositions of cerium  $x = 0.8$  and iron  $y = 0.8$ . In all three cases, the ASR values are lower (promising) as compared to the results from other perovskites of this type [17, 85, 183, 204] showing that these cathodes can be used in the LIT–SOFC.

Table 5.1 combines all current and power densities obtained for cathode nanocomposites materials synthesized by CVD method at different operating temperatures under all tested cell

configurations. It can be seen from the table that, the cathode tested under asymmetrical and symmetrical cells configurations have high current and power densities. In the single cells testing, high current densities are observed in the MWCNT/Ce<sub>0.2</sub>Sr<sub>0.8</sub>Fe<sub>0.2</sub>Co<sub>0.8</sub>O<sub>3</sub> composite cathode. In the symmetrical cells the MWCNT/Ce<sub>0.6</sub>Sr<sub>0.4</sub>Fe<sub>0.8</sub>Co<sub>0.2</sub>O<sub>3</sub> composite cathode possesses high current densities. Asymmetrical cells have high current densities on the MWCNT/Ce<sub>0.2</sub>Sr<sub>0.8</sub>Fe<sub>0.2</sub>Co<sub>0.8</sub>O<sub>3</sub> and MWCNT/Ce<sub>0.6</sub>Sr<sub>0.4</sub>Fe<sub>0.8</sub>Co<sub>0.2</sub>O<sub>3</sub> this can be assigned to the reduced crystallite sizes for the cathode with x = 0.6 and y = 0.8.

**Table 5.1:** Electrochemical performances of MWCNT/Ce<sub>x</sub>Sr<sub>1-x</sub>Fe<sub>y</sub>Co<sub>1-y</sub>O<sub>3</sub> cathode materials synthesized by CVD

Electrode Material	x	y	Cell Type	Current Density/mA.cm <sup>-2</sup>			Power Density/mW.cm <sup>-2</sup>		
				300 °C	400 °C	500 °C	300 °C	400 °C	500 °C
1CNT:3CSF C	0.2	0.2	single	229.0	226.3	225.0	40.42	73.20	106.8
1CNT:3CSF C	0.6	0.8	single	225.7	226.1	224.5	43.01	73.54	108.9
1CNT:3CSF C	0.8	0.8	single	230.4	239.1	239.5	40.62	68.38	104.1
1CNT:3CSF C	0.2	0.2	symmetrical	132.9	133.4	133.8	43.24	65.66	79.12
1CNT:3CSF C	0.6	0.8	symmetrical	244.6	242.8	242.3	43.68	73.85	110.2
1CNT:3CSF C	0.8	0.8	symmetrical	238.6	237.2	237.4	42.43	72.81	109.1
1CNT:3CSF C	0.2	0.2	asymmetrical	248.0	246.3	244.1	43.32	72.94	111.3
1CNT:3CSF C	0.6	0.8	asymmetrical	246.7	247.0	246.2	44.27	74.03	117.1
1CNT:3CSF C	0.8	0.8	asymmetrical	243.3	241.8	240.8	44.41	75.20	110.6

The increase in the cerium and iron compositions in the perovskite structure is significant in the electrochemical performance in terms of current and power densities of this cathode. As

observed in Chapter 4 from XRD results, full perovskite phases were formed in the compositions with increased amounts of cerium and iron and the perovskite with high compositions of cerium and iron had reduced crystallite sizes. Lanthanides have a positive effect in the electrochemical activity for oxygen reduction reaction due to their redox couples like  $\text{Ce}^{3+} \leftrightarrow \text{Ce}^{4+}$ . The perovskite systems containing high compositions of lanthanides (Ce) possess high reaction rates due to the catalytic redox couple of Ce ( $\text{Ce}^{4+}$  or  $\text{Ce}^{3+}$ ). Consequently, the oxygen reduction steps are enhanced. Since there are more oxygen vacancies, then, the oxidation state of the B-site cations changes ( $\text{Co}^{2+} \rightarrow \text{Co}^{3+} \rightarrow \text{Co}^{4+}$ ,  $\text{Fe}^{2+} \rightarrow \text{Fe}^{3+} \rightarrow \text{Fe}^{4+}$ ) [5]. .

## **5.2 Electrochemical Properties of MWCNT/CSFC Perovskite Nanocomposites Synthesized by Sol–Gel method**

In this section, nanocomposites materials synthesized using sol–gel method are tested electrochemically. The effects of firstly different mass ratios of MWCNTs: CSFCs then varying x and y ratios of the perovskites is investigated. The performance is tested as in the CVD method discussed in section 5.1 and all the polarization curves are collected under the same conditions such as gases used and electrodes thickness. Since the materials in this section are synthesized by a wet chemical method, there should be a reduction of the operating temperature and decrease in the interfacial polarization resistances when investigating.

### **5.2.1 Influence of different ratios of MWCNT/CSFC Perovskite on Polarization Curves**

MWCNT/  $\text{Ce}_{0.6}\text{Sr}_{0.4}\text{Fe}_{0.8}\text{Co}_{0.2}\text{O}_3$  composites with different ratios 1:1, 1:2 and 1:3 were tested to investigate the effect of different loadings of CSFCs on the electrochemical performance of the cathode materials. Figure 5.5 shows the current and power densities of the cells with varying ratios operated at a temperature of 500 °C using symmetrical cells. The composite materials were used both as the anode and the cathode. There seems not to be a significant difference for the different ratios in terms of electrochemical activity. The polarization curves exhibited a linear fall in voltage as the current density increased as was seen to cells built from CVD method. This drop in voltage is termed overvoltage and it needs to be minimized so that the fuel can operate as efficiently as possible. The overvoltage is due to

the resistance flow occurring in the cathode, which indicates an increase in the overvoltage because of the increase in the current density [189, 190]. The open circuit voltage (OCV) of these cells was stable at 0.7 V, and this value is lower than the theoretical value (1.2 V) because of the reduction in hydrogen pressure at the anode/electrolyte interface [105, 191-193, 204].

In the 1:1 mass ratio the obtained current and power densities are  $245.2 \text{ mA.cm}^{-2}$  and  $105.9 \text{ mW.cm}^{-2}$  and in the 1:2 and 1:3 composites obtained current densities were  $245.1 \text{ mA.cm}^{-2}$ ,  $245.3 \text{ mA.cm}^{-2}$  and the corresponding peak power densities are  $111.6 \text{ mW.cm}^{-2}$  and  $116.9 \text{ mW.cm}^{-2}$ , respectively. The current densities are not significantly different from those obtained from the composites synthesized by CVD method and tested at  $500 \text{ }^\circ\text{C}$ . The power density is high at 1:3 ratio in the composite synthesized by CVD method. The minimum slopes (ASR) values are lower for all composites with different ratios,  $0.2332 \text{ } \Omega.\text{cm}^2$  (1:1),  $0.2330 \text{ } \Omega.\text{cm}^2$  (1:2) and  $0.2321 \text{ } \Omega.\text{cm}^2$  (1:3) at  $500 \text{ }^\circ\text{C}$ . These ASR values are much lower than that reported for other perovskites such as BSFC; and this indicates that CSFC has a catalytic activity for oxygen reduction reaction [5, 183, 186]. There was a general slight decrease associated with the ratios, these materials can also be used as cathodes in the LT-SOFCs [183-185]. Based on these results, the 1:3 composites were used to further test electrochemical performance. This is also because the composite had strong perovskite phases from the powder XRD.

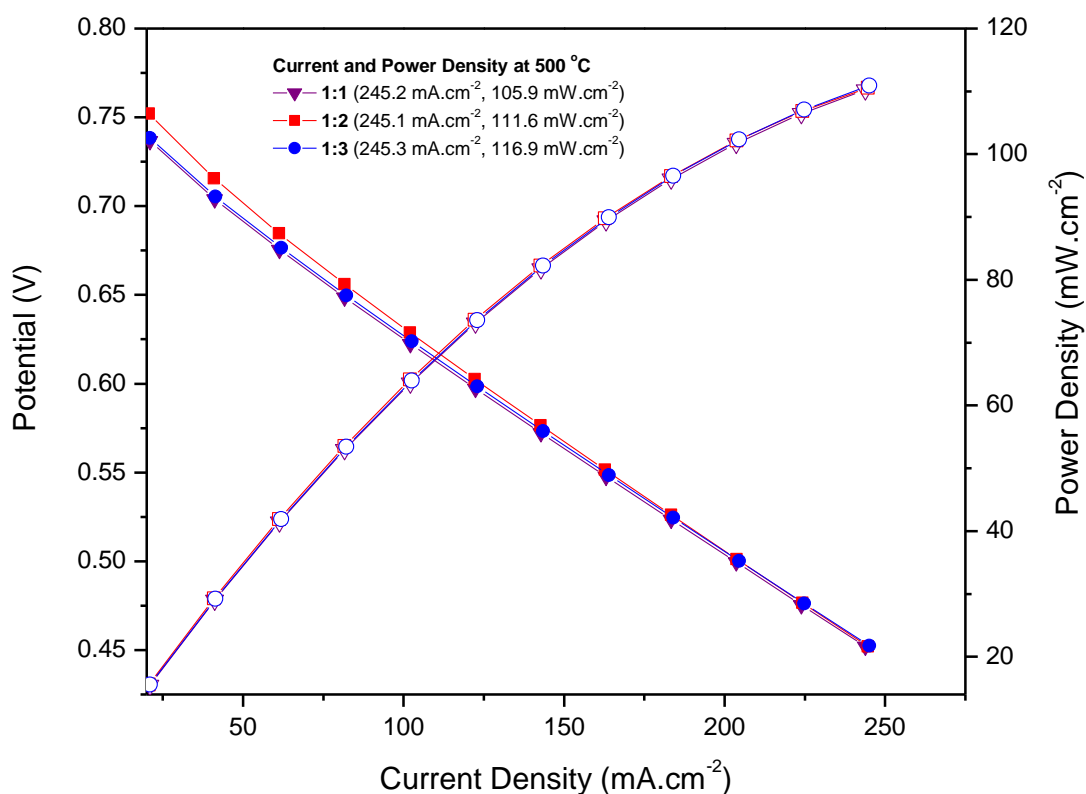


**Figure 5.5:** *I-V* and *I-P* curves of MWCNT/Ce<sub>0.6</sub>Sr<sub>0.4</sub>Fe<sub>0.8</sub>Co<sub>0.2</sub>O<sub>3</sub> composite cathodes with different ratios synthesized by sol-gel method. The cathodes were tested under symmetrical cells for 2 hours at each temperature under air (100 mL.min<sup>-1</sup>) as an oxidant and humidified H<sub>2</sub> as a fuel (200 mL.min<sup>-1</sup>)

## 5.2.2 Influence of Varying x and y ratio with a 1:3 MWCNT/CSFC mass ratio

For the second time, the nanocomposites cathode materials were tested under different cell configurations (half-cells, symmetrical cells and asymmetrical cells) as in the CVD method. The investigation was on the effects of the different cell geometries. The compositions of x and y in the perovskite structure were varied in the manner  $x = y = 0.2$ ,  $x = 0.6$  and  $y = 0.8$ , and  $x = y = 0.8$ . The investigation was on the electrochemical performance of different perovskite compositions over MWCNTs at different temperatures 300, 400 and 500 °C. Furthermore, the effect of changing the composition of cerium and iron in the perovskite structure was also studied as before. This is because these mixed ionic-electronic conductors

(MIECs) are known to act positively in the electrochemical activity for oxygen reduction reaction due to their redox couples like  $\text{Ce}^{3+} \leftrightarrow \text{Ce}^{4+}$  as stated before [5].

### **5.2.2.1 Half-Cell Testing on 1 MWCNT/3 CSFC with $x = y = 0.2$ , $x = 0.6$ , $y = 0.8$ and $x = y = 0.8$ in cerium and in iron**

Figure 5.6 shows the polarization curves of the composite cathodes with different perovskite compositions. The electrochemical performance of the MWCNT/CSFC composite cathodes was investigated by applying the composite as the cathode without the anode (single cell). The obtained polarization curves exhibited a linear fall in voltage as the current density increases. This overvoltage limits the fuel to operate as efficiently as possible and is due to the resistance flow in the cathode electrode which indicates an increase in the overvoltage because of the increase in the current density. This is associated to the fact that there is a resistance to current flow within the fuel cell. As the current density increases, the voltage drops, this effect is referred to Ohm's Law [5]. At very high current densities, the hydrogen reaction rate is high, however, the hydrogen cannot diffuse to the electrolyte fast enough to react [38, 184, 187]. There is also a decrease in the OCV from a theoretical value because of the reduction in hydrogen pressure in the anode/electrolyte interface. In Figure 5.6, it can be seen that all cathode materials perform significantly better at 400 and 500 °C and this is ascribed to an improvement on the oxygen reduction process taking place in the cathode and high ionic conductivities in the electrolyte. There is a huge drop in the power density at 300 °C and this is attributed to the conductivity of the YSZ electrolyte which performs well at higher temperatures. As the measuring temperature increases from 400–500 °C the ionic conductivity of the electrolyte increases, this influence the reduction of adsorbed molecular oxygen to  $\text{O}^{2-}$  ions and improves the diffusion of these ions to the electrode/electrolyte interface [199]. The increase in temperature increases the diffusion of the ions in the electrodes, the discharge of the ions to form hydrogen atoms and oxygen atoms on the surface of the electrode and the formation of water molecules [194]. An increase in the overall rate of the diffusion process reduces polarisation resistance; and the losses are smaller at 400 and 500 °C.

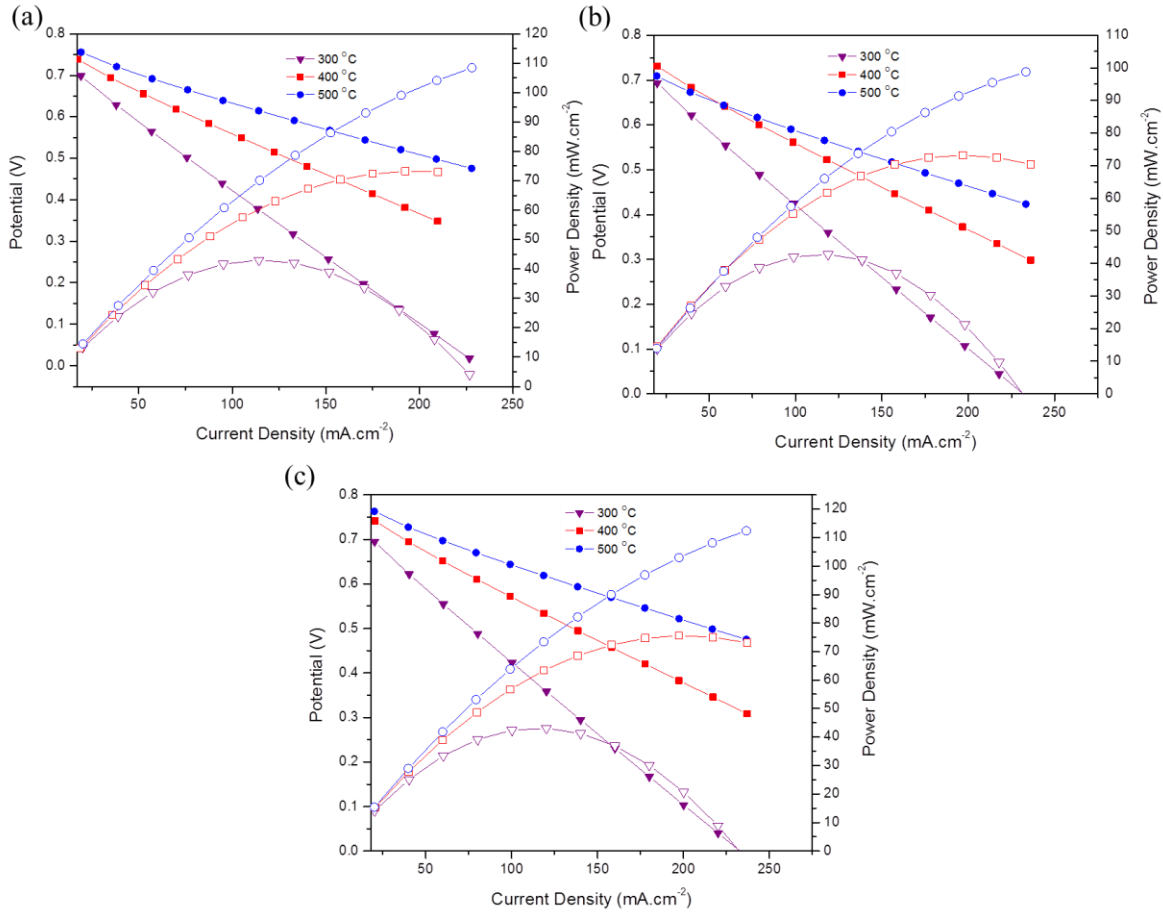


**Figure 5.6:**  $I$ - $V$  and  $I$ - $P$  curves of 1MWCNT/3Ce<sub>x</sub>Sr<sub>1-x</sub>Fe<sub>y</sub>Co<sub>1-y</sub>O<sub>3</sub> synthesized by sol-gel method. (a)  $x = y = 0.2$ , (b)  $x = 0.6$ ,  $y = 0.8$  and (c)  $x = y = 0.8$ . The cathodes were tested under single cells for 2 hours at each temperature under air (100 mL.min<sup>-1</sup>) as an oxidant and humidified H<sub>2</sub> as a fuel (200 mL.min<sup>-1</sup>)

The cathode with  $x = y = 0.2$  show maximum current densities of 226.7, 209.7 and 228.0 mA.cm<sup>-2</sup> with peak power densities of 42.9, 73.2 and 109.4 mW.cm<sup>-2</sup> at 300, 400 and 500 °C (Figure 5.6 (a)). When the compositions of cerium and iron were raised in the composites with Ce<sub>0.6</sub>Sr<sub>0.4</sub>Fe<sub>0.8</sub>Co<sub>0.2</sub>O<sub>3</sub> perovskite structure, obtained maximum current densities are 231.8, 232.9 and 230.6 mA.cm<sup>-2</sup> with corresponding peak power densities of 42.74, 73.16 and 98.74 mW.cm<sup>-2</sup> at tested temperature (Figure 5.6 (b)). The current densities obtained in the composites synthesized by sol-gel method are slightly high than those from the CVD method under the same cell configuration. While the power densities are quite the same except at 300 and 400 °C but at 500 °C the composite synthesized by sol-gel method have improved results. Further, improvement in the performance was observed in the cathode composite with high compositions of cerium  $x = 0.8$  and iron  $y = 0.8$ . This cathode material

produced maximum current densities of 240.4, 236.9 and 236.6 mA.cm<sup>-2</sup> and the peak power densities of 43.02, 75.59 and 112.4 mW.cm<sup>-2</sup> at 300, 400 and 500 °C, respectively (Figure 5.6 (c)). The current densities for this cathode increased slightly as compared to those of the composite with x = 0.6 and y = 0.8 discussed above. In terms of power outs, the cathode material showed improved performance especially at 400 and 500 °C. The minimum ASR values in Figure 5.6 (a) are lower for all temperatures, 0.2261 Ω.cm<sup>2</sup> at 300 °C, 0.2090 Ω.cm<sup>2</sup> at 400 °C and 0.2273 Ω.cm<sup>2</sup> at 500 °C. In the cathode with x = 0.6 and y = 0.8, the ASR values are also lower for all temperatures and comparable to the literature values: CNT/Pr<sub>0.6</sub>Sr<sub>0.8</sub>Fe<sub>0.2</sub>Co<sub>0.8</sub>O<sub>3</sub> = 0.14 and 0.23 Ω.cm<sup>2</sup> (at 700 and 600 °C, respectively) [17]; MWCNT/Ce<sub>0.6</sub>Sr<sub>0.8</sub>Fe<sub>0.2</sub>Co<sub>0.8</sub>O<sub>3</sub> = 0.2118, 0.2127 and 0.2111 Ω.cm<sup>2</sup> (at 300, 400 and 500 °C, respectively). There was no significant difference in the ASR values of the cathode with x = y = 0.8, 0.2397 Ω.cm<sup>2</sup> at 300 °C, 0.2362 Ω.cm<sup>2</sup> at 400 °C and 0.2358 Ω.cm<sup>2</sup> at 500 °C. The slopes of the curves (ASR), decreases in high current densities because of the decreasing internal resistances in the cell. These values are lower than those for the perovskites of this type reported elsewhere [5, 17, 48, 183, 186, 204] showing that these cathodes can be used in the LIT-SOFC.

### **5.1.2.2 Symmetrical Cell Testing on 1 MWCNT/3 CSFC with x = y = 0.2, x = 0.6, y = 0.8 and x = y = 0.8 in cerium and in iron**

The polarization curves of the cathodes synthesized by sol-gel method and tested in symmetrical cells [composite |YSZ| composite] are shown in Figure 5.7. The cathode with x = y = 0.2 has maximum current densities of 243, 240 and 240 mA.cm<sup>-2</sup> and peak power densities of 57.23, 75.44 and 112.2 mW.cm<sup>-2</sup> at 300, 400 and 500 °C, respectively (Figure 5.7 (a)). The cathode with x = 0.6 in cerium and y = 0.8 in iron has maximum current densities of 245.2, 245.1 and 244.3 mA.cm<sup>-2</sup> with peak power densities of 43.63, 74.42 and 105.9 mW.cm<sup>-2</sup> at 300, 400 and 500 °C, respectively (Figure 5.7 (b)). The composite cathode containing high compositions of cerium and iron in the perovskite structure shows no significant difference on the performance in the current densities as compared to the composite with x= 0.6 and y = 0.8 compositions discussed above. As the cerium and iron compositions were increased to x = y = 0.8, the obtained current and power densities are 246.8, 245.6 and 244.1 mA.cm<sup>-2</sup> and 44.34, 73.97 and 113.4 mW.cm<sup>-2</sup> at 300, 400 and 500 °C, respectively (Figure 5.7 (c)). The peak power output has improved at 500 °C when

compared to that of the cathode with  $x = 0.6$  and  $y = 0.8$ . There is a significant improvement in the performance of these cathodes when tested under symmetrical cells in terms of current and power densities. This might be attributed to the fact that electrochemical properties in both reducing and oxidising conditions have been enhanced because of the high compositions of cerium and iron. When the same materials but synthesized by CVD method were tested under symmetrical cells, current and power densities were exceptional low. The improvement here could also be assigned to the reduced crystallite size achieved by sol-gel method in the  $x = y = 0.2$  cathode [200, 201]. For the cathodes with high compositions of cerium and iron, the improvement in the current and power densities can be assigned to the enhanced ionic conductivities.

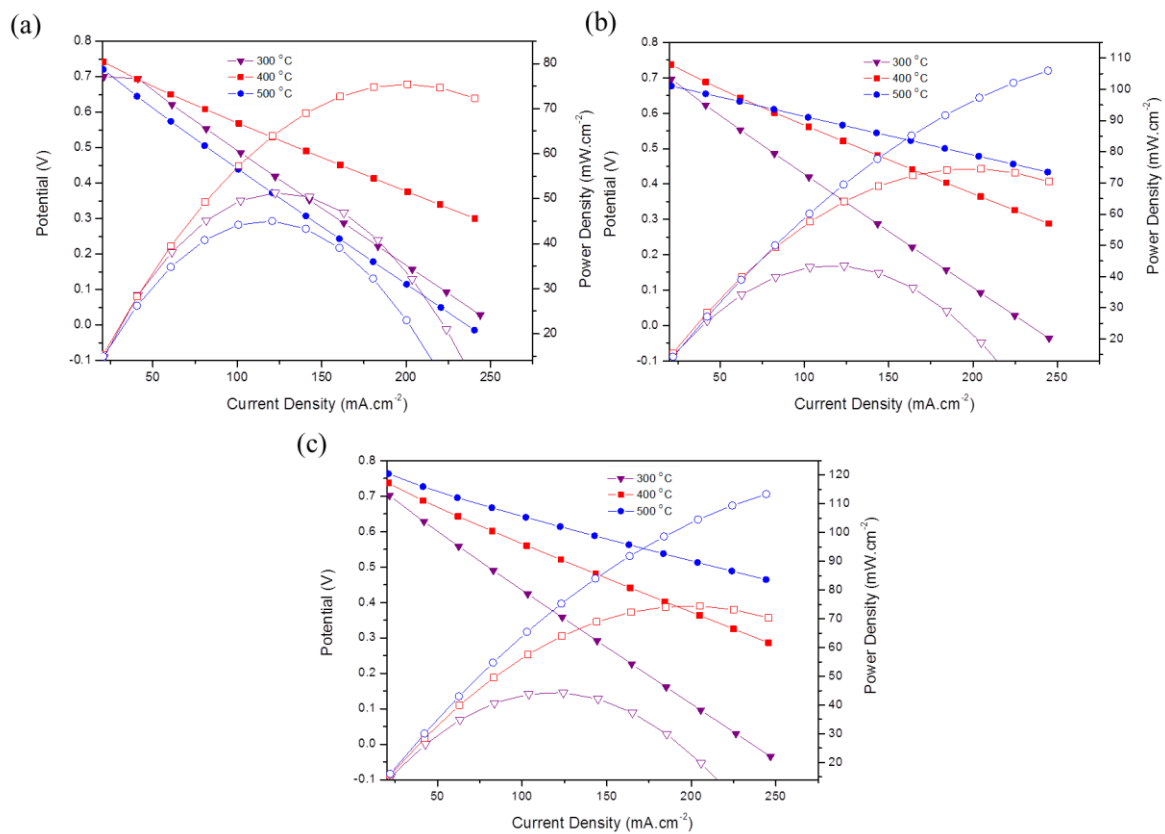


**Figure 5.7:**  $I-V$  and  $I-P$  curves of  $1\text{MWCNT}/3\text{Ce}_x\text{Sr}_{1-x}\text{Fe}_y\text{Co}_{1-y}\text{O}_3$  composite cathodes synthesized by sol-gel method. (a)  $x = y = 0.2$ , (b)  $x = 0.6$ ,  $y = 0.8$  and (c)  $x = y = 0.8$ . The cathodes were tested under symmetrical cells for 2 hours at each temperature under air ( $100\text{ mL}\cdot\text{min}^{-1}$ ) as an oxidant and humidified  $\text{H}_2$  as a fuel ( $200\text{ mL}\cdot\text{min}^{-1}$ )

A linear fall in voltage is observed from the  $I-V$  curves of these cathodes as the current density increases. This loss in voltage can be explained as before, as due to the resistance to flow within the fuel cell. In Figure 5.7 (a), it can be seen that the loss is occurring at both 300 and 500 °C. The performance of this cathode is not satisfactory at these temperatures. This is attributed to the microstructure of this cathode. There is an increase in the oxygen reduction rate in the cathode, and ionic conductivity of electrolyte is high at these temperatures especially at 400 °C. The performance at 300 and 500 °C is low and the material start to degrade at an earlier current density. In Figure 5.7 (b), the performance of the cathode is higher at 400 and 500 °C because of the improved ionic conductivities in the YSZ electrolyte and increased cerium and iron compositions in the perovskite. Here the OCV is higher at 400 °C and it is dropping as the temperature increase to 500 °C. The cathode performance is exceptionally good in the perovskite with  $x = y = 0.8$ . This is because of the microstructure and enhanced ionic conductivities of the cathode. The calculated ASR values for the cathode in Figure 5.7 (a) are 0.2432, 0.2400 and 0.2398  $\Omega\cdot\text{cm}^2$  at 300, 400 and 500 °C, respectively. For the cathode with  $x = 0.6$  and  $y = 0.8$ , the ASR values are 0.2444  $\Omega\cdot\text{cm}^2$  at 300 °C, 0.2444  $\Omega\cdot\text{cm}^2$  at 400 °C and 0.2436  $\Omega\cdot\text{cm}^2$  at 500 °C (Figure 5.7 (b)). Lastly, in the cathode shown in Figure 5.7 (c), the ASR values became 0.2461, 0.2449 and 0.2434  $\Omega\cdot\text{cm}^2$  at 300, 400 and 500 °C, respectively. It must be stressed that, in overall these cathode materials have better electrochemical performance at low to intermediate temperature solid oxide fuel cell (LIT-SOFC) in terms of current and power densities.

### **5.2.2.3 Asymmetrical Cell Testing on 1 MWCNT/3 CSFC with $x = y = 0.2$ , $x = 0.6$ , $y = 0.8$ and $x = y = 0.8$ in cerium and in iron**

The electrochemical performance of the cathode materials was tested under asymmetrical cells employing nickel oxide and YSZ as the anode with the cell configuration [NiO-YSZ | YSZ | composite]. In the polarization curves shown in Figure 5.8, there is a linear fall in the voltage as the current density increases and this is due to the resistance flow present in the cathode which shows an increase in the current density. The OCV increased with an increase in the operating temperature and stabilized at 0.7 V. It can be seen from the polarization curves that, the performance of the cells increases with temperature especially at 400 to 500 °C. At 300 °C there is a huge drop in the voltage (ohmic loss) because of low ionic

conductivity of YSZ electrolyte at low temperatures (is not optimized). In Figure 5.8 (a) for the cathode with low compositions of cerium and iron,  $x = y = 0.2$ , the obtained maximum current densities were 237.7, 236.5 and 235.5 mA.cm<sup>-2</sup> with peak power densities of 43.60, 73.93 and 111.7 mW.cm<sup>-2</sup> at 300, 400 and 500 °C, respectively. The minimum ASR values for this cell decreases with an increase in temperature: 0.2370, 0.2358 and 0.2348 Ω.cm<sup>2</sup> at 300, 400 and 500 °C. The cathode 1MWCNT/ 3Ce<sub>0.6</sub>Sr<sub>0.4</sub>Fe<sub>0.8</sub>Co<sub>0.2</sub>O<sub>3</sub> showed current densities of 245.5, 244.1 and 242.2 mA.cm<sup>-2</sup> with peak power densities of 42.52, 75.68 and 116.9 mW.cm<sup>-2</sup> (Figure 5.8 (b)). The performance of this composite cathode is higher than that of the cathode with  $x = 0.2$  and  $y = 0.2$  perovskite compositions. The power output has significantly improved for the composites with  $x = y = 0.2$  and  $x = 0.6$  and  $y = 0.8$  from a value of 111.7 to 116.9 mW.cm<sup>-2</sup> at 500 °C. The improvement in the current and power densities is attributed to the increase in the composition of cerium and iron in the perovskite structure ( $x = 0.6$  and  $y = 0.8$ ) which then enhances the redox couples. The obtained ASR values for the cathode with  $x = 0.6$  and  $y = 0.8$  were low at all operating temperatures, 0.2441, 0.2434 and 0.2454 Ω.cm<sup>2</sup> at 300, 400 and 500 °C, respectively (Figure 5.8 (b)). The MWCNT/CSFC composite cathode material with  $x = y = 0.8$  possess maximum current densities of 242.2, 240.7 and 240.2 mA.cm<sup>-2</sup> with the corresponding peak power densities of 43.85, 73.01 and 113.6 mW.cm<sup>-2</sup> at 300, 400 and 500 °C, respectively (Figure 5.8(c)). The minimum ASR values are 0.2415 Ω.cm<sup>2</sup> at 300 °C, 0.2400 Ω.cm<sup>2</sup> at 400 °C and 0.2394 Ω.cm<sup>2</sup> at 500 °C. The slopes of the curves (ASR) decreases in high current densities because of the decreasing internal resistance in the cell [183].

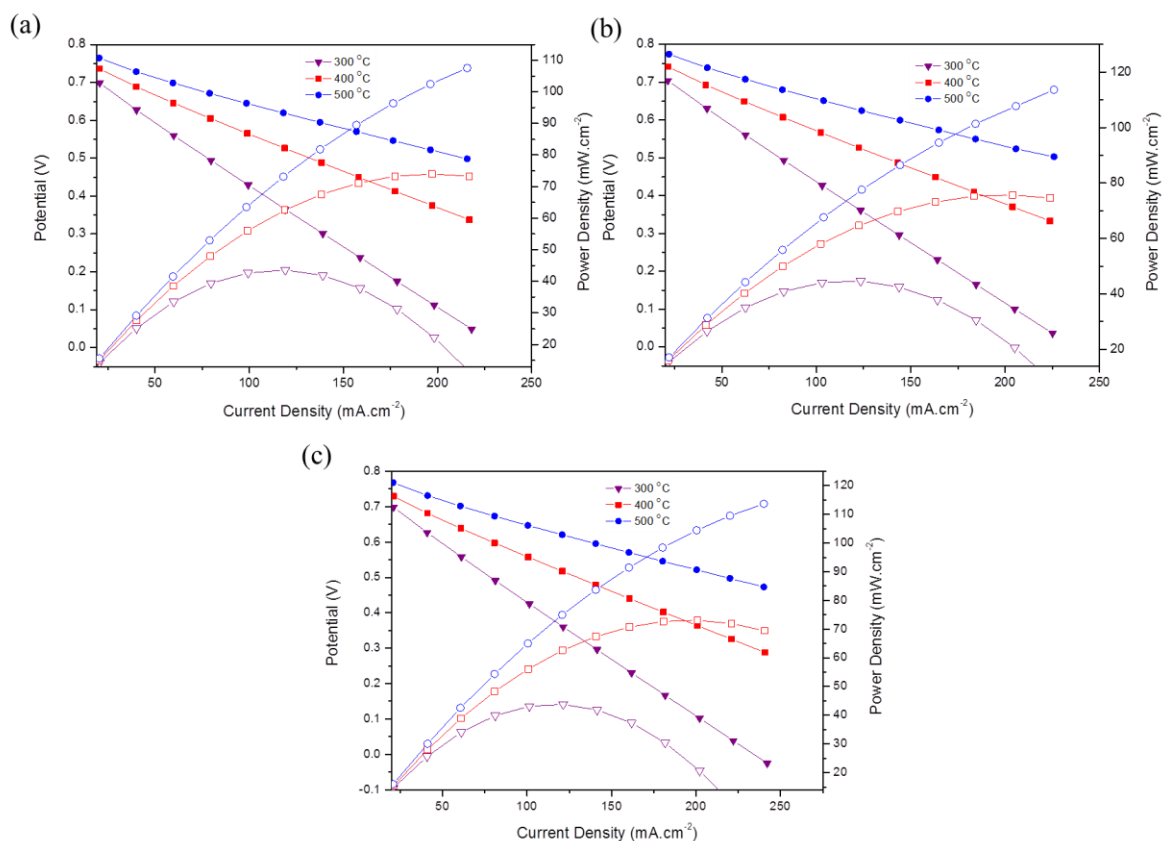


**Figure 5.8:**  $I$ - $V$  and  $I$ - $P$  curves of 1MWCNT/3Ce<sub>x</sub>Sr<sub>1-x</sub>Fe<sub>y</sub>Co<sub>1-y</sub>O<sub>3</sub> composite cathodes synthesized by sol-gel method. (a)  $x = y = 0.2$ , (b)  $x = 0.6$ ,  $y = 0.8$  and (c)  $x = y = 0.8$ . The cathodes were tested under asymmetrical cells with NiO-YSZ as the anode for 2 hours at each temperature under air (100 mL.min<sup>-1</sup>) as an oxidant and humidified H<sub>2</sub> as a fuel (200 mL.min<sup>-1</sup>)

Table 5.2 combines all current and power densities obtained for cathode nanocomposites materials synthesized by sol-gel method at different operating temperatures under all tested cell configurations. The cathodes tested under asymmetrical and symmetrical cells configurations have high current and power densities. In the single cells testing, high current densities are observed in the composite cathode with  $x = y = 0.8$ . In the symmetrical cells the composites cathodes with high compositions of cerium and iron (both 0.6 and 0.8) possess high current and power densities. Asymmetrical cells also have high current and power densities on the composite with high compositions of cerium and iron.

**Table 5. 2:** Electrochemical performance of MWCNT/Ce<sub>x</sub>Sr<sub>1-x</sub>Fe<sub>y</sub>Co<sub>1-y</sub>O<sub>3</sub> cathode materials synthesized by sol-gel technique

Electrode Material	x	y	Cell Type	Current Density/mA.cm <sup>-2</sup>			Power Density/mW.cm <sup>-2</sup>		
				300 °C	400 °C	500 °C	300 °C	400 °C	500 °C
1CNT:3CSFC	0.2	0.2	single	226.7	209.7	228.0	42.91	73.18	109.4
1CNT:3CSFC	0.6	0.8	single	231.8	232.9	230.6	42.74	73.16	98.74
1CNT:3CSFC	0.8	0.8	single	240.4	236.9	236.6	43.02	75.59	112.4
1CNT:3CSFC	0.2	0.2	symmetrical	243.9	240.7	240.5	57.23	75.44	112.2
1CNT:3CSFC	0.6	0.8	symmetrical	245.2	245.1	244.3	43.67	74.42	105.9
1CNT:3CSFC	0.8	0.8	symmetrical	246.8	245.6	244.1	44.34	73.97	113.4
1CNT:3CSFC	0.2	0.2	asymmetrical	237.7	236.5	235.5	43.60	73.93	111.7
1CNT:3CSFC	0.6	0.8	asymmetrical	245.5	244.1	246.2	42.52	75.68	116.9
1CNT:3CSFC	0.8	0.8	asymmetrical	242.2	240.7	240.2	43.85	73.01	113.6

In the single cell configuration, the performance exhibited by the nanocomposites cathodes (with low amounts of cerium and iron) synthesized by both CVD and sol-gel methods are not significantly different. The difference was observed when the amount of cerium and iron were raised to  $x = 0.6$ ,  $0.8$  and  $y = 0.8$  in the perovskite structure. In the cathode nanocomposites synthesized by CVD method, there is no such improvement at high compositions of cerium and iron. Even in the case of composite cathode with high values of cerium ( $x = 0.8$ ) and iron ( $y = 0.8$ ) a slight change was observed for the nanocomposites synthesized by CVD method and tested under single cells but for the same material synthesized from sol-gel method there was super high performance when compared to the above discussed results. The difference in the performance is due to the synthetic route undertaken, so, the sol-gel synthesized cathode nanocomposites have high performance under single cells.

In the symmetrical cells configurations there is a drastical decrease in the performance for the cathode with low values of cerium  $x = 0.2$  and iron  $y = 0.2$  synthesized from CVD method while for the sol-gel synthesized cathodes there is a significant improvement. In the cathode with  $x = 0.6$  and  $y = 0.8$  there is no significant difference observed from both CVD and sol-gel methods. Lastly, the performance has decreased in the cathode nanocomposites with  $x = y = 0.8$  in the perovskite structure when synthesized by CVD method as compared to that from the sol-gel method.

The CVD synthesized cathodes only have high performance when tested under asymmetrical cells with NiO–YSZ as the anode and the MWCNT/CSFC as the cathode with all compositions of cerium and iron. But there is a slight difference in the performance which is attributed to the perovskites formed in the CVD method while in the sol–gel method perovskites did not form well because of low operating temperatures. The results for the asymmetrical cells were supposed to be higher than that of both single and symmetrical cells but did not. The explanation for this might be based on the incomplete reduction of NiO to Ni metal. There was no correlation between the crystallite size and electrochemical performance. In most cases, the nanoparticles were not controlled enough in order to obtain very small sizes and hence good performance. Particles have agglomerated into complex structures. It was also observed that the nanocomposites cathodes synthesized by sol–gel method have slightly high performance than those synthesized by CVD method under single and symmetrical cells. For the asymmetrical cells, perovskites nanocomposites synthesized by CVD method have high performance.

### **5.3 Stability over long period**

The cathode nanocomposite with  $x = 0.6$  in cerium and  $y = 0.8$  in iron was used for the study of long term performance. In Figure 5.9, the voltage is plotted as a function of time for the symmetrical cells with configuration [composite |YSZ| composite] operating at 500 °C. The performance of the cathode material was very stable under a cell voltage of 0.7 V at 500 °C for more than 15 hours, demonstrating stable power output without observable degradation.

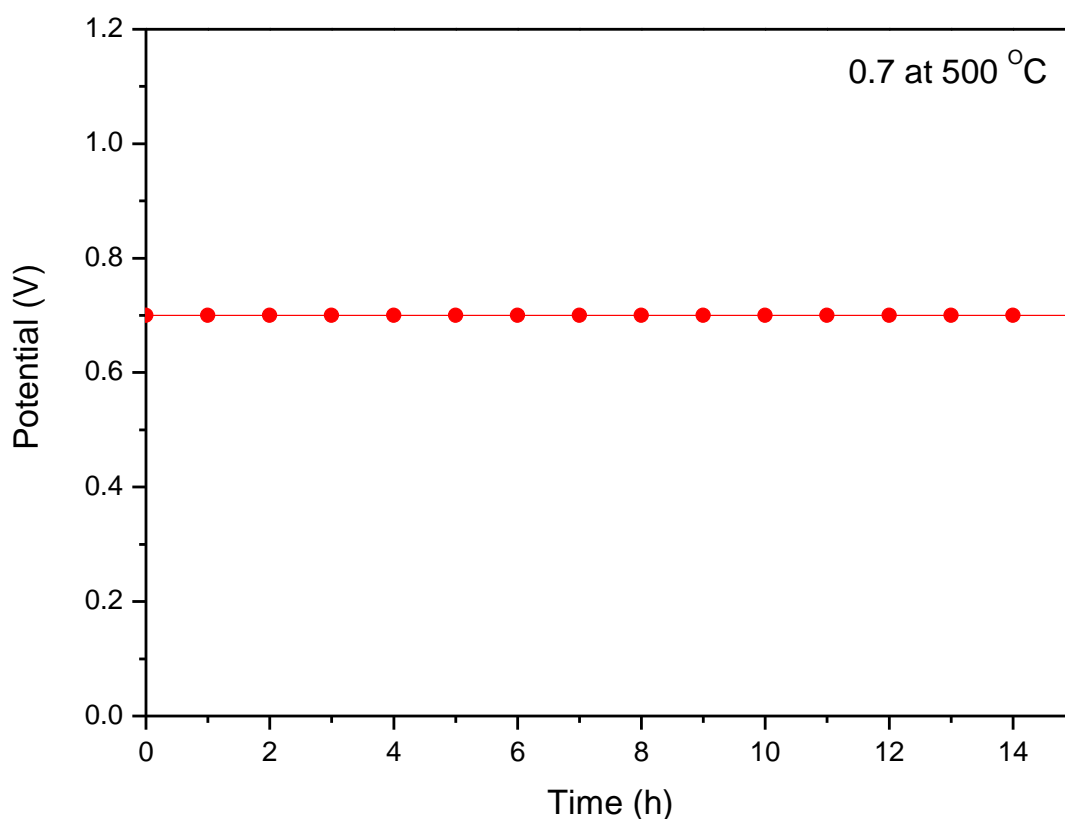


**Figure 5.9:** Long term stability measurement for a test cell, 1MWCNT/3Ce<sub>0.6</sub>Sr<sub>0.4</sub>Fe<sub>0.8</sub>Co<sub>0.2</sub>O<sub>3</sub> |YSZ|1MWCNT/3Ce<sub>0.6</sub>Sr<sub>0.4</sub>Fe<sub>0.8</sub>Co<sub>0.2</sub>O<sub>3</sub> synthesized by sol-gel method and tested under symmetrical cells at a constant cell voltage of 0.7 V at 500 °C for 15 hours

SEM/TEM was used to check the presence of MWCNTs, after the stability test. Figure 5.10 (a) and (b) show the SEM micrograph of cathode after testing for 15 hours at 500 °C, and it show the presence of MWCNTs (shown with arrows). When the samples were view under TEM, it was noticed that the oxidation of the tubes occurred, since the tubes are now chopped into small parts. The dominating species in the composites are only perovskite oxides after the test at 500 °C (Figure 5.10 (c) and (d)). From the micrographs the composites with low values of current and power densities has the highest amount of MWCNTs than that with high values. This means that the rate of oxidation reaction is higher in the former cathodes.

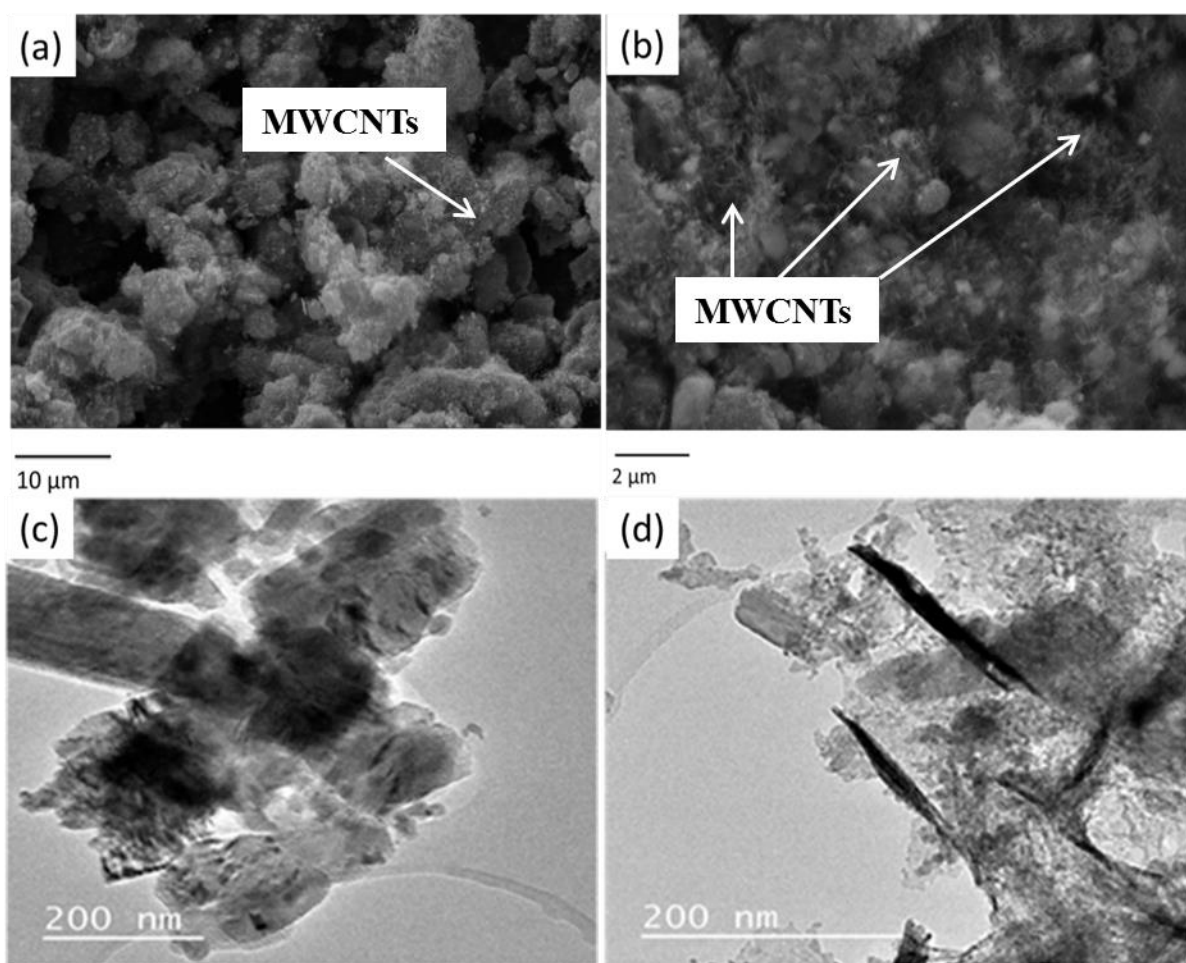


**Figure 5.10:** (a) and (b) SEM images of the cathode composite after a test for over 15 hours, (c) and (d) TEM images of low performance (1MWCNT/3Ce<sub>0.6</sub>Sr<sub>0.4</sub>Fe<sub>0.8</sub>Co<sub>0.2</sub>O<sub>3</sub>) and high performance (1MWCNT/3Ce<sub>0.6</sub>Sr<sub>0.4</sub>Fe<sub>0.8</sub>Co<sub>0.2</sub>O<sub>3</sub>), respectively

#### 5.4 Conclusions

Cathode composite materials showed low current density and power output for the cathode operated under single cell. The composite with  $x = y = 0.2$  synthesized by CVD and tested under symmetrical cells possess very low electrical performances ( $132 \text{ mA}\cdot\text{cm}^{-2}$ ) at low to intermediate temperature from  $300\text{--}500 \text{ }^\circ\text{C}$ . While the asymmetrical cells with the same compositions of cerium and iron in the perovskite structure have high current and power densities of  $248.0 \text{ mA}\cdot\text{cm}^{-2}$  and  $111.3 \text{ mW}\cdot\text{cm}^{-2}$  at  $500 \text{ }^\circ\text{C}$ . The composites with high values of  $x$  and  $y$  have improved performance under both symmetrical and asymmetrical cells. The materials performance in terms of fuel cell stability was determined to be promising, since the cell was stable for up to 15 hours at  $500 \text{ }^\circ\text{C}$ . It was observed that, the OCV was

significantly lower than reported values by others 0.7 V [183, 195]. The microstructure of the composite cathodes was not controlled enough; hence the composites possess decreased performances. Furthermore, gas leakage between the anode, cathode and electrolyte interfaces was the cause of this decreased in electrochemical performance. Current methods presented in Chapter 3 do not improve performance at low to intermediate temperatures, because the crystallite sizes formed were not consistent. It was interesting to observe from TEM images that the composites with low electrical performance have incomplete oxidation of MWCNT while in that with high performance all MWCNTs have been oxidized completely. The obtained area specific resistances for all the cathodes were small and this showed that the materials can be used as cathodes in the low to intermediate solid oxide fuel cells.

Results obtained prove that the cathodes with small particle sizes and high loadings of cerium and iron have high performances. In most cases synthetic route has an impact on electrochemical performance of these cathodes nanocomposites materials. The observed change can be further attributed to the structure of the perovskite nanoparticle materials. There is still room for improvement in the present cathodes in order to enhance cell performance. This can be achieved by further controlling the microstructure and morphology of the electrodes and by using materials with super high electrical conductivities. Replacing YSZ electrolyte with the electrolyte possessing high ionic conductivities such as samarium doped ceria (SDC) at low temperatures will be an alternative. Hypothetically, there is a need for fabricating button cells of these cathode materials by pressing the powders together because the present paint brushing method might lead to contamination problems.

## Chapter Six

### General Conclusions

Perovskites nanoparticles alone as well as within (outside) the MWCNTs as templates have been successfully synthesized using both dry CVD and sol-gel methods under heat treatment at 400 °C for 8 hours. The presence of MWCNTs has facilitated the formation of nanoparticles at low temperatures from 300 to 600 °C and carbon nanotubes acted as bundles for controlling the crystallite size growth more significantly in the *in-situ* experiment. The *in-situ* XRD experiment showed the formation of nano perovskite under the CVD method. But for the sol-gel method, there was incomplete perovskite formation, perovskite together with starting materials (metal oxides). For the CVD method, the acacs present in metals have aided the formation of perovskites nanoparticles while in the sol-gel method a non-ionic surfactant Pluronic F-127 has been used to form a networking array of MWCNTs and CSFC perovskites after heat treatments. *In-situ* was used to deduce the temperature at which perovskites phases start to develop. In room temperature XRD experiments, perovskites nanoparticles were detected from both CVD and sol-gel methods at 400 °C. Different compositions of CSFC perovskites have been prepared on MWCNTs surfaces with varying compositions of cerium and iron in the perovskite structure. Finally the testing of electrochemical performance for these nano materials has been done by examining polarization curves at 300, 400 and 500 °C.

The MWCNT/Ce<sub>x</sub>Sr<sub>1-x</sub>Fe<sub>y</sub>Co<sub>1-y</sub>O<sub>3</sub> (0.2 ≤ (x, y) ≤ 0.8) nanocomposite powders were successfully fabricated by the sol-gel and CVD methods with grain size in the range of 25.37–497.67 Å. The grain size has been controlled using MWCNTs as templates. The low operating temperature did not allow the formation of full perovskites phases under sol-gel with changing composition (x and y) in the structure. Different amounts of perovskites have been added to the carbon nanotubes in order to obtain the smallest grain size and hence improved electrochemical performances. The requirements for SOFC materials in terms of microstructure modification have not been met because inconsistent particle sizes have been formed. Heat treatment reduces the disorder on the MWCNTs walls; moreover, high loadings of Ce<sub>x</sub>Sr<sub>1-x</sub>Fe<sub>y</sub>Co<sub>1-y</sub>O<sub>3</sub> on the surface of nanotubes reveal the decrease in defects after heat treatment with higher amount of CSFC. MWCNTs have been coated with

perovskites nanoparticles in an effort of enhancing electrochemical performances, and the performance of the composites is higher than that of the control system (perovskites alone). This means that, the composite approach is significant in enhancing electrochemical properties of the composites. This has been done at reduced temperatures (400 °C), and hence SOFCs operating costs has been lowered. To sum up, the observed properties of MWCNT/Ce<sub>x</sub>Sr<sub>1-x</sub>Fe<sub>y</sub>Co<sub>1-y</sub>O<sub>3</sub> implies that, these nanocomposites powders can be used as cathode materials in the SOFCs at low to intermediate temperatures because they give some values of current and power densities.

The tested materials showed performance that is not satisfactory as compared to the literature. Cathodes synthesized from CVD method with low amounts of cerium and iron has shown maximum current density of 132 mA.cm<sup>-2</sup> at 500 °C when tested under symmetrical cells. While the same composites show better performance with maximum current density of 248 mA.cm<sup>-2</sup> in asymmetrical cells at 500 °C with NiO–YSZ as the anode. There was a slight change in the electrochemical performances of these materials as the composition of cerium and iron changes. Electrochemical performance of these materials depends on the conductivity of the materials under test. The increase in the composition of cerium and iron in the perovskite structure result in the enhanced electronic conductivities of the cathode which is than good for hydrogen reduction reactions. The oxidation of MWCNT during the test has resulted in damaging the surface of the MWCNTs. In the samples with low current and power densities, the surface of MWCNTs is not completely damaged. While in the samples with high current and power densities, all MWCNTs have been violated. There was no significant change in the performance of the samples with different composition of perovskites and carbon nanotubes. Single cell tested materials have low performance beaten by the symmetrical and asymmetrical cells. In the symmetrical cells there is a huge loss because the MWCNT/CSFC cannot act as anode, so it blocks the movement of oxygen ions on the anode side. Materials tested under asymmetrical cells are not promising because the anode was not porous and nickel was not reduced properly to Ni metal which then led to low performances in these materials.

## 6.1 Recommendations and Future Work

For recommendations and future work, more research based on the modification of the microstructure of the new cathodes need to be done aiming to achieve higher performances of

the cells. This can be achieved by the use of micro-SOFC to take advantage of CNTs mechanical, thermal and electrical properties. The use of MWCNTs arrays need to be studied since these will allow high operating temperature without burning MWCNTs. It is also required to employ electrolytes that are optimized for low temperature and the use of perovskite materials that are optimized for 300–400 °C to avoid degradation of CNTs. Lastly, for further performance analysis we will have to employ Electrochemical Impedance Spectroscopy (EIS) on these cathode materials and button cells in the near future.

## References

1. Yamamoto, O., *Solid Oxide Fuel Cells: Fundamental Aspects and Prospects*. Electrochimica Acta, 2000. **45**(15–16): p. 2423-2435.
2. McIntosh, S. and R.J. Gorte, *Direct Hydrocarbon Solid Oxide Fuel Cells*. Chemical Reviews, 2004. **104**(10): p. 4845-4866.
3. Lou, Z., Peng, J., Dai, N., Qiao, J., Wang, Z., Yan, Y., Wang, J. and Sun, J., *High Performance  $La_3Ni_2O_7$  Cathode Prepared by a Facile Sol–Gel Method for Intermediate Temperature Solid Oxide Fuel Cells*. Electrochemistry Communications, 2012. **22**(0): p. 97-100.
4. Ma, Y., *Ceria-Based Nanostructured Materials for Low-Temperature Solid Oxide Fuel Cells*, 2012, Royal Institute of Technology, US.
5. Vert, V.B. and J.M. Serra, *Improvement of the Electrochemical Performance of  $Ln_{0.58}Sr_{0.4}Fe_{0.8}Co_{0.2}O_{3-\delta}$  IT-SOFC Cathodes by Ternary Lanthanide Combinations (La-Pr-Sm)*. Fuel Cells, 2010. **10**(4): p. 693-702.
6. Vargas, J.V.C., J.C. Ordonez, and A. Bejan, *Constructal PEM Fuel Cell Stack Design*. International Journal of Heat and Mass Transfer, 2005. **48**(21–22): p. 4410-4427.
7. Carrette, L., K.A. Friedrich, and U. Stimming, *Fuel Cells – Fundamentals and Applications*. Fuel Cells, 2001. **1**(1): p. 5-39.
8. Haile, S.M., *Fuel Cell Materials and Components*. Acta Materialia, 2003. **51**(19): p. 5981-6000.
9. Sharaf, O.Z. and M.F. Orhan, *An overview of Fuel Cell Technology: Fundamentals and Applications*. Renewable and Sustainable Energy Reviews, 2014. **32**(0): p. 810-853.
10. Ellis, M.W., M.R. von Spakovsky, and D.J. Nelson, *Fuel Cell Systems: Efficient, Flexible Energy Conversion for the 21st Century*. Proceedings of the IEEE, 2001. **89**(12): p. 1808-1818.
11. Singhal, S.C., *Solid Oxide Fuel Cells for Stationary, Mobile, and Military Applications*. Solid State Ionics, 2002. **152**: p. 405-410.
12. Weber, A. and E. Ivers-Tiffée, *Materials and Concepts for Solid Oxide Fuel Cells (SOFCs) in Stationary and Mobile Applications*. Journal of Power Sources, 2004. **127**(1–2): p. 273-283.

13. Larminie, J., A. Dicks, and M.S. McDonald, *Fuel Cell Systems Explained*. Vol. 2. 2003: Wiley Chichester, UK. p 207-225.
14. Di, J., Chen, M., Wng, C., Zheng, J., Fan, L. and Zhu, B., *Samarium-Doped Ceria–(Li/Na)<sub>2</sub>CO<sub>3</sub> Composite Electrolyte and its Electrochemical Properties in Low Temperature Solid Oxide Fuel Cell*. Journal of Power Sources, 2010. **195**(15): p. 4695-4699.
15. Muhammed Ali, S.A., Muchtar, A., Sulong, A.B., Muhamad, N. and Majlan, E.H., *Influence of Sintering Temperature on the Power Density of Samarium-Doped-Ceria Carbonate Electrolyte Composites for Low-Temperature Solid Oxide Fuel Cells*. Ceramics International, 2013. **39**(5): p. 5813-5820.
16. Santillán, M.J., Caneiro, A., Lovey, F.C., Quaranta, N. and Baccaccini, A.R., *Electrophoretic Codeposition of La<sub>0.6</sub>Sr<sub>0.4</sub>Co<sub>0.8</sub>Fe<sub>0.2</sub>O<sub>3-δ</sub> and Carbon Nanotubes for Developing Composite Cathodes for Intermediate Temperature Solid Oxide Fuel Cells*. International Journal of Applied Ceramic Technology, 2010. **7**(1): p. 30-40.
17. Pinedo, R., Ruiz de Larramendi, I., Jimenez de Aberasturi, D., Gil de Muro, I., Aguayo, A.T., Ruiz de Larramendi, J.I. and Rojo, T., *A Straightforward Synthesis of Carbon Nanotube–Perovskite Composites for Solid Oxide Fuel Cells*. Journal of Materials Chemistry, 2011. **21**(28): p. 10273-10276.
18. Tarancón, A., Pena-Martinez, J., Marrero-Lopez, D., Morata, A., Ruiz-Morales, J.C. and Nunez, P., *Stability, Chemical Compatibility and Electrochemical Performance of GdBaCo<sub>2</sub>O<sub>5+x</sub> Layered Perovskite as a Cathode for Intermediate Temperature Solid Oxide Fuel Cells*. Solid State Ionics, 2008. **179**(40): p. 2372-2378.
19. Tarancón, A., Skinner, S.J., Chater, R.J., Hernandez-Ramirez, F. and Kilner, J.A., *Layered Perovskites as Promising Cathodes for Intermediate Temperature Solid Oxide Fuel Cells*. Journal of Materials Chemistry, 2007. **17**(30): p. 3175-3181.
20. Al-Yousef, Y.M. and M. Ghouse, *Preparation of La<sub>0.6</sub>Ba<sub>0.4</sub>Co<sub>0.2</sub>Fe<sub>0.8</sub>O<sub>3</sub> (LBCF) Nanoceramic Cathode Powders by Sol-Gel Process for Solid Oxide Fuel Cell (SOFC) Application*. Energy and Power Engineering, 2011. (3): p. 382-39
21. Cioateră, N., Parvulescu, V., Rolle, N., Vannier R.N., *Enhanced Ionic Conductivity of Sm, Gd-Doped Ceria Induced by Modification of Powder Synthesis Procedure*. Ceramics International, 2012. **38**(7): p. 5461-5468.
22. Pinedo, R., R., Ruiz de Larramendi, I., Jimenez de Aberasturi, D., Ortiz-Vitoriano, N. and Rojo, T., *Nanotechnology for Improving Solid Oxide Fuel Cells*. Materials and Processing for Energy, 2013.

23. Kulkarni, A. and S. Giddey, *Materials Issues and Recent Developments in Molten Carbonate Fuel Cells*. Journal of Solid State Electrochemistry, 2012. **16**(10): p. 3123-3146.
24. Ivers-Tiffée, E., Weber, A. and Herbristrit, D., *Materials and Technologies for SOFC-Components*. Journal of the European Ceramic Society, 2001. **21**(10–11): p. 1805-1811.
25. Nédélec, R., Uhlenbruck, S., Haanappel, V.A.C., Buchkremer, H.P. and Stover, D., *Dense Ytria-Stabilised Zirconia Electrolyte Layers for SOFC by Reactive Magnetron Sputtering*. Journal of Power Sources, 2012. **205**(0): p. 157-163.
26. Gorte, R.J. and J.M. Vohs, *Novel SOFC Anodes for the Direct Electrochemical Oxidation of Hydrocarbons*. Journal of Catalysis, 2003. **216**(1–2): p. 477-486.
27. Jiang, S. and S. Chan, *A Review of Anode Materials Development in Solid Oxide Fuel Cells*. Journal of Materials Science, 2004. **39**(14): p. 4405-4439.
28. Vohs, J.M. and R.J. Gorte, *High-Performance SOFC Cathodes Prepared by Infiltration*. Advanced Materials, 2009. **21**(9): p. 943-956.
29. Gross, M.D., J.M. Vohs, and R.J. Gorte, *Recent Progress in SOFC Anodes for Direct Utilization of Hydrocarbons*. Journal of Materials Chemistry, 2007. **17**(30): p. 3071-3077.
30. Mizutani, Y., Tamura, M. and Kawai, M., *Development of High-Performance Electrolyte in SOFC*. Solid State Ionics, 1994. **72, Part 2**(0): p. 271-275.
31. Tietz, F., *Thermal Expansion of SOFC Materials*. Ionics, 1999. **5**(1-2): p. 129-139.
32. Jacobson, A.J., *Materials for Solid Oxide Fuel Cells*. Chemistry of Materials, 2010. **22**(3): p. 660-674.
33. Chen, Y., Orlovskaya, N., Klimov, M., Huang, X, Cullen, D., Graule, T. and Kuebler, J., *Layered YSZ/SCSZ/YSZ Electrolytes for Intermediate Temperature SOFC Part I: Design and Manufacturing*. Fuel Cells, 2012. **12**(5): p. 722-731.
34. Zhu, B., L. Fan, and P. Lund, *Breakthrough Fuel Cell Technology Using Ceria-Based Multi-Functional Nanocomposites*. Applied Energy, 2013. **106**(0): p. 163-175.
35. Hancock, C.A., et al., *Oxyanions in Perovskites: from Superconductors to Solid Oxide Fuel Cells*. Dalton Transactions, 2015.
36. Schaak, R.E. and T.E. Mallouk, *Perovskites by Design: A Toolbox of Solid-State Reactions*. Chemistry of Materials, 2002. **14**(4): p. 1455-1471.
37. Gorte, R.J. and J.M. Vohs, *Nanostructured Anodes for Solid Oxide Fuel Cells*. Current Opinion in Colloid & Interface Science, 2009. **14**(4): p. 236-244.

38. Wang, W., Chao, S., Wu, Y., Ran, R., and Shao, Z., *Progress in Solid Oxide Fuel Cells with Nickel-Based Anodes Operating on Methane and Related Fuels*. Chemical Reviews, 2013. **113**(10): p. 8104-8151.
39. Zimicz, M.G., Nunez, P., Ruiz-Morales, J.C., Lamas, D.G. and Larrond, S.A., *Electro-Catalytic Performance of 60%NiO/Ce<sub>0.9</sub>Zr<sub>0.1</sub>O<sub>2</sub> Cermets as Anodes of Intermediate Temperature Solid Oxide Fuel Cells*. Journal of Power Sources, 2013. **238**(0): p. 87-94.
40. Kaur, G. and S. Basu, *Performance Studies of Copper–Iron/Ceria–Yttria Stabilized Zirconia Anode for Electro-Oxidation of Butane in Solid Oxide Fuel Cells*. Journal of Power Sources, 2013. **241**(0): p. 783-790.
41. Sun, C., R. Hui, and J. Roller, *Cathode Materials for Solid Oxide Fuel Cells: A Review*. Journal of Solid State Electrochemistry, 2010. **14**(7): p. 1125-1144.
42. Ding, D., Xiayi, L., Samson Yuxiu, L., Kirk, G. and Meilin, L. *Enhancing SOFC Cathode Performance by Surface Modification Through Infiltration*. Energy & Environmental Science, 2014. **7**(2): p. 552-575.
43. Sayers, R., Rieu, M., Lenormand, P., Ansart, F., Kilner, J.A. and Skinner, S.J., *Development of Lanthanum Nickelate as a Cathode for Use in Intermediate Temperature Solid Oxide Fuel Cells*. Solid State Ionics, 2011. **192**(1): p. 531-534.
44. Chueh, W.C. and S.M. Haile, *Electrochemistry of Mixed Oxygen Ion and Electron Conducting Electrodes in Solid Electrolyte Cells*. Annual Review of Chemical and Biomolecular Engineering, 2012. **3**: p. 313-341.
45. Kim, J.J., Kuhn, M., Bishop, S.R. and Tuller, H.L., *Cathodic and Defect Properties of Ba<sub>x</sub>Sr<sub>1-x</sub>Ti<sub>1-y</sub>Fe<sub>y</sub>O<sub>3-y/2+δ</sub> Mixed Conducting Oxides*. Solid State Ionics, 2013. **230**(0): p. 2-6.
46. Xu, D. and S.F. Xu. *Preparation and Properties of Ni-Doped Ce<sub>0.85</sub>Sm<sub>0.15</sub>O<sub>1.925</sub> Ceramics for Use as Electrolytes in IT-SOFCs in Advanced Materials Research*. 2013. Trans Tech Publications: p.105-112.
47. Muhammed Ali, S., Muchtar, A., Muhamad, N. and Sulong, A.B., *A Review on Preparation of SDC-Carbonate as Composite Electrolyte Material for Intermediate Temperature Solid Oxide Fuel Cells (IT-SOFC)*, Clean Energy and Technology (CET), 2011. p. 394-399.
48. Pinedo, R., Ruiz de Larramendi, I., Jimenez de Aberasturi, D., Gil de Muro, I., Ortiz-Vitoriano, N. and Rojo, T., *Novel Pr<sub>0.6</sub>Sr<sub>0.4</sub>Fe<sub>0.8</sub>Co<sub>0.2</sub>O<sub>3</sub>: Ce<sub>0.8</sub>Sm<sub>0.2</sub>O<sub>2</sub> Composite*

- Nanotubes for Energy Conversion and Storage*. Journal of Power Sources, 2012. **201**: p. 332-339.
49. Beie, H., Blum, L., Drenckhahn, W., Greiner, H., Rudolf, B. and Schichl, H., *SOFC Development at Siemens. in the Proc. of 5th Inter. Symposium on SOFC. Aachen, Germany*. 1997.
  50. Lee, K.T. and E.D. Wachsman, *Role of Nanostructures on SOFC Performance at Reduced Temperatures*. MRS Bulletin, 2014. **39**(09): p. 783-791.
  51. Liu, Z., Ding, D., Liu, M., Ding, X., Chen, D., Li, X., Xia, C. and Liu, M., *High-Performance, Ceria-Based Solid Oxide Fuel Cells Fabricated at Low Temperatures*. Journal of Power Sources, 2013. **241**(0): p. 454-459.
  52. Zhang, S.-L., Li, C., Li, C., Yang, G. and Han, Z., *Scandia-Stabilized Zirconia Electrolyte with Improved Interlamellar Bonding by High-Velocity Plasma Spraying for High Performance Solid Oxide Fuel Cells*. Journal of Power Sources, 2013. **232**(0): p. 123-131.
  53. De Volder, M.F.L., Tawfick, S.H., Baughman, R.H. and Hart, A.J., *Carbon Nanotubes: Present and Future Commercial Applications*. Science, 2013. **339**(6119): p. 535-539.
  54. Minh, N.Q., *Solid Oxide Fuel Cell Technology—Features and Applications*. Solid State Ionics, 2004. **174**(1–4): p. 271-277.
  55. Bai, C. and M. Liu, *From Chemistry to Nanoscience: Not Just a Matter of Size*. Angewandte Chemie International Edition, 2013. **52**(10): p. 2678-2683.
  56. Mijatovic, D., J. Eijkel, and A. van Den Berg, *Technologies for Nanofluidic Systems: Top-Down vs. Bottom-Up—A Review*. Lab on a Chip, 2005. **5**(5): p. 492-500.
  57. Baughman, R.H., A.A. Zakhidov, and W.A. de Heer, *Carbon Nanotubes-The Route Toward Applications*. Science, 2002. **297**(5582): p. 787-792.
  58. Sharma, P. and M. Bhargava, *Applications and Characteristics of Nanomaterials in Industrial Environment*. Research and Development (IJCSEIERD), 2013. **3**(4): p. 63-72.
  59. Cao, G., *Nanostructures and Nanomaterials*. 2004: Imperial College Press. World Scientific Publishing, Singapore, 2011. p. 1-40.
  60. Edwards, B. and D. Turrent, *Sustainable Housing: Principles and Practice*. 2013: Taylor & Francis. p. 1-11.

61. Zäch, M., Hagglund, C., Chekorov, D. and Kasemo, B., *Nanoscience and Nanotechnology for Advanced Energy Systems*. Current Opinion in Solid State and Materials Science, 2006. **10**(3): p. 132-143.
62. Boudghene Stambouli, A. and E. Traversa, *Fuel Cells, an Alternative to Standard Sources of Energy*. Renewable and Sustainable Energy Reviews, 2002. **6**(3): p. 295-304.
63. Mao, S.S. and Chen, X., *Selected Nanotechnologies for Renewable Energy Applications*. International Journal of Energy Research, 2007. **31**(6-7): p. 619-636.
64. Nakada, K., Fujita, M., Dresselhaus, G. and Dresselhaus, M.S., *Edge State in Graphene Ribbons: Nanometer Size Effect and Edge Shape Dependence*. Physical Review B, 1996. **54**(24): p. 17954-17961.
65. Jain, P.K. and M.A. El-Sayed, *Surface Plasmon Coupling and Its Universal Size Scaling in Metal Nanostructures of Complex Geometry: Elongated Particle Pairs And Nanosphere Trimers*. The Journal of Physical Chemistry C, 2008. **112**(13): p. 4954-4960.
66. Sun, C.Q., *Dominance of Broken Bonds and Nonbonding Electrons at the Nanoscale*. Nanoscale, 2010. **2**(10): p. 1930-1961.
67. Sohlberg, K., *Introducing The Core Concepts of Nanoscience and Nanotechnology: Two Vignettes*. Journal of Chemical Education, 2006. **83**(10): p. 1516-1520.
68. Wang, Y. and N. Herron, *Nanometer-Sized Semiconductor Clusters: Materials Synthesis, Quantum Size Effects, and Photophysical Properties*. The Journal of Physical Chemistry, 1991. **95**(2): p. 525-532.
69. Zhang, J.Z., *Optical Properties and Spectroscopy of Nanomaterials*. 2009: World Scientific. University of California, Santa Cruz, USA. p. 24-26.
70. Whitesides, G.M. and B. Grzybowski, *Self-Assembly at All Scales*. Science, 2002. **295**(5564): p. 2418-2421.
71. Martin, C.R., *Membrane-Based Synthesis of Nanomaterials*. Chemistry of Materials, 1996. **8**(8): p. 1739-1746.
72. Huczko, A., *Template-Based Synthesis of Nanomaterials*. Applied Physics A, 2000. **70**(4): p. 365-376.
73. Mackenzie, J.D. and E.P. Bescher, *Chemical Routes in the Synthesis of Nanomaterials Using the Sol–Gel Process*. Accounts of Chemical Research, 2007. **40**(9): p. 810-818.
74. Kodas, T.T. and M.J. Hampden-Smith, *The Chemistry of Metal CVD*. 2008: John Wiley and Sons. Weinhein, New York. p. 23-127.

75. Xu, Y. and X.-T. Yan, *Introduction to Chemical Vapour Deposition*. Chemical Vapour Deposition: An Integrated Engineering Design for Advanced Materials, 2010: p. 1-28.
76. Vahlas, C., Caussat, B., Serp, P. and Angelopoulos, G.N., *Principles and Applications of CVD Powder Technology*. Materials Science and Engineering: R: Reports, 2006. **53**(1): p. 1-72.
77. Archer, N.J., *Chemical Vapour Deposition*. Physics in Technology, 1979. **10**. p. 152-160.
78. Choy, K.L., *Chemical Vapour Deposition of Coatings*. Progress in Materials Science, 2003. **48**(2): p. 57-170.
79. Piszczek, P., Szymanska, I.B., Talik, E. and Heimann, J., *Deposition of Thin Copper Layers using Copper (II) Carboxylate Complexes with tert-Butylamine as New CVD Precursors*. Chemical Vapor Deposition, 2013. **19**(7-8-9): p. 251-259.
80. Georgi, C., Hildebrandt, A., Waechter, T., Schulz, S.E., Gessner, T. and Lang, H., *A Cobalt Layer Deposition Study: Dicobaltatetrahydroxides as Convenient MOCVD Precursor Systems*. Journal of Materials Chemistry C, 2014. **2**: p. 4676-4682.
81. Pedersen, H. and S.D. Elliott, *Studying Chemical Vapor Deposition Processes with Theoretical Chemistry*. Theoretical Chemistry Accounts, 2014. **133**(5): p. 1-10.
82. Prasek, J., Drbohlavova, J., Chomoucka, J., Hubalek, J., Jasek, O., Adam, V. and Kizek, R., *Methods for Carbon Nanotube Synthesis—Review*. Journal of Materials Chemistry, 2011. **21**(40): p. 15872-15884.
83. Serp, P., P. Kalck, and R. Feurer, *Chemical Vapor Deposition Methods for the Controlled Preparation of Supported Catalytic Materials*. Chemical Reviews, 2002. **102**(9): p. 3085-3128.
84. Reddy, A.L.M. and S. Ramaprabhu, *Nanocrystalline Metal Oxides Dispersed Multiwalled Carbon Nanotubes as Supercapacitor Electrodes*. The Journal of Physical Chemistry C, 2007. **111**(21): p. 7727-7734.
85. Liu, Y., Rauch, W., Zha, S. and Liu, M., *Fabrication of  $Sm_{0.5}Sr_{0.5}CoO_{3-\delta}$ - $Sm_{0.1}Ce_{0.9}O_{2-\delta}$  Cathodes for Solid Oxide Fuel Cells using Combustion CVD*, 2004. **166**(3-4): p. 261-268.
86. Kong, L., Wang, J., Luo, T., Meng, F., Chen, X. and Liu, J., *Novel Pyrenehexafluoroisopropanol Derivative-Decorated Single-Walled Carbon*

- Nanotubes for Detection of Nerve Agents by Strong Hydrogen-Bonding Interaction*. Analyst, 2010. **135**(2): p. 368-374.
87. Garcia, G., Merino, R.I., Orera, V.M, Larrea, A., Pena, J.I., Laguna-Barcero, M.A., Pardo, J.A., Santiso, J. and Figueras, A., *Ytria-Stabilized Zirconia Thin Film Deposition on NiO-CSZ Anodes by Pulse Injection MOVCD for Intermediate Temperature SOFC Applications*. Chemical Vapour Deposition, 2004. **10**(5): p. 249-252.
  88. Kikuchi, K., Okada, K. and Mineshige, A., *Growth Mechanism of Thin Films of Ytria-Stabilized Zirconia by Chemical Vapor Infiltration using NiO–Ceria Substrate as Oxygen Source*. Journal of Power Source, 2006. **162**(2): p. 1060-1066.
  89. Torres-Huerta A.M., Vargas-García, J.R. and Domínguez-Crespo, M.A., *Preparation and Characterization of IrO<sub>2</sub>–YSZ Nanocomposite Electrodes by Metal Oxide Chemical Vapour Deposition*. Solid State Ionics, 2007. **178**(29-30): p. 1608-1616.
  90. El Habra, A.S., Marco B., Monica F., Maurizio C., Stefano B. and Lioudmila G.R., *A Study on Sc<sub>2</sub>O<sub>3</sub>-Stabilized Zirconia Obtained by MOCVD as a Potential Electrolyte for Solid Oxide Fuel Cells*. Chemical Vapour Deposition, 2012. **18**(10-12): p. 289-294.
  91. Toro, D.M.R. Fiorito, Fragalà, M.E., Barbuccib, A., Carpaneseb, M.P. and Malandrino, G., *A Novel MOCVD Strategy for the Fabrication of Cathodes in a Solid Oxide Fuel Cell: Synthesis of La<sub>0.8</sub>Sr<sub>0.2</sub>MnO<sub>3</sub> Films on YSZ Electrolyte Pellets*. Materials Chemistry and Physics, 2010. **124**(2-3): p. 1015-1021.
  92. Schlupp, M.V.F., Krlov, A., Hwang, J., Zang, Z., Son, J.W. and Gauckler, L.J., *Gadolinia Doped Ceria Thin Films Prepared by Aerosol Assisted Chemical Vapour Deposition and Applications in ITSOFC*. Fuel Cells, 2013. **13**(5): p.658-665.
  93. Sansernnivet, M., Leosiripojana, N., Assabumrungrat, S. and Charojrochkul, S., *Fabrication of La<sub>0.8</sub>Sr<sub>0.2</sub>CrO<sub>3</sub>-Based Perovskite Film via Flame-Assisted Vapor Deposition for H<sub>2</sub> Production by Reforming*. Chemical Vapour Deposition, 2010. **16**(10-12): p. 311-321.
  94. Oldroyd, D.R., *Mineralogy and the 'Chemical Revolution'*. Centaurus, 1975. **19**(1): p. 54-71.

95. Bergman, T. and Paulin, J., *Dissertatio Gradualis de Primordiis Chemiae*. Typis Johan. Edman. p. 1735-1784.
96. Berner, R.A. and Maasch, K.A., *Chemical Weathering and Controls on Atmospheric O<sub>2</sub> and CO<sub>2</sub>: Fundamental Principles were Enunciated by JJ Ebelmen in 1845*. *Geochimica et Cosmochimica Acta*, 1996. **60**(9): p. 1633-1637.
97. Graham, T., *On the Properties of Silicic Acid and Other Analogous Colloidal Substances*. *Journal of Chemical Society*, 1864. **17**: p. 318-327.
98. Hench, L.L. and Orefice, R., *Sol-Gel Technology*. *Encyclopedia of Chemical Technology*, 1998. John Wiley and Sons: p. 1-28.
99. Hench, L.L. and West, J.K., *The Sol-Gel Process*. *Chemical Reviews*, 1990. **90**(1): p. 33-72.
100. Minami, T., *Advanced Sol-Gel Coatings for Practical Applications*. *Journal of Sol-Gel Science and Technology*, 2013. **65**(1): p. 4-11.
101. Ciriminna, R., *The Sol-Gel Route to Advanced Silica-Based Materials and Recent Applications*. *Chemical Reviews*, 2013. **113**(8): p. 6592-6620.
102. Debecker, D.P., V. Hulea, and P.H. Mutin, *Mesoporous Mixed Oxide Catalysts via Non-Hydrolytic Sol-Gel: A Review*. *Applied Catalysis A: General*, 2013. **451**(0): p. 192-206.
103. Courtina, P., Boy, P., Piquero, T., Vulliet, J., Poirot, N. and Laberty-Robert, N., *A Composite Sol-Gel Process to Prepare a YSZ Electrolyte for Solid Oxide Fuel Cells*. *Journal of Power Sources*, 2012. **206**: p. 77-83.
104. Kim, S.D., Hyun, S.H., Moon, J., Kim, J. and Song, R.H., *Fabrication and Characterization of Anode-Supported Electrolyte Thin Films for Intermediate Temperature Solid Oxide Fuel Cells*. *Journal of Power Sources*, 2005. **139**(1-2): p. 67-72.
105. Yoon, S.P., Han, J., Nam, S.W., Lim, T., Oh, I., Hong, S., Yoo, Y. and Lim, H.C., *Performance of Anode-Supported Solid Oxide Fuel Cell with La<sub>0.85</sub>Sr<sub>0.15</sub>MnO<sub>3</sub> Cathode Modified by Sol-Gel Coating Technique*. *Journal of Power Sources*, 2002. **106**(1): p. 160-166.
106. Laberty-Robert, C., Long, J.W., Lucas, M.E., Pettigrew, K.A., Stroud, R.M., Doescher, M.S. and Rolison, D.R., *Sol-Gel-Derived Ceria Nanoarchitectures: Synthesis, Characterization, and Electrical Properties*. *Chemistry of Materials*, 2006. **18**(1): p. 50-58.

107. Kim, S.G., Yoon, S.P., Nam, S.W., Hyun, S. and Hong, S., *Fabrication and Characterization of a YSZ/YDC Composite Electrolyte by a Sol–Gel Coating Method*. Journal of Power Sources, 2002. **110**(1): p. 222-228.
108. Gaudon, M., Laberty-Robert, C., Ansart, F.A., Stevens, P. and Rousset, A., *Preparation and Characterization of  $La_{1-x}Sr_xMnO_{3+\delta}$  ( $0 \leq x \leq 0.6$ ) Powder by Sol–Gel Processing*. Solid State Sciences, 2002. **4**(1): p. 123-133.
109. Zhang, Q.L., O'Brien, S.C., Heath, J.R., Liu, Y., Curl, R.F., Kroto, H.W. and Smalley, R.E., *Reactivity of Large Carbon Clusters: Spheroidal Carbon Shells and their Possible Relevance to the Formation and Morphology of Soot*. The Journal of Physical Chemistry, 1986. **90**(4): p. 525-528.
110. Iijima, S., *Helical Microtubules of Graphitic Carbon*. Nature, 1991. **354**(6348): p. 56-58.
111. Kokai, F., Takahashi, K., Yudasaka, M., Yamada, R., Ichihashi, T. and Iijima, S., *Growth Dynamics of Single-Wall Carbon Nanotubes Synthesized by  $CO_2$  Laser Vaporization*. The Journal of Physical Chemistry B, 1999. **103**(21): p. 4346-4351.
112. Weiss, V., Thiruvengadathan, R. and Regev, O., *Preparation and Characterization of a Carbon Nanotube–Lyotropic Liquid Crystal Composite*. Langmuir, 2005. **22**(3): p. 854-856.
113. Tasis, D., Tagmatarchis, N., Bianco, A. and Prato, M., *Chemistry of Carbon Nanotubes*. Chemical Reviews, 2006. **106**(3): p. 1105-1136.
114. Popov, V.N., *Carbon Nanotubes: Properties and Application*. Materials Science and Engineering: R: Reports, 2004. **43**(3): p. 61-102.
115. Lehman, J.H., Terrones, M, Mansfield, E., Hurst, K.E. and Meunier, V., *Evaluating the Characteristics of Multiwall Carbon Nanotubes*. Carbon, 2011. **49**(8): p. 2581-2602.
116. Mansfield, E., Kar, A., Wang, C.M. and Chiaromonti, A.N., *Statistical Sampling of Carbon Nanotube Populations by Thermogravimetric Analysis*. Analytical and Bioanalytical Chemistry, 2013. **405**(25): p. 1-7.
117. Ávila-Orta, C., Raudry-Lopez, C.E., Davila-Rodriguez, V.J., Neira-Velazquez, M.G., Medellin-Rodriguez, F.J. and Hsiao, B.S., *Morphology, Thermal Stability, and Electrical Conductivity of Polymer Nanocomposites of Isotactic Polypropylene/Multi-Walled Carbon Nanotubes*. International Journal of Polymeric Materials and Polymeric Biomaterials, 2013. **62**(12): p. 635-641.

118. Omachi, H., Segawa, Y. and Itami, K., *Synthesis of Cycloparaphenylenes and Related Carbon Nanorings: a Step Toward the Controlled Synthesis of Carbon Nanotubes*. *Accounts of Chemical Research*, 2012. **45**(8): p. 1378-1389.
119. An, Z., Furmanchuk, A., Ramachandramoorthy, R., Filletter, T., Roenbeck, M.R., Espinosa, H.D., Schatz, G.C. and Nguyen, S.T., *Inherent Carbonaceous Impurities on Arc-Discharge Multiwalled Carbon Nanotubes and their Implications for Nanoscale Interfaces*. *Carbon*, 2014. **80**: p. 1-11.
120. Zhang, Y.L., Liu, C. and Cheng, H., *De-Bundling of Single-Wall Carbon Nanotubes Induced by an Electric Field During Arc Discharge Synthesis*. *Carbon*, 2014. **74**: p. 370-373.
121. Holloway, B.C., Eklund, P.C., Smith, M.W., Jordan, K.C. and Shinn, M., *Laser Ablation for the Synthesis of Carbon Nanotubes*. Jefferson Sciences Associates, 2012, p. 2-8.
122. Ka, I., Le Borgne, V., Ma, D. and El Khakani, M.A., *Pulsed Laser Ablation Based Direct Synthesis of Single-Wall Carbon Nanotube/PbS Quantum Dot Nanohybrids Exhibiting Strong, Spectrally Wide and Fast Photoresponse*. *Advanced Materials*, 2012. **24**(47): p. 6288-6288.
123. Bamoharram, F.F., Ahmadpour, A. and Heravi, M.M., *Synthesis of Carbon Nanotubes via Catalytic Chemical Vapor Deposition Method and Their Modification with Preyssler Anion,  $[NaP_5W_{30}O_{110}]^{14-}$* . *Nano*, 2011. **6**(04): p. 349-355.
124. Elliott, J.A., Shibuta, Y., Amara, H., Bichara, C. and Neyts, E.C., *Atomistic Modelling of CVD Synthesis of Carbon Nanotubes and Graphene*. *Nanoscale*, 2013. **5**(15): p. 6662-6676.
125. Kumar, M. and Ando, Y., *Chemical Vapor Deposition of Carbon Nanotubes: a Review on Growth Mechanism and Mass Production*. *Journal of Nanoscience and Nanotechnology*, 2010. **10**(6): p. 3739-3758.
126. Paradise, M. and T. Goswami, *Carbon Nanotubes—Production and Industrial Applications*. *Materials and Design*, 2007. **28**(5): p. 1477-1489.
127. Belin, T. and Epron, F., *Characterization Methods of Carbon Nanotubes: A Review*. *Materials Science and Engineering: B*, 2005. **119**(2): p. 105-118.
128. Che, G., Lakshmi, B.B., Martin, C.R. and Fisher, E.R., *Metal-Nanocluster-Filled Carbon Nanotubes: Catalytic Properties and Possible Applications in Electrochemical Energy Storage and Production*. *Langmuir*, 1999. **15**(3): p. 750-758.

129. Hinds, B.J., Chopra, N., Rantell, T., Andrews, R., Gavalas, V. and Bachas, L.G., *Aligned Multiwalled Carbon Nanotube Membranes*. Science, 2004. **303**(5654): p. 62-65.
130. Wang, J., Musameh, M. and Lin, Y., *Solubilization of Carbon Nanotubes by Nafion toward the Preparation of Amperometric Biosensors*. Journal of the American Chemical Society, 2003. **125**(9): p. 2408-2409.
131. Thostenson, E.T., Ren, Z. and Chou, T.W., *Advances in the Science and Technology of Carbon Nanotubes and their Composites: A Review*. Composites Science and Technology, 2001. **61**(13): p. 1899-1912.
132. Pan, X. and Bao, X., *The Effects of Confinement Inside Carbon Nanotubes on Catalysis*. Accounts of Chemical Research, 2011. **44**(8): p. 553-562.
133. Santangelo, S., Piperopoulos, E., Faggio, G., Lanza, M., Messina, G. and Milone, C., *Taguchi-Optimized Catalytic Growth of Carbon Nanotubes for Applications in Electro-Catalysis*. J. Chem, 2013. **7**: p. 748-758.
134. Lai, S.C., Dudin, P.V., Macpherson, J.V. and Unwin, P.R., *Visualizing Zeptomole (Electro) Catalysis at Single Nanoparticles within an Ensemble*. Journal of the American Chemical Society, 2011. **133**(28): p. 10744-10747.
135. Jiang, S.P., *Nanoscale and Nano-Structured Electrodes of Solid Oxide Fuel Cells by Infiltration: Advances and Challenges*. International Journal of Hydrogen Energy, 2012. **37**(1): p. 449-470.
136. Cox, P., *The Surface Science of Metal Oxides*. 1994: Cambridge University Press, New York: p. 1-425.
137. Islam, M.A., Rondinelli, J.M., and Spanier, J.E., *Normal Mode Determination of Perovskite Crystal Structures with Octahedral Rotations: Theory and Applications*. Journal of Physics: Condensed Matter, 2013. **25**(17): p. 175902.
138. Boulahya, K., Ruiz-Morales, J.C., Hernando, M., Gonzalez-Calbet, J.M. and Parras, M., *Synthesis, Structural, Magnetic, and Electrical Study of BaSrCo<sub>2</sub>O<sub>5</sub>, a Highly Disordered Cubic Perovskite*. Chemistry of Materials, 2009. **21**: p. 2045–2054.
139. Byrappa, K., Dayananda, A.S., Sajan, C.P., Basavalingu, B., Shayan, M.B., Soga, K. and Yoshimure, M., *Hydrothermal Preparation of ZnO:CNT and TiO<sub>2</sub>:CNT Composites and their Photocatalytic Applications*. Journal of Materials Science, 2008. **43**(7): p. 2348-2355.

140. Chalmers, J.M., Edwards, H.G. and Hargreaves, M.D., *Vibrational Spectroscopy Techniques: Basics and Instrumentation*. Infrared and Raman Spectroscopy in Forensic Science, 2012: p. 9-15.
141. Kazarian, S.G. and Chan, K.A., *ATR-FTIR Spectroscopic Imaging: Recent Advances and Applications to Biological Systems*. Analyst, 2013. **138**(7): p. 1940-1951.
142. Kuzmany, H., Burger, B., Thess, A. and Smalley, R.E., *Vibrational Spectra of Single Wall Carbon Nanotubes*. Carbon, 1998. **36**(5): p. 709-712.
143. Kuznetsova, A., Mawhinney, D.B., Naumenko, V., Yates Jr, J.T., Liu, J. and Smalley, R.E., *Enhancement of Adsorption Inside of Single-Walled Nanotubes: Opening the Entry Ports*. Chemical Physics Letters, 2000. **321**(3): p. 292-296.
144. Eklund, P., Holden, J. and Jishi, R., *Vibrational Modes of Carbon Nanotubes; Spectroscopy and Theory*. Carbon, 1995. **33**(7): p. 959-972.
145. Dresselhaus, M.S., Dresselhaus, G., Saito, R. and Jorio, A., *Raman Spectroscopy of Carbon Nanotubes*. Physics Reports, 2005. **409**(2): p. 47-99.
146. Smith, E. and G. Dent, *Modern Raman Spectroscopy: A Practical Approach*. 2013: John Wiley and Sons. USA.
147. Rai, N., Lakshmana, A.Y., Namboodiri, V.V. and Umapathy, S., *Basic Principles of Ultrafast Raman Loss Spectroscopy*. Journal of Chemical Sciences, 2012. **124**(1): p. 177-186.
148. Jorio, A., Pimenta, M.A., Souza Filho, A.G., Saito, R., Dresselhaus, G. and Dresselhaus, M.S., *Characterizing Carbon Nanotube Samples with Resonance Raman Scattering*. New Journal of Physics, 2003. **5**(1): p. 139.1-139.17.
149. Dresselhaus, M.S., Jorio, A., Hofmann, M., Dresselhaus, G. and Saito, R., *Perspectives on Carbon Nanotubes and Graphene Raman Spectroscopy*. Nano Letters, 2010. **10**(3): p. 751-758.
150. Casiraghi, C., Hartschuh, A., Qian, H. and Piscanec, S, *Raman Spectroscopy of Graphene Edges*. Nano Letters, 2009. **9**(4): p. 1433-1441.
151. Prime, R.B., Bair, H.E., Vyazovkin, S., Gallogher, P.K. and Riga, A., *Thermogravimetric Analysis (TGA)*. Thermal Analysis of Polymers, Fundamentals and Applications, Wiley, Hoboken, NJ, 2009: p. 241-317.
152. Al-Jughiman, M.K., Al-Omair, M.A., van Arsdell, G.S., Morell, V.O. and Jacobs, M.L., *D-Transposition of the Great Arteries with Ventricular Septal Defect and Left Ventricular Outflow Tract Obstruction (D-TGA/VSD/LVOTO): A Survey of Perceptions, Preferences, and Experience*. Pediatric cardiology, 2015: p. 1-10.

153. Wiedemann, H., *Simultaneous TGA-DTA Measurements In Connection with GAS—Analytical Investigations*. Thermal Analysis V1: Instrumentation, Organic Materials, and Polymers, 2012. **1**: p. 229.
154. Craig, D.Q. and M. Reading, *Thermal Analysis of Pharmaceuticals*. 2014: CRC Press. Boca Raton, USA: p. 139-193.
155. Nanda, J., Martha, S., Porter, W.D., Wang, H., Dudney, N.J., Rdin, M.D. and Siegel, D.T., *Thermophysical Properties of LiFePO<sub>4</sub> Cathodes with Carbonized Pitch Coatings and Organic Binders: Experiments and First-Principles Modeling*. Journal of Power Sources, 2014. **251**: p. 8-13.
156. Haines, P.J., *Principles of Thermal Analysis and Calorimetry*. 2002: Royal Society of Chemistry. Farnham, UK. p. 1-30.
157. Bom, D., *Thermogravimetric Analysis of the Oxidation of Multiwalled Carbon Nanotubes: Evidence for the Role of Defect Sites in Carbon Nanotube Chemistry*. Nano Letters, 2002. **2**(6): p. 615-619.
158. Almeida, V., Balzaretto, N.M., Costa, T.M., Machodo, G.B. and Gallas, M.R., *Surfactants for CNTs Dispersion in Zirconia-Based Ceramic Matrix by Sol-Gel Method*. Journal of Sol-Gel Science and Technology, 2013. **65**(2): p. 143-149.
159. Guinebretière, R., *X-ray Diffraction by Polycrystalline Materials*. 2013: John Wiley & Sons.
160. Glazer, A., *The First Paper by WL Bragg—What and When?* Crystallography Reviews, 2013. **19**(3): p. 117-124.
161. Tessonier, J.-P., *Analysis of the Structure and Chemical Properties of some Commercial Carbon Nanostructures*. Carbon, 2009. **47**(7): p. 1779-1798.
162. Briggman, K.L. and D.D. Bock, *Volume Electron Microscopy for Neuronal Circuit Reconstruction*. Current Opinion in Neurobiology, 2012. **22**(1): p. 154-161.
163. Klein, T., E. Buhr, and C. Georg Frase, *Chapter 6-TSEM: A Review of Scanning Electron Microscopy in Transmission Mode and Its Applications*, in *Advances in Imaging and Electron Physics*, W.H. Peter, Editor. 2012, Elsevier. p. 297-356.
164. Bogner, A., *A History of Scanning Electron Microscopy Developments: Towards “Wet-STEM” Imaging*. Micron, 2007. **38**(4): p. 390-401.
165. Fultz, B. and J.M. Howe, *Transmission Electron Microscopy and Diffractometry of Materials*. 2012: Springer, Berlin, Heidelberg, New York, USA. p. 1-48.

166. Hayat, M., *Basic techniques for transmission electron microscopy*. 2012: Elsevier. London, UK. p. 100-300.
167. Flannigan, D.J. and A.H. Zewail, *4D Electron Microscopy: Principles and Applications*. Accounts of Chemical Research, 2012. **45**(10): p. 1828-1839.
168. Spence, J.C., *High-Resolution Electron Microscopy*. 2013: Oxford University Press. p. 88-303.
169. Meyer, J.C., Kurasch, S., Park, H.J., Skakalova, V., Kunzel, D., Grob, A., Chuvilin, A., Algara-Siller, G., Roth, S., Iwasaki, T. Starke, U., Smet, J.H. and Kaiser, U., *Experimental Analysis of Charge Redistribution Due to Chemical Bonding by High-Resolution Transmission Electron Microscopy*. Nature Materials, 2011. **10**(3): p. 209-215.
170. Milewski, J., *A Mathematical Model of SOFC: A Proposal*. Fuel Cells, 2012. **12**(5): p. 709-721.
171. Zhu, H. and R.J. Kee, *A General Mathematical Model for Analyzing the Performance of Fuel-Cell Membrane-Electrode Assemblies*. Journal of Power Sources, 2003. **117**(1): p. 61-74.
172. Keith, J., *Tafel Equation and Fuel Cell Kinetic Losses*. 2010. Michigan Technology University. p. 80-90.
173. Yang, S., Chen, T., Wang, Y., Peng, Z. and Wang, W.G., *Electrochemical Analysis of an Anode-Supported SOFC*. International Journal of Electrochemical Science, 2013. **8**. p. 2330-2344.
174. Lanzini A., Santarelli, M., Asinari P. and Cali M., *Polarization Analysis and Microstructural Characterization of SOFC Anode and Electrolyte Supported Cells*. The Society for Solid State and Electrochemical Science and Technology, 2006. **12**(1): p. 343-353.
175. Lijun, Y., Tongbo, W., Jianchang, Y., Zhe, L., Junxi, W. and Jinmin, L., *MOCVD Epitaxy of InAlN on Different Templates*. Journal of Semiconductors, 2011. **32**(9): p. 1088-1674.
176. Howe, K.S., *Design Improvements of Micro-Tubular Solid Oxide Fuel Cells for Unmanned Aircraft Applications*. Centre for Hydrogen and Fuel Cell Research, 2013. University of Birmingham, Edgbaston. p. 4-90.
177. He, W., Zou, J., Wang, B., Vilayurganapathy, S., Zhou, M., Lin, X., Zhang, K.H.L., Lin, J., Xu, P. and Dickerson, J.H., *Gas Transport in Porous Electrodes of Solid*

- Oxide Fuel Cells: A Review on Diffusion and Diffusivity Measurement*. Journal of Power Sources, 2013. **237**(0): p. 64-73.
178. Khan, A, Khan, K, Mahmood, A., Murtaza, G., Akhtar, M.N., Ali, I., Shahid, M., Shakir, I. and Warsi, M.F., *Nanocrystalline  $La_{1-x}Sr_xCo_{1-y}Fe_yO_3$  Perovskites Fabricated by the Micro-Emulsion Route for High Frequency Response Device Fabrications*. Ceramics International, 2014. **40**(8, Part B): p. 13211-13216.
179. Stobinski, L., Lesiak, B., Kover, L., Toth, J., Biniak, S., Trykowski, G. and Judek, J., *Multiwall Carbon Nanotube Purification and Oxidation by Nitric Acid Studied by the FTIR and Electron Spectroscopy Methods*. Journal of Alloys and Compounds, 2010. **501**(1): p. 77-84.
180. Janardhanan, V.M., V. Heuveline, and O. Deutschmann, *Performance Analysis of a SOFC under Direct Internal Reforming Conditions*. Journal of Power Sources, 2007. **172**(1): p. 296-307.
181. Xu, D., Lu, P., Dai, P., Wang, H. and Ji, S., *In-Situ Synthesis of Multiwalled Carbon Nanotubes over  $LaNiO_3$  as Support of Cobalt Nanocluster Catalyst for Catalytic Applications*. The Journal of Physical Chemistry C, 2012. **116**(5): p. 3405-3413.
182. Shen, C. and L. Shaw, *FTIR Analysis of the Hydrolysis Rate in the sol-gel Formation of Gadolinia-Doped Ceria with Acetylacetonate Precursors*. Journal of Sol-Gel Science and Technology, 2010. **53**(3): p. 571-577.
183. Preis, W., Bucher, E. and Sitte, W., *Modeling of the Area-Specific Resistance of SOFC Cathodes by Application of a Square Grain Model Involving Grain Boundaries*. Fuel Cells, 2012. **12**(4): p. 543-549.
184. Meng, X., Gong, X., Yang, N., Tan, X., Yin, Y. and Ma, Z., *Fabrication of  $Y_2O_3$ -Stabilized- $ZrO_2$ (YSZ)/ $La_{0.8}Sr_{0.2}MnO_{3-\delta}$ -YSZ Dual Layer Hollow Fiber for the Cathode - Supported Micro-Tubular Solid Oxide Fuel Cells by Co-Spinning/Co-Sintering Technique*. Journal of Power Sources, 2013. **237**: p. 277-284.
185. Lee, S.-B., Khan, M.S., Wahyudi, W., Song, R., Lee, J., Lim, T. and Park, S., *Development of Anode Materials for SOFCs Having Enhanced Durability by Employing Sintering Inhibitors*. The Electrochemical Society, 2014. **14**(2): p. 5-9.
186. Thiele, D., Zuttel, A., *Electrochemical Characterization of Air Electrodes Based on  $La_{0.6}Sr_{0.4}CoO_3$  and Carbon Nanotubes*. Journal of Power Sources, 2008. **183**: p. 590-594.

187. Wang, X., Yang, Z., Sun, X., Li, X., Wang, D., Wang, P. and He, D., *NiO Nanocone Array Electrode with High Capacity and Rate Capability for Li-Ion Batteries*. Journal of Materials Chemistry, 2011. **21**(27): p. 9988-9990.
188. Sawant, P., Varma, S., Gonal, M.R., Wani, B.N., Prakash, D. and Bharadwaj, S.R., *Effect of Ni Concentration on Phase Stability, Microstructure and Electrical Properties of BaCe<sub>0.8</sub>Y<sub>0.2</sub>O<sub>3-δ</sub>-Ni Cermet SOFC Anode and its Application in Proton Conducting ITSOFC*. Electrochimica Acta, 2014. **120**: p. 80-85.
189. Pirkandi, J., Ghassemi, M., Hamed, M.H. and Mahammadi, R., *Electrochemical and Thermodynamic Modeling of a CHP System using Tubular Solid Oxide Fuel Cell (SOFC-CHP)*. Journal of Cleaner Production, 2012. **29**: p. 151-162.
190. Marina, O.A., Coyle, C.A., Edwards, D.J. and Stevenson, J.W., *Effect of Fuel Utilization on the Performance of Nickel/Zirconia Anode-Supported SOFCs*, 2012. The Electrochemical Society.
191. Cui, S.-H., Li, J., Zhou, X., Wang, G., Luo, J., Chaung, K.T., Bai, Y. and Qiao, L., *Cobalt Doped LaSrTiO<sub>3-δ</sub> as an Anode Catalyst: Effect of Co Nanoparticle Precipitation on SOFCs Operating on H<sub>2</sub>S-Containing Hydrogen*. Journal of Materials Chemistry A, 2013. **1**(34): p. 9689-9696.
192. Yoon, K.J., Lee, S., An, H., Kim, J., Son, J., Lee, J., Je, H., Lee, H. and Kim, B., *Gas Transport in Hydrogen Electrode of Solid Oxide Regenerative Fuel Cells for Power Generation and Hydrogen Production*. International Journal of Hydrogen Energy, 2014. **39**(8): p. 3868-3878.
193. Ye, L., Lv, W., Mao, Y., Yan, P. and He, W., *An Electrochemical Device for the Knudsen and Bulk Diffusivity Measurement in the Anodes of Solid Oxide Fuel Cells*. International Journal of Hydrogen Energy, 2014. **39**(27): p. 15057-15062.
194. Li, T., Wu, Z. and Li, K., *A Dual-Structured Anode/Ni-Mesh Current Collector Hollow Fibre for Micro-Tubular Solid Oxide Fuel Cells (SOFCs)*. Journal of Power Sources, 2014. **251**: p. 145-151.
195. Choi, S., Yoo, S., Kim, J., Park, S., Jun, A., Sengodan, S., Kim, J., Shin, J., Jeong, H.Y., Choi, Y., Kim, G. and Liu, M., *Highly Efficient and Robust Cathode Materials for Low-Temperature Solid Oxide Fuel Cells: PrBa<sub>0.5</sub>Sr<sub>0.5</sub>Co<sub>2-x</sub>Fe<sub>x</sub>O<sub>5+δ</sub>*. Scientific Report, 2013. **10**(3): p. 3-5.

196. Kaur, G., Pandey, O.P. and Singh, K., *Microstructural Analysis of Interfaces between Lanthanum Contained Glass and Two Different Electrolytes for SOFC Applications*. Fuel Cells, 2012. **12**(5): p. 739-748.
197. Chen, G.Z., Shaffer, M.S.P., Coleby, D., Dixon, G., Zhou, W., Fray, D.J. and Windle, A.H., *Carbon Nanotube and Polypyrrole Composites: Coating and Doping*. Advanced Materials, 2000. **12**(7): p. 522-526.
198. Desclaux, P., Nurnberger, S., Rzepka, M. and Stimming, U., *Investigation of Direct Carbon Conversion at the Surface of a YSZ Electrolyte in a SOFC*. International Journal of Hydrogen Energy, 2011. **36**(16): p. 10278-10281.
199. Fabbri, E., Bi, L., Pergolesi, D. and Traversa, E., *Towards the Next Generation of Solid Oxide Fuel Cells Operating Below 600° C with Chemically Stable Proton-Conducting Electrolytes*. Advanced Materials, 2012. **24**(2): p. 195-208.
200. Qiao, Y.Q., Tu, J.P., Xiang, J.Y., Wang, X.L., Mai, Y.J., Zhang, D. and Liu, W.L., *Effects of Synthetic Route on Structure and Electrochemical Performance of  $\text{Li}_3\text{V}_2(\text{PO}_4)_3/\text{C}$  Cathode Materials*. Electrochimica Acta, 2011. **56**(11): p. 4139-4145.
201. Zheng, M., Cao, J., Liao, S., Liu, J., Chen, H., Zhao, Y., Dai, W., Ji, G., Cao, J. and Tao, J., *Preparation of Mesoporous  $\text{Co}_3\text{O}_4$  Nanoparticles via Solid-Liquid Route and Effects of Calcination Temperature and Textural Parameters on Their Electrochemical Capacitive Behaviors*. The Journal of Physical Chemistry C, 2009. **113**(9): p. 3887-3894.
202. Yoshizumi, T., Taniguchi, S., Shiratori, Y. and Sasaki, K., *Sulfur Poisoning of SOFCs: Voltage Oscillation and Ni Oxidation*. Journal of the Electrochemical Society, 2012. **159**(11): p. 693-701.
203. Banger, K. K., Yamashita, Y., Mori, K., Peterson, R.L., Leedham, T., Rickard, J. and Sirringhaus, H., *Low-Temperature, High-Performance Solution-Processed Metal Oxide Thin-Film Transistors Formed by A 'Sol-Gel on Chip' Process*. Nature Materials, 2010. **10**(45-50).
204. Wu, W., Wang, G.L., Gaun, W.B., Zhenn, Y.F. and Wang, *Effect of Contact Method Between Interconnects and Electrodes on Area Specific Resistance in Planar Solid Oxide Fuel Cells*. Fuel Cells, 2013. **13**(5): p. 743-750.

